Plasmonic Gratings in Optoelectronics and Fluorescence Enhancement

by

Maryamossadat Amiri Naeini

A thesis submitted to the University of Ottawa
in partial fulfillment of the requirements for the degree of
Doctor of Philosophy in Physics

Department of Physics
Faculty of Science
University of Ottawa

© Maryamossadat Amiri Naeini, Ottawa, Canada, 2025

Abstract

This thesis is an article-based report on the investigation and innovations which highlight the importance of plasmonic gratings in new device physics studies, fluorescence enhancement, and novel telecommunication chips.

Plasmonic gratings are nanostructures created by periodically patterning a metal film with nanogrooves. These structures are capable of efficiently compensating the momentum mismatch between incident optical illumination and surface plasmon polariton (SPP) modes propagating along the metal film. Whilst a SPP mode is present on the film, one can benefit from their numerous advantageous features such as strong field enhancement in sub-diffraction-limit dimensions, and energetic hot carrier generation on the metal, to design new devices or study device physics. Plasmonic gratings can also perform as efficient structures in coupling the SPP modes on the surface to radiation channels.

A metal-oxide-semiconductor (MOS) based high speed electro optic modulator is reported encompassing a plasmonic grating on the metal layer. The incident optical beam excites SPP mode on the MOS structure via plasmonic grating. Applying the electrical data as a drive voltage to the MOS structure, modifies the effective refractive index of SPP mode through carrier refraction effect in semiconductor layer (Silicon), thereby, modulating the coupling efficiency of incident beam to SPP mode. This provides an intensity modulated beam at the reflection. Numerical analysis, and experimental passive and active characterization of the device is reported. The 5 μm modulator works up to 22 GHz with 4 dB insertion loss and modulation depth of 2% over an optical bandwidth of 100 nm. The modulator offers an innovative solution for non-contact wafer-level testing—a critical and costly step in wafer manufacturing that presents challenges and creates a bottleneck in the transition to smaller technology nodes.

The tunneling current in a similar MOS structure is measured and investigated theoretically. Studying the band diagram of the MOS device under accumulation and inversion regimes, shows that only Fowler-Nordheim tunneling is possible for the carriers transferring through the 5 nm thick Hafnium-dioxide (HfO_2) layer of the MOS structure. Theoretical modeling of the measured tunneling current shows a modified Fowler-Nordheim tunneling (MFN) law rules the dark current and photocurrent under inversion regime, fitting perfectly to the experimental results, and providing an opportunity to extract information such as the type and effective mass of the tunneling species, tunneling barrier height, and available population of carriers to initiate each tunneling process. A new tunneling channel of energetic holes created by SPPs on the metal surface is shown to be initiated from metal towards the semiconductor upon device illumination with an optical beam.

Plasmonic silver gratings had been previously shown to create fluorescing carbon emitters from fabrication residues. In this thesis, the role of SPPs on a plasmonic grating to excite fluorophores strongly and enhance the fluorescence intensity by creating fast and competitive radiation channels, is investigated experimentally. SPPs propagating on the plasmonic grating can couple to the grating diffraction orders, resulting in highly directive radiation which is studied via numerical simulations. Available SPP modes near fluorophores, also reduce the emitters' lifetime through the Purcell factor. This phenomenon is theoretically modelled and emitters' lifetime on the plasmonic grating is measured experimentally.

New fluorescence lifetime measurement method and plasmonic nanoantenna design for controlled localisation of fluorescence enhancement on a periodic structure surface is suggested as possible future research paths.

This thesis is dedicated to my wonderful and lovely husband, Mohammad, who stood by me with his whole heart and with an unshakable willingness to do whatever it took during my toughest moments. He truly believed in me when I could not, and his unwavering love and support helped me to find my path and happiness.

Acknowledgements

I would like to express my deepest gratitude to my supervisor, Professor Pierre Berini, for their invaluable guidance, encouragement, and patience throughout my PhD journey. I am truly grateful, first, for the precious opportunity to work in a leading research group with access to the state-of-the-art nanofabrication facilities and advanced electro-optical laboratory instrumentation, and second, for the trust and confidence my supervisor placed in me at every stage, which motivated me to bring my best to the exciting and novel research I pursued. I have learned tremendously and grown both personally and professionally through our many long hours of close collaboration and countless in-depth scientific discussions. None of this would have been possible without such a knowledgeable yet approachable supervisor, from whom I gained invaluable scientific insights, and learned greatly both professionally and personally.

I extend my sincere appreciation to all my colleagues in the lab and the nanofabrication facility, whose discussions, assistance, and camaraderie made both the research and everyday lab life enjoyable and stimulating. Special thanks to Dr. Saba Siadat Mousavi, Mr. Anthony Oliviery, and Dr. Jaspreet Walia for their genuine support, invaluable scientific contributions, and close companionship throughout this journey.

My heartfelt thanks go to my family —my sister Hengameh and my parents Shahin and Jamal —for their unwavering support, care, encouragement, understanding, and love from afar. Thank you for all the efforts you made throughout my journey to remain strong and cheerful, no matter how difficult things sometimes were back home, and for the patience you showed in enduring my absence for so many years. Who I am today is a reflection of the countless sacrifices you made and the confidence you placed in me at each and every stage.

Last and foremost, I would like to thank my wonderful and lovely husband, Mohammad, my best and dearest friend, and a true companion in every step of this journey. Thank you for your unwavering love and support, for countless hours of both scientific and joyful discussions, for all your patience and sacrifices, for believing in me even when I did not believe in myself, and for your invaluable companionship through all the ups and downs of this journey. Knowing that you are always there, understanding even the hardest moments without a word, gives me the strength and warmth to move forward strongly.

Table of Contents

Abstract i
Acknowledgements iii
Table of Contents iv
List of Figures v
1 Introduction 1
1.1 Thesis Scope and Outline 4
2 Literature Review 6
2.1 Plasmonic Electro-Optic Modulators 7
2.2 Plasmon Assisted Tunneling 12
2.3 Plasmon Enhanced Fluorescence 16
2.3.1 Plasmon Grating Enhanced Fluorescence 18
2.3.2 Lifetime Measurement Methods 21
3 High-Speed Electro-Optic Plasmonic Modulator for CMOS Non-Contact Wafer-Level Testing 27
3.1 Summary 27
3.2 Contribution 27
4 Infrared Surface Plasmons Open a Hole Tunneling Channel in Metal–Oxide–Semiconductor Structures 37
4.1 Summary 37
4.2 Contribution 37
5 Surface Plasmon Enhanced Photoluminescence of Carbon Dots Formed in-situ on Silver Gratings 55
5.1 Summary 55
5.2 Contribution 55
5.3 Additional Measurements (Amplified Spontaneous Emission) 82
6 Conclusion and Future Work 83
6.1 Concluding Remarks 83
6.2 Future work 83
7 Appendix 85
7.1 Silver Dipole Nano Antenna for Fluorescence Enhancement 85
7.2 Surface Plasmons on Silver Gratings Transform Pyrolytic Carbon into Luminescent Graphitized Carbon Dots 87
References 105

List of Figures

Figure 1(a) Dispersion relation of SPP mode at a metal-air interface [11]. (b) Top: schematic SPP surface charge density and electric field. Bottom: the magnitude of electric field component normal to the interface decays exponentially away from the interface [12]. 2
Figure 2 Surface plasmons excited by metallic grating coupler [12]. (a) Dispersion curves for the incident light (dashed grey), first order diffracted light by the grating (grey), and SPP modes propagating in the +x and -x direction (red). Blue lines show the Brillouin zone boundaries in k-space. Plasmons can only be excited at the frequencies where an intersection happens between the diffraction lines and the SPP mode line. (b) and (c) are two excited SPP modes with opposite propagation direction..... 3
Figure 3 Different fields of plasmonic hot carrier engineering for high performance infrared optoelectronic devices [17]. 6
Figure 4 Common mechanisms for electrical manipulation of carrier concentration shown in the waveguide cross section [20]. (a) Carrier accumulation behind an oxide barrier. (b) Carrier injection into intrinsic region. (c) Carrier depletion in a p-n junction..... 7
Figure 5 Plasmonic modulators using an organic electro optic material. (a) MZM phase modulator coupled to silicon waveguides [43] [44]. (b) MZI plasmonic modulator including a metal layer on arbitrary substrate and vertical grating couplers [45]. (c) A monolithic integration of plasmonic transmitter with CMOS electronics solving speed limit, thermal sensitivity, co-packaging [46]. 9
Figure 6 Ring resonator low-loss modulators [47] [48]. (a) Top and cross section view of the MIM ring modulator [47]. (b) Insertion loss against active plasmonic losses of the slot waveguide in MZM and slot resonator of ring resonator modulator. The arrows compare the two designs at equal performance in terms of modulation depth. Horizontal deviation of the arrows show that for same modulation performance, the resonance structure needs shorter active plasmonic section which lowers the plasmonic and transmission losses [47]. (c) Ring resonator with embedded plasmonic phase modulator and its performance principle based on resonance shift with applied voltage [48]. 10
Figure 7 PlasMOStor (MOS based silicon waveguide modulator) [49]. (a) Device cross section with source and drain channels represented. (b) Structure integrated with a p-i-n photodiode for all-optical silicon-based modulation. (c) Dispersion curves of the structure under depletion state with dark grey curves corresponding to optimal solutions and the grey scale representing the modes linewidths. SiO2 light line (black solid), silicon light line (cyan solid), plasmonic mode curve (lying to the right of silicon line), and photonic mode curve (lying to the left of the silicon line) are represented. The lower dotted line shows the 1550 nm wavelength and red and blue arrows show the modes propagating at this wavelength. The photonic mode has a relatively flat curve around this wavelength. 11
Figure 8 Role of quantum effects in the resonance of a plasmonic dimer [54]. (a) Classical predictions deviate from the real response of the system as quantum tunneling gets stronger for smaller dimer separations: filed enhancement is reduced strongly for gap sizes smaller than 1 nm. (b) Plasmonic resonance classically red shifts as the dimer gap shrinks, however, for smaller than 1 nm separation, the CTP mode appears which resonance blue shifts by lowering the gap size. 12
Figure 9 Evolution of plasmonic mode to quantum CTP mode as the inter particle distance changes. dQR is a crossover for gap distance at which the quantum and classical predictions diverge, defining the critical distance limit for classical plasmonic mode and fundamentally limiting the optical field confinement in the plasmonic cavity [57]. 13
Figure 10 Different tunneling regimes of sub nanometer size gap (0.4, 0.6, 0.8 nm) between plasmonic nano particles dependant on gap electric field magnitude and size [64]. In panel (b), grey area shows the energy levels of electrons initiating the tunneling process. In saturation regime, barriers are lowered below

electrons energy due to strong electric field across the gap, leading to the highest conductivity limited only by the population of supplied electrons from the first nanoparticle. 14
Figure 11 Schematic of the MIM structure of gold-h-BN-gold tunneling junction with the segmented and nanostructured bottom electrode controlling the optical properties of emission. Inset shows the band diagram of inelastic tunneling generating a photon [71]. 15
Figure 12 Fluorescence emission over a gold grating [110]. (a) Emission angle dependence on grating pitch. The black curve was resonantly excited at $\theta = 8.06°$ and the red curve excited at $\theta = 15°$ with TM-polarized beam and polarization independent collection. (b) Solid angle imaging of total fluorescence intensity for the sample with red curve in figure (a). (c) Solid angle imaging of polarization-controlled excitation and detection. (d) Line scans of images in figure (c). 19
Figure 13 Fluorescence enhancement of dye molecules over silver grating [112]. (a) Fluorescence intensity normalized to emission far from SPP resonance vs grating height. (b) Normalized emission intensity vs dye layer thickness. (c) Normalized SPP electric field magnitude above grating surface and along the groove of one grating period. The fluorescence emission intensity depends linearly on the local field intensity. 20
Figure 14 Study of $Eu3+$ ions above metallic grating [114]. (a) Lifetime of a monolayer of ions above silver grating with pitch of 415 nm and ridge height of 30 nm and 68 nm as a function of ion surface distance (solid circles). Open circles show the data for silver mirror. (b) Decay transients of ion monolayer 83 nm above a silver mirror on a grating with 415 nm pitch and 130 nm height. Lower panels show solid lines as the single exponential fit to measured data (open circles) and upper panels show the deviation between fit results and measure data. (c) Radiation pattern of ion monolayer 10.4 nm above silver grating with 415 nm pitch and 30 to 130 nm grating ridge heights. 21
Figure 15 Fluorescence lifetime measurement methods [96]. (a) Time-Domain method (pulse fluorometry). (b) Frequency-Domain method. (c) TCSPC method. From left to right: emission waveform if many photons were emitted per excitation pulse, time stamp of detected emission photons for excitation pulses numbered on the vertical axis, and the recorded histogram of fluorescence emission photons distribution against time for many excitation pulses. 22
Figure 16 Simple TCSPC measurement setup [117]. The laser driver provides a synchronization signal for the TCSPC (timing) electronics, each time a short laser pulse is hitting the sample. This signal is used to time stamp the excitation photon in the electronics. A photomultiplier tube (PMT) generates an electrical voltage pulse upon detecting a fluorescent photon which is used by electronics to time stamp the arrived emission photon and build up the histogram based on the delay between these two photons. 23
Figure 17 Ideal and actual situations in a fluorescence measurement system and the role of system's IRF on the measured decay curve [121]. 24
Figure 18 Frequency domain fluorescence measurement and setup [96]. (a) Phase and modulation depth frequency responses and the proper frequency range for different lifetime ranges. (b) Common measurement setup. 25
Figure 19 Suggested frequency domain fluorescence measurement setup using a VNA and a high speed photoreceiver. 26
Figure 20 ASE investigation of carbon dots on silver gratings. (a) Recorded emission spectrum for 14 different incident pump powers. (b) Spectrums integrated intensity vs incident pump power. 85
Figure 21 (a) Normalized reflectance spectrum of plasmonic dipole nanoantenna periodic structures designed to resonate at different visible wavelengths. (b) Magnitude of normalized total electric field at a plane 5 nm above the nanoantenna in numerical calculation environment including a quarter of unit cell plotted at the resonance wavelength of the structure designed at λ=633 nm. (c) schematic of a unit cell of the periodic structure. 88

1 Introduction

This thesis pertains to surface plasmon polaritons (SPPs), their capabilities, and prospective roles in next generation chip manufacturing technology, device physics study, and study and development of fluorescent emitters.

SPPs are surface transverse magnetic (TM) electromagnetic waves, occurring and propagating along a metal-dielectric interface, composed of collective oscillations of the metal free electrons coupled to an electromagnetic field. SPP modes are inherently confined to small scales in the order of sub-diffraction-limit and provide strong localised electromagnetic field enhancements. These are important features, enabling plasmonic based nanostructures to provide encouraging solutions in energy efficient photonic integrated circuits [1], biosensors [2], electrochemistry [3], novel semiconductor device physics [4], and fluorescence enhancement [5] and surface enhanced Raman scattering (SERS) for sensing and molecular studies [6] [7], or single photon, ultrafast light sources [8] [9].

Here, we try to shed light on the role of plasmonic grating structures in introducing new semiconductor device physics, novel solutions for chip manufacturing processes in smaller technology nodes, and fluorescence emission directivity and enhancement. In order to understand plasmonic gratings and their underlying physics, theoretical understanding of SPP modes are beneficial.

Solving Maxwell equations at the metal-dielectric interface, yields the dispersion relation of the SPP mode [10]:

$$k_{SPP} = \frac{\omega}{c_0}\sqrt{\frac{\varepsilon_d \varepsilon_m}{\varepsilon_d + \varepsilon_m}} \tag{1}$$

where ε_d and ε_m are the dielectric and metal relative permittivities respectively, c_0 is the speed of light in free space, and ω is the angular frequency. The metal dielectric function can be written using Drude model for a free electron plasma [10]:

$$\varepsilon_m = 1 - \frac{\omega_p^2}{\omega^2 + i\gamma\omega} \tag{2}$$

where ω_p is the plasma frequency and γ is the damping rate (electron collision frequency) in the metal. Assuming an ideal free electron plasma in the metal (negligible damping), the dispersion curve for the SPP mode at a metal/air interface can be plotted as Fig. 1(a). The SPP mode resembles a photon propagating in free space at low frequencies, but the dispersion curve deviates from the light line as the frequency increases, reaching an asymptotic limit at the surface plasmon frequency of $\omega_{sp} = \frac{\omega_p}{\sqrt{1+\varepsilon_d}}$ [10].

As the frequency approaches ω_{sp}, the wavenumber goes to infinity and the group velocity approaches zero, conferring to the SPP an electrostatic character. Between ω_{sp} and ω_p, there is a prohibited band where no electromagnetic surface wave can propagate for the ideal metal. However, in real metals with a complex relative permittivity, absorption due to interband transitions modifies the SPP dispersion curve, especially in this frequency range. As a result, k_{SPP} grows to a finite maximum wavenumber near ω_{sp} introducing a minimum to the wavelength for which excitation of SPP mode is possible. This also limits the amount of mode confinement perpendicular to the interface with decaying factor defined as $e^{-|k_z||z|}$ where $k_z =$

$\sqrt{k_{SPP}^2 - \varepsilon_d \left(\frac{\omega}{c_0}\right)^2}$. This frequency range allows for quasibound surface leaky waves on real metals [10] [11]. Figure 2(b) shows the SPP mode electric field and charge density at such an interface and the SPP electric field exponential decay away from the surface.

For frequencies above ω_p, the metal supports propagation of electromagnetic waves with group velocity of $v_g = \frac{d\omega}{dk} < c$ [10] [11].

It is clear from Fig. 1(a) that the SPP resides on the right side of the light line of the dielectric material and can not be excited by incident light due to its larger momentum. As a result, a prism near the metal surface or a grating structure on the metal layer is required for phase (momentum) matching between the incident electromagnetic wave and the SPP mode to excite the latter along the interface [10]. Grating structures are of strong interest due to their compact size and convenience for different applications.

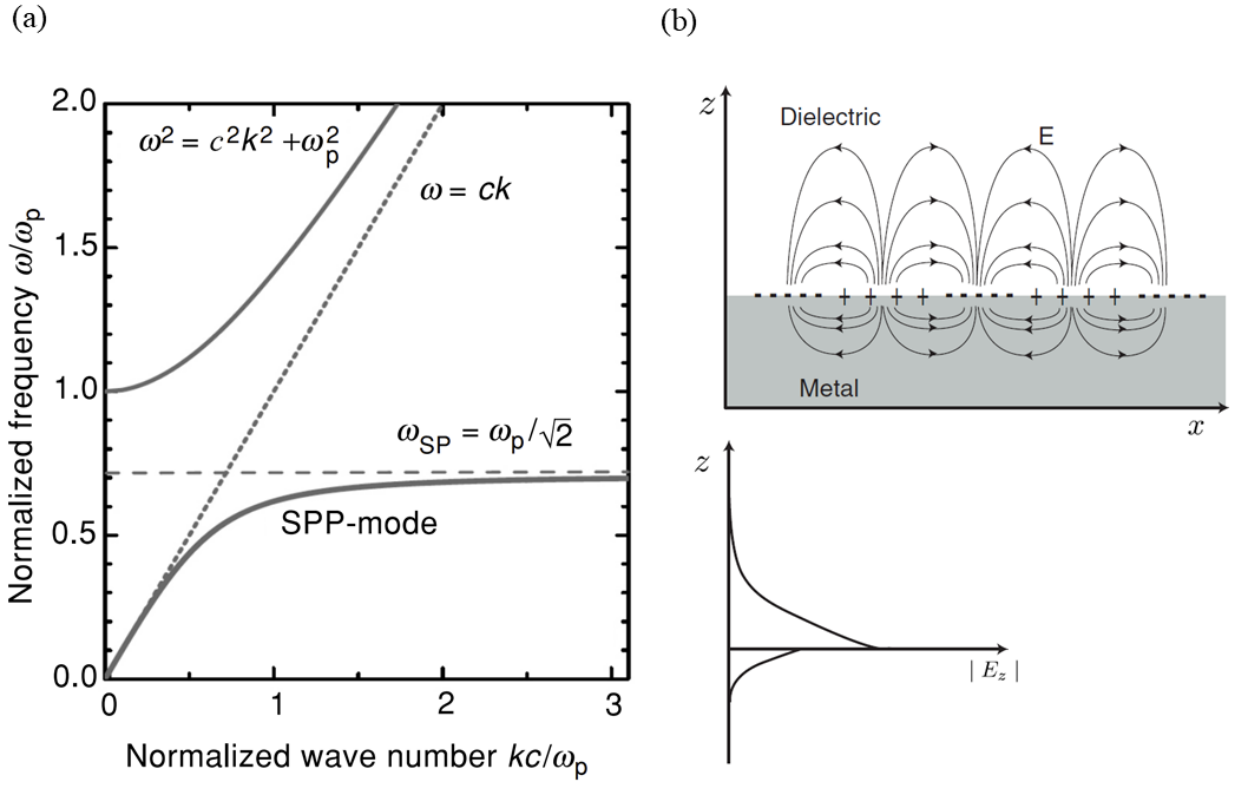

Figure 1(a) Dispersion relation of SPP mode at a metal-air interface [11]. (b) Top: schematic SPP surface charge density and electric field. Bottom: the magnitude of electric field component normal to the interface decays exponentially away from the interface [12].

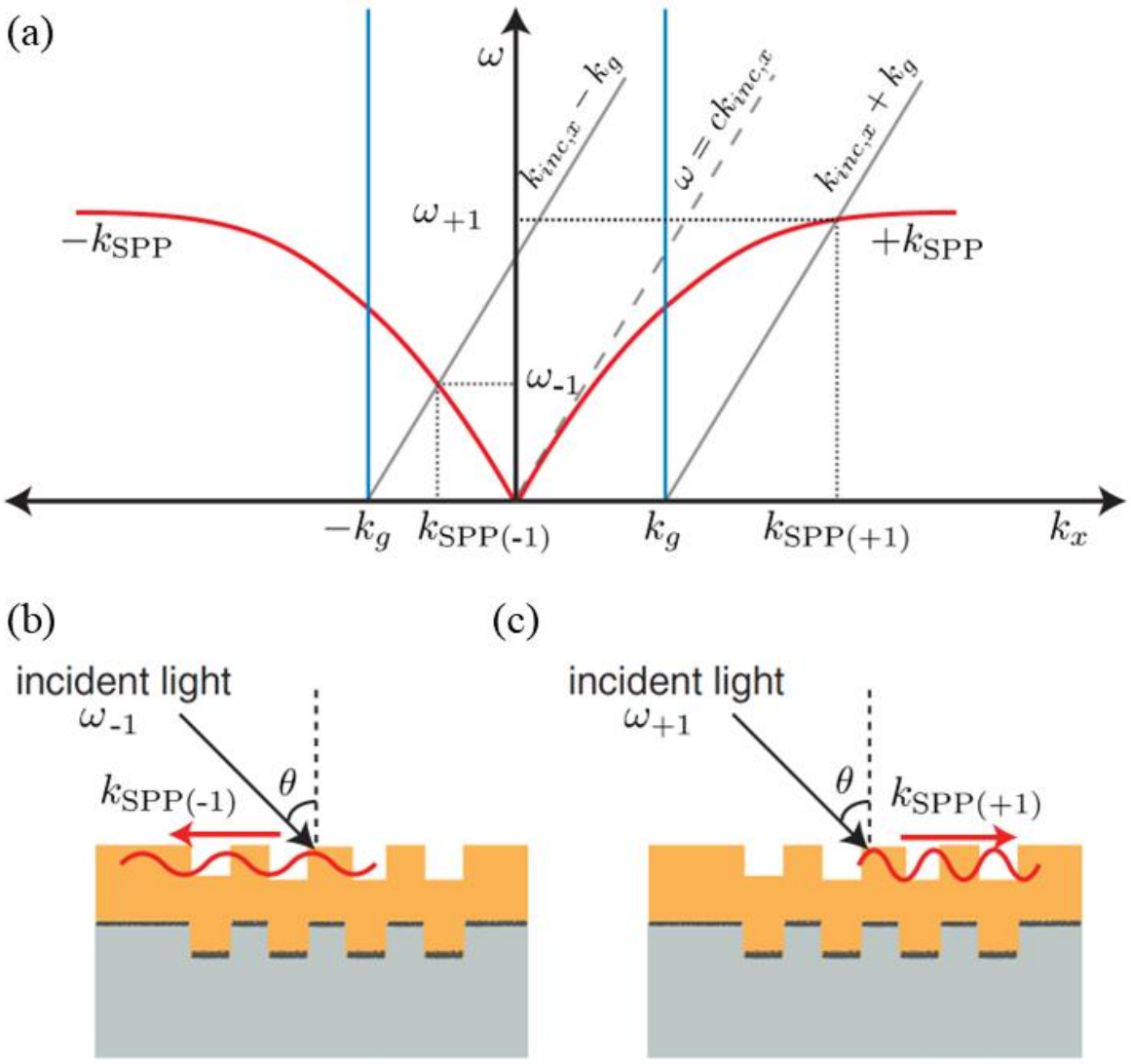

Figure 2 Surface plasmons excited by metallic grating coupler [12]. (a) Dispersion curves for the incident light (dashed grey), first order diffracted light by the grating (grey), and SPP modes propagating in the +x and -x direction (red). Blue lines show the Brillouin zone boundaries in k-space. Plasmons can only be excited at the frequencies where an intersection happens between the diffraction lines and the SPP mode line. (b) and (c) are two excited SPP modes with opposite propagation direction.

In this thesis, plasmonic gratings have been used for different purposes. To create a plasmonic grating, a metal layer is periodically patterned with shallow grooves and the created stripes are called grating fingers. The wavevector (reciprocal vector) of the grating is given by [10] [12]

$$k_g = \frac{2\pi}{\Lambda} \tag{3}$$

where Λ is the grating finger period. Assuming a light beam hits the grating at an angle θ with respect to the normal, the light diffracted by the grating acquires wavevector components of $\frac{\omega}{c_0} sin\theta \pm N k_g$ in the direction perpendicular to the grating fingers, with $N = 1, 2, 3,\ldots$ being integers.

If a SPP wavenumber becomes equal to any of these components, as [10]

$$\frac{\omega}{c_0} sin\theta \pm N\frac{2\pi}{\Lambda} = \pm k_{SPP} = \pm\frac{\omega}{c_0}\sqrt{\frac{\varepsilon_d \varepsilon_m}{\varepsilon_d + \varepsilon_m}} \quad (4)$$

then it is excited and starts propagating along the interface. Fig. 2(a) shows the two SPP modes excited and propagating in opposite directions by a plasmonic grating at two different frequencies on the dispersion curve. It can be seen from the dispersion curve equations, that the mode propagating towards right has larger angular frequency and wavenumber resulting in shorter wavelength. This is schematically shown in figures 2(b) and 2(c). If the beam hits the grating at normal incidence, the two SPP modes are excited at the same frequency [10] [12].

On the other hand, if a SPP mode exists and propagates along a plasmonic grating structure, it can couple the emission into the grating diffraction orders if the conditions in Eq. 4 are satisfied [13].

1.1 Thesis Scope and Outline

This thesis reports results on numerous applications of plasmonic gratings including small footprint electro-optic reflection modulators and new high-speed tunneling devices physics for telecommunication and electronic chip testing, to enhancing visible photoluminescence due to the Purcell effect.

Several numerical calculations are performed using FEM (finite element method) for design and analysis of plasmonic grating integrated with MOS (metal oxide semiconductor) structures. FDTD (finite difference time domain) method calculations have been used to determine Purcell factors and the lifetime of photoluminescent emitters on gratings. Theoretical modeling is also introduced and performed to model the measured tunneling behaviour of plasmonic hot carriers in MOS based devices.

Experimental methods and setups are introduced for non-contact wafer level chip testing of CMOS (complementary MOS) electronics and for lifetime measurement of photoluminescent emitters on plasmonic gratings.

The thesis includes scientific articles each presented as separate chapter and is organized as follows.

Chapter two provides an overview of previous research work on optical and plasmonic modulator designs and plasmonic induced tunneling phenomenon in different structure geometries. The chapter also includes a review on physics of fluorescence enhancement in plasmonic structures specially gratings and different fluorescence lifetime measurement methods.

Chapter three presents a MOS based electro-optic modulator designed based on the carrier refraction effect for surface plasmons propagating on a gold grating integrated with a MOS structure. The suggested device enables a non-contact wafer level testing method which is a paradigm shifting testing solution for CMOS electronics.

Chapter four reveals a new tunneling channel enabled by generating plasmonic energetic carriers in the metal layer of a plasmonic MOS structure. This new channel provides an opportunity to study hole tunneling behavior in different oxide materials. Considering that tunneling is an ultra fast process, the concept can be optimized for higher efficiency as a tunneling high speed photodetector which combined with the modulator introduced in chapter three, can provide a complete transmitter-receiver interface for the contact free wafer-level testing of electronics.

Chapter five discusses the use of surface plasmons to create, excite and outcouple the photoemission of carbon dots on a silver grating. Surface plasmons play several distinct and very interesting roles in the process. By enhanced localized fields, surface plasmons create energetic carriers in the silver layer via

absorption therein, facilitating the transformation of carbonaceous residue on the silver layer into carbon emitters. After these carbon emitters are created on the plasmonic grating surface, excitation of SPPs on the grating then excites the carbon dots (in an oxygen depleted environment) thereby producing fluorescence emission. This photoluminescence then excites surface plasmons propagating along the same grating structure at a longer wavelength than the excitation SPPs wavelength. The plasmonic grating enhances fluorescence through the Purcell effect and outcouples the emission to free space via grating orders.

2 Literature Review

Surface plasmons are known for their distinguished ability in localizing fields, producing strong field enhancement and subwavelength spatial confinement. These are important features since strong fields help achieve a more pronounced functionality with the same incident optical power, and subwavelength field distribution enables light manipulation at small scales in fabricated nanostructures. As a result of the tightly localized field enhancement, surface plasmons are highly sensitive to localized and small modifications in the optical properties of the medium they propagate in [14]. This important feature is the basic characteristic used for biosensing applications or telecommunication devices designed based on, *e.g.*, the carrier refraction effect.

On the other hand, excited surface plasmons on a metal-insulator interface decay in the metal and create energetic carriers therein, thanks to their wave-particle nature and enhanced localized electromagnetic fields. This advantage has been the underlying phenomenon used in designing different experiments and devices for electrochemistry, infrared (IR) and telecommunication applications [15] [16] [17]. Figure 3 shows how plasmonic hot carriers can be engineered to bring in different benefits for IR applications.

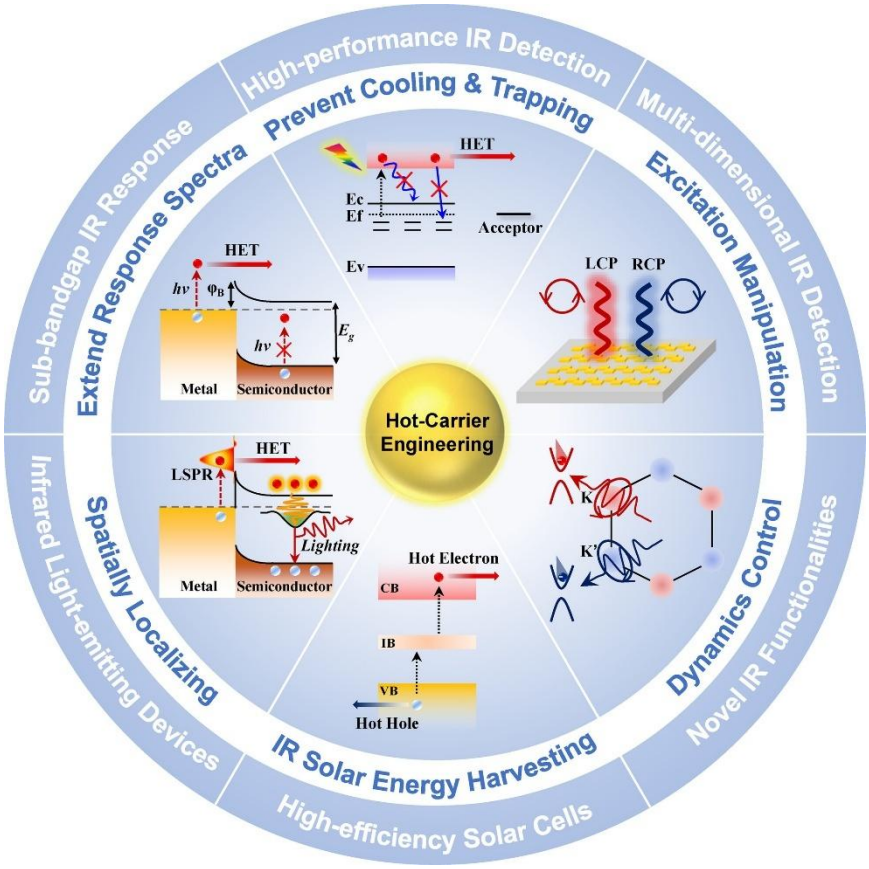

Figure 3 Different fields of plasmonic hot carrier engineering for high performance infrared optoelectronic devices [17].

For example, energetic carriers can overcome the tunneling barrier in a metal oxide semiconductor (MOS) structure more easily than equilibrium carriers in the metal, providing enhanced photocurrent upon surface plasmon excitation.

Energetic carriers can also enhance reactions involving homo and lumo levels in photochemistry process which helps light assisted material modification controlled by hot spots created via surface plasmon excitation. They also help in the excitation of photoluminescent species to an upper state. Relaxation of these species occurs differently if there are available SPP modes in the electromagnetic environment as the local optical density of states is altered and the Purcell effect may be present.

This chapter reviews the features and applications of surface plasmons in designing high speed modulators for telecommunications, enhancing tunneling through small gaps beneficial for device physics studies, and in Purcell factor enhancement to improve fluorescent emission into desired channels in free-space.

2.1 Plasmonic Electro-Optic Modulators

The rapid growth of artificial intelligence and communication systems has significantly increased data transfer demands. However, conventional electronic telecommunications systems are approaching their capacity limits, creating a bottleneck that necessitates a transition from electronics to optical technologies. With the advent of lasers and fiber optics in the industry scale, optical fiber communication technology has replaced many of radio frequency (RF) data transfer links. Optical fibers take advantage of photons as means of data transfer at the speed of light with low power consumption, and more security and reliability over long haul channels compared to satellites and ground to ground RF channels. An important aspect which enabled information to travel long distances on an optical carrier without the need for electrical regeneration via repeaters, is optical modulation in which bits of data are encoded on the optical carrier. Semiconductor lasers which are the most commonly used type of source in optical communications, can be directly intensity modulated via the drive current. This is a cheaper and simpler approach compared to using external modulation. However, direct modulation leads to fundamental problems of frequency chirp and wavelength excursion when it comes to higher bit rates and longer distances. The current benchmark for the trade off between direct to external modulation is 10 Gb/s over 80 km or longer distance on standard fiber [18]. This highlights the need for electro optical modulators which have been extensively researched and developed [19].

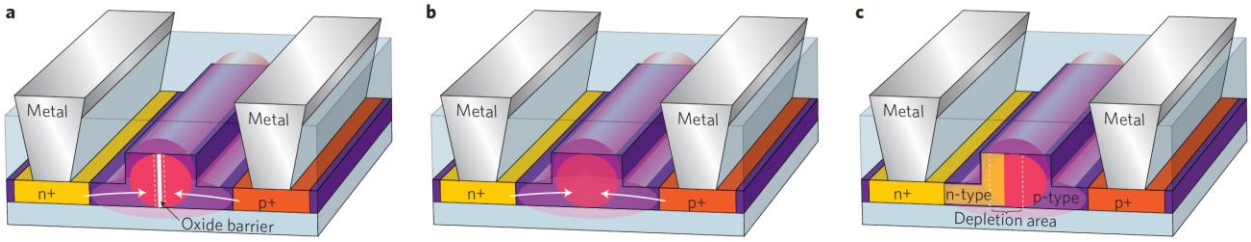

Figure 4 Common mechanisms for electrical manipulation of carrier concentration shown in the waveguide cross section [20]. (a) Carrier accumulation behind an oxide barrier. (b) Carrier injection into intrinsic region. (c) Carrier depletion in a p-n junction.

There are two types of optical modulators which are widely used: lithium niobate ($LiNbO_3$) Mach-Zehnder interferometer (MZI) and III-V semiconductor modulators based on electro-absorption with only former being used as stand-alone external modulator and the latter integrated with semiconductor lasers [18]. $LiNbO_3$ modulators are more expensive, not integrable with semiconductor technology, and very hard to fabricate [18] [21]. III-V modulators on the other hand, are cheaper but they do not offer as low loss, low chirp, and wide bandwidth performance as the $LiNbO_3$ modulators [18] [22].

On the other hand, silicon modulators are a matter of research and interest because they can be easily fabricated and integrated with the current fabrication and electronic wafer technology [23] [24]. Since electro-absorption and electro-refraction effects both are inexistent in silicon at telecommunication

wavelengths (1.3 and 1.5 μm), silicon modulators use the plasma dispersion effect either in a MZI geometry with long interaction arm or in a resonator structure like silicon ring resonators coupled to silicon waveguides. In plasma dispersion, the carrier concentration in silicon is electrically manipulated to change the real and imaginary parts of the refractive index. This is achieved via carrier injection, accumulation, or depletion mechanisms, as shown in Fig.4 for a waveguide structure [20]. The carrier density changes the refractive index and absorption as [18] [20]:

$$\Delta n = \Delta n_e + \Delta n_h = -(8.8 \times 10^{-22} \times \Delta n_e + 8.5 \times 10^{-18} \times (\Delta n_h)^{0.8})$$
$$\Delta \alpha = \Delta \alpha_e + \Delta \alpha_h = 8.5 \times 10^{-18} \times \Delta n_e + 6.0 \times 10^{-18} \times \Delta n_h \quad (5)$$

The change in the refractive index is used in a MZI to shift relative phase of the waves in two propagation arms and achieve a constructive or destructive interference for an intensity modulated beam at the output. In a device including a resonant structure, changing the refractive index, shifts the resonance and changes the transmitted light through the modulator waveguide. In both cases, the process is accompanied by a loss due to the free carriers' absorption [18] [20].

Silicon modulators have shown speeds of up to 112 Gb/S using slow light concept [25]. Recent efforts are towards reducing size and power consumption by adding germanium to the silicon and using the Franz-Keldysh effect for electro-absorption in bulk material [26] [27] or quantum-confined stark effect in quantum wells [28] [29] [30] [31] [32]. However, commercially available silicon modulators have only reached speeds of ~20 GHz [33]. Currently, the best modulator geometry for inter chip and intra chip optical communication in digital electronics is based on ring resonators due to smaller size, higher efficiency, higher modulation speed, and compatibility to the CMOS technology [34].

Although compatible with CMOS technology, silicon photonic based components are bulky compared to electronic chips and occupy valuable area on the wafer adding up to the acknowledged challenges in chip downsizing and compactness. Plasmonic modulators can take advantage of the features of SPP modes and offer device sizes smaller than the diffraction limit. Plasmonic device fabrication techniques can be implemented with industrial standard silicon-based tools [35]. By manipulating photons at nanoscale dimensions, plasmonic passive structures and optoelectronics including modulators, combine the compactness with high speed, which are not available simultaneously in electronic (speed limited by interconnect delay time) and photonic (diffraction limited size) circuits [36].

On the other hand, traditional methods of integration of high-speed electronics with photonic circuitry include assembling separate modules with external cables, or hybrid integration methods like bond-wire and flip-chip assembly, but they are currently bandwidth limited with the bond-wire being state-of-the-art technology for highest speed co-integration. Monolithic integration as an emerging method, combines photonics and electronics on the same substrate providing the highest speed interfacing with lower parasitics at a lower cost [37]. Plasmonic circuits provide compact size and high speed interconnects with lower losses at micron scale distances compared to electronics, and seem very promising for monolithic integration [37] [38] [39].

There are many different plasmonic modulator designs suggested using different materials and principles of operation. Plasmonic modulators were suggested based on Pockels and Kerr electro-optic effects, elasto-optic effects, plasma dispersion effect, thermo-optic and magneto-optic effects, and material phase transition effect [40]. The plasma dispersion effect, also known as free carrier dispersion effect, was discussed earlier in this section. This is the most important and dominant effect to achieve a fast modulation and is available in silicon and transparent conducting oxides like indium tin oxide (ITO) [40]. Since this effect is weak in silicon, bulky structures are needed to increase the interaction of light with the refractive

index perturbation which reduces the integration density for photonic-based circuits. However, the same effect can be used much more efficiently with plasmonic structures, thanks to subwavelength confined, highly enhanced electromagnetic fields. These features help modulators operate as high-speed lumped elements with interaction lengths as short as 10 µm and speed limited only by the RC-time constant and not the waveguide walk-off [41] [42].

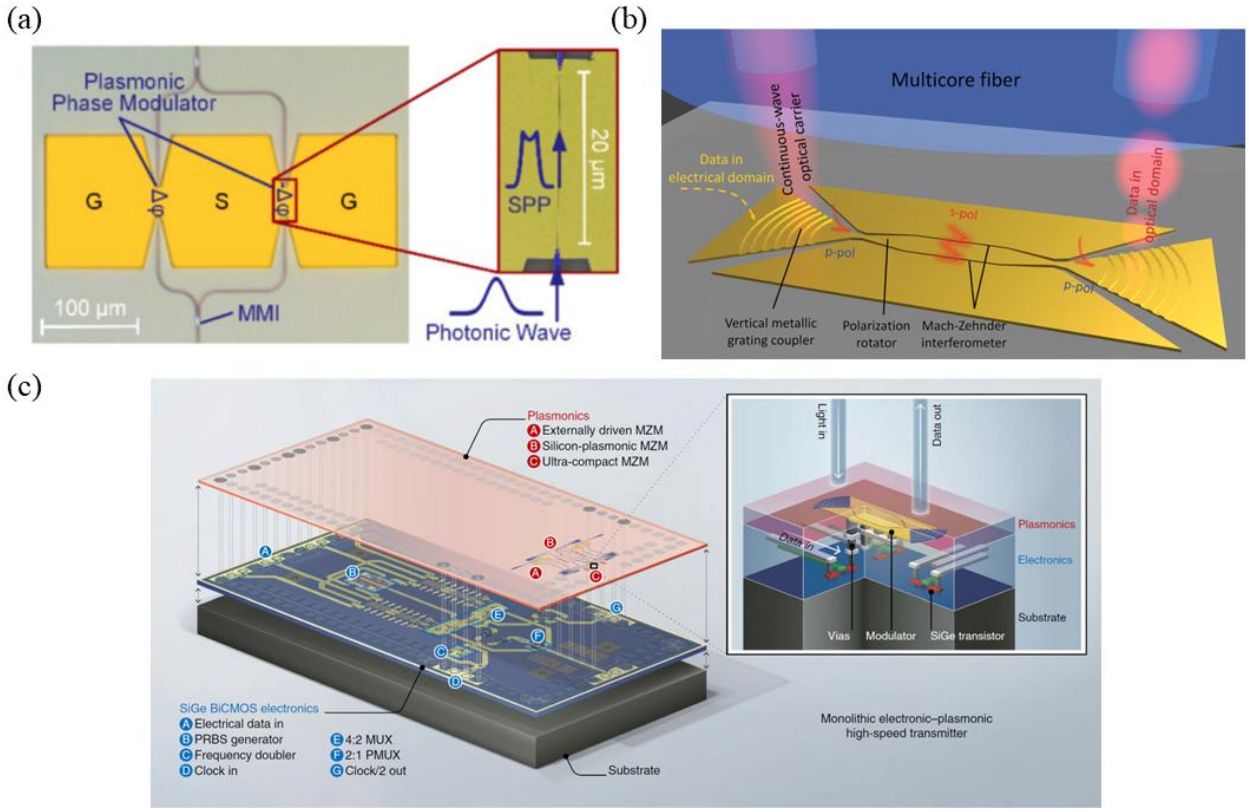

Figure 5 Plasmonic modulators using an organic electro optic material. (a) MZM phase modulator coupled to silicon waveguides [43] [44]. (b) MZI plasmonic modulator including a metal layer on arbitrary substrate and vertical grating couplers [45]. (c) A monolithic integration of plasmonic transmitter with CMOS electronics solving speed limit, thermal sensitivity, co-packaging [46].

The highest speed plasmonic modulator with a MZM design consists of a metal-insulator-metal (MIM) plasmonic waveguide filled with an organic nonlinear material and tapered to silicon waveguides at the input and output ports as shown in Fig. 5(a). Due to the Pockel's effect, the waveguide refractive index and the SPP mode phase are modulated by the applied electric field. The plasmonic arm has 20 µm length and the modulator shows a flat response up to 500 GHz in a radio over fiber link test around 1550 nm [44]. The same nonlinear organic electro optic (OEO) material was used in another MZM all plasmonic modulator in Fig. 5(b), comprising a single metal layer and vertical grating couplers on an arbitrary substrate layer. The modulator worked up to 116 Gbit/S around 1560 nm [45]. Later, the two modulator design principles were used in a monolithic integration with bipolar CMOS electronics as shown in Fig. 5(c), creating an electro-optic transmitter with symbol rates of beyond 100 GBd [46]. Figure 5c shows the high-speed transmitter comprising an all-plasmonic layer with the MZM plasmonic modulator included and monolithically integrated with an all-electronic layer at the bottom. These designs, however, are not fully compatible with current CMOS technology fabrication since they have an organic material in their structure which also degrades with time and may not be suitable for long-duration operation.

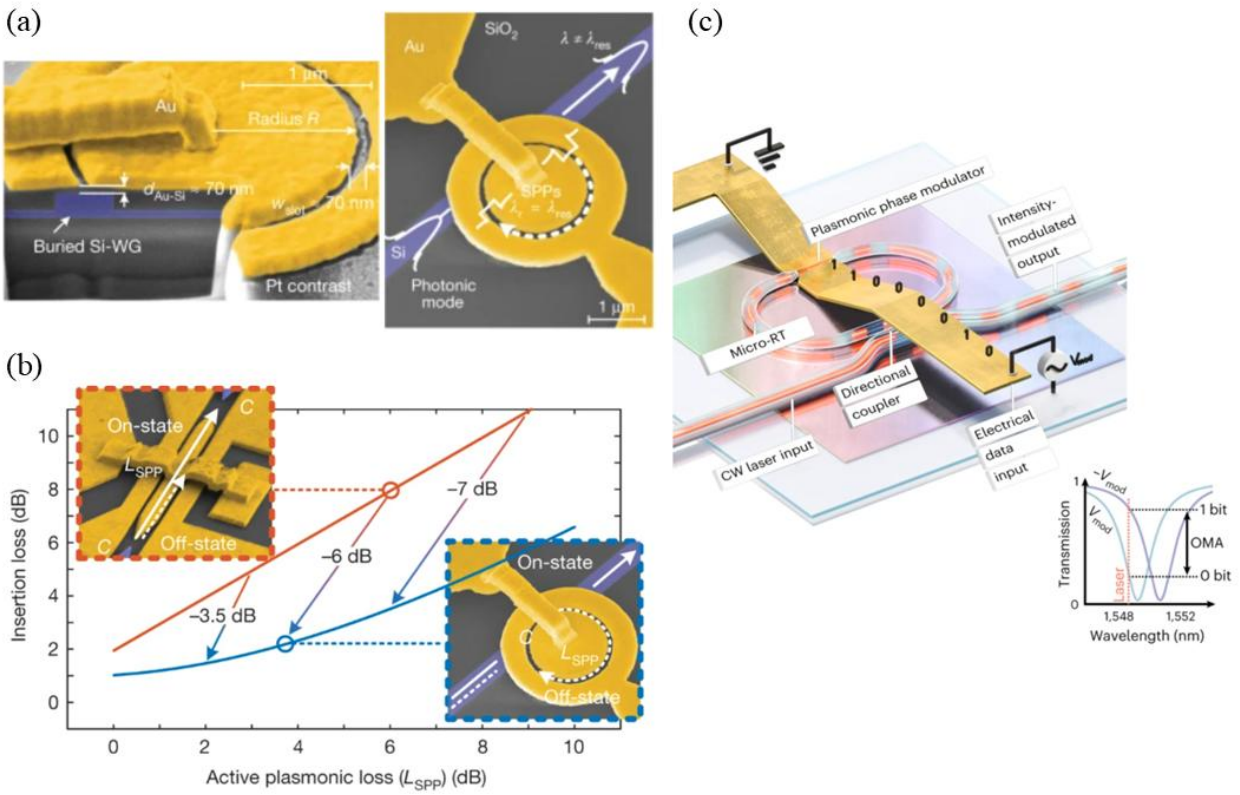

Figure 6 Ring resonator low-loss modulators [47] [48]. (a) Top and cross section view of the MIM ring modulator [47]. (b) Insertion loss against active plasmonic losses of the slot waveguide in MZM and slot resonator of ring resonator modulator. The arrows compare the two designs at equal performance in terms of modulation depth. Horizontal deviation of the arrows show that for same modulation performance, the resonance structure needs shorter active plasmonic section which lowers the plasmonic and transmission losses [47]. (c) Ring resonator with embedded plasmonic phase modulator and its performance principle based on resonance shift with applied voltage [48].

The same group also designed a low-loss modulator based on a MIM plasmonic ring resonator filled with the electro-optic polymer in the gap and coupled to a buried silicon waveguide. Light travelling in the silicon waveguide gets coupled to the SPP resonant mode only in the off state of the modulator, reducing both the plasmonic and transmission losses compared to the MZI counterparts. Figure 6 shows the modulator structure and the performance comparison with plasmonic based MZI [47]. Another resonance based plasmonic modulator was later suggested with lower loss, higher bandwidth (up to 176 GHz), better thermal stability (no self-heating effect), and low driving voltage (0.6 V_p) compared to previous silicon and plasmonic resonance-based modulators with a footprint similar to common silicon ring resonator modulators. The modulator uses a plasmonic phase modulator like the structure represented in Fig. 5(a) integrated inside a silicon ring resonator as shown in Fig. 6(c). Applying the modulating voltage to the MIM junction modulates the refractive index of the electro-optics material in the junction and causes a shift in the resonance wavelength which results in a modulated output intensity [48].

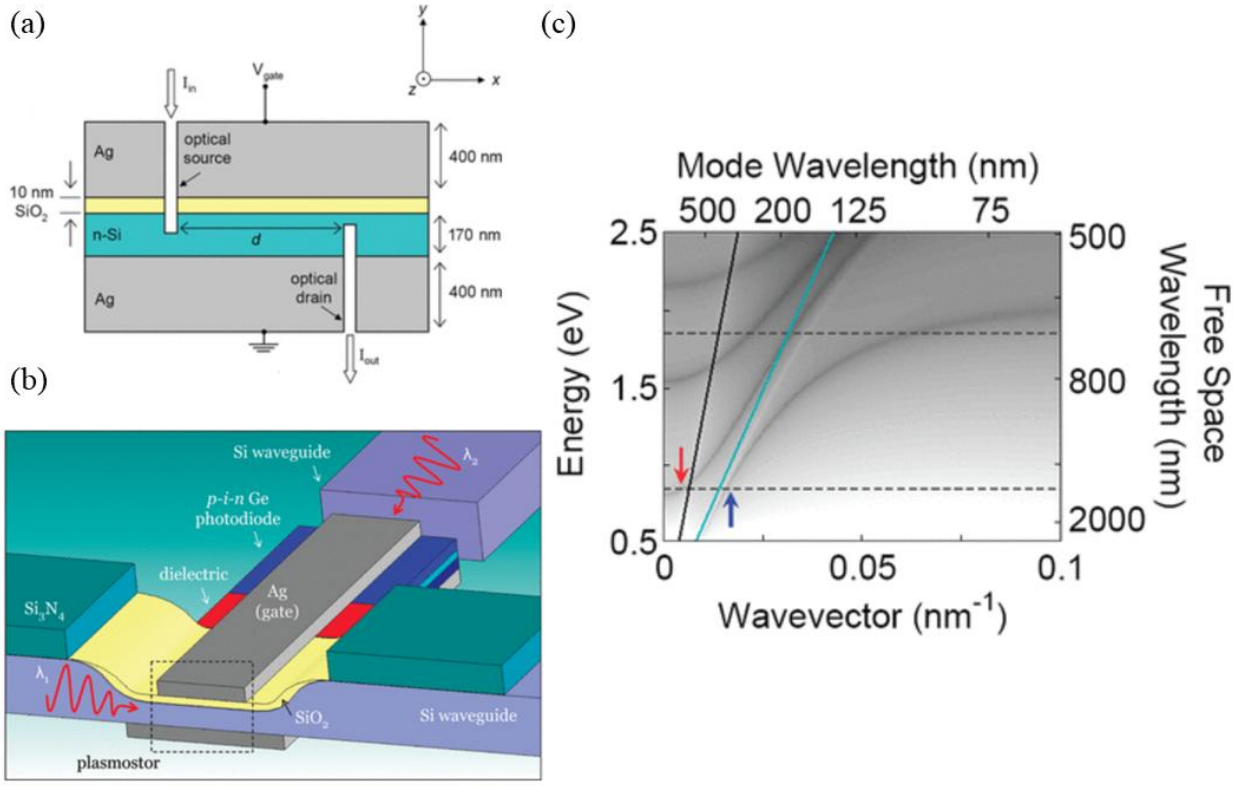

Figure 7 PlasMOStor (MOS based silicon waveguide modulator) [49]. (a) Device cross section with source and drain channels represented. (b) Structure integrated with a p-i-n photodiode for all-optical silicon-based modulation. (c) Dispersion curves of the structure under depletion state with dark grey curves corresponding to optimal solutions and the grey scale representing the modes linewidths. SiO_2 light line (black solid), silicon light line (cyan solid), plasmonic mode curve (lying to the right of silicon line), and photonic mode curve (lying to the left of the silicon line) are represented. The lower dotted line shows the 1550 nm wavelength and red and blue arrows show the modes propagating at this wavelength. The photonic mode has a relatively flat curve around this wavelength.

A metal oxide semiconductor (MOS) based modulator integrated with a silicon waveguide was suggested in [49] and shown in Fig. 7. The MOS structure is under depletion before applying a bias voltage and the modulator supports both photonic and plasmonic modes propagating along the silicon core and SiO_2 channel respectively. By applying a positive voltage to the gate, the MOS modulator is driven into accumulation and the change in the carrier density of silicon core, changes its refractive index. As a result, the photonic mode which has a flat dispersion curve around 1550 nm, is pushed into the cutoff and only the plasmonic mode can propagate along the thin SiO_2 channel. The plasmonic mode then couples to the optical drain channel increasing the output power by 10 dB compared to the off (depletion) state. If integrated with a high-speed p-i-n photodiode, as shown in Fig. 7(b), the modulator has a 15 GHz bandwidth.

All plasmonic modulator designs introduced up to now, are in order of tens or hundreds of microns in size and some of them present complexities to full integration with current CMOS technology fabrication processes due to the inclusion of Pockel's effect organic materials, which are incompatible and may degrade over time under modulation.

In chapter three of this thesis a CMOS compatible, compact (5 μm), broadband (22 GHz), low loss (4 dB) modulator is reported, which can be monolithically integrated into current CMOS platforms. Due to its compact size, and the fact that it can be arbitrarily placed anywhere on the wafer, it is aligned with the current goal of high-density integration of chips.

2.2 Plasmon Assisted Tunneling

Quantum tunneling, where electrons pass through barriers that are classically forbidden, can serve as a bridge between electronics and plasmonics. By enabling these two fields to work together, the new field of plasmon enhanced tunneling is defined, an interesting interdisciplinary area of study to explore new device physics, potentially advancing nanotechnology, optoelectronics, and quantum devices which have applications in opto-electrochemistry, quantum sensing, and optically or electrically excited luminescence [50] [51] [52] [53].

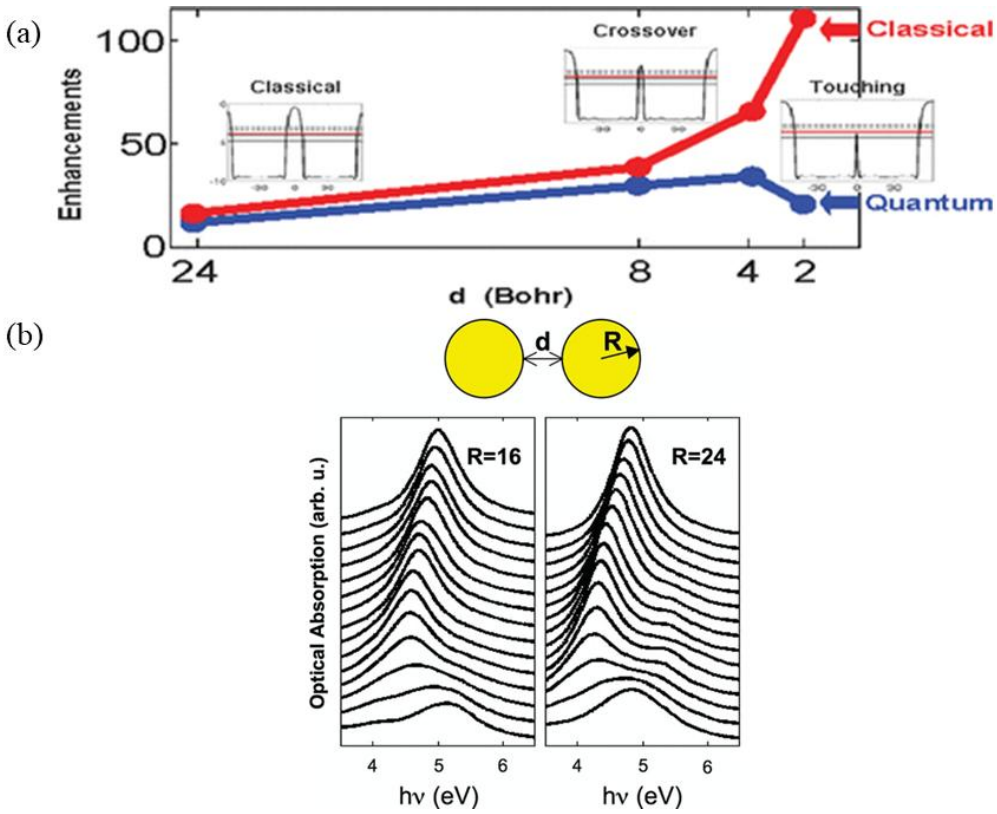

Figure 8 Role of quantum effects in the resonance of a plasmonic dimer [54]. (a) Classical predictions deviate from the real response of the system as quantum tunneling gets stronger for smaller dimer separations: filed enhancement is reduced strongly for gap sizes smaller than 1 nm. (b) Plasmonic resonance classically red shifts as the dimer gap shrinks, however, for smaller than 1 nm separation, the CTP mode appears which resonance blue shifts by lowering the gap size.

As a result, the study and modeling of tunneling current in plasmonic gaps will be beneficial [55]. Earlier research works present that quantum tunneling can modify plasmon resonances of a nanoparticle dimer with gap sizes below 1 nm. It was theoretically shown that for small dimer separations, electron tunneling across the dimer junction and the resultant screening of localized surface plasmons drastically reduce the electromagnetic field enhancement compared to classical calculations. This is not the case for larger dimer separations. For gap sizes smaller than 0.5 nm, a conductive regime exists which creates a charge transfer plasmon (CTP) mode, agreeing with experimental results [56]. In this mode, the Fermi level of a dimer system is above the potential barrier and conduction electrons can flow back and forth between nanoparticles. The resonance wavelength of this mode blue shifts as the interparticle separation is decreased which contrasts with the classical behaviour observed for large gap sizes as represented in Fig. 8 [54]. A similar concept was shown experimentally by Savage *et al*. in a sub-nanometer plasmonic cavity created by two AFM tips shown in Fig. 9 [57]. These results agree with the quantum corrected theoretical model

for plasmonic resonances in sub-nanometer sized gaps in which classical models fail due to increasing quantum effects of electron tunneling and non-local screening [58].

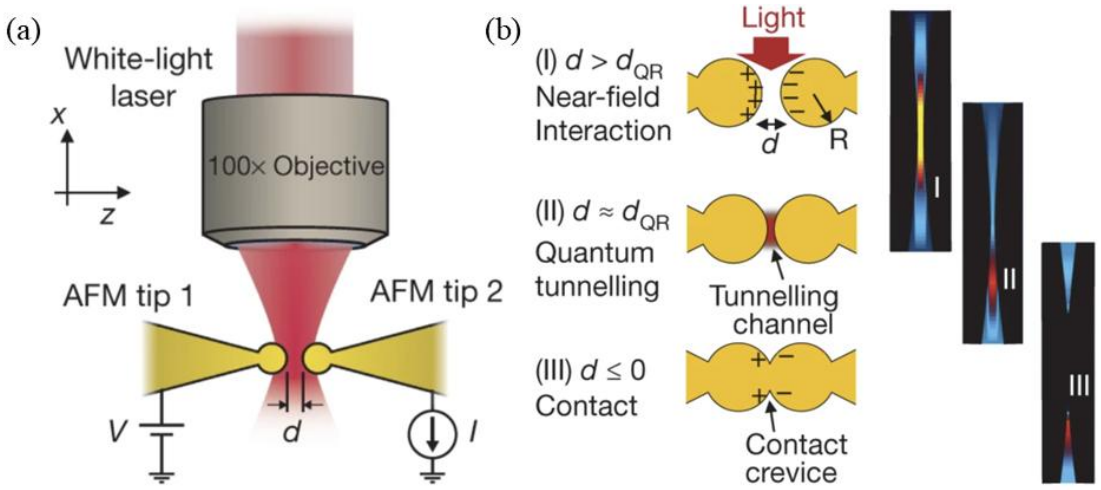

Figure 9 Evolution of plasmonic mode to quantum CTP mode as the inter particle distance changes. d_{QR} is a crossover for gap distance at which the quantum and classical predictions diverge, defining the critical distance limit for classical plasmonic mode and fundamentally limiting the optical field confinement in the plasmonic cavity [57].

The fabrication of structures with inter-particle distances as small as sub-nanometer dimensions is a challenging process [59]. Tan *et al*. suggested to insert self-assembled molecules inside the plasmonic gap as a means to alleviate tunneling through the gap compared to vacuum filled gaps [50]. They then were able to control the plasmon induced tunneling frequency by changing the type of molecule in the gap which have different HOMO (highest occupied molecular orbital)-LOMO (lowest occupied molecular orbital) energy separations [60]. The charge transport mechanism was shown to be almost gap size independent and as a result, the structure can be fabricated by available processes. By introducing chiral host molecules in such plasmonic gaps, where plasmonic hot electron transport is controlled by laser illumination, it has been shown that the gap conductance increases by 50 times when a chiral guest binds to the host in the cavity, opening opportunities for single molecule electronics and chiroptic sensing [61].

In [62] a self-consistent theoretical model of tunneling current in plasmonic MIM junctions was provided considering the space charge effects and reliable for different tunneling regimes. It is shown that the Simmons model only is accurate for limited conditions in direct tunneling. However, it deviates from experimental results if the oxide thickness is increased, or the barrier height is lowered.

For the first time, Wu *et. al*. studied the CTP mode via Fowler-Nordheim (FN) tunneling through sub-nanometer sized gap between plasmonic nanoparticles. When there is a wide tunneling barrier between nanoparticles, electrons can not tunnel directly to the other side of the barrier and instead, they tunnel from the conduction band of the first nanoparticle into the conduction band of the gap region, and then are swept towards the second nanoparticle by a strong electric field which has created a sloped energy profile across the gap (band-bending in band diagram) [63]. This phenomenon creates a space charge region distributed in the gap area enabling CTP mode between nearly touching nanoparticles. The damping rate and strength of this mode is controlled by changing the incident light intensity which changes the electric field inside the gap. This is because the illuminating light intensity affects the number of excited plasmons and hence the tunneling electron density and conductivity of the gap and as a result, can be beneficial in new quantum-

based devices such as switches [64]. Figure 10 shows how gap size and gap electric field affect the regime that tunneling mode follows. Figure 10(b) also shows the band bending for each tunneling regime at the two limit points of gap size. The density of electrons that can directly tunnel through the barrier increases as gap size shrinks, but when the gap conductivity reaches to a saturation, tunneling electrons are only limited by available sources from the initial conductor and is gap size independent. The grey are in Fig. 10(b) shows the tunneling electrons energy band. Electrons have less energy than the barrier height in direct tunneling regime, comparable energy levels in FN regime, and higher energy for saturation regime in which the gap is completely conductive. A gap nanoantenna interacting with ultrafast laser pulses in the Fowler-Nordheim tunneling regime was presented in [65]. The rectified electron packets in the rectenna follow the time scale of incident ultrafast short pulses with high repetition rate. These femtosecond electron pulses can be used for ultrafast optoelectronic devices, studying temporal dynamics of electronic devices, or nonlinear effects in plasmonic gaps [66], and local sources for terahertz radiation [67].

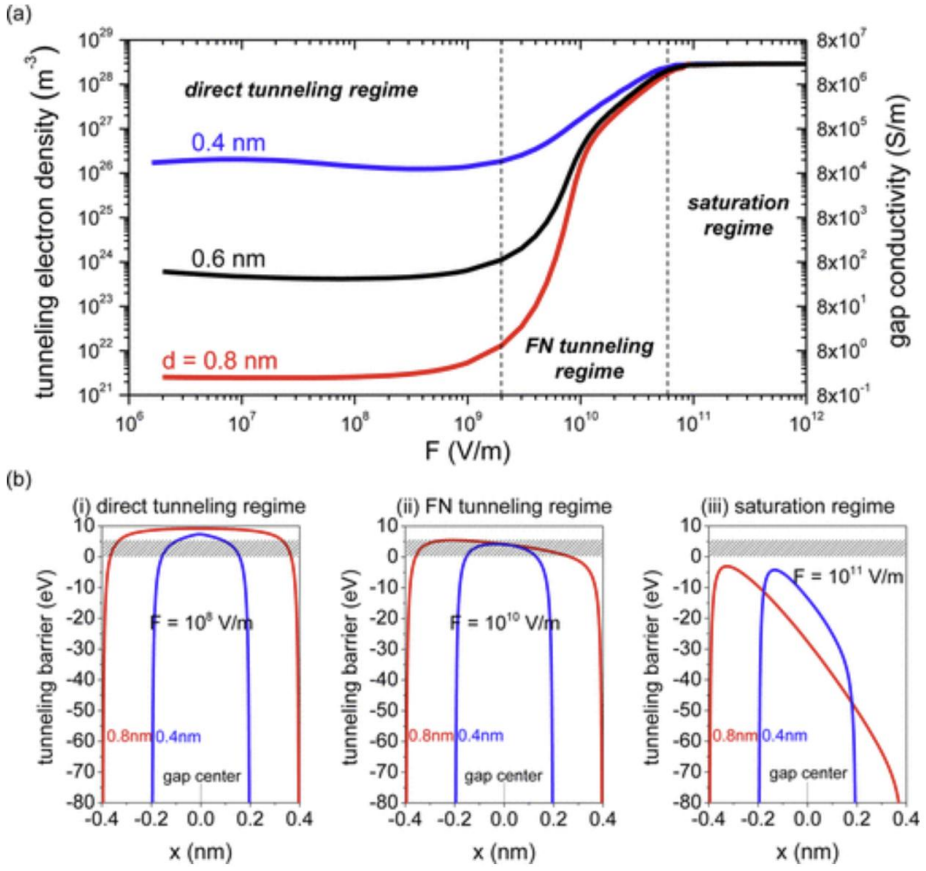

Figure 10 Different tunneling regimes of sub nanometer size gap (0.4, 0.6, 0.8 nm) between plasmonic nano particles dependant on gap electric field magnitude and size [64]. In panel (b), grey area shows the energy levels of electrons initiating the tunneling process. In saturation regime, barriers are lowered below electrons energy due to strong electric field across the gap, leading to the highest conductivity limited only by the population of supplied electrons from the first nanoparticle.

Tunneling events are ultrafast processes and it has been shown theoretically and experimentally that tunneling through a metal insulator metal (MIM) junction can occur on femtosecond timescales [68]. As a result, tunneling based devices perform significantly faster than conventional semiconductor devices that rely on diffusive transport of electrons [69]. Electrons have the possibility to interact with the plasmons and this phenomenon opens enhanced tunneling channels in structures such as MIM or MOS. Tunneling through

these structures can be beneficial in material characterization, electroluminescence, optical transmission [70], modulation, and detection in the photonic integrated circuits [69].

Parzefall *et al*. showed inelastic electron tunneling in a MIM structure of gold-hexagonal boron nitride (h-BN) - gold junction converts to free-space photon emission by exciting surface plasmons and coupling them to free-space emission in a resonant slot antenna structure as shown in Fig. 11. They achieved resonantly enhanced emission which was polarized and directional by inducing inelastic tunneling in the junction driven with RF (radio frequency) signals with frequencies of up to 1 GHz achieving a modulated emission at the output [71]. This is promising for designing light sources at small scales that can be directly modulated at high speeds without encountering the bandwidth limiting due to recombination in semiconductor lasers. In a different work, the group studied the mechanism responsible for tunneling light emission in a gold-h-BN-graphene junction and suggested an independent controlling ability over electronic and optical properties of such MIM-SPP systems, providing a platform for designing more complex systems using van der Waals heterostructures [72].

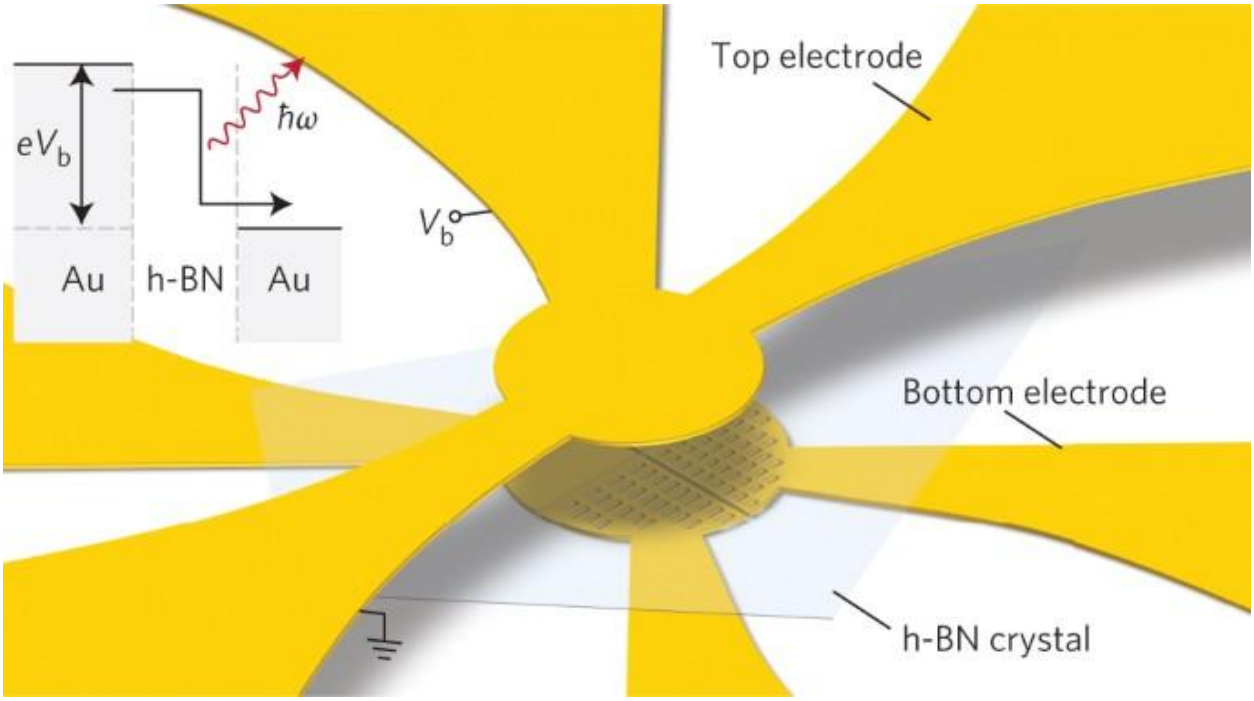

Figure 11 Schematic of the MIM structure of gold-h-BN-gold tunneling junction with the segmented and nanostructured bottom electrode controlling the optical properties of emission. Inset shows the band diagram of inelastic tunneling generating a photon [71].

Wang *et al*. designed an electrically driven plasmonic metasurface including 10^{11} tunnel junctions per square centimeter in which the presence of hot electrons in the junctions activate oxidation and reduction reactions [73].

Chalabi *et al*. presented photodetection (photocurrent generation) in a MIM junction due to tunneling of hot electrons originating form photons or SPP absorption in the metallic contact and suggested a 5-step model for hot electron tunneling through the MIM junction. In this model the first step is to generate a hot electron per each incident photon on the metallic surface of the detector. This phenomenon has a very low efficiency in a regular MIM structure but can be enhanced by structuring the metal surface into a plasmonic metasurface which then makes MIM structures a great candidate for future device designs which do not rely on electron-hole pair generation in a semiconductor [74].

Rectification of optical beams have high importance in applications other than design of high-speed photodetectors. On the roadmap to further miniaturize electronic circuits, the need for smaller field effect transistors (FET) [75] is manifest. This has led to design of single molecule electronics [76] in which plasmon induced effects, specifically interaction of plasmons with electrons in the quantum tunneling regime, can play important and beneficial roles [77]. There is a substantial amount of work in which optical switching and rectification was achieved and analyzed in different types of plasmonic tunnel junctions [78] [79] [80] [81] [82].

Many research works used inelastic tunneling in MIM plasmonic resonator structures to produce SPPs on the metal surface and create transducers leading to highly efficient light sources [83] [84] [85] [86] [87] [67] [88].

Based on the potential that plasmon assisted tunneling phenomena can provide, in Chapter 4 of this thesis, surface plasmon assisted tunneling in a MOS structure is studied. MOS structures are of interest due to their compatibility with current chip technology, but their tunneling characteristics coupled to plasmonic modes have not been explored very extensively in previous studies. In this study we show a new tunneling channel opening due to the excitation of SPPs on the metal layer of a MOS device. This tunneling behavior follows a modified Fowler-Nordheim tunneling law as shown theoretically and experimentally.

2.3 Plasmon Enhanced Fluorescence

Initially discovered by Purcell, the lifetime (spontaneous emission rate) of an excited quantum emitter depends strongly on its local electromagnetic environment [89]. The Purcell effect results from modification of the available local density of optical states (LDOS) in the emitter's environment, including enhanced fields. The probability of spontaneous emission (γ_{ij}) is dependent on the overlap of wavefunctions between the excited and lower energy states (M_{ij}) and the LDOS (ρ) at the transition frequency (ν_{ij}) also known as photonic mode density (PMD) following the Fermi golden rule [90] [91]:

$$\gamma_{ij} = \left|M_{ij}\right|^2 \rho\left(\nu_{ij}\right) \tag{6}$$

It is well-known that placing an excited molecule near a metallic mirror modifies the boundary conditions of electromagnetic fields around the molecule and opens a new coupling channel to surface plasmon polariton modes, and hence, increases the fluorophore excitation (γ_{exc})/emission (γ_r) rates and the quantum yield (η), providing high emission directionality (D), leading to modulation of the fluorescence intensity, emitter's decay rate, and spatial distribution of radiation [90] [92] [93] [94]. The confined electromagnetic fields of surface plasmon polaritons create hot spots with enhanced fields at desired locations along a metal surface. These enhanced fields can interact with fluorophores in two manners; firstly, they increase their excitation rate compared to free-space excitation rate (γ_{exc}^0) by increasing the absorption cross section of fluorophores as [95]:

$$\sigma(x,y) = |EF(x,y)|^2 \sigma_0 \tag{7}$$

where $\sigma(x,y)$ and σ_0 are absorption cross sections near the surface and in free space, respectively, and $EF(x,y)$ is the electric field enhancement factor.

Secondly, the increased LDOS (due to available SPPs) provides means for fluorophores to decay at a higher rate [90] which lowers their lifetime and, if designed purposefully, enhances the fluorescence emission of the system [96] into desirable spatial emission channels [90] [97]. Previous studies have shown that the radiative decay rate of emitters coupled to SPP modes (γ_r) can be enhanced proportionally to the square of the field enhancement factor (EF) with respect to an unperturbed emitter (γ_r^0) following Eq. 7:

$$\gamma_r = |EF|^2 \gamma_r^0 \tag{8}$$

The reciprocity theorem [98] [99] [100] introduced between the excitation enhancement and emission enhancement processes also confirms Eq. 8 [95] [101].

In principle, the quantum yield of fluorophores near a metallic system not only depends on the intrinsic radiative (γ_r^0) and nonradiative (γ_{nr}^0) characteristics of the emitter, but also on the radiative (γ_r) and nonradiative channels provided by the electromagnetic environment, following [93] [102]:

$$\eta = \frac{\gamma_r}{\gamma_r + \gamma_{nr}^0 + \gamma_{LSW} + \gamma_{abs}} \tag{9}$$

where γ_r is the total radiative decay rate of the emitter in its environment and is related to emitter's intrinsic radiative decay rate by the field enhancement factor via Eq. 8. γ_{nr}^0, γ_{LSW}, and γ_{abs} are intrinsic nonradiative decay rate of the fluorophore, the dissipation rate into lossy and nonradiative electromagnetic modes at the surface, and the absorption rate into the environment and metal respectively. The denominator in Eq. 9 is the total decay rate (γ) of the system and $\tau = 1/\gamma$ is the lifetime of the species.

When measuring the fluorescence emission of a system, the fluorescence photons can be counted in time. The photon count rate depends on the photo luminescence (PL) detection efficiency (ζ), the fluorophores' quantum yield (η), the fluorophore's absorption cross section (σ), and the time averaged excitation photon flux density at the emitters' position (I) far from metallic structures [95]:

$$R = \zeta \eta \sigma I \tag{10}$$

The lifetime of the emitters in their environment (τ) can also be extracted from the measurements. By knowing the unperturbed lifetime (τ_0) and count rate (R_0), one can calculate the normalized lifetime and count rates from which the quantum yield, radiative decay rate, and nonradiative decay rate of emitters in their environment can be extracted [95]:

$$R_N \tau_N = \eta^2 \tag{11}$$

$$R_N / \tau_N = (\gamma_r^N)^2 = EF^4 \tag{12}$$

$$\gamma_{nr} = \left(\frac{1}{\eta} - 1\right)\gamma_r = \gamma_{nr}^0 + \gamma_{LSW} + \gamma_{abs} \tag{13}$$

where R_N, τ_N, γ_r^N are normalized count rate, lifetime, and radiative decay rate to their unperturbed counterparts respectively.

By designing proper plasmonic structures, one can couple incident light in the absorption spectrum of the fluorophores to SPP modes, for which the electromagnetic fields are confined and enhanced at the emitter location. This will improve absorption of incident light by the fluorophores, thereby enhancing the excitation rate [95]. Excited fluorophores then decay into relaxed states by emitting energy quanta into SPP modes supported by the designed structure. For the latter to happen, the resonance wavelength of the plasmonic structure and fluorophore emission wavelength should coincide. This latter phenomenon improves the emission efficiency in different ways: providing higher LDOS due to the localized and enhanced fields of SPP modes, thereby opening a quick radiative decay channel that is more competitive with nonradiative channels [96], and engineering the emission into desired free space channels by specific design of the nanostructures [97]. Plasmonic grating couplers happen to be great candidates to fulfill these requirements. The resonance of a plasmonic grating is broad and can be engineered to overlap with both the absorption and emission wavelengths. The grating wavenumber provides momentum mismatch

compensation between free space photons and SPPs as discussed in chapter 1, which is beneficial for both the excitation and emission processes. They also have strongly confined fields over a large portion of the surface. Building on previous experimental work on carbon emitters created by SPPs on silver gratings [103], we report in chapter 5, a theoretical investigation of the emission of dipole emitters (representative of carbon emitters) on a shallow silver grating.

2.3.1 Plasmon Grating Enhanced Fluorescence

There is an extensive body of research and interest regarding spontaneous emission enhanced by nanostructures [102] [104] [105]. Greffet *et al*. have introduced the local form of Kirchhoff's law as means to analyze and design complex photoluminescent or electroluminescent systems as well as thermal emitters [106]. In its local form, Kirchhoff's law suggests the equality between local absorption rate per unit volume and the local thermal emission rate per unit volume in situations where subsystems have local thermodynamic equilibrium and are not at an equilibrium with respect to each other [107]. The group then used Kirchhoff's formalism to design and calculate the emission characteristics of nano structures by first studying and modifying (maximizing) their absorption features. To achieve this, ensembles of quantum dots on metasurface or grating [108] structures were described as an optical material layer, properties of which affects the system optical mode density. As a result, two main factors creating an interplay have been considered in this model: one is the emission spectrum of the emitters, and the second is the emission properties of the nanostructure which is embodying thermal emitters, and its geometry and optical properties which are also affected by these emitters [109]. The model has been used to design, fabricate and test a silver metasurface hosting semiconductor nanocrystals emitting at a narrow spectral range, with high directivity benefiting from the surface plasmon modes [97]. They offered plasmonic grating as an efficient tool to achieve coherent thermal light sources with polarized, highly directive emission at narrow spectral range, in which the propagation length of surface plasmons is directly linked to the spatial coherence or directivity of the source [106].

Knoll *et al*. measured the fluorescence intensity emitted by dye molecules on a gold plasmonic grating [110]. They have shown that the angle of maximum fluorescence can be controlled by engineering the grating pitch as shown in Fig. 12(a) supporting the theory that the fluorescence emission emerges from fluorophores relaxing into red-shifted surface plasmons which then decay radiatively via the plasmonic grating at the diffraction angles that satisfy Eq. 4 [111]. The measured fluorescence was highly enhanced, polarized, and directive. Figure 12(b) shows that measured total intensity through a full solid angle over the sample shows two main lobes satisfying resonance angles . Polarization controlled measurements shown in figures 12(c) and 12(d) confirm that TM excitation / TM detection dominates the fluorescence intensity based on which authors argue that fluorophore excitation mostly happens due to the surface plasmons coupling, and for a strong emission intensity, the dye molecule must emit before depolarization so their TM emission can couple efficiently to the SPPs which radiate via the grating [110].

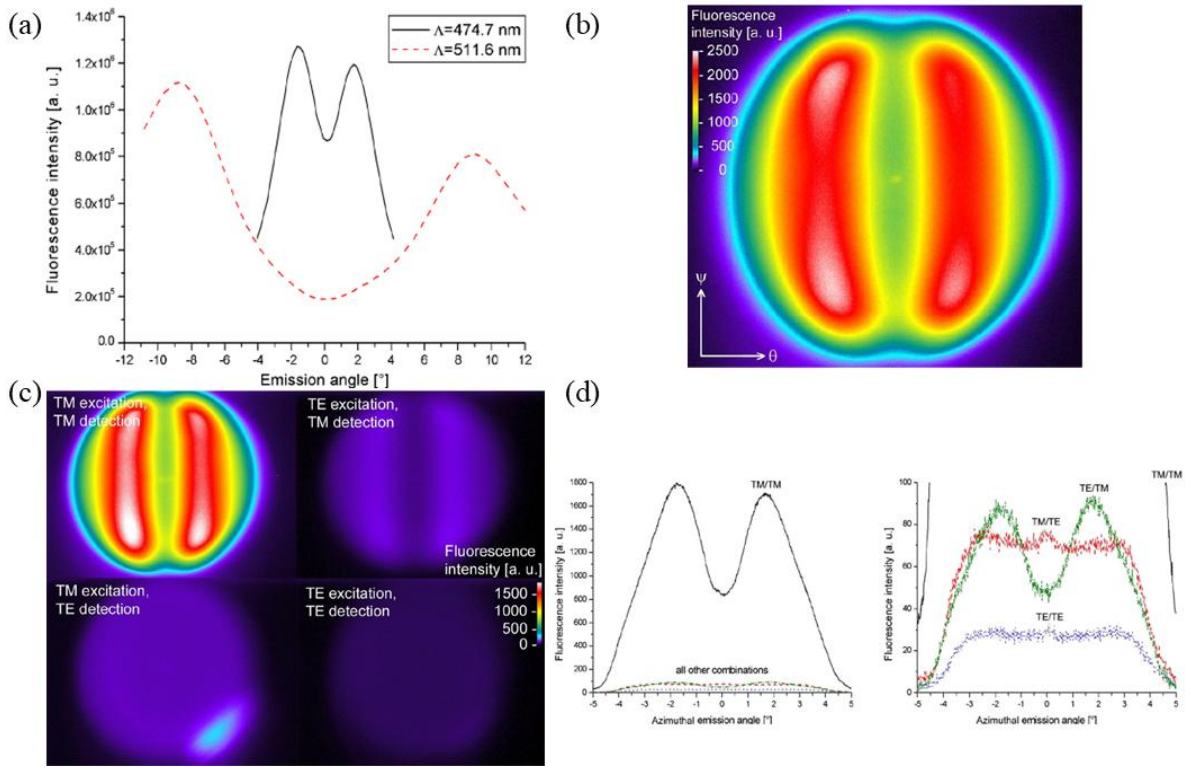

Figure 12 Fluorescence emission over a gold grating [110]. (a) Emission angle dependence on grating pitch. The black curve was resonantly excited at $\theta = 8.06°$ and the red curve excited at $\theta = 15°$ with TM-polarized beam and polarization independent collection. (b) Solid angle imaging of total fluorescence intensity for the sample with red curve in figure (a). (c) Solid angle imaging of polarization-controlled excitation and detection. (d) Line scans of images in figure (c).

It has been shown that when dye molecules are positioned close to a metallic grating, SPP radiation via grating diffraction dominates over the molecules' direct emission. This is attributed to the Purcell effect, which results in strong quenching of direct emission due to metal absorption or its coupling into well-defined direction rather than isotropic emission [112]. Barnes *et. al*. also showed that there is an optimum grating amplitude and dye layer thickness for which the fluorescence emission is more enhanced (figures 13(a) and 13(b)). The former is due to damping of SPPs with higher grating amplitudes and the latter is due to SPPs absorption in the dye layer before successful outcoupling. They suggest silver as the best option to support SPPs in the visible due to its lower absorption in this range. Figure 13(c) also shows that the magnitude of SPP mode electric field at different heights above the grating and along one grating period which is in direct relation with fluorescence emission enhancement.

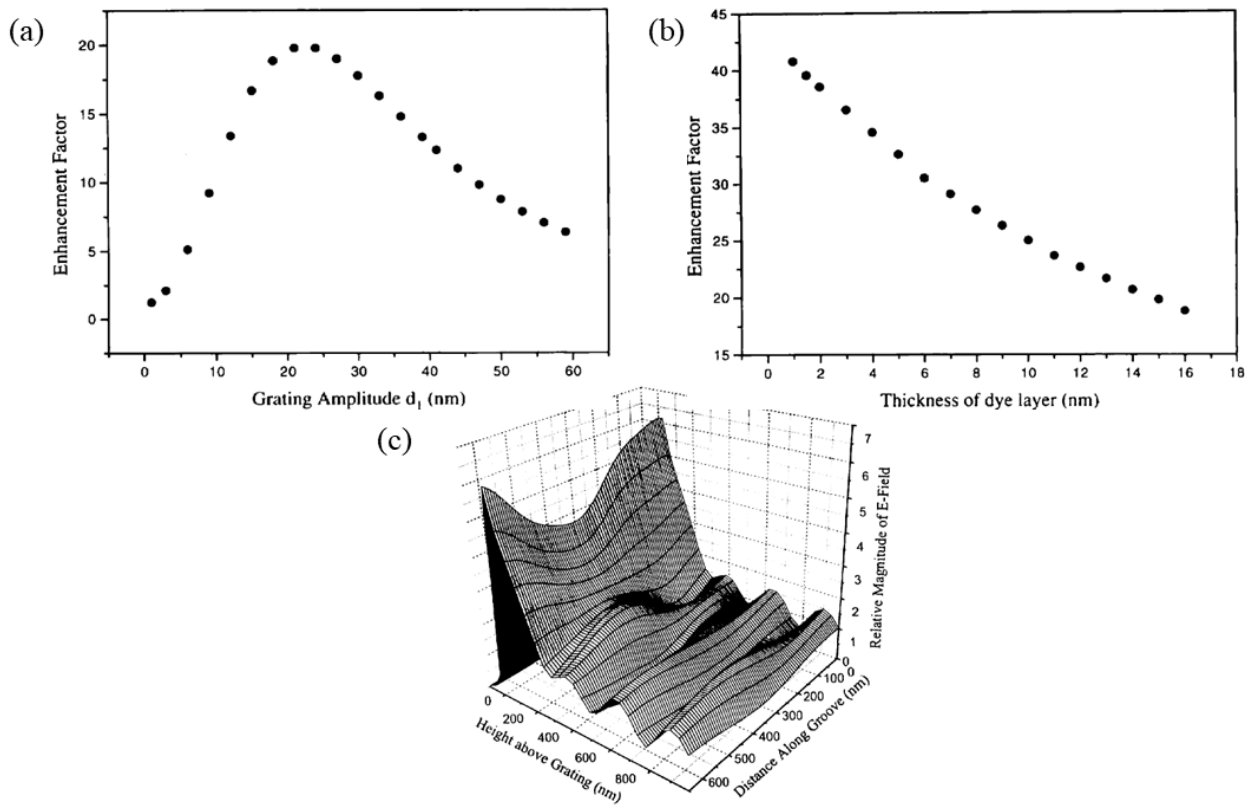

Figure 13 Fluorescence enhancement of dye molecules over silver grating [112]. (a) Fluorescence intensity normalized to emission far from SPP resonance vs grating height. (b) Normalized emission intensity vs dye layer thickness. (c) Normalized SPP electric field magnitude above grating surface and along the groove of one grating period. The fluorescence emission intensity depends linearly on the local field intensity.

A theoretical study supported by experimental measurements also showed spatially inhomogeneous excitation and emission maxima for dye molecules near a gold grating surface. It also represented spatially inhomogeneous photobleaching of molecules due to field localisation [113].

It has been shown that the spontaneous emission of Eu^{3+} ions above a metallic mirror and above a shallow grating structure (with depth to pitch ratios of less than 0.1) do not differ much in terms of dependency on distance from the structure surface [114]. The difference is significant for deeper grating structures as shown in Fig. 14(a). For a deep grating the SPP mode wave vector increases resulting in a greater density of available SPP modes per unit wave vector at each frequency that the fluorophores can couple to, thus, increasing their emission rate [115]. This fact has also been shown by comparing radiation patterns of metallic mirror, shallow grating and deep grating in Fig. 14(c). The fluorescence decay curves for metallic mirror or shallow grating cases are perfectly fitted to single exponential form, however, for the deep grating, this was not the case as shown in Fig. 14(b), indicating the variation of fluorophore lateral positions above the structure [114].

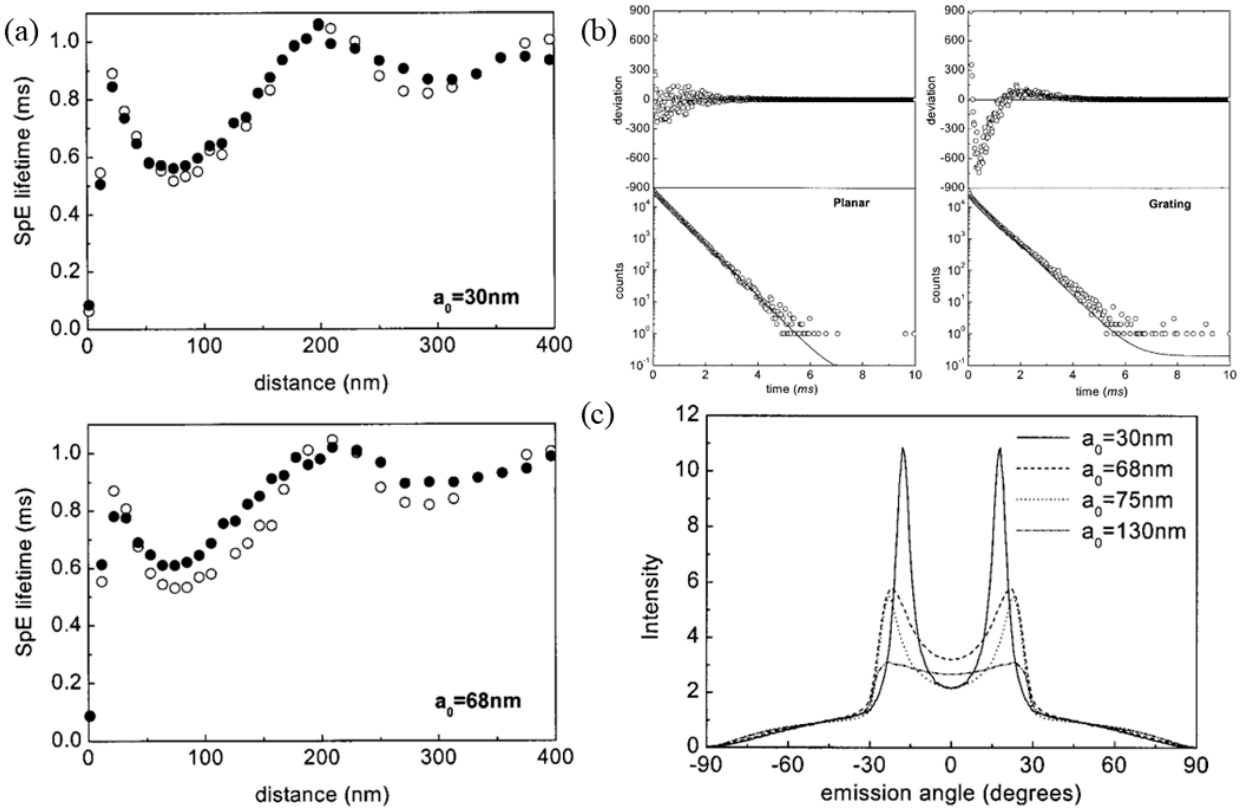

Figure 14 Study of Eu^{3+} ions above metallic grating [114]. (a) Lifetime of a monolayer of ions above silver grating with pitch of 415 nm and ridge height of 30 nm and 68 nm as a function of ion surface distance (solid circles). Open circles show the data for silver mirror. (b) Decay transients of ion monolayer 83 nm above a silver mirror on a grating with 415 nm pitch and 130 nm height. Lower panels show solid lines as the single exponential fit to measured data (open circles) and upper panels show the deviation between fit results and measure data. (c) Radiation pattern of ion monolayer 10.4 nm above silver grating with 415 nm pitch and 30 to 130 nm grating ridge heights.

2.3.2 Lifetime Measurement Methods

Time resolved measurements of fluorescence yields more information than steady-state fluorescence measurements. In steady-state fluorescence, fluorophores are excited with a continuous-wave (CW) laser beam and the resulting emission is detected and studied but such measurement only carries information about the intensity and spectrum of the emission [116]. Time resolved fluorescence decay measurements include such information but also informs about the molecular structure, static and dynamic quenching, resonance energy transfer, purity of the emitters, and donor-to-acceptor distance [96].

Assuming the sample containing fluorophores is excited with a sharp δ function light pulse, the sample then has a population n_0 of fluorophores in the excited state. This population decays with a rate of $\gamma_r + \gamma_{nr}$ following:

$$\frac{dn(t)}{dt} = (\gamma_r + \gamma_{nr})n(t) \tag{14}$$

with $n(t)$ being the number of molecules in the excited state as a function of time. The emission is a random process, and all molecules have same probability of decay and emission in each time interval. Following Eq. (14), an exponential decay of the excited state population results as $n(t) = n_0 \exp\left(-\frac{t}{\tau}\right)$ or as:

$$I(t) = I_0 \exp\left(-\frac{t}{\tau}\right) \tag{15}$$

in terms of emission intensity $I(t)$ with I_0 the intensity at time 0 and $\tau = (\gamma_r + \gamma_{nr})^{-1}$. It is worth noting that not all fluorophores emit at a time delay of one lifetime. In fact, due to the randomness of the emission, many emitters emit before τ and some emit after τ, leading to the intensity exponential decay curve. For a single exponential decay, the lifetime is equal to the statistical average of the time that fluorophores remain in the excited state before emission:

$$< t >= \frac{\int_0^\infty tI(t)\,dt}{\int_0^\infty I(t)\,dt} = \tau \tag{16}$$

If the sample is more complex and the decay curve includes a multi-exponential or non-exponential behaviour, then the right side of Eq. 16 does not hold.

There are two main approaches that have been broadly followed by researchers for the lifetime measurement of fluorophores. One is a time-resolved measurement, and the other is frequency-domain fluorometry. In this section the theory and implementation of these two methods are explained and a new frequency-domain lifetime measurement technique is suggested. A schematic representing these two methods is shown in Fig. 15.

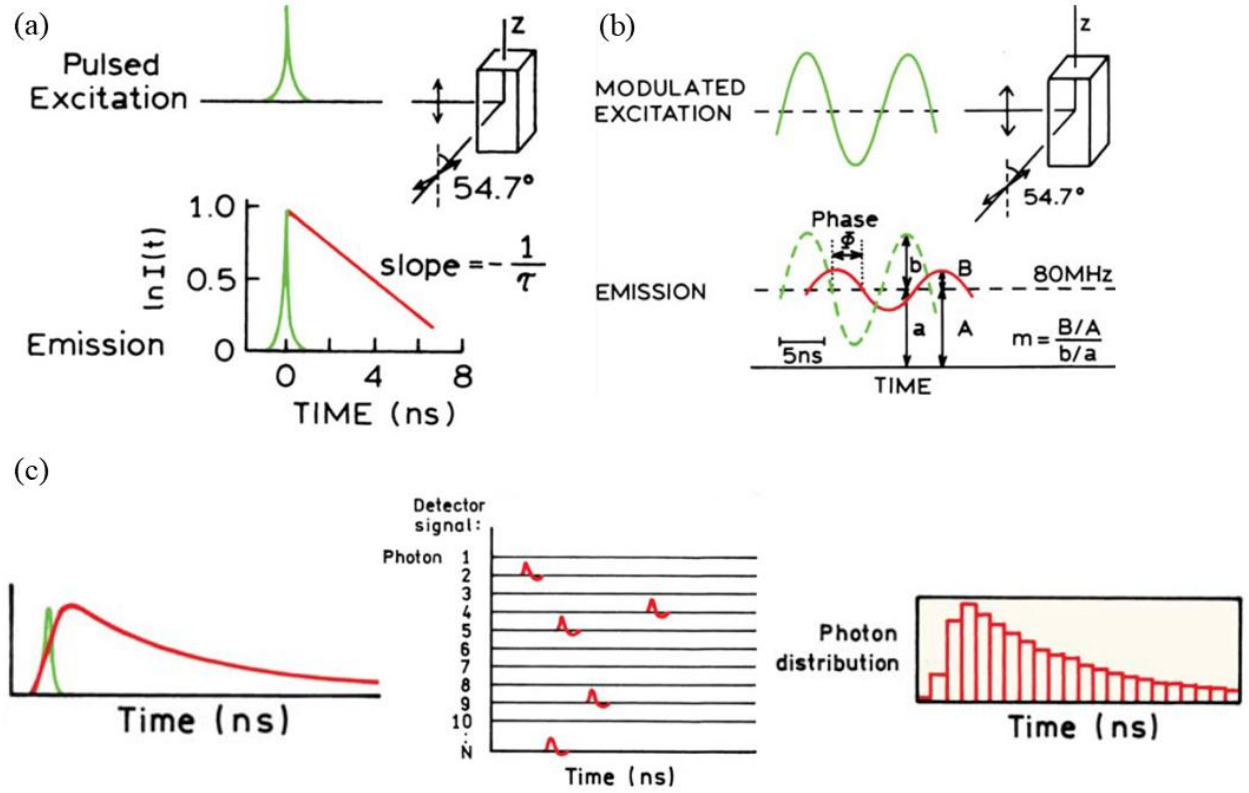

Figure 15 Fluorescence lifetime measurement methods [96]. (a) Time-Domain method (pulse fluorometry). (b) Frequency-Domain method. (c) TCSPC method. From left to right: emission waveform if many photons were emitted per excitation pulse, time stamp of detected emission photons for excitation pulses numbered on the vertical axis, and the recorded histogram of fluorescence emission photons distribution against time for many excitation pulses.

Time-Domain Lifetime Measurement

In this method, also known as pulse fluorometry, emitters are excited with a short pulse of light, the duration of which is made as short as possible, and preferably much shorter than the decay time of the emitters (τ). Following that, the time dependant intensity of the emission ($I(t)$) is recorded versus time and the decay time (τ) is calculated from the slope of $\log(I(t))$ plot against t or from the time it takes for the intensity to drop to $1/e$ magnitude of $I(0)$.

Most of the samples, display more than one decay lifetime which means Eq. 15 has more than one term. Samples can have identical fluorophores but in different environments which causes different absorption and lifetimes, and a more complex decay behaviour, or samples can have a mixture of different fluorophores. Thus, Eq. 15 must be rewritten as:

$$I(t) = \sum_i \alpha_i \exp(-t/\tau_i) \tag{17}$$

with α_i proportional to the fractional population of species with different fluorescence behaviour. For the samples with one fluorophore type, α_i values show the fraction of molecule population at each environmental condition at $t = 0$ and for complex samples, α_i depend on concentration, absorption, quantum yield, and intensity of fluorophore emission at each wavelength. This causes the $\log I(t)$ plot to be curved rather than a straight line for a single exponential. Each pair of α_i and τ_i parameters are correlated which makes it very difficult to determine their exact values while interpreting data and curve fitting analysis.

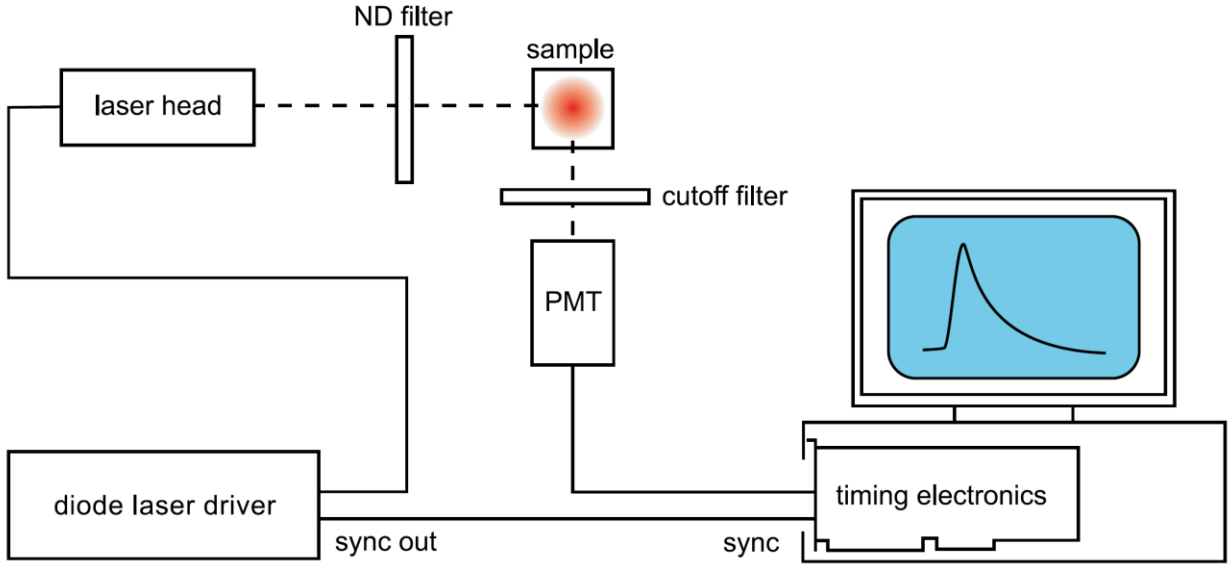

Figure 16 Simple TCSPC measurement setup [117]. The laser driver provides a synchronization signal for the TCSPC (timing) electronics, each time a short laser pulse is hitting the sample. This signal is used to time stamp the excitation photon in the electronics. A photomultiplier tube (PMT) generates an electrical voltage pulse upon detecting a fluorescent photon which is used by electronics to time stamp the arrived emission photon and build up the histogram based on the delay between these two photons.

Most time-domain lifetime measurements are performed using the time-correlated single-photon counting (TCSPC) method [118] [119]. In this method, the sample is excited with a short light pulse and results in an emission waveform as represented in Fig. 15 (c) if many photons are emitted from many excited fluorophores. However, the method is modified to detect only one (or less) photon per excitation pulse, e.g., usually one photon per 100 laser pulses. The time delay between the excitation pulse and the detected photon is stored in a histogram as shown in Fig. 15 (c). By repeating this measurement process for numerous

excitation pulses, enough emission photons get detected to construct a histogram that represents the decay curve. If more than one photon is emitted per excitation pulse, the histogram will be biased towards shorter times because only the first arriving photon can be detected by current TCSPC electronics. The electronics that are available at present, are fast enough to detect multiple photons per excitation pulse only if the decay time is near a microsecond or longer.

The intensity in Eq. 17 assumes an impulse function excitation with no temporal width and a direct measurement of fluorescence response. However, in reality, the excitation pulse has a temporal width, and the detector and timing electronics can not also respond immediately. For TCSPC measurements, it is important to know the system's impulse response function (IRF) or its response to a zero-lifetime sample. This is given by the convolution of impulse responses of the instrument timing electronics and the detector, and the laser pulse duration [120], and is normally gathered by exciting a scattering sample with no fluorescence emission (zero lifetime for reflected/scattered light). The collected decay curve in this case shows the shortest lifetime that can be measured with the system. The temporal duration of this response is as follows [121]:

$$FWHM_{IRF}^2 = FWHM_{exc}^2 + FWHM_{TTS}^2 + FWHM_{jitter}^2 + FWHM_{dsp}^2 \quad (18)$$

where $FWHM_{exc}$, $FWHM_{TTS}$, $FWHM_{jitter}$, and $FWHM_{dsp}$ are the full width at half maximum of temporal duration of excitation pulse, detector transit time spread, electronics jitter, and optical components dispersion, respectively. As a result, the measured decay curve of a fluorescent sample is also the convolution of the system's IRF and the fluorophores' impulse response. To obtain the lifetime of the fluorophores, especially for lifetimes close to the IRF FWHM, one needs to deconvolve the measured system's IRF from measured decay curve [120] as in Fig. 17.

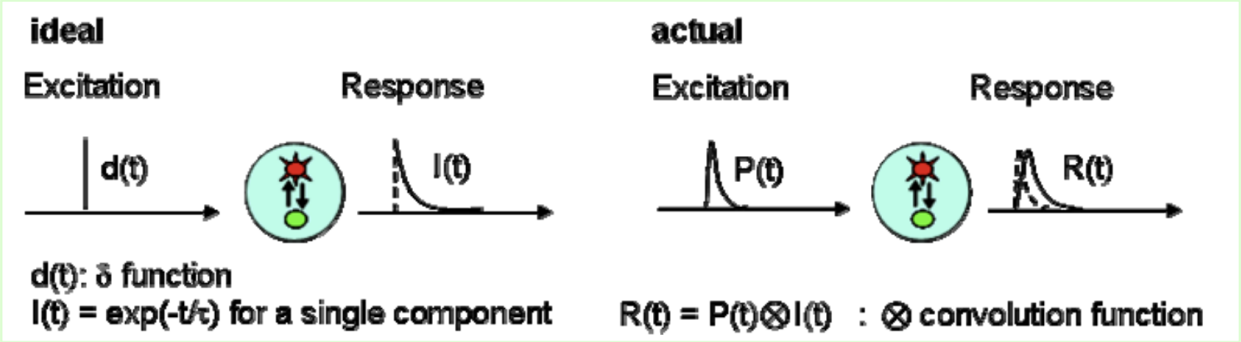

Figure 17 Ideal and actual situations in a fluorescence measurement system and the role of system's IRF on the measured decay curve [121].

Frequency-Domain Lifetime Measurement

In the alternate method, also known as phase modulation method, the sample is excited with intensity-modulated (typically a sinusoid) light with a modulation frequency comparable to $(1/\tau)$. As a result of this excitation, the fluorescence emission would also be a modulated intensity with the same sinusoid but time-delayed as imposed by the lifetime (τ) with respect to the excitation. This delay can be measured as a phase shift (ϕ) between the excitation and emission intensities and can be used to calculate the decay time using:

$$\tan \phi_\omega = \omega \tau_\phi \quad (18)$$

The lifetime of the species also decreases the peak-to-peak amplitude of the fluorescence emission compared to the excitation. This is due to the fact that when the excitation is at its minimum, the fluorophores which were excited at the excitation maximum, continue to emit light. The modulation depths

of excitation and emission intensities are given as (b/a) and (B/A) respectively with "a" and "A" being the corresponding average intensities and "b" and "B" being the corresponding peak-to-peak heights. The demodulation factor is defined as modulation depth of emission relative to the modulation depth of excitation, "$m = (\frac{B}{A})/(\frac{b}{a})$". The demodulation parameter (m) can also be used to extract the lifetime following:

$$m_\omega = \frac{1}{\sqrt{1+\omega^2\tau_m^2}}; \qquad \tau_m = \frac{1}{\omega}\left[\frac{1}{m_\omega^2} - 1\right]^{1/2} \tag{19}$$

If the intensity decay includes a single exponential, equations 19 and 20 must give similar and correct values for the decay lifetime (τ). If the emission behavior is a multi-exponential or non-exponential decay, as is true for many samples, the two equations yield apparent lifetimes which are complex weighted averages of all decay components present [96]. Under these conditions, it is necessary to measure the phase shift and modulation depth not only at one modulation frequency but rather over a wide frequency range. In fact, for the shortest lifetimes, the higher the modulation frequency, the more accurate the extracted lifetime will be. It is obvious that the values of ϕ and m depend on the relative difference between the measured lifetime and the period of modulation. As the modulation frequency increases, the phase shift increases, and the modulation depth of emission decreases which makes it easier to extract the τ value from them. However, it is worth mentioning that when the frequency is too high, the modulation depth reaches zero and becomes unmeasurable. On the other hand, the phase shift also reaches 90°, remaining constant and frequency independent. Fig. 18 (a) shows the phase shift and modulation depth frequency responses for different lifetimes with solid bar lines representing the useful frequency range for extracting τ.

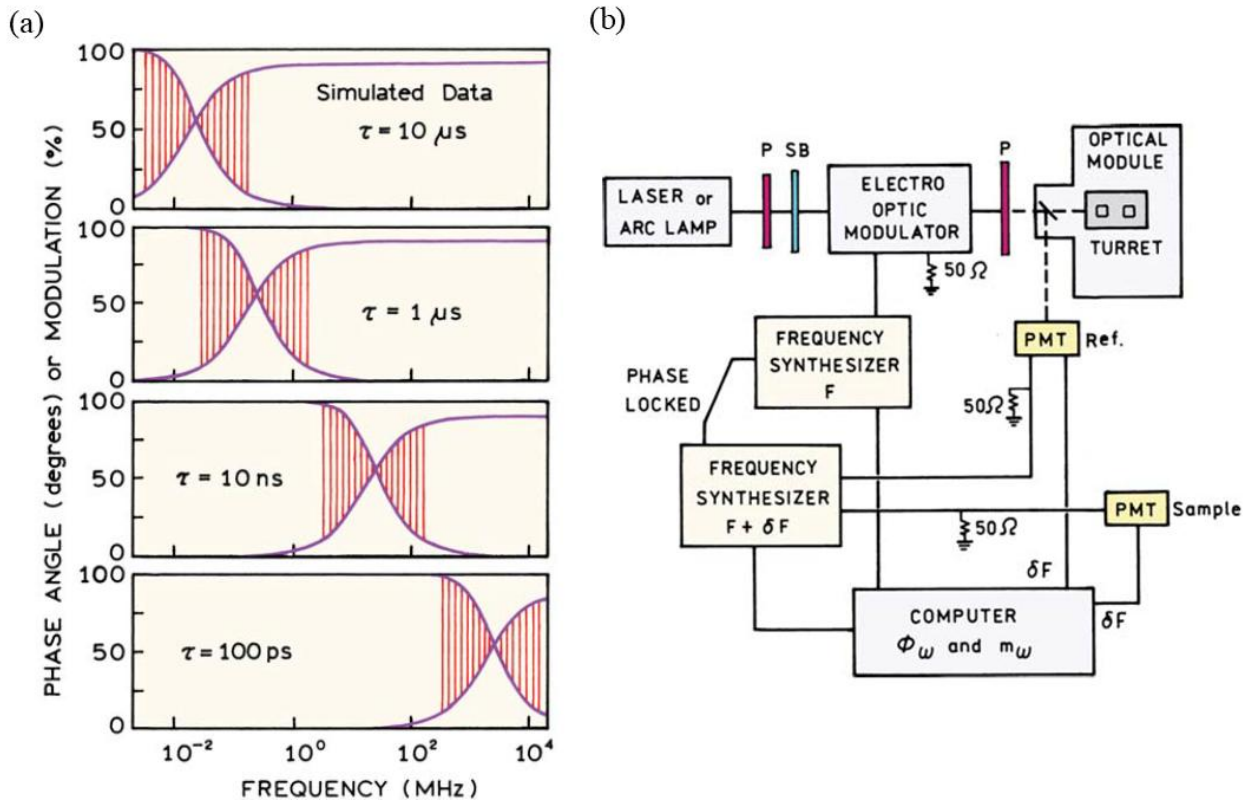

Figure 18 Frequency domain fluorescence measurement and setup [96]. (a) Phase and modulation depth frequency responses and the proper frequency range for different lifetime ranges. (b) Common measurement setup.

Most of current frequency domain fluorescence measurements are limited to an upper frequency limit of 200 MHz unless using the harmonic frequency content of a laser pulse train. However, it is desirable to do measurements over wider frequency bands especially for lifetimes in the range of 100 ps or lower based on Fig. 18 (a). There are two reasons for this limitation: one is that light sources typically used in fluorescence measurements can not be modulated at high speeds, and the second is that photo multiplier tubes (PMTs) can not follow faster signals.

Figure 18 (b) shows a typical frequency domain fluorescence measurement setup called cross correlation method. In this method, the detector gain gets modulated at a frequency slightly offset (δF) from the excitation source modulation frequency (F) while the two synthesizers producing sine-waves at these frequencies are phase locked (zero phase difference). When a modulated signal at frequency "F" hits the detector, the gain modulation will bring the detector electrical signal output at the lower frequency of "δF" carrying all the phase and modulation information included on the optical input signal. The system uses two detectors with this method; one for detecting reflected excitation light or zero lifetime sample response, and one for detecting the fluorescence emission. The reflecting and fluorescing samples are normally on a rotating stage, meaning everything else remains the same in the setup. As a result any phase and modulation difference between these detectors' outputs which are measured by frequency domain electronics is only due to the lifetime of fluorophores. This process is performed for all the frequency points in the testing range with the same value of frequency offset (δF). This method prevents unwanted harmonics and noise at other frequencies impacting the results due to extracting the phase and modulation information at low frequencies [96].

As a potential alternative method, one can use a vector network analyzer (VNA) and a high-speed photoreceiver instead of two PMTs and frequency synthesizers as in Fig. 18 (b). In this method, an electro-optic modulator is used to modulate the excitation laser CW output with the VNA electrical signal output. The resulting modulated fluorescence emission then can be detected with a high-speed photoreceiver and sent back to second port of the VNA. The electronics inside the VNA include phase locked local oscillators and mixers and are able to extract the relative modulation depth and phase difference between their output and input electrical signals for wide frequency sweeps. The suggested alternative setup can be as shown in Fig. 19.

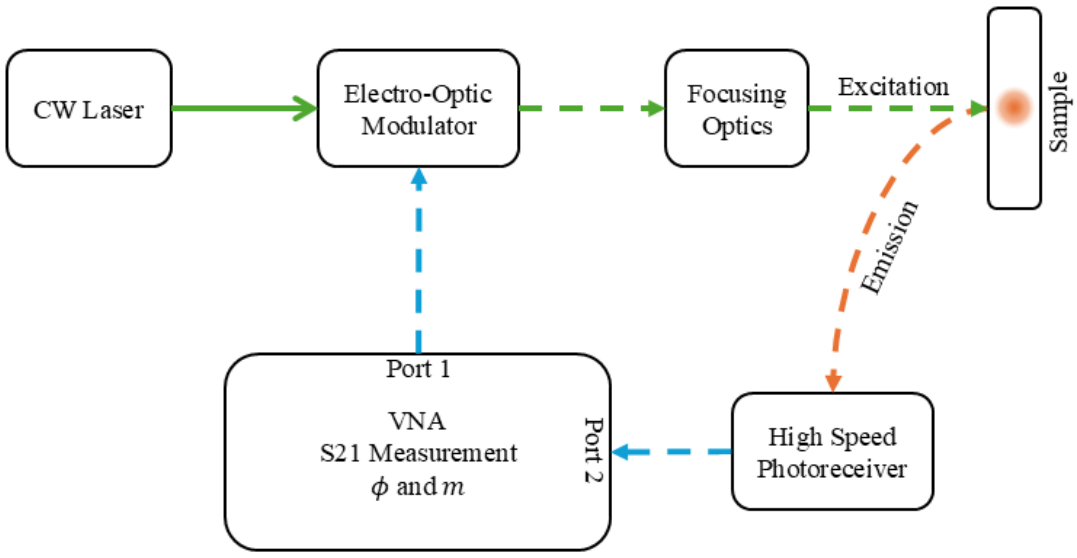

Figure 19 Suggested frequency domain fluorescence measurement setup using a VNA and a high speed photoreceiver.

3 High-Speed Electro-Optic Plasmonic Modulator for CMOS Non-Contact Wafer-Level Testing

3.1 Summary

In this chapter a CMOS compatible electro-optic plasmonic modulator is introduced and experimentally characterized and analyzed. The modulator is a paradigm-shifting solution specifically for wafer-level testing of electronics. This testing procedure is a crucial step in CMOS device fabrication for quality control and yield estimates before packaging. Wafer level testing is currently performed by physical contact between test needles and electronic pads on the wafer, a costly process which sacrifices both devices and pads, and the test needles themselves on expensive and specially designed probe cards. This compact modulator can be placed anywhere in wafer layout, helping to use unused tight spaces on the wafer and saving the valuable space otherwise used by contact pads. The modulator combined with a similar structure (like the structure introduced in Chapter 4) used as a high-speed photodetector, provides a platform for full non-contact communication between the devices on the wafer and testing instruments. Photodetectors are used to receive an optical carrier modulated with data and test instructions (green channel in Fig. 1 of the following journal article) coming out of an optical fiber. Photodetector converts the optical data into electrical test instructions used to drive CMOS circuitry. Once an electrical test is completed, the resulting electrical data drives a reflection modulator (the device introduced in this chapter). Modulator modulates intensity of incident CW optical carrier at the reflection with electrical test results (red channel in Fig. 1 of the following journal article) which is collected using another optical fiber. It is experimentally shown that the modulator works up to 22 GHz and over 100 nm of optical bandwidth with a 0.12% modulation depth and 4 dB insertion loss showing reasonable performance for wafer level testing requirements. The device has a small footprint (5 μm diameter) making it a good candidate for compact design needs in current wafer technology.

3.2 Contribution

The research work provided in this chapter was published in and is reproduced with permission from the IEEE Journal of Selected Topics in Quantum Electronics [122]. I performed the numerical analysis for modeling the electro-optic response of the device. I designed and made the electro-optic setup required for measurements. I performed all the optical, electrical, and electro-optic measurements required for characterizing the modulators. I modeled and extracted the equivalent circuit of the device for bandwidth performance estimation. I interpreted and analysed theoretical and experimental results and wrote the manuscript. Professor Berini contributed to the device and measurement setup proposal, wafer level testing method proposal, interpretation of results, and revision of the manuscript.

High-Speed Electro-Optic Plasmonic Modulator for CMOS Non-Contact Wafer-Level Testing

Maryam Sadat Amiri Naeini and Pierre Berini, *Fellow, IEEE*

***Abstract*—Wafer-level testing is an important step for process and quality control of electronic chips in integrated circuit (IC) manufacturing which occurs before packaging. The process of wafer probing in its conventional contacting schemes, becomes more complicated as ICs move to smaller technology nodes and more compact designs, greatly increasing testing costs. Non-contact optical wafer probing can overcome physical probing complications, reducing costs, and increasing throughput and reliability. In this article, a CMOS compatible, broadband (22 GHz), small footprint (5 μm dia.) plasmonic electro-optic modulator of low insertion loss (4 dB) and wide optical working bandwidth (100 nm) is proposed and demonstrated as a potential solution for wafer-level optical testing. The device modulates in reflection an incident optical carrier emerging from an optical fiber in a non-contact arrangement, to work as a data output channel from the wafer. A modulation depth of over 2% is achieved which should be sufficient to meet the requirements of wafer-level testing. The device can be placed anywhere on wafer.**

***Index Terms*—CMOS compatible, high-speed modulator, low insertion loss, plasmonic modulator, wafer-level probing.**

I. Introduction

IN THE ever-growing landscape of semiconductor electronics, the demand for smaller, faster, more efficient and more powerful electronic devices has led to continuous evolution in design and manufacturing processes. These innovations apply increasing pressure on the crucial step of wafer testing (probing) [1], [2], [3], [4], [5], [6], [7], [8], which serves to assess the performance of high-volume, high-density, and high-value Si CMOS ICs (complementary metal oxide semiconductor integrated circuits) such as microprocessors, memories, and systems-on-a-chip. Wafer testing occurs after wafer manufacturing and test data are used for yield estimates, process quality control and product verification before die singulation and packaging – wafer test is a gateway to completed and qualified electronic products.

Traditional wafer probing methods involve physical engagement between hundreds of needles in probe cards with electrical pads on wafer, a process laden with a variety of challenges, including the manufacturing of customized probe cards which is complicated and costly, damage and material accumulation on probe needles after several touchdowns, wafer and device damage due to probe contact, limited bandwidth of test signals, electromagnetic interference and impedance mismatch, low test throughput, and limited scalability. Non-contact wafer probing would be paradigm-shifting, motivating the investigation of a variety of innovative approaches involving e-beam [9], [10], plasmas [9], ultra-violet lasers [11] and other optical interrogation methods [12], [13], capacitive coupling to an AFM (atomic force microscope) probe [14], [15], [16], [17], and broadside-coupled striplines [18], all of which are only used for defect inspection at small scales and mostly aren't suitable for volume testing. Near field radio frequency interrogation by inductive coupling has also been proposed [11] but this approach suffers from limitations in scalability due to crosstalk, and difficulty in maintaining the small distance required between the wafer and the test head. Considering the challenges posed by various methods, optical solutions are promising if they can be integrated into industrial electronics manufacturing processes [12]. However, more work is required involving new designs and techniques, especially for system-in-package (SiP) and 3D IC testing.

The primary criteria for a successful practical solution include three key factors: (*i*) optoelectronic performance that is sufficient to establish communication between electronics on-wafer and the test instrument, (*ii*) optoelectronic device compatibility with CMOS fabrication processes [19], and (*iii*) optoelectronic device dimensions that are of the same size (or smaller) than the test pads on chip that would be replaced. In this context, CMOS compatible metal-oxide-semiconductor (MOS) based plasmonic optoelectronic devices, such as electro-optic modulators and photodetectors hold the promise of a potential solution. The scheme could be implemented using plasmonic optoelectronic devices probed by a fiber array probe card, as suggested in Fig. 1.

In such a scheme, a photodetector on chip would be used to receive an optical carrier modulated with test instructions and data, e.g., via NRZ on-off keying, as the input signal from the test instrument. The photodetector then converts this modulated signal to an electric signal which is amplified by transimpedance

Manuscript received 30 January 2024; revised 16 May 2024; accepted 29 July 2024. Date of publication 2 August 2024; date of current version 8 August 2024. This work was supported by the Natural Sciences and Engineering Research Council of Canada under Grant 210396. *(Corresponding author: Pierre Berini.)*

Maryam Sadat Amiri Naeini is with the Department of Physics, University of Ottawa, Ottawa, ON K1N 6N5, Canada, and also with the Nexus for Quantum Technologies Institute - NEXQT, University of Ottawa, Ottawa, ON K1N 6N5, Canada (e-mail: .....).

Pierre Berini is with the School of Electrical Engineering and Computer Science, University of Ottawa, Ottawa, ON K1N 6N5, Canada, also with the Department of Physics, University of Ottawa, Ottawa, ON K1N 6N5, Canada, and also with the Nexus for Quantum Technologies Institute - NEXQT, University of Ottawa, Ottawa, ON K1N 6N5, Canada (e-mail: .....).

Color versions of one or more figures in this article are available at https://doi.org/10.1109/JSTQE.2024.3437193.

Digital Object Identifier 10.1109/JSTQE.2024.3437193

1077-260X © 2024 IEEE. Personal use is permitted, but republication/redistribution requires IEEE permission.
See https://www.ieee.org/publications/rights/index.html for more information.

Authorized licensed use limited to: University of Ottawa. Downloaded on March 14,2025 at 19:57:09 UTC from IEEE Xplore. Restrictions apply.

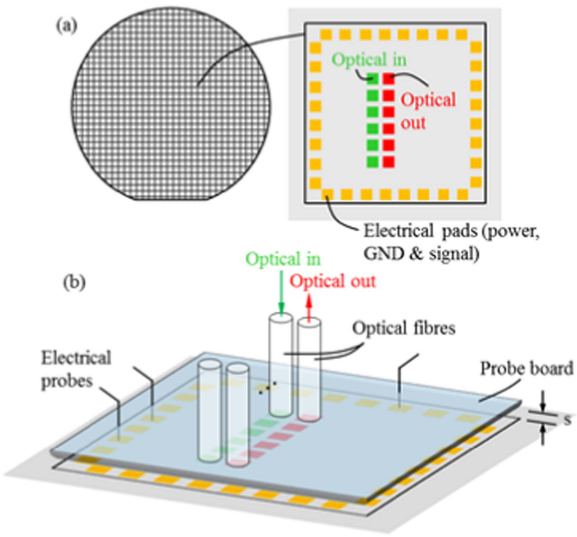

Fig. 1. (a) Sketch of a Si wafer and of a die in expanded view showing power, ground and signal pads on the periphery and optical inputs (photodetectors – green squares) and outputs (modulators – red squares) in the central region. (b) Non-contact optical interrogation of a die under test using an array of fibers mounted to a probe card aligned to photodetectors and modulators on chip. The photodetectors receive a data stream on a modulated optical carrier (green), whereas the modulators receive a CW beam and return by modulated reflection, a data stream on the same beam (red).

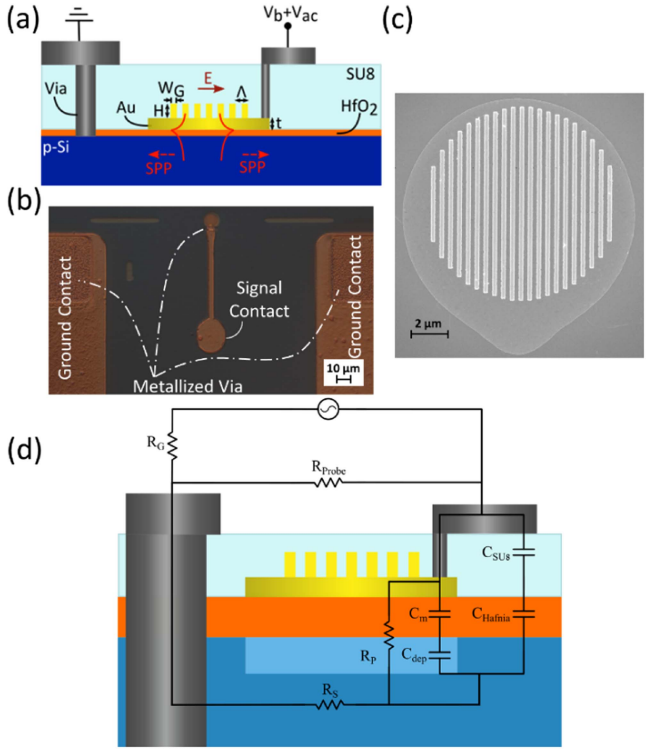

Fig. 2. (a) Schematic of the modulator cross-section. (b) Optical microscope image of an 11 μm diameter modulator with ground-signal-ground contact pads. (c) Scanning electron microscope (SEM) image of an 11 μm diameter gold pad bearing a grating coupler (die O6) acquired during fabrication. (d) Equivalent circuit superimposed on the modulator structure in panel (a), showing the origin of each circuit element, including the capacitance associated with the depletion layer in Si shown as the light blue region. The generator and probe are also shown connected to the equivalent circuit.

and limiting amplifiers, to then drive CMOS circuitry used to implement testing routines such as built-in self-tests or scanning chains. Once a built-in self-test or scanning chain is completed, the resulting data is sent to an amplifier which drives a reflection modulator on chip used to modulate an incident CW (continuous-wave) optical carrier, thereby sending test data off chip to the test instrument as modulated reflected light. The compact nature of plasmonic elements, enabled by the strong confinement of surface plasmon polaritons (SPPs), allows for their dimensions to be very small, e.g., of the size or smaller than a diffraction-limited incident beam, which ensures minimal consumption of valuable area on wafer.

There have been substantial study and development of silicon [20] and silicon MOS based modulators [21]. Due to the indirect bandgap of Si and the lack of a linear electro-optic effect, the most common modulation approaches have involved interference or ring-resonator designs [20], [21], [22], exploiting the carrier refraction effect [23]. Interferometers have large footprints and ring resonators have high sensitivity to temperature and require tight fabrication tolerances, precluding the use of such structures for testing applications. Recently, plasmonic and hybrid-plasmonic modulators have also received significant attention due to the enhanced light-matter interaction which enables small active areas [24], [25]. The enhancement is due to the tight light confinement within the active area. However, such designs need to be integrated with silicon waveguides resulting in enlarged final device dimensions [22], [24], [25], [26], [27]. Furthermore, the light coupling methods in these devices are not well-suited to wafer probing purposes where the optical inputs and outputs should be accessible via the top surface of the wafer (*cf.*, Fig. 1), and the materials used for the active region are not part of CMOS material sets [28], [29]. These properties make existing plasmonic modulator concepts unsuitable for non-contact wafer probing applications.

Building on previous work carried out at low frequencies [30], we introduce in this article a high-speed MOS-based plasmonic reflection modulator on Si that has the electro-optic bandwidth, modulation depth, optical insertion loss, and a coupling method and fabrication intolerance suitable for wafer testing applications. Their compact dimension (down to 5 μm in diameter) enables operation up to 22 GHz as lumped elements, and in principle, can be integrated anywhere on wafer while consuming very little area. Combining the modulators with plasmonic photodetectors, based on tunnelling in a MOS structure [31], or on internal photoemission in a Schottky structure [32], could lead to a full non-contact optical test solution for electronic wafers following the approach of Fig. 1.

II. Device Structure and Concept

As shown in Fig. 2, the reflection modulator consists of a MOS capacitor bearing a plasmonic grating as the top metal contact. The grating enables plasmon excitation along the MOS structure upon optical illumination at perpendicular incidence at the grating design wavelength and with a polarization aligned perpendicular to the grating fingers. The MOS device is biased

Authorized licensed use limited to: University of Ottawa. Downloaded on March 14,2025 at 19:57:09 UTC from IEEE Xplore. Restrictions apply.

around the flat-band voltage and driven between the accumulation and depletion regimes by applying an AC drive voltage. The AC voltage modulates the density of accumulated carriers in the semiconductor near the oxide layer, which modulates the effective index of the surface plasmons via the carrier refraction effect [21], thereby modulating the fraction of incident light that is coupled to the surface plasmons [30]. As a result, the light intensity reflected by the modulator is modulated by the applied signal.

Modulator chips were designed as circular parallel plate MOS capacitors of various diameters (5, 11, 17, 22 and 28 μm) formed as a t = 20 nm thick gold layer on 5 nm thick hafnium dioxide (HfO_2) layer on a heavily doped p-Si ($\rho = 0.001$–$0.005\ \Omega$ cm) substrate. The gold layer was covered by a plasmonic grating of thickness H = 80 nm and of pitch selected in the range of $\Lambda = 420$–480 nm, following the momentum conservation condition at the working wavelength for the case of a normally incident Gaussian beam ($\Lambda = \lambda_0/n_{eff}$), where n_{eff} is the effective refractive index of plasmons propagating along the bottom surface of the gold patch (along the MOS structure), and λ_0 is the free-space working wavelength ($\lambda_0 = 1470$–1680 nm). The chips were then passivated by a 554 nm SU8 protective layer and electrical contact pads were fabricated on this layer connected to the gold and silicon layers through metallized vias. The pitch of the pads was selected to accommodate 40 GHz ground-signal-ground (coplanar waveguide) probes. Further details on the fabrication of the modulators can be found elsewhere [33]. The schematic cross-section of the modulator in Fig. 2(a) illustrates the construction of the modulator including the materials, dimensions, and electrical contact vias. Fig. 2(b) gives a microscope image of a complete 11 μm diameter reflection modulator, including a signal contact and two ground contacts designed to minimize electrical parasitics. Fig. 2(c) gives a scanning electron microscope (SEM) image of the gold pad of an 11 μm diameter device bearing a plasmonic grating taken during the fabrication process. p-Si and HfO_2 are Si CMOS materials, but gold is not – gold was used in our experimental devices but could be replaced with a CMOS metal, e.g., copper.

III. Theoretical

A. Optical Modelling

To study the performance of various designs, numerical calculations were performed in 2D for device diameters of 5, 11, 17, and 28 μm, illuminated by a 5 μm diameter Gaussian beam aligned and focused on the plasmonic grating at normal incidence, in a scheme comparable to envisage concept (Fig. 1) and our experimental set-up. To account for the carrier refraction effect, a thin (1 nm) layer in the semiconductor adjacent to the oxide was assumed to have carrier density and refractive index perturbations associated with the applied AC voltage of $\Delta N_a = 10^{20}\ cm^{-3}$, $\Delta n = -0.5$ and $\Delta k = 0.1$ [30]. Simulations were done using a commercial finite element method (FEM) analysis tool and the structure was surrounded by perfectly matched layers bounded by scattering boundary conditions to avoid any artificial numerical back reflections. The gold and doped silicon permittivity were adopted from the literature [34].

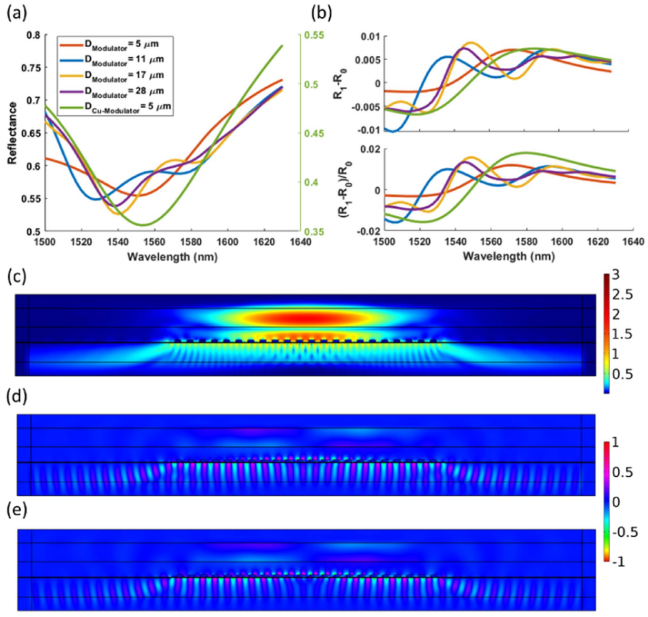

Fig. 3. (a) Calculated reflectance response of modulators of different diameters. The copper device response is plotted on a different scale on the right. (b) Calculated reflectance modulation (top panel) and normalized reflectance modulation (bottom panel) of devices in Part (a). (c) Total electric field magnitude (V/m) at $\lambda = 1527$ nm for the 11 μm diameter gold modulator. (d), (e) Real part of transverse electric field, $Re\{E_y\}$, (V/m) at $\lambda = 1527$ nm and $\lambda = 1574$ nm. The incident field strength in all cases was set to 1 V/m.

The thickness and refractive index of the hafnia layer were taken as $H_{HfO_2} = 5$ nm and $n_{HfO_2} = 1.88$ [35] respectively. The refractive index of the SU8 cover layer was assumed as $n_{SU8} = 1.57$ [36]. A thin (1 nm) native silicon dioxide layer was added to the silicon substrate below hafnia.

Fig. 3(a) shows the calculated reflectance of modulators of different diameters, designed for operation at $\lambda_0 = 1550$ nm, with a grating pitch of $\Lambda = 440$ nm, ridge width of $W_G = 220$ nm (50% duty cycle), and ridge thickness of H = 81 nm, in the absence of the thin perturbed layer (i.e., the carrier density and refractive index of the silicon substrate adjacent to the oxide layer are unperturbed and set to bulk doped silicon). The plot reveals the main reflectance resonance along with a shoulder on the long-wavelength side for the 11, 17 and 28 μm diameter devices.

Comparing the transverse electric field at the main resonance wavelength and at its shoulder, as plotted in Fig. 3(d) and (e) for the 11 μm diameter device, suggests that the propagating surface plasmons are reflected from the edges of the circular plasmonic patch and interfere to create a standing wave along the patch which causes the appearance of another resonance in the reflection spectrum of the devices [37]. This secondary resonance can also appear if a tightly focused beam is incident on a device of greater area because it contains a broad spectrum of *k*-vectors, or if a device is illuminated by a plane wave or beam incident at an angle [38]. The latter can be observed in Fig. 4(c) where a 3-degree misalignment from normal incidence of the Gaussian beam creates a second resonance in the reflectance spectrum of the grating (discussed further in the Experimental Section).

Authorized licensed use limited to: University of Ottawa. Downloaded on March 14,2025 at 19:57:09 UTC from IEEE Xplore. Restrictions apply.

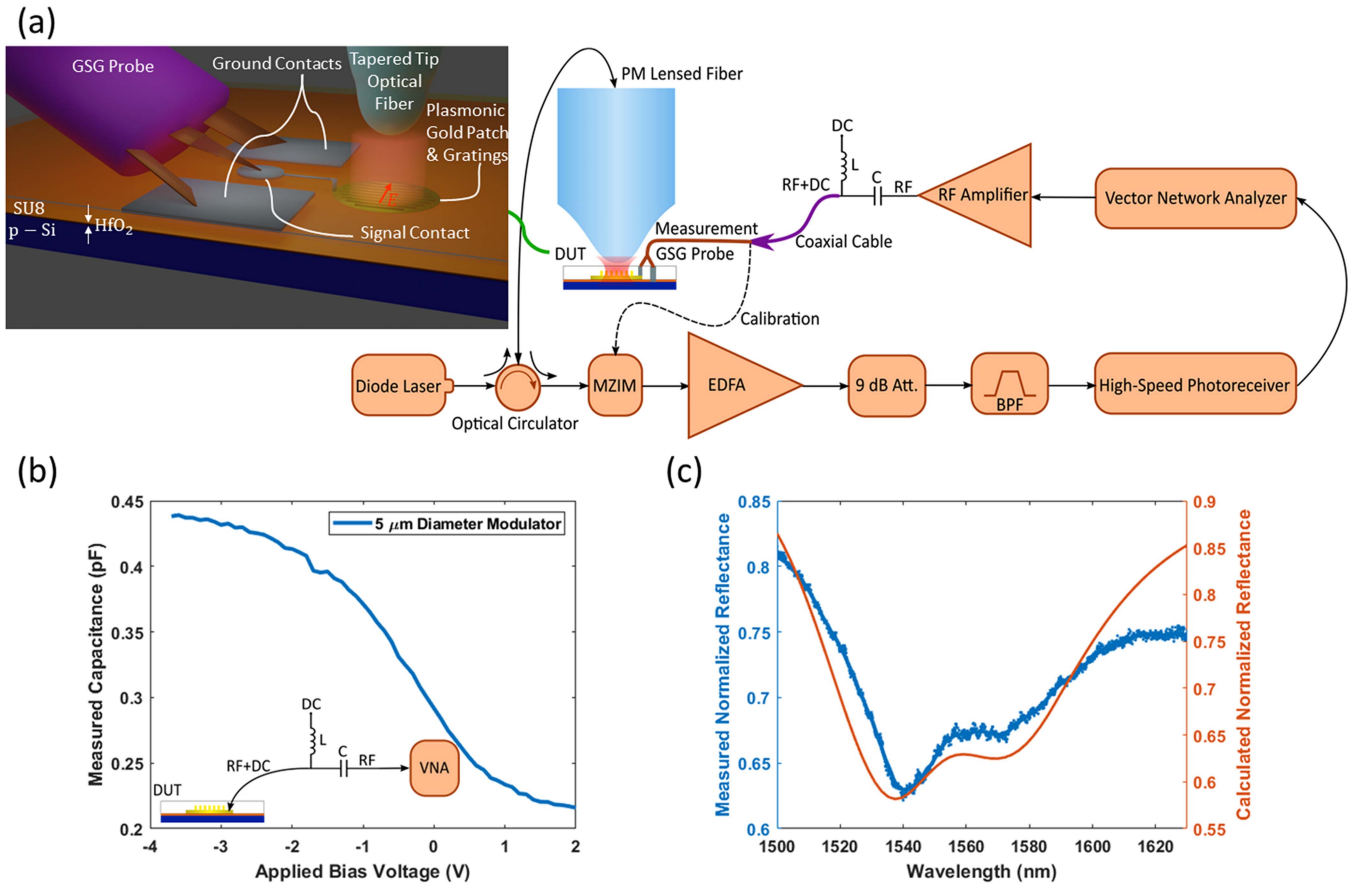

Fig. 4. (a) Sketch of the calibration and measurement setup for the optoelectronic characterisation of modulators via S21 measurements. The sketch in inset presents a closer view of the device probed by a ground-signal-ground probe and illuminated by a tapered optical fiber. (b) Measured high frequency (500 MHz) CV characteristic of a 5 μm diameter modulator. Inset shows the simplified RF setup for S11 measurements. (c) Experimental and theoretical normalized reflectance response of a 28 μm diameter modulator (plotted on different scales).

Fig. 3(b) presents the reflectance modulation response produced by alternating between the unperturbed (R_0) and perturbed (R_1) cases, corresponding to unchanged carrier density with respect to the bulk silicon, and accumulated carriers in silicon adjacent to the oxide, respectively. It is observed that the reflectance modulation has a broad optical bandwidth due to the broad nature of the plasmonic resonance, which peaks around the resonance wavelength where plasmons are most efficiently excited along the bottom metal surface bounded by the oxide and semiconductor regions. Fig. 3(c) clearly reveals the excitation of SPPs along this bottom surface.

A similar study for a 5 μm diameter copper modulator with $\Lambda = 420$ nm and $W_G = 210$ nm is also plotted in Fig. 3(a) and (b), producing a comparable performance to a gold device. These results confirm that substituting gold with copper, which is a CMOS metal, maintains performance. The copper permittivity was adopted from the literature [34].

B. Equivalent Circuit

The equivalent electrical circuit of the modulators is shown in Fig. 2(d) which illustrates the origin of the elements relative to the device cross-section. The MOS structure has a depletion capacitance which is DC bias dependent, modelled as a parallel plate capacitor [39]:

$$C_{dep} = \frac{\in_0 \in_{Si} A_m}{x_d} \tag{1}$$

where $\in_0$ and $\in_{Si} = 11.9$ are the vacuum permittivity and DC relative permittivity of the silicon substrate, respectively, A_m is the area of the modulator, and x_d is the bias dependant depletion width, given by [39]:

$$x_d = \sqrt{\frac{2\in_0 \in_{Si} \phi_S}{qN_A}} \tag{2}$$

where N_A is the equilibrium density of holes in bulk Si and q is the electron charge. Φ_S is the surface potential of the MOS structure at the applied bias. Assuming we have reached strong inversion at the bias voltage of $V_{Bias} = 2$ V, $\phi_S \cong 2\phi_{Bp}$, where ϕ_{Bp} is the potential difference between the Fermi and intrinsic levels of the semiconductor [39]. A bias voltage of $V_{Bias} = 2$ V yields $x_d = 7$ nm and $C_{dep} = 0.4$ pF for the 5 μm diameter device. The depletion capacitance appears in series with the oxide capacitance C_m which is calculated using a parallel plate capacitor model similar to (1), but for a 5.5 nm thick HfO_2 layer as the insulating oxide with $\in_{HfO_2} \cong 10.7$ (relative permittivity) [31]. An oxide capacitance of $C_m = 0.44$ pF is obtained for the 5 μm diameter device, which is very close to

Authorized licensed use limited to: University of Ottawa. Downloaded on March 14,2025 at 19:57:09 UTC from IEEE Xplore. Restrictions apply.

the capacitance measured in the accumulation regime in Fig. 4(b) (*cf.*, Experimental section). Parasitic capacitances between the signal pads and the grounded silicon substrate also appear. These capacitances each include two capacitive contributions in series due to the SU8 and HfO_2 layers separating the pads from ground, calculated as $C_{SU8} = 3$ fF ($\in_{SU8} = 4$ is the relative permittivity of SU8 [40], [41]) and $C_{HfO_2} = 0.86$ pF. The total capacitance of the equivalent circuit for the 5 μm diameter device is then $C_T \cong 0.21$ pF which is close to the minimum capacitance measured in the inversion region of Fig. 4(b) (*cf.*, Experimental section). The parasitic series resistance of the modulators was assumed to originate from the metalized vias and was determined by measuring the resistance of via pairs in 10 interconnected rows of vias, yielding a value of $R_S = 9\ \Omega$. The shunt resistance of the devices was extracted from LCR measurements and found to be least $R_P = 1$ MΩ.

IV. Experimental

A. Experimental Set-Up

Fig. 4(a) illustrates the optoelectronic measurement setup. The modulator chips were illuminated by a polarization maintaining (PM) tapered cone fiber (WT&T, model CL5) at $\lambda = 1550$ nm, with a focal spot diameter of 5 μm at a working distance of ~40 to 50 μm. The polarized output of a tunable diode laser (Photonetics Tunics Plus) was injected into this lensed fiber by first passing through a PM in-fiber optical circulator (OZ Optics).

The intensity-modulated beam reflected from the chip was then coupled back to the lensed fiber and directed out of the third port of the circulator. The modulated optical signal was injected into a fiber-coupled Mach-Zehnder interferometer modulator (MZIM) (JDSU OC-192) operating as a transparent patch cord during the measurements (undriven), or as an intensity modulator to calibrate the set-up. The modulated beam was then amplified using an Er-doped fiber amplifier (EDFA, JDSU AFC) with a fixed 15 dB gain, and attenuated to maintain the optical power to just below the 1 mW maximum input of our high-speed photoreceiver (Thorlabs PDA8GS). The beam was also filtered using a narrow band-pass in-fiber filter (OZ Optic TF) to reduce the amplified spontaneous emission (ASE) noise produced by the EDFA.

To drive the modulators electrically, the chips were contacted using a 50 Ω terminated ground-signal-ground (GSG) microwave probe (Picoprobe, model 40A). The probe was connected to a bias Tee network (Minicircuits ZBT-K283+) by a short RF cable (Minicircuits KBL-2FT-LOW+) to reduce loss and parasitic effects. The appropriate DC bias and AC drive voltages were then superimposed using the bias Tee. The chips were biased around an optimum DC voltage of $V_{Bias} = -1$ V which is close to the flat-band condition of the MOS structure ($V_{FB} = -0.8$ V) using a source meter unit (Keithley 2400). The output of a vector network analyzer (VNA HP8510B) was amplified by an RF amplifier (Minicircuits ZVA-02303HP+) to achieve an AC voltage of $V_{pp} \cong 4$ V, driving the MOS structure into deep accumulation in the negative half-cycle, then into depletion during the next half-cycle. This ensures maximum intensity modulation of the beam. The electrical modulation was recovered by detecting the intensity-modulated beam using a wideband photoreceiver, which was then used to drive an oscilloscope or redirected to the receiving port of the VNA for S21 measurements.

B. Optical and Electrical Characterisation

Before carrying out electro-optic measurements, the modulator chips were characterised optically and electrically. The electrical measurements consisted of acquiring capacitance-voltage (CV) characteristics. To do so, the electrical path presented in Fig. 4(a) was modified by removing the RF amplifier and substituting the terminated probe by an open-circuit probe (Picoprobe, model 40A) as sketched in the inset of Fig. 4(b). The VNA was then calibrated to the reference planes set by the tip of the probe by contacting elements on a calibration substrate (GGB industries CS-5). The reflection coefficient (S11) of the chip was then measured at different DC bias points keeping the frequency and the small AC voltage amplitude constant. The device capacitance was then extracted, and a CV characteristic obtained, as plotted in Fig. 4(b) for a 5 μm diameter device.

The optical response of a plasmonic grating patch was then obtained by measuring its reflectance response in a free-space telescope setup [30]. Fig. 4(c) gives an example response for a 28 μm diameter modulator measured under open-circuit conditions, normalized to the response of a mirror of similar diameter (a modulator without a plasmonic grating). Fig. 4(c) also plots the theoretical response (computed following the details given in the theoretical section) for a modulator of the same diameter, excited by a Gaussian beam of 15 μm waist diameter, following the conditions in our free space telescope setup and assuming a 3-degree misalignment with respect to normal incidence. The theoretical and measurement results match very well including the second resonance feature. The secondary resonance is not present if a loosely focused beam is incident on a device at normal incidence (*cf.*, Theoretical section). The resonance is slightly deeper in the calculations. This could be explained by deviations in material and/or structural properties between the theoretical model and the experimental structure. Furthermore, small translational misalignments along the optical beam path in the free-space setup can also affect the response of the device.

The optical insertion loss of the modulators was determined by comparing its output optical power at the third port of the circulator relative to that of a broadband perfect mirror placed at the same location as the modulator in the set-up of Fig. 4(a). The insertion loss of the modulators depends on the device size and varies from IL $\cong 4.2$ dB to IL $\cong 2$ dB for the 5 and 28 μm diameter modulators at their working wavelength ($\lambda_0 = 1550$ nm), respectively. These insertion loss values are relative to the incident free space optical beam and represent those of the modulator alone (without the effect of the ancillary components in the set-up).

The frequency response and experimental equivalent circuit of modulators were determined by measuring the S11 response using open-circuit and 50 Ω terminated probes in the simplified setup presented in inset of Fig. 4(b), then extracting an equivalent

Authorized licensed use limited to: University of Ottawa. Downloaded on March 14,2025 at 19:57:09 UTC from IEEE Xplore. Restrictions apply.

circuit model (Fig. 2(d)) from the measurements. Fig. 5(a) presents the response of a 5 μm diameter device measured using the open circuit probe, at a DC bias point of $V_{Bias} = 2$ V (which produces the lowest capacitance and broadest response), and Fig. 5(b) shows the results obtained using the 50 Ω terminated probe on the same device at the same bias point. For the measurements using the open-circuit probe, the VNA and probe were calibrated as described in the previous section (as for CV measurements), but for the measurements with the terminated probe, the VNA reference plane was set by calibration to the end of the RF cable (before the probe) and an electrical delay was added to account for the electrical length of the probe. The measurement of Fig. 5(b) yields an electrical 3 dB bandwidth of BW ≅ 22 GHz.

Fig. 5(c) presents the S11 responses of a 11 μm diameter modulator obtained using the 50 Ω terminated probe at bias points of $V_{Bias} = -1, 0,$ and 1 V, from which 3 dB electrical bandwidths of BW = 5, 7 and 9 GHz are observed, respectively. It can be concluded that by moving the bias point towards the inversion regime (positive bias voltages), the 3 dB bandwidth of the modulators increases due to a decrease in the device capacitance, as also supported by the CV characteristics of Fig. 4(b). However, to achieve the best modulation depth, the devices must be driven into deep accumulation to benefit from the carrier refraction effect. As a result, a DC bias point of $V_{Bias} = -1$ V was chosen for the forthcoming electro-optic measurements.

Using the equivalent circuit discussed in the Theoretical section (Fig. 2(d)), the calculated S11 frequency response of the 5 μm diameter modulator is plotted in Fig. 5(a) for the case of probing with the open-circuit probe ($R_{Probe} = \infty$) and in Fig. 5(b) for the terminated probe ($R_{Probe} = 50$) - excellent agreement with the measurements is noted in both cases. The electrical bandwidth of the modulators can be calculated as $BW = (2\pi R_T C_T)^{-1}$ where:

$$C_T = \frac{C_m C_{dep}}{C_m + C_{dep}} + \frac{C_{SU8} C_{Hafnia}}{C_{SU8} + C_{Hafnia}} = 0.21 \text{ pF} \qquad (3)$$

and

$$R_T = (R_S + (R_{Probe} \| R_g)) \| R_p = 34\ \Omega \qquad (4)$$

are the total capacitance and resistance of the equivalent circuit. Using these values, the BW works out to 22 GHz when probed with the 50 Ω terminated probe, in agreement with the measurement (Fig. 5(b)). It's worth noting that probing the modulator chips with a terminated 50 Ω probe, which is impedance matched to an RF system of 50 Ω characteristic impedance, broadens the working bandwidth by reducing the total resistance of the circuit.

C. Electro-Optic Measurements

Fig. 6(a) shows the measured electro-optic transmission coefficient (S21, normalized) of two modulator chips of 11 and 5 μm diameter, each at two bias points, at $\lambda_0 = 1550$ nm. These devices are the highest speed devices among all designs. The electro-optic calibration path for S21 measurements is as sketched in Fig. 4(a), and includes the modulator under test, and all RF and optical components in the measurement path except for the microwave GSG probe. To calibrate the set-up, the MZIM

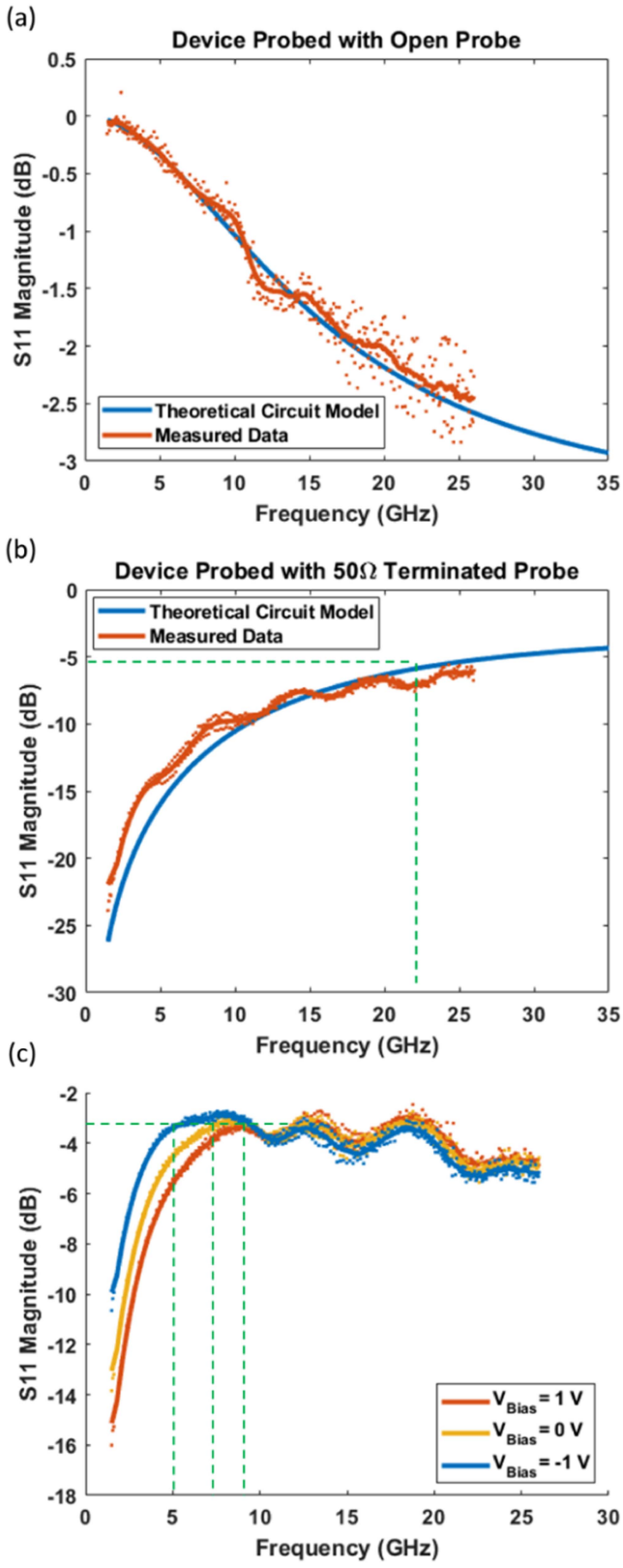

Fig. 5. (a) S11 experimental and theoretical (equivalent circuit) frequency responses of a 5 μm diameter modulator probed with an open circuit probe and biased at $V_{Bias} = 2$ V. (b) Experimental and theoretical S11 frequency responses of the same modulator as in Part (a) ($V_{Bias} = 2$ V) but probed with a 50 Ω terminated probe. (c) S11 frequency responses of a 11 μm diameter modulator measured with a 50 Ω terminated probe, at bias voltages of $V_{Bias} = -1$, 0 and 1 V. A moving average of window length 20 is superimposed on the measured data points in Parts (a) to (c).

Authorized licensed use limited to: University of Ottawa. Downloaded on March 14,2025 at 19:57:09 UTC from IEEE Xplore. Restrictions apply.

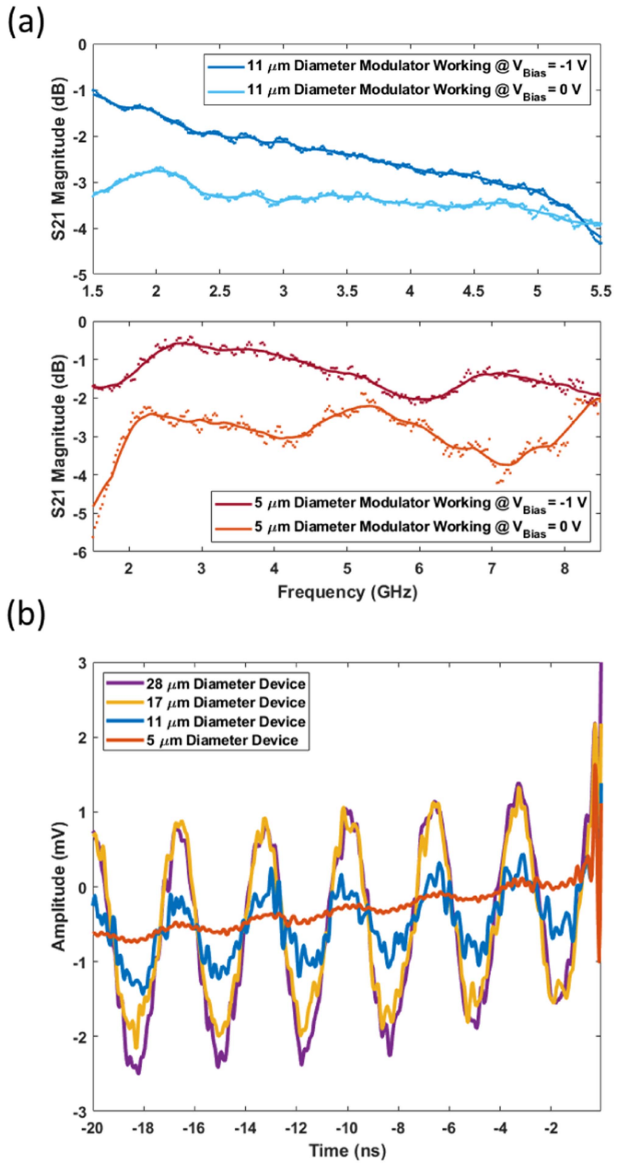

Fig. 6. (a) Measured normalized electro-optic transmission coefficient magnitude (|S21|) for 11 and 5 μm diameter modulators at different bias voltages. A moving average of window length 20 is superposed on the measured data points. (b) Low frequency (300 MHz) modulated signal detected by a photoreceiver and measured on an oscilloscope for modulators of different diameters, (averaged over 50 waveforms).

was excited with similar RF ($V_{pp} = 4$ V) and optical (0.4 mW) signals and the measured S21 response of the chain taken as the calibrated response in the VNA. Thus, all subsequent modulator measurements are relative to the MZIM response.

From Fig. 6(a), a 3 dB electro-optic bandwidth of BW $\cong$ 5 GHz is evident from the S21 frequency response of the 11 μm device at $V_{Bias} = -1$ V, in agreement with the bandwidth obtained from the S11 measurements presented in Fig. 5(c) for the same bias point. For a bias voltage closer to the inversion regime, the 3 dB bandwidth of the same device increases, and the response becomes flatter. This is evident from the S21 curve presented in Fig. 6(a) for $V_{Bias} = 0$ V and agrees with the BW of 7 GHz extracted from Fig. 5(c). However, the modulation depth decreases as the bias point moves towards the inversion regime, which reduces the magnitude of S21. A similar behaviour is observed for the 5 μm diameter device at the same two bias points. The measured electro-optic S21 frequency response of the 5 μm modulator was limited by the bandwidth of our photoreceiver (8.5 GHz), but its 3 dB electrical bandwidth is ~22 GHz as measured previously (Fig. 5(b)). The larger bandwidth of this device results in improved flatness of the S21 frequency response compared to that of the 11 μm diameter device.

Fig. 6(b) shows the low-frequency modulation signal from devices of different diameters, measured on an oscilloscope (Tektronics TDS694C), and averaged over 50 waveforms to reduce noise. For the low frequency measurements, a different RF power amplifier (mini-circuits TVA-11-422) and bias-tee circuit (mini-circuits ZX85-12G-S+) were used. The modulation signal amplitude decreases with the device diameter under similar experimental conditions. This can be explained by the fact that alignment of the beam with a spot diameter of 5 μm at the output of our lensed fiber, is more challenging as the device diameter shrinks. The area of the 5 μm diameter modulator does not overlap with the entire area of the incident beam, so part of the latter is scattered.

The normalized reflectance modulation, also referred to as the modulation depth (MD), is:

$$\mathrm{MD} = \left|\frac{R_1 - R_0}{R_0}\right| = \left|\frac{P_{max} - P_{min}}{P_{min}}\right| = \left|\frac{V_{max} - V_{min}}{V_{min}}\right| \quad (5)$$

where the third equality emerges by recognizing that the voltage measured on the oscilloscope is proportional to the power output from the modulator (P_{max}, P_{min}). Using the measured modulation traces at the working wavelength of devices ($\lambda_0 = 1550$ nm), as shown in Fig. 6(b), we find MD = 0.12%, 1.3%, 1.9% and 2.3% for the 5, 11, 17, and 28 μm diameter modulators, respectively, which are in good agreement with our numerical results plotted on Fig. 3(b). The modulation depth is low but should be adequate for wafer probing purposes assuming high-quality receiver optoelectronics. The modulation depth can be improved by choosing, e.g., epsilon near zero materials (transparent conductive oxides) [21], [24], however, adherence to CMOS material sets represents a tight constraint that should be respected for a wafer testing application.

V. Discussion

Based on testing more than 50 different devices with different diameters and grating pitches, each modulator produced a modulation depth of at least 0.12% at the expected working wavelength. This outcome implies a high tolerance to fabrication deviations, such that the modulator should present a reliable solution for wafer testing applications. This is due to several reasons. The first is that if the device diameter deviates from the target dimensions, a detectable modulation remains achievable if the incident beam has a reasonable overlap (~80% of optical beam power) with the modulator area, such that only the capacitance and bandwidth of the device are affected. Tighter beam diameters can improve the modulation response to depths of up

Authorized licensed use limited to: University of Ottawa. Downloaded on March 14,2025 at 19:57:09 UTC from IEEE Xplore. Restrictions apply.

to 2% as measured for the 17 and 28 μm diameter devices. Also, deviation of fabricated grating dimensions from target values can shift the modulator working wavelength. However, given the broad optical bandwidth of the plasmonic resonance (Fig. 3(b)), deviations of up to 15 nm from the target operating wavelength barely showed a change in modulation performance during experiments. This eases fabrication tolerances to $\pm$10 nm for the grating pitch with respect to the target value. Our simulation results in Fig. 3, also show that the optical bandwidth of the modulation reaches up to 100 nm. The angle of incidence of the Gaussian beam affects the optical spectrum by adding a shoulder resonance and blue-shifting the main resonance as shown in the Theoretical Section. However, due to the broad optical bandwidth of the resonance, and based on our numerical simulations, a deviation of up to 5 degrees would still yield detectable modulation response.

VI. Conclusion

A MOS based plasmonic modulator concept of small footprint (5 μm diameter), wide optical (100 nm) and electrical (22 GHz) working bandwidths, and low insertion loss (4 dB) was proposed and demonstrated. The modulation depth of the modulators is about 2%, which should be adequate for the device to operate as a data output modulator in non-contact wafer-level testing. Wafer testing impacts the Si CMOS wafer manufacturing industry and has significant economic consequences. The electro-optic modulator concept proposed and investigated in this article meets the main requirements for a non-contact solution to this problem. By changing the metal from Au to, e.g., Cu the modulators could be monolithically integrated with Si CMOS electronics, consuming a diameter of about 5 μm on wafer, and they would scale without crosstalk.

Acknowledgment

The authors are grateful to Anthony Olivieri and Saba Siadat Mousavi for device fabrication, and to Jan Hoppe for fruitful discussions.

References

[1] M. Pecht, T. Shibutani, M. Kang, M. Hodkiewicz, and E. Cripps, "A fusion prognostics-based qualification test methodology for microelectronic products," *Microelectronics Rel.*, vol. 63, pp. 320–324, 2016.

[2] S. Bahukudumbi and K. Chakrabarty, *Wafer-level Testing and Test During Burn-In For Integrated Circuits*. Norwood, MA, USA: Artech House, 2010.

[3] S. Bahukudumbi, "Wafer-level testing and test planning for integrated circuits," Ph.D. dissertation, *Dept. Elect. Comput. Eng.*, Duke Univ., Durham, NC, USA, 2008.

[4] D. Appello, P. Bernardi, M. Grosso, and M. S. Reorda, "System-in-package testing: Problems and solutions," *IEEE Des. Test Comput.*, vol. 23, no. 3, pp. 203–211, May–Jun. 2006.

[5] F. Pan and M. Tang, "A vertical probe card design for high-speed wafer test," in *Proc. Int. Conf. Microw. Millimeter Wave Technol.*, IEEE, 2023, pp. 1–3.

[6] H.-Y. Chang, W.-F. Pan, and S.-M. Lin, "Experimental and theoretical investigation of needle contact behavior of wafer level probing," *Precis. Eng.*, vol. 35, no. 2, pp. 294–301, 2011.

[7] Y. Chen, D. Niu, Y. Xie, and K. Chakrabarty, "Cost-effective integration of three-dimensional (3D) ICs emphasizing testing cost analysis," in *Proc. IEEE/ACM Int. Conf. Comput.-Aided Des.*, San Jose, 2010, pp. 471–476.

[8] W. R. Mann, F. L. Taber, P. W. Seitzer, and J. J. Broz, "The leading edge of production wafer probe test technology," in *Proc. Int. Conf. Test*, Charlotte, 2004, pp. 1168–1195.

[9] KLA, "Defect inspection review," 2024. [Online]. Available: https://www.kla.com/products/chip-manufacturing/defect-inspection-review

[10] JEOL, "JFAS-7000BT beam tracer," Product Literature, 2006. [Online]. Available: www.jeol.com

[11] E. J. Marinissen et al., "Contactless testing: Possibility or pipe-dream?," in *Proc. Des. Automat. Test Europe Conf. Exhib.*, Nice, France, 2009, pp. 676–681.

[12] J. Zhu et al., "Optical wafer defect inspection at the 10 nm technology node and beyond," *Int. J. Extreme Manuf.*, vol. 4, no. 3, 2022, Art. no. 032001.

[13] M. Abd Al Rahman and A. Mousavi, "A review and analysis of automatic optical inspection and quality monitoring methods in electronics industry," *IEEE Access*, vol. 8, pp. 183192–183271, 2020.

[14] C. Shin et al., "Fast, exact and non-destructive diagnoses of contact failures in nano-scale semiconductor device using conductive AFM," *Sci. Rep.*, vol. 3, no. 1, 2013, Art. no. 2088.

[15] T.-F. Yao, A. Duenner, and M. Cullinan, "In-line metrology of nanoscale features in semiconductor manufacturing systems," *Precis. Eng.*, vol. 47, pp. 147–157, 2017.

[16] O. Jeandupeux et al., "Use of scanning capacitance microscopy for controlling wafer processing," *Microelectronics Rel.*, vol. 42, no. 2, pp. 225–231, 2002.

[17] C. Yang, C.-Q. Dang, W.-L. Zhu, and B.-F. Ju, "High-speed atomic force microscopy in ultra-precision surface machining and measurement: Challenges, solutions and opportunities," *Surf. Sci. Technol.*, vol. 1, no. 1, 2023, Art. no. 7.

[18] A. Renbi and J. Delsing, "Contactless testing of circuit interconnects," *J. Electron. Testing*, vol. 31, pp. 229–253, 2015.

[19] "International Technology Roadmap for devices and Systems," 2023.

[20] G. T. Reed, G. Mashanovich, F. Y. Gardes, and D. J. Thomson, "Silicon optical modulators," *Nature Photon.*, vol. 4, pp. 518–526, 2010.

[21] W.-C. Hsu, B. Zhou, and A. X. Wang, "MOS capacitor-driven silicon modulators: A mini review and comparative analysis of modulation efficiency and optical loss," *IEEE J. Sel. Topics Quantum Electron.*, vol. 28, no. 3, May–Jun. 2021, Art. no. 3400211.

[22] K. Liu, C. R. Ye, S. Khan, and V. J. Sorger, "Review and perspective on ultrafast wavelength-size electro-optic modulators," *Laser Photon. Rev.*, vol. 9, no. 2, pp. 172–194, 2015.

[23] A. Chen and E. Murphy, *Broadband Optical Modulators: Science, Technology, and Applications*. Boca Raton, FL, USA: CRC Press, 2011.

[24] D. Chauhan, Z. Sbeah, R. P. Dwivedi, J.-M. Nunzi, and M. S. Thakur, "An investigation and analysis of plasmonic modulators: A review," *J. Opt. Commun.*, vol. 45, 2022.

[25] C. Koos et al., "Silicon-organic hybrid (SOH) and plasmonic-organic hybrid (POH) integration," *J. Lightw. Technol.*, vol. 34, no. 2, pp. 256–268, Jan. 2015.

[26] C. Haffner et al., "Plasmonic organic hybrid modulators—Scaling highest speed photonics to the microscale," *Proc. IEEE*, vol. 104, no. 12, pp. 2362–2379, Dec. 2016.

[27] J. A. Dionne, K. Diest, L. A. Sweatlock, and H. A. Atwater, "PlasMOStor: A metal− oxide− Si field effect plasmonic modulator," *Nano Lett.*, vol. 9, no. 2, pp. 897–902, 2009.

[28] M. Ayata et al., "High-speed plasmonic modulator in a single metal layer," *Science*, vol. 358, no. 6363, pp. 630–632, 2017.

[29] M. Burla et al., "500 GHz plasmonic Mach-Zehnder modulator enabling sub-THz microwave photonics," *APL Photon.*, vol. 4, no. 5, 2019, Art. no. 056106.

[30] A. Olivieri et al., "Plasmonic nanostructured metal–oxide–semiconductor reflection modulators," *Nano Lett.*, vol. 15, no. 4, pp. 2304–2311, 2015.

[31] M. S. Amiri Naeini and P. Berini, "Infrared surface plasmons open a hole tunneling channel in metal–Oxide–Semiconductor structures," *ACS Photon.*, vol. 10, no. 9, pp. 3321–3330, 2023.

[32] M. Alavirad, A. Olivieri, L. Roy, and P. Berini, "High-responsivity subbandgap hot-hole plasmonic Schottky detectors," *Opt. Exp.*, vol. 24, no. 20, pp. 22544–22554, 2016.

[33] S. Siadat Mousavi, A. Olivieri, and P. Berini, "Fabrication of a high-speed plasmonic reflection/transmission modulator," *AIP Adv.*, vol. 11, no. 2, 2021, Art. no. 025023.

[34] E. D. Palik, *Handbook of Optical Constants of Solids*, vol. 3. San Diego, CA: Academic, 1998.

[35] J. M. Khoshman and M. E. Kordesch, "Optical properties of a-HfO2 thin films," *Surf. Coatings Technol.*, vol. 201, no. 6, pp. 3530–3535, 2006.

[36] "photoresist, SU-82000 permanent epoxy negative," Micro-chem, 2019.

Authorized licensed use limited to: University of Ottawa. Downloaded on March 14,2025 at 19:57:09 UTC from IEEE Xplore. Restrictions apply.

[37] Y. Kurokawa and H. T. Miyazaki, "Metal-insulator-metal plasmon nanocavities: Analysis of optical properties," *Phys. Rev. B*, vol. 75, no. 3, 2007, Art. no. 035411.
[38] K. Edee, "Understanding the plane wave excitation of the metal-insulator-metal gap plasmon mode of a nanoribbons periodic array: Role of insulator-metal-insulator lattice mode," *OSA Continuum*, vol. 2, no. 2, pp. 389–399, 2019.
[39] S. M. Sze, Y. Li, and K. K. Ng, *Physics of Semiconductor Devices*. Hoboken, NJ, USA: John Wiley & Sons, 2021.
[40] G. M. Sardi et al., "Analysis of dielectric constant behavior of thermally treated SU-8 polymer up to 18 GHz," *Mater. Res. Bull.*, vol. 150, 2022, Art. no. 111775.
[41] A. Ghannam, C. Viallon, D. Bourrier, and T. Parra, "Dielectric microwave characterization of the SU-8 thick resin used in an above-IC process," in *Proc. Eur. Microw. Conf.*, Rome, Italy, 2009, pp. 1041–1044.

Maryam Sadat Amiri Naeini received the B.Sc. degree in electrical engineering focusing on telecommunications and the M.Sc. degree in electrical engineering focusing on microwave and photonics from the Isfahan University of Technology, Isfahan, Iran, in 2014 and 2017, respectively. She is currently working toward the Ph.D. degree in physics focusing on plasmonic electro-optic devices with the University of Ottawa, Ottawa, ON, Canada. Her main research interest is electro-optic semiconductor devices for communication applications.

Pierre Berini (Fellow, IEEE) received the B.Sc. and B.E.Sc. degrees in electrical engineering and computer science from the University of Western Ontario, London, ON, Canada, and the M.Sc. A. and Ph.D. and degrees in electrical Engineering from the École Polytechnique de Montréal, Montréal, QC, Canada.He is currently a Distinguished University Professor of electrical engineering and of physics with the University of Ottawa, Ottawa, ON, Canada. He is also the University Research Chair of surface plasmon photonics, former Director with the Centre for Research of photonics with the University of Ottawa, and the Founding Director of the uOttawa NanoFab which is a core facility housing cleanroom tools. He was the Founder and Chief Technology Officer of a venture capital financed company and he collaborates on an ongoing basis with industry. His research interests include nanophotonics, with surface plasmons, metasurfaces and their applications being of present interest. Dr. Berini was the recipient of the NSERC Steacie Fellowship, NSERC Discovery Accelerator, Premier of Ontario Research Excellence Award, University of Ottawa Young Researcher of the Year Award, URSI Young Scientist Award, George S. Glinski Award for Excellence in Research, and is a Canada Foundation for Innovation researcher. He was an Associate Editor for *Optics Express* and the Managing Editor of *Nanophotonics*, and is also an Associate Editor for *Optica*. He contributes on an ongoing basis to the organization of several international conferences in photonics. He is a Fellow of the OSA, APS, Canadian Academy of Engineering, and Royal Society of Canada.

Authorized licensed use limited to: University of Ottawa. Downloaded on March 14,2025 at 19:57:09 UTC from IEEE Xplore. Restrictions apply.

4 Infrared Surface Plasmons Open a Hole Tunneling Channel in Metal–Oxide–Semiconductor Structures

4.1 Summary

A similar plasmonic MOS structure as introduced in Chapter 3 has been studied as a tunneling device. New device physics and a new plasmon-initiated tunneling channel for plasmonic hot holes through hafnium dioxide (oxide barrier of the device) is revealed. The tunneling current of the device under dark conditions (no illumination) was measured and characterized theoretically, and it was shown that it follows the modified Fowler-Nordheim tunneling law. This current is due to the tunneling of inversion electrons in the semiconductor (silicon) layer of the MOS device through the oxide and into the metal layer. Photo response of the device was recorded and modeled theoretically under different polarization conditions and optical powers. The measured photocurrent follows the modified Fowler-Nordheim tunneling theory but originates from tunneling of plasmonic-excited energetic holes travelling from the metal to the semiconductor. Studying the band diagram of the structure under inversion shows that this hole tunneling channel does not exist under dark conditions, when SPPs were not present on the structure. Tunneling theories fit to the measured results allowed extraction of the tunneling effective masses of both carrier types passing through oxide layer and extraction of the number of available carriers to initiate each tunneling process. The number of available holes contributing to the photocurrent was shown to increase linearly with optical power. It was also shown that the barrier height for tunneling holes is lowered at the same rate as increasing incident photon energy, confirming the creation of energetic tunneling holes by excitation of SPPs on the metal layer.

4.2 Contribution

The material provided in this chapter was published in and is reproduced with permission from the ACS Photonics journal [123]. I performed the numerical simulations for modeling the optical performance of the devices. I designed and implemented the electro-optic test setup required for measurements. I performed all of the optical, electrical, and electro-optic measurements required for MOS device characterization and recording the tunneling current under different conditions. I performed the theoretical study of the device band diagram under different bias conditions in accumulation and inversion and suggested the modified Fowler-Nordheim tunneling theory as best law explaining the physics of the devices. I analysed the experimental data and theoretical fit results and extracted different parameters from the theoretical fits under various conditions. I interpreted the results and wrote the manuscript. Professor Berini contributed to the device and measurement setup proposal, interpretation of results, and revision of the manuscript.

ACS Photonics

pubs.acs.org/journal/apchd5

Article

Infrared Surface Plasmons Open a Hole Tunneling Channel in Metal−Oxide−Semiconductor Structures

Published as part of the ACS Photonics virtual special issue " Frontiers and Applications of Plasmonics and Nanophotonics ".

Maryam Sadat Amiri Naeini and Pierre Berini*

Cite This: *ACS Photonics* 2023, 10, 3321−3330

Read Online

ACCESS | Metrics & More | Article Recommendations | Supporting Information

ABSTRACT: Plasmonic hot carriers on metal−oxide−semiconductor (MOS) diodes hold the promise of innovative optoelectronics on structures of fundamental technological importance. We report the photoresponse of MOS diodes due to the tunneling of hot holes created in the metal contact via the absorption of infrared ($\lambda_0 \approx 1550$ nm, $\hbar\omega \approx 0.8$ eV) surface plasmons therein. In the absence of illumination, only one tunneling channel exists under inversion, that of inversion electrons tunneling from the semiconductor conduction band through the oxide barrier into the metal, leading to the dark current. Under illumination, the excitation and decay of surface plasmons in the metal opens a second channel, that of hot holes created in the metal, tunneling through the oxide into the semiconductor valence band, leading to the photocurrent—this channel does not exist otherwise due to the absence of holes in a metal. Theoretical modeling of all tunneling current components (dark and photo) using the Fowler−Nordheim and Modified Fowler−Nordheim models are in excellent agreement with the measurements, and their fit allows extraction of the tunneling effective masses of both carrier types in the oxide of our MOS structures (hafnia). This new plasmon-induced tunneling channel on MOS structures opens the possibility of novel infrared optoelectronic devices on this technologically important structure..

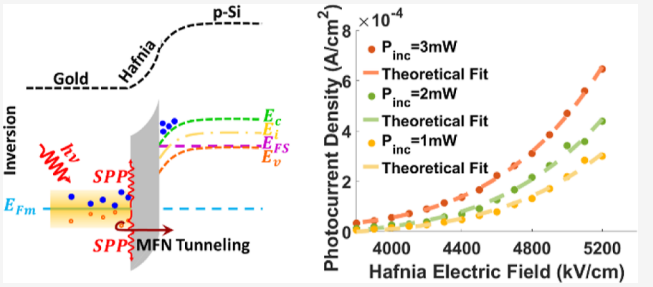

KEYWORDS: *metal−oxide−semiconductor, CMOS compatible, plasmonics, hot carriers, Fowler−Nordheim, tunneling*

Downloaded via UNIV OF OTTAWA on February 13, 2025 at 23:14:20 (UTC).
See https://pubs.acs.org/sharingguidelines for options on how to legitimately share published articles.

INTRODUCTION

Surface plasmon polaritons (SPPs) are optical surface waves on a metal, comprising a free electron charge density wave coupled to electromagnetic fields. SPPs have interesting attributes, such as enhanced electromagnetic fields (relative to the source) and fields localized to subwavelength scales—attributes that lead to new phenomena and inspire novel applications. SPPs exhibit both wave- and (bosonic) particle-like behavior. They are damped by the metal surface, into which they decay by creating energetic (nonequilibrium) carriers in the metal, also known as hot electrons and/or hot holes.[1−4]

The creation of hot carriers and their manipulation are topics of considerable current interest in plasmonics because they hold the potential of new device physics or opening new chemical reaction pathways, leading to novel applications in photochemistry,[2,5,6] photocatalysis,[7,8] photovoltaic devices,[9] biosensors,[10] and photodetectors on Schottky contacts,[11−14] metal−semiconductor−metal (MSM) structures,[15] and metal−insulator−metal (MIM) structures.[16,17]

MIM structures have also been used as optical rectifying tunneling-gap nanoantennas,[18,19] and as electrically driven optical nanoantennas for surface plasmon generation and light emission via inelastic tunneling.[20−26] The ability of MIM tunnelling junctions to create and detect surface plasmons can be combined to introduce high-speed compact electronic-plasmonic transceivers.[27]

Metal−oxide−semiconductor (MOS) structures are of high technological importance, given their prevalence (dominance) in integrated electronics. Optical effects in such structures have also been investigated. For example, MOS tunneling diodes have been combined with optically resonant structures for electromagnetic rectification.[28] Hot electrons created by UV absorption in the metal layer of such structures enable UV detection with low background noise.[29] It has also been shown that an oxide interlayer in Schottky contacts can increase photodetection efficiency by interfacial passivation[30] or by

Received: June 6, 2023
Published: August 8, 2023

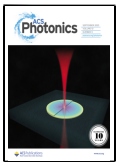

ACS Publications

© 2023 American Chemical Society

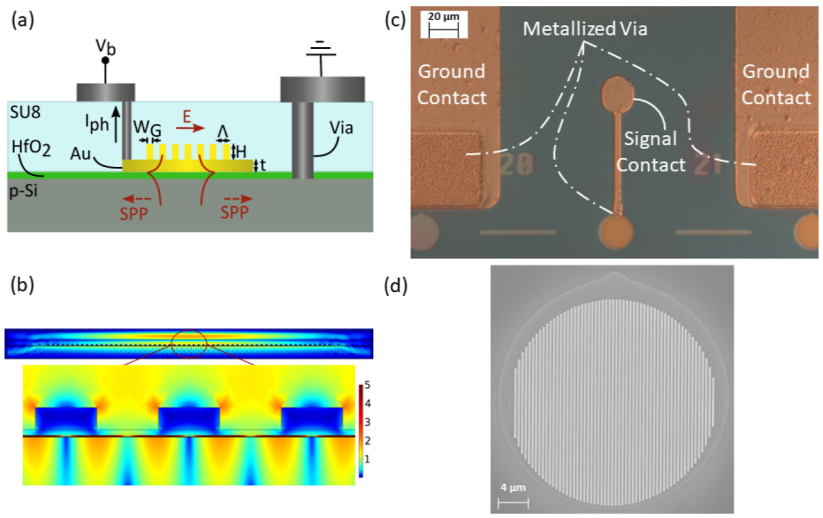

Figure 1. (a) Cross-section of the plasmonic MOS device of interest. (b) Calculated total electric field magnitude normalized to the incident electric field at the resonance (maximum coupling) wavelength. The bottom panel shows SPP fields localized along the bottom surface of the gold patch. The color bar represents field enhancement. (c) Optical microscopy image of a 22 μm diameter device with ground−signal−ground contact pads. (d) SEM image of a 28 μm diameter gold patch (I3−B15) bearing a plasmonic grating of pitch 450 nm obtained during fabrication.

introducing trap-assisted and oxygen vacancies-assisted charge transfer.[31] MOS structures driven under accumulation have also been used with SPPs for electro-optic reflectance modulation.[32] However, the investigation of plasmonic hot carrier generation, tunneling, and harvesting in MOS structures has not been widely investigated. Yet this topic is well-motivated given the widespread use of such junctions, and the potential opportunities for new device designs and applications.

In this paper, we report the observation of plasmon-induced tunneling current in MOS structures on p-Si. The metal electrode of our MOS devices was structured as a grating that couples normally incident infrared light to SPPs propagating along the metal−oxide interface. SPP absorption in the metal generates energetic carriers−hot electrons and holes−near the interface, such that under an inversion bias hot holes can tunnel from the metal to the semiconductor, leading to a photocurrent. We first describe the device structure and the experimental methods. We then summarize and discuss the results and give concluding remarks.

DEVICE STRUCTURE AND DESIGN

The structure of interest, shown schematically in Figure 1a, is a metal−oxide−semiconductor (MOS) device, designed and constructed such that surface plasmons can be excited on the metal contact, along the metal−oxide interface. The device is driven in the inversion regime by applying a positive bias to the gold layer relative to the silicon substrate, V_b, or in the accumulation regime by applying a negative bias.

Devices comprise a thin (t = 20 nm) circular gold patch of different diameters (5, 11, 17, 22, and 28 μm), deposited on a thin (5 nm) hafnium dioxide (hafnia) layer, on a highly boron-doped silicon substrate (ρ = 0.001−0.005 Ω cm; acceptor density taken as $N_a = 2.13 \times 10^{19}$ cm^{-3} for ρ = 0.005 Ω cm). Periodic gold ridges were deposited on the gold patch forming a plasmonic grating. The structure was covered by a 554 nm thick polymer (SU-8) layer. Electrical connections to the gold patch (signal) and the semiconductor substrate (ground) of the MOS structure were extended to the top of the SU-8 cover layer through metalized vias to ground-signal-ground contact pads formed on the SU-8 cover layer. Details of the fabrication processes applied are reported elsewhere.[33] Figure 1c gives an optical microscope image of a fabricated structure, showing the ground−signal−ground contact pads, and Figure 1d gives a scanning electron microscopy (SEM) image of the gold patch bearing a grating, as imaged during fabrication.

The grating pitch was designed following the grating equation, ensuring conservation of momentum for normally incident light ($\Lambda = \lambda_0/n_{eff}$), where n_{eff} is the effective refractive index of the SPP localized and propagating along the gold/oxide interface and λ_0 is the free-space wavelength. The pitch varies between Λ = 420 and 480 nm for operation at free-space wavelengths in the range of λ_0 = 1470 to 1680 nm. The ridge thickness was set to H = 80 nm and the width of the ridges to W_G = 220 to 250 nm such that the gratings have a duty cycle of ∼50%.

Figure 1b shows the calculated normalized magnitude of the total electric field distribution on a 28 μm diameter device bearing a grating of pitch Λ 453 nm, ridge width W_G = 230 nm and ridge thickness H = 79 nm. The dimensions used in the numerical analysis are the actual dimensions of the fabricated device measured using atomic force microscopy (AFM) and SEM.[33] The thickness of the gold film supporting the grating is t = 20 nm. The permittivity data for the gold and doped silicon substrate were taken from the literature.[34] The hafnia thickness and refractive index were taken as H_{HfO_2} = 5 nm and H_{HfO_2} = 1.68, the latter ∼10% lower than the reported value of bulk hafnia,[35] following our extracted DC ϵ_{HfO_2} (which is also lower than the bulk value, *cf.* Results and Discussion section). A native silicon dioxide layer of 1 nm was inserted between the hafnia layer and silicon substrate. A cover layer of SU8, of thickness and refractive index H_{SU8} = 554 nm and n_{SU8} = 1.57,[36] was placed on top of the plasmonic grating. The field distribution is plotted at the resonance wavelength of λ_0 = 1570 nm where maximum coupling occurs. The structure is assumed illuminated by a normally incident 2D Gaussian beam of focused waist width 20 μm and electric field polarized perpendicular to the grating ridges. As shown in the plot, the plasmonic grating couples the incident p-polarized beam to

https://doi.org/10.1021/acsphotonics.3c00766
ACS Photonics 2023, 10, 3321−3330

SPPs localized and propagating along the gold/oxide interface (bottom surface of the gold patch).

The oxide is essentially lossless. The silicon substrate is transparent at the wavelengths of interest but exhibits free-carrier absorption due to doping that is nonetheless negligible compared to absorption in gold. Thus, SPPs decay primarily into the gold layer, where their absorption creates hot electrons and hot holes. The structure is therefore well-suited to the investigation of tunneling processes involving hot carriers created in the metal.

EXPERIMENTAL SETUP AND METHODS

Figure 2 shows a three-dimensional schematic of the experimental setup used to characterize the structure. An

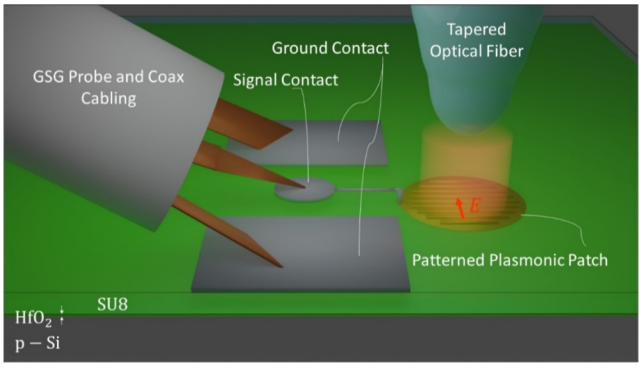

Figure 2. 3D schematic of a device under test in the measurement setup. The device is electrically contacted using a GSG (ground−signal−ground) probe and illuminated by a continuous-wave p-polarized optical beam emerging from a polarization-maintaining tapered optical fiber producing a focal spot diameter of 5 μm.

open-circuit ground-signal-ground (GSG) microwave probe (Picoprobe, model 40A) was used to contact the device electrically.

The electronic performance of a MOS device was characterized by obtaining current−voltage (*IV*) and capacitance−voltage (*CV*) measurements. For the *IV* characteristics, the probe was connected to a Keithley 2400 source-meter via a shielded coaxial cable (to reduce noise), DC bias voltages were applied, and the corresponding current was measured. Around 15 back and forth voltage sweeps were performed on each new device to stabilize its *IV* characteristics (burn-in) before collecting any data.

To obtain *CV* characteristics, the probe was connected through a bias tee to an HP8510B vector network analyzer (VNA), and S_{11} was measured at a frequency of f = 200 MHz for an applied peak-to-peak AC voltage of 350 mV and various DC bias voltages. The VNA was calibrated to the reference plane set by the probe by probing a calibration substrate (GGB industries calibration substrate CS-5). The capacitance was then deduced from the (calibrated) measured S_{11} parameter.

To perform optoelectronic measurements, a polarization-maintaining tapered cone lensed optical fiber (WT&T, model CL5) producing a focal diameter of 5 μm at a working distance of ∼40 to 50 μm was used to illuminate the device with a continuous-wave optical beam polarized perpendicularly to the grating ridges, generated by a laser (Photonetics Tunics Plus) tuned to the desired wavelength.

RESULTS AND DISCUSSION

***CV* Characteristic.** Figure 3a shows the high-frequency *CV* characteristic measured for a 22 μm diameter MOS device, typical of characteristics measured on several devices. The *CV* characteristic reveals the bias voltages required to reach the accumulation or inversion regimes. Strong accumulation occurs at bias voltages near −3.5 V and strong inversion occurs near 2.5 V.

The capacitance in accumulation is that of the oxide layer, whereas in inversion, the capacitance of the oxide layer combines in series with the capacitance of the depletion layer (for high frequency measurements). Under strong accumulation, the relative permittivity of the oxide can be determined using the parallel-plate capacitor formula

$$\in_{HfO_2} = \frac{C_{HfO_2} d}{\in_0 A_c} \quad (1)$$

where d and A_c are the oxide thickness and the device area, respectively. Using the measured capacitance under accumulation of C_{HfO_2} = 6.7 pF (Figure 3a), we extract the relative permittivity of hafnia as ϵ_{HfO_2} = 10.45. Our extracted value, for a 5 nm thick hafnia film, agrees with literature reports on thin films,[32,37,38] but is near the low end of the range for crystalline and mixed phase material (ϵ_{HfO_2} = 12−25)[39] (see Supporting Information, Section 1 for additional details extracted from the *CV* measurements).

Dark *IV* Characteristic. Figure 3a also plots the *IV* characteristic measured for the same 22 μm diameter device. For a current to flow through the MOS structure, carriers must tunnel through the oxide layer to be collected at the opposite terminal. It can be seen from the *IV* curve of Figure 3a that the tunneling current in the inversion regime is higher than in the accumulation regime, and that tunneling occurs at a smaller bias voltage in inversion. This asymmetry can be explained by constructing and inspecting the energy band diagram of the MOS structure under accumulation and inversion.

Figure 4 depicts the energy band diagrams to scale of a Au-HfO_2−Si MOS device under bias voltages for accumulation (V_b = −1.75 V in Figure 4a) and for inversion (V_b = 2.6 V in Figure 4b). These bias voltages were selected such that the electric field magnitude inside the oxide layer is the same in both cases, $E_{HfO_2} \cong$ 3170 kV/cm ($\ll E_{bd}$), with the inversion bias also satisfying the condition for strong inversion[40] (see Supporting Information, Section 2 for more details about the construction of the energy band diagram).

The holes (majority carriers) in silicon that accumulate along the oxide under a strong negative bias (V_b = −1.75 V in Figure 4a) must surmount the oxide barrier of height 2.6 eV to tunnel to the gold contact. Alternatively, electrons (minority carriers) in silicon that accumulate in the inversion layer along the oxide under a strong positive bias (V_b = 2.6 V in Figure 4b) must surmount a smaller oxide barrier of height 2.05 eV to tunnel to the gold contact. This explains the asymmetry in the dark *IV* characteristic observed in Figure 3a.

Theoretical Dark Current under Inversion. Under inversion (Figure 4b), electrons must tunnel through only a portion of the oxide barrier thickness due to band bending in the oxide. This charge transfer process is known as Fowler−Nordheim tunneling,[40] in which the relationship between the tunneling current density and the electric field amplitude inside the oxide layer, E_{HfO_2}, is given by eq S7 (see Supporting

https://doi.org/10.1021/acsphotonics.3c00766
ACS Photonics 2023, 10, 3321−3330

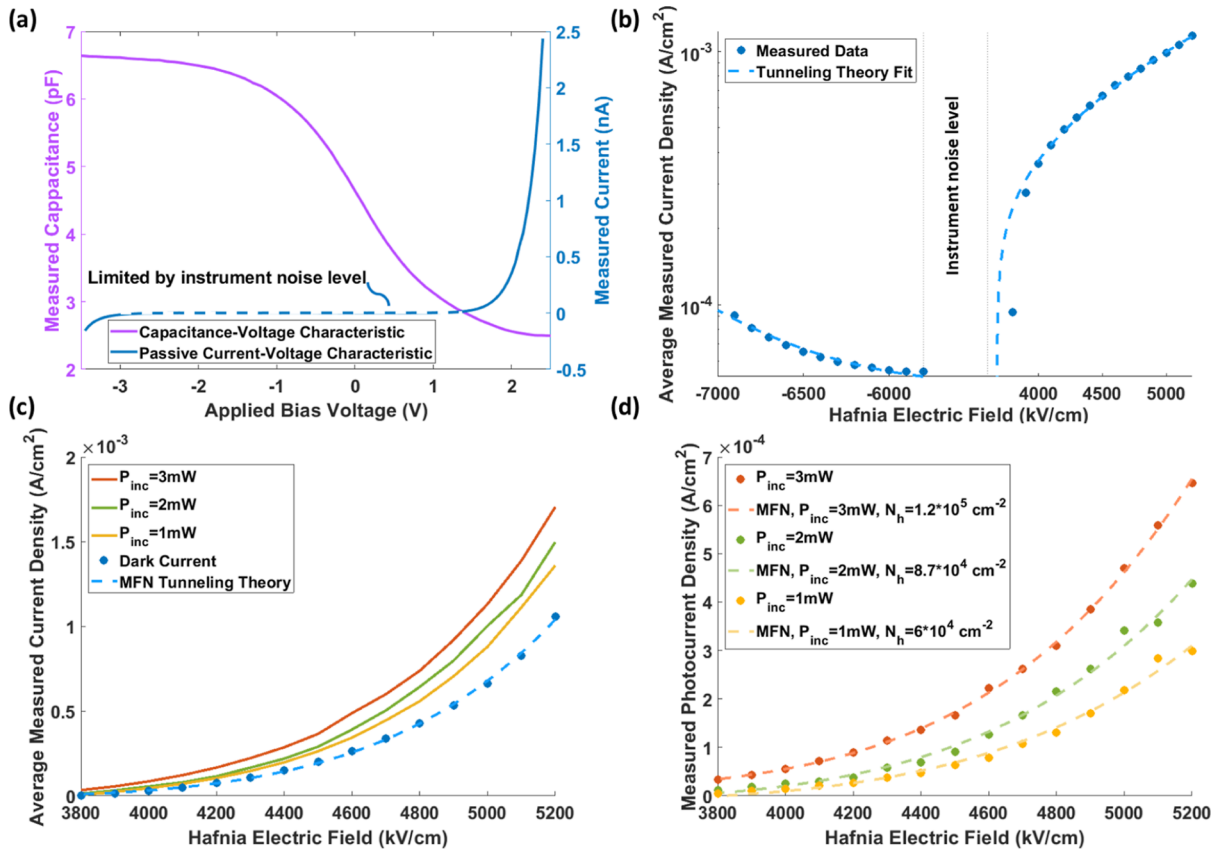

Figure 3. (a) Measured high-frequency *CV* and DC *IV* characteristics of a 22 μm diameter device (H3-D11) under dark conditions. The diode is driven into inversion by applying a positive bias or into accumulation by applying a negative bias. (b) Fowler–Nordheim and modified Fowler–Nordheim (MFN) fits on a semilogarithmic scale to the absolute value of measured dark current in the accumulation and inversion regimes for tunneling of holes and electrons, respectively. (c) Measured (total) current density vs applied electric field for the 22 μm diameter device (H3-D11) under different optical illumination powers at λ_0 = 1540 nm, and MFN tunneling model fit to the dark current data on a linear scale. (d) MFN tunneling model fits to the measured photocurrents of part (c).

Information, Section 3 for a summary of the Fowler–Nordheim and Modified Fowler–Nordheim tunneling theories).[40,41]

Equation S7 assumes that the surface potential in the semiconductor is negligible compared to the voltage drop inside the oxide layer ($|\phi_s| < |V_{HfO_2}|$) and the tunneling field has access to enough charge carriers for transfer to the other side of the potential barrier.[42]

However, for a tunneling process that originates from an inverted highly doped semiconductor, the tunneling equation (eq S7) must be modified due to three reasons. First, an inversion layer has a limited number of charge carriers available for tunneling and this shortage gets more severe as the doping level of the semiconductor increases.[42] Second, band bending at the semiconductor–oxide interface creates a potential well such that inversion carriers occupy discrete (quantized) energy bands therein, with a finite probability and number density at each energy level.[43,44] Third, for a MOS structure with a thin oxide layer under strong inversion, the condition $|\phi_s| < |V_{HfO_2}|$ is not respected—the voltage drop through the oxide is comparable to the surface potential in the semiconductor.[42]

To account for all of these effects, a modified Fowler–Nordheim (MFN) tunneling theory was applied to fit our measured data.[42] The MFN tunneling theory assumes that the number of inversion layer electrons involved in the tunneling process does not increase proportionally with the surface (oxide) electric field at high bias voltages, and the tunneling current becomes limited by carrier generation in the space-charge region of the semiconductor (not by the surface electric field amplitude as in conventional Fowler–Nordheim tunneling theory). As a result, the tunneling current density grows with the oxide electric field at a lower rate (factor of E_{HfO_2}) compared to the Fowler–Nordheim theory (factor of $E_{HfO_2}^2$). This behavior is represented in Figure 3b where saturation of the inversion tunneling electron current and deviation from linear growth on the semilogarithmic scale can be observed in the measured data, and in the fitted MFN theory. The MFN tunneling theory yields a relationship between tunneling current density and the electric field inside the oxide layer given by eq S10.[42]

Equation S10 was fit to the measured dark current of Figure 3a, over applied bias voltages ≥ 1.9 V, where the current measurements are above the noise level of the instrument, using $a_{D'}$ N_{inv} and b_D as fitting parameters. Figure 3b,c shows the measured dark current density, and the MFN tunneling equation fit to these data, on semilog (Figure 3b) and linear (Figure 3c) scales, revealing a high-quality fit.

Over the fitted voltage range, strong inversion exists because the bias voltage is above the threshold inversion voltage of V_T = 1.85 V given by eq S12.[40] Since there is a strongly inverted layer at the silicon and hafnia interface, the electrons are trapped in a potential well constrained by the silicon

https://doi.org/10.1021/acsphotonics.3c00766
ACS Photonics 2023, 10, 3321–3330

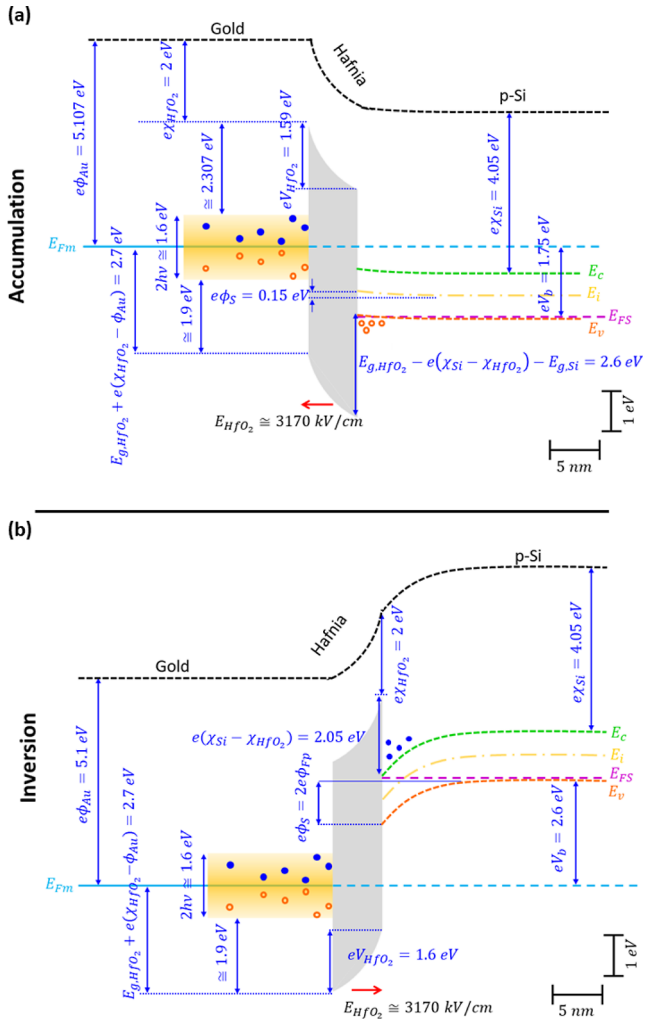

Figure 4. Energy band diagrams of the MOS tunneling diode biased under (a) accumulation ($V_b = -1.75$ V) and (b) inversion ($V_b = 2.6$ V), ensuring that the electric field magnitude inside the oxide layer is the same in both cases, $E_{HfO_2} \cong$ **3170** kV/cm. The diagrams are to scale (scale bars provided). The dashed black curves correspond to the reference vacuum level. Energetic electrons (solid blue circles) and energetic holes (hollow red circles) are sketched in the gold contact.

conduction band edge and hafnia conduction band edge.[44] As a result, electrons occupy discrete energy bands, and the lowest energy level or sub-band can be calculated as $E_0 \simeq 0.34$ eV with respect to the silicon conduction band edge via[43]

$$E_0 = 1.61\left(\frac{e\hbar}{\sqrt{m_{si}^*}}E_{si}\right)^{2/3} \quad (2)$$

where $m_{si}^* = 0.916m_0$ is the effective mass of electrons in ⟨100⟩ silicon and E_{si} is the electric field in silicon at the interface causing electron motion perpendicular to the interface. This electric field is calculated from the electric field in the oxide using the boundary condition for normal electric fields at the hafnia and silicon interface. We assume that almost all inversion electrons reside in the lowest energy sub-band, such that the barrier height for tunneling drops from 2.05 eV (Figure 4b) to $e\phi_B \simeq 1.66$ eV.

The fitting parameter b_D (eq S9) depends on the effective mass of the electrons as they tunnel through the hafnia layer. Assuming the barrier height calculated above ($e\phi_B \simeq 1.66$ eV), yields $m_{HfO_2,e}^* = 0.15m_0$ which is close to previously reported values for ALD hafnia.[45] Using these data, the fitting coefficient $a_D N_{inv}$ can then be used to extract the surface number density of inversion electrons, yielding $N_{inv} \simeq 1.85 \times 10^7$ cm^{-2}.

Theoretical Dark Current under Accumulation. Figure 3b also gives a Fowler–Nordheim fit (eqs S7 to S9) to the measured dark current data in the accumulation regime, where accumulated holes in the semiconductor tunnel through the oxide barrier. A tunneling effective mass of $m_{HfO_2,h}^* = 0.0421m_0$ was extracted from the tunneling parameter b_D.

Tunneling Photocurrent under Inversion. By illuminating the MOS tunneling device with a continuous wave optical beam at the resonant wavelength of the plasmonic grating, the incident beam is coupled to SPPs propagating along the bottom surface of the gold film (*cf.* Figure 1). The SPPs penetrate several nm's into the gold film where they are absorbed. The absorption of SPP energy quanta ($\hbar\omega \sim 0.8$ eV for $\lambda_0 = 1540$ nm) creates energetic (hot) electron–hole pairs localized to a very thin layer near the surface of the gold film ($\Delta L = \nu_F\, \omega \sim 7$ nm).[3] Since the distance of these hot carriers from the surface is lower than the mean free path length of electrons and holes in Au,[46,47] about half of the hot carriers excited by this process succeed in reaching the bottom gold surface. This absorption process of SPPs (Landau damping) yields newly generated hot carriers with an average excess energy of $\hbar\omega/2$.[3] The k-vector angular distribution of these energetic carriers is such that their probably of impinging normally on the bottom gold surface is 4× higher than an isotropic k-vector distribution.[3] Figure 4 sketches the hot carriers created via SPP absorption in the gold contact with their density proportioned to their distribution along the energy and position axes.

Figure 3c shows the measured total current under inversion passing through a 22 μm diameter MOS tunneling device with a grating coupler designed for $\lambda_0 = 1540$ nm, for different optical illumination powers. The departure of the illuminated IV characteristic from the dark characteristic is due to an increase in tunneling current under illumination. In the inversion regime, hot holes in the metal of energy up to $\hbar\omega \sim 0.8$ eV, see (effectively) a reduced barrier height of ~1.9 eV, thereby increasing their probability to tunnel through the 5 nm hafnia layer and be collected in the semiconductor. This tunneling current component is additive to the dark current causing the total current to increase in the device under illumination. By increasing the optical power, the number of photons incident on the device and coupling to SPPs increases, which in turn increases the number of hot holes in the gold that may tunnel through the hafnia. As a control experiment, the tunneling current from a similar MOS device without a plasmonic grating was measured under dark and illumination conditions and no difference was observed between tunneling currents.

The Simmons model[48] has been used to model the photocurrent (and dark current) in MIM structures. Here, we apply MFN tunneling theory because the structure is a MOS device. Figure 3d shows the measured photocurrent, obtained from the total current in Figure 3c by subtracting the dark current, for the three optical powers, fitted to the MFN eq (eq S10) rewritten as

https://doi.org/10.1021/acsphotonics.3c00766
ACS Photonics 2023, 10, 3321−3330

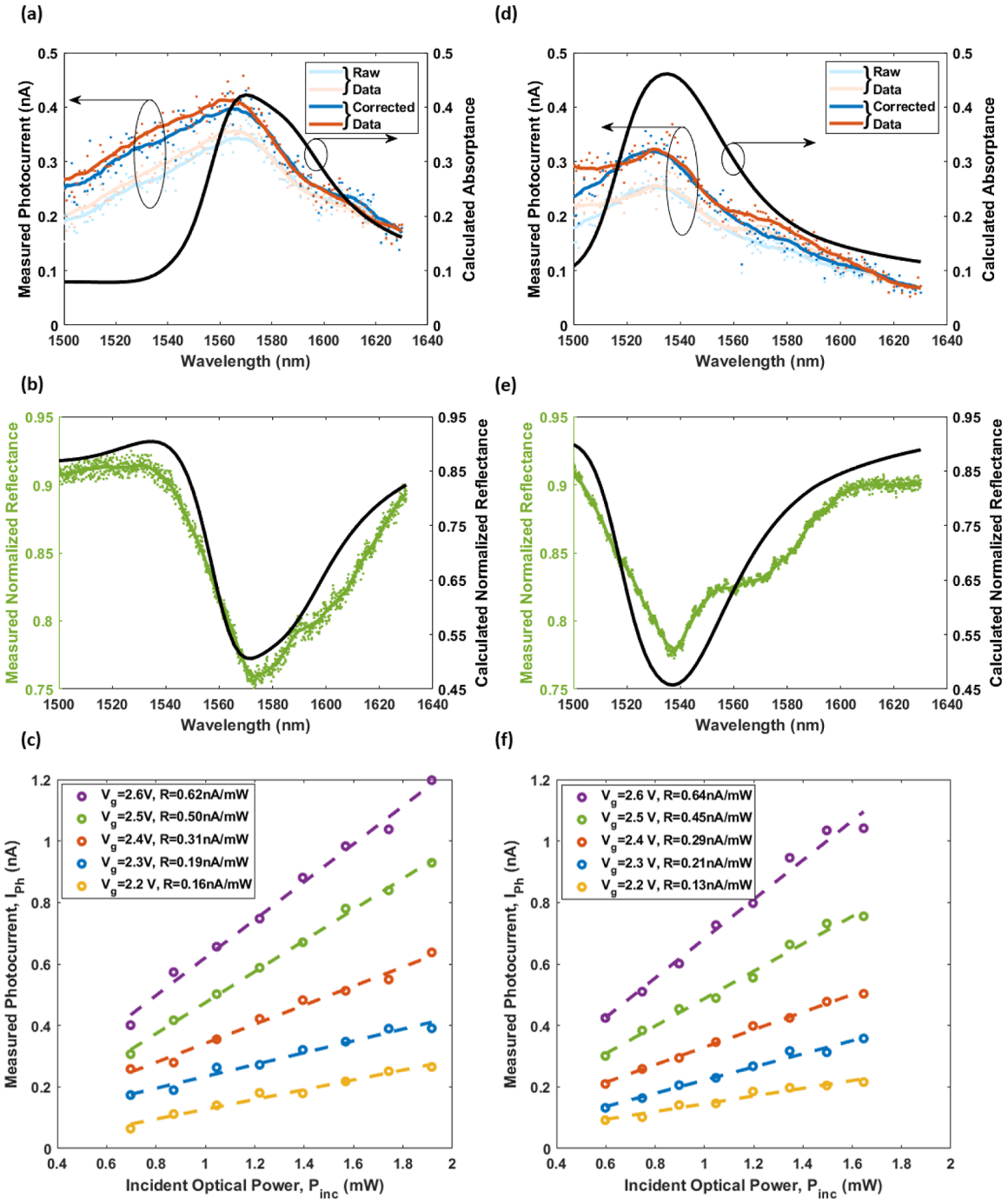

Figure 5. (a) Measured photocurrent response and calculated absorptance response of a 28 μm diameter device of pitch 450 nm designed for λ_0 = 1570 nm (R9-B15). The blue trend line shows a forward wavelength sweep and the red trend line shows a backward sweep. (b) Experimental and theoretical normalized reflectance of the same device, plotted on different scales. (c) Optoelectronic responsivity of the same device at different bias voltages. (d–f) Similar set of results on a similar device but of pitch 440 nm designed for λ_0 = 1540 nm (R9-E9).

$$J_{\mathrm{Ph}} = a'_{\mathrm{Ph}} N_{\mathrm{h}} E_{\mathrm{HfO_2}} e^{-b_{\mathrm{Ph}}/E_{\mathrm{HfO_2}}} \quad (3)$$

In this equation, N_{h} represents the surface number density of hot holes available for tunneling, and the parameters $a_{\mathrm{Ph}'}$ and b_{Ph} are as defined by eqs S11 and S9, respectively, wherein the barrier height and oxide effective mass take on values appropriate for hot holes.

Using the hot hole barrier height of $e\phi_{\mathrm{B}} \simeq 1.9$ eV for operation at the optical wavelength of λ_0 = 1540 nm, and the three b_{Ph} parameters obtained by fitting each curve in Figure 3d, a tunneling effective mass of $m_{\mathrm{HfO_2,h}}{}^* = 0.052m_0$ for holes in hafnia was extracted using eq S9, which is similar to the hole tunneling effective mass extracted from the dark current under accumulation ($m_{\mathrm{HfO_2,h}}{}^* = 0.0421m_0$, Figure 3b). N_{h} was also extracted from the fitted curves, as given in the legend of Figure 3d, and is observed to increase linearly with incident optical power, supporting our explanation for the optical creation of hot holes in the metal and their tunneling to produce the photocurrent.

https://doi.org/10.1021/acsphotonics.3c00766
ACS Photonics 2023, 10, 3321−3330

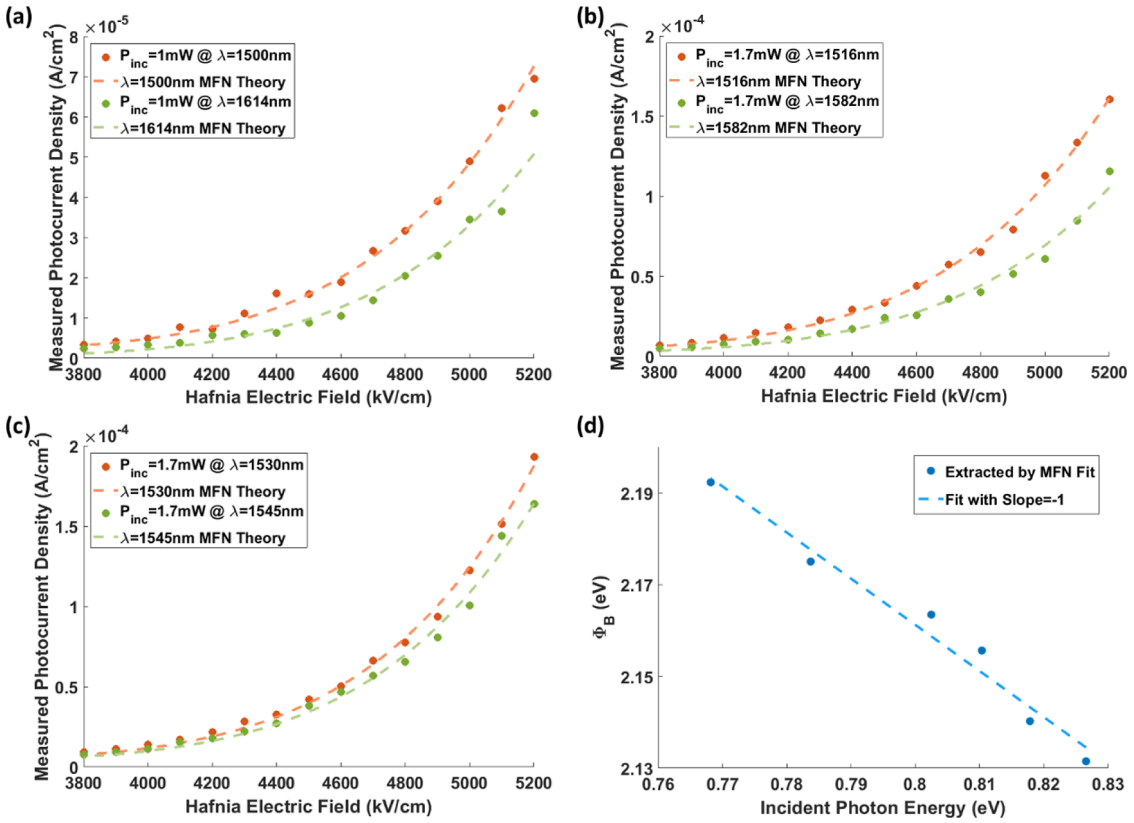

Figure 6. (a–c) MFN tunneling model fits to the photocurrent measured at optical wavelength pairs having the same grating coupling efficiency to SPPs on a 28 μm diameter device (R9-E9). The optical response of the device is shown in Figure 5d. (d) The barrier height for plasmonic hot holes vs the incident photon energy with a best fit slope of −1. The barrier height values were extracted from the fits in parts (a–c).

In contrast, we observed no tunneling photocurrent under accumulation. We note that the barrier for the hot electrons created in the metal remains large at the photon energies investigated (~2.3 eV, Figure 4a).

Wavelength Dependence. The MOS structures comprise plasmonic gratings designed for different working wavelengths. Coupling of incident photons to SPPs occurs with greater efficiency at the resonant wavelength of the grating. This is confirmed experimentally in Figure 5a,d which shows the wavelength response of the measured photocurrent for two 28 μm diameter MOS devices of different grating pitch. The faded data points and curves correspond to the raw data, and the bright color data points and curves are corrected for laser power variations over wavelength.

Figure 5a shows the measured photocurrent of a MOS device of grating pitch 450 nm designed to couple at λ_0 = 1570 nm, and Figure 5d shows similar results for a grating pitch of 440 nm designed to operate at λ_0 = 1540 nm. The measured photocurrent data points are taken as the instantaneous difference between the total current under illumination at one wavelength and the total dark current (no illumination). Each dark or illuminated current is acquired at a DC bias voltage of V_b = 2.4 V applied to the MOS device, and by averaging over 10 measured samples and integrating over 10 pulse line cycles in the source-meter unit to reduce readout noise. The solid curves show the moving average of the gathered data over a sliding window of size 20.

Figure 5b,e shows the measured reflectance responses of the devices of Figure 5a,d under open-circuit conditions, normalized to the reflectance response of a similar device without the grating. The wavelength responses were obtained using a free-space telescope setup with Gaussian beam focal spot diameter of 20 μm (similar to the setup described in previous work).[32] It is observed that the resonance wavelengths of the reflectance responses agree well with the wavelengths where the largest photocurrent was measured, and that they redshift with the increase in grating pitch.

Responsivity. Figure 5c,f shows the responsivity of the devices of Figure 5a,d measured at the most efficient wavelength for photocurrent generation (λ_0 = 1570 nm, and λ_0 = 1540 nm, respectively), and at different bias voltages. The circles show the measured data, and the dotted lines show linear fits to the data. The slopes of the linear fits are taken as the responsivity for each biasing condition. The photocurrent increases linearly with the incident optical power at each bias voltage, suggesting that more photons impinging on the device leads to the excitation of more SPPs that decay into more hot electron–hole pairs in the gold film.[3] More of these hot holes then have a high enough probability to tunnel through the oxide barrier to increase the photocurrent. We point out that the responsivity levels, of the order of 10^{-4} to 10^{-3} mA/W, are lower than similar plasmonic structures on Schottky junctions which produce responsivities of the order of 10 mA/W at similar wavelengths.[12] The responsivity of tunneling-based devices can be improved by reducing the thickness of the oxide layer or using materials with different band gaps and work functions.

After passing the threshold inversion point in the MOS structure by applying bias voltages greater than V_b = 1.85 V, the surface potential of the semiconductor remains almost

https://doi.org/10.1021/acsphotonics.3c00766
ACS Photonics 2023, 10, 3321–3330

constant at $e\phi_S = 2e\phi_{FP} = -1.12$ eV and band bending in the oxide increases. The resulting trapezoidal shape of the band lowers (effectively) the thickness of oxide that holes must tunnel through. Increased bending of the oxide bands also increases the electric field magnitude in the oxide, providing a stronger propelling force for the carriers. This explains the observed higher responsivity at higher bias voltages (and the increasing photocurrent with bias observed in Figure 3d).

Optical Modeling. Figure 5a also plots the calculated absorptance response of the device. Computations were carried out using the 2D FEM and the computational domain was enclosed by absorbing/scattering boundary conditions. The reflectance (R) and transmittance (T) of the structure were calculated on cutlines above the structure, outside of the SU8 layer, and below the MOS structure layers, inside the silicon, respectively. The absorptance (A) response was then calculated as $A = 1 - T - R$ and plotted in Figure 5a. The reflectance response of the device was normalized in the same way as the measurements (*cf.* subsection entitled Wavelength Dependence) and plotted in Figure 5b. Figure 5d,e and 5e give the corresponding simulation results for the other device tested.

The computed reflectance responses plotted in Figure 5b,e can be compared directly with the measurements. The spectral shapes and locations of the coupling wavelengths agree quite well, but the reflectance depth is shallower in the measurements (note the different vertical scales for theory and experiment). This difference in the reflectance depths is due in part to alignment errors of the focused beam on the plasmonic grating in the free space setup, as the response is sensitive to translational and angular displacements of the device from the focal point and from normal incidence. Fabrication imperfections (e.g., roughness) and material quality also affect the agreement between the model and the experiment. Except for the reflectance depth, the agreement between theory and experiment is rather good.

We compare the calculated absorptance responses with the measured photocurrent responses in Figure 5a,d. It is evident that the photocurrent follows the absorptance, with maxima for both occurring at about the same wavelengths, which coincide with the wavelengths where the gratings couple maximally the incident beam to SPPs. Thus, the maximum photocurrent coincides with the wavelength where SPPs are most strongly excited and where the absorptance is maximum.

SPP (Photon) Energy. Figure 5a,d shows that the photocurrent on the short-wavelength side of the maximum is higher than the photocurrent on the long-wavelength side, which suggests that SPPs (photons) carrying higher energy quanta, $\hbar\omega$, produce more energetic holes in the metal which have a higher probability of tunneling. Since the calculated absorptance response is symmetric near the maximum, the coupling efficiency for SPPs on either side is similar, so the higher photocurrent at shorter wavelengths must be due to higher energy quanta carried by the SPPs.

To investigate this effect more deeply, the IV characteristics at pairs of wavelengths on either side of the reflectance minimum (having identical measured normalized reflectance values) were acquired. Based on the numerical simulations, such wavelength pairs also have a very similar absorptance, and correspondingly, very similar coupling efficiencies to SPPs. Thus, any difference between the IV characteristics of the wavelength pairs can be attributed to the difference in energy $\hbar\omega$, which in turn affects the barrier height that hot holes see in the tunneling process (because they are more energetic). Figure 6a−c show the measured photocurrent versus bias voltage in inversion, for three wavelength pairs satisfying this condition, for the device of Figure 5d,f. The plots show consistently higher photocurrents at shorter wavelengths, which we attribute to their higher energy quanta, $\hbar\omega$.

The MFN model [eqs 3 (S9 and S11)] was fit to these photocurrents and are also plotted in Figure 6a−c. In the fitting process, the effective mass of holes tunneling through hafnia was taken as constant throughout, extracted as $m_{HfO_2,h}^* = 0.052m_0$ from previous fit results (*cf.* subsection entitled Tunneling Photocurrent under Inversion). It was also assumed that N_h (the surface number density of hot holes available for tunneling) was the same for both wavelengths in a pair because the measurements were performed for the same incident optical power. Following these assumptions, we extract the hot hole barrier height from the fits.

Figure 6d plots the extracted hot hole barrier heights for the six wavelengths investigated versus SPP energy, $\hbar\omega$. The plot reveals a linear decrease of hot hole barrier height with increasing SPP energy following a slope of −1. As the energy of hot holes increases linearly with SPP energy, a commensurately lower tunneling barrier height is observed. Furthermore, the differences in the barrier height of each wavelength pair in Figure 6a−c ($\Delta\phi_{B(1500-1614)} \simeq 0.061$ eV, $\Delta\phi_{B(1516-1582)} \simeq 0.053$ eV), and $\Delta\phi_{B(1530-1545)} \simeq 0.0078$ eV), agree with the differences in the photon energy of each wavelength pair.

Alternate Hypothesis. An alternate hypothesis to explain the tunneling photocurrent is the optical enhancement of tunneling inversion electrons (which are responsible for the dark current). Simulation results show that a small fraction of SPP power is absorbed by electrons in the thin inversion layer in silicon due to free carrier absorption. Such absorption could raise some inversion electrons to higher energy levels within the potential well-defined by the inversion layer. These electrons would see a smaller barrier and their tunneling probability would increase leading to a photocurrent. However, SPP absorption in the inversion layer is about 2 orders of magnitude smaller than SPP absorption in the metal. Moreover, the extracted effective tunneling mass of electrons based on the photocurrent data is 3× higher than that based on the dark current data, which is inconsistent. Finally, the tunneling barrier height for excited inversion electrons decreases with photon energy, but the slope of the best fitting linear model is −0.5 (instead of −1 for hot hole tunneling, Figure 6d). These points rule out enhanced tunneling of inversion electrons and motivate our assignment of the photocurrent to the tunneling of hot holes created in the metal (see Supporting Information, Section 4 for details of this alternate hypothesis).

Thermal Effects. Although it is well-known that thermal effects can mask plasmonic hot carrier effects,[49] we find no reason to invoke them in our interpretation. The optical powers applied in our measurements are low (<10 mW), and the substrate (highly doped Si) is thermally conductive and placed on a metal chuck which works effectively as a heat sink. Furthermore, the MFN tunneling model that was adopted fits very well all dark and illuminated current measurements, and it has no explicit thermal dependence. Finally, the photocurrent measurements comparing photon energies at the same incident power and coupling efficiency (Figure 6) reveal a clear

https://doi.org/10.1021/acsphotonics.3c00766
ACS Photonics 2023, 10, 3321−3330

dependence on photon energy, which would not hold if the photocurrent was induced thermally.

CONCLUSIONS

We showed that hot carriers created by SPP absorption in the metal contact of a MOS device leads to a photo response due to hole tunneling. Theoretical investigation and modeling support ascribing the response to hot holes excited in the metal contact which then tunnel through the oxide into the valence band of the semiconductor. This tunneling mechanism was not observed in the absence of SPP excitation because holes do not exist in metals unless created by an external stimulus. The tunneling effective masses of electrons and holes through hafnia were extracted by fitting FN and MFN tunneling theories to the measured dark currents and the photocurrent. The mechanism holds promise for hot carrier based optoelectronic devices and, as a proof of principle, can pave the way toward applications in high-speed transceivers for on-chip data transfer and wafer level testing.

ASSOCIATED CONTENT

Supporting Information

This material is available free of charge *via* ACS Publications Web site at. The Supporting Information is available free of charge at https://pubs.acs.org/doi/10.1021/acsphotonics.3c00766.

> Theoretical investigation of the *CV* measurements, calculations regarding the energy band diagram, Fowler–Nordheim and modified Fowler–Nordheim tunneling theory and equations for modeling the dark current of the MOS structure, computational results for the absorption of the incident optical beam in different layers of the MOS structure, and MFN fit results to the photocurrent assuming tunneling of inversion electrons (PDF)

AUTHOR INFORMATION

Corresponding Author

Pierre Berini − *Department of Physics, University of Ottawa, Ottawa, Ontario K1N 6N5, Canada; Nexus for Quantum Technologies Institute-NEXQT, University of Ottawa, Ottawa, Ontario K1N 6N5, Canada; School of Electrical Engineering and Computer Science, University of Ottawa, Ottawa, Ontario K1N 6N5, Canada;* orcid.org/0000-0002-6795-7275; Email: .....

Author

Maryam Sadat Amiri Naeini − *Department of Physics, University of Ottawa, Ottawa, Ontario K1N 6N5, Canada; Nexus for Quantum Technologies Institute-NEXQT, University of Ottawa, Ottawa, Ontario K1N 6N5, Canada;* orcid.org/0000-0002-0296-5506

Complete contact information is available at: https://pubs.acs.org/10.1021/acsphotonics.3c00766

Funding

Natural Sciences and Engineering Research Council of Canada

Notes

The authors declare no competing financial interest.

ACKNOWLEDGMENTS

Authors would like to acknowledge Anthony Olivieri and Saba Siadat Mousavi for device fabrication.

REFERENCES

(1) Sundararaman, R.; Narang, P.; Jermyn, A. S.; Goddard, W. A., III; Atwater, H. A. Theoretical Predictions for Hot-Carrier Generation from Surface Plasmon Decay. *Nat. Commun.* **2014**, *5* (1), 5788.

(2) Brongersma, M. L.; Halas, N. J.; Nordlander, P. Plasmon-Induced Hot Carrier Science and Technology. *Nat. Nanotechnol.* **2015**, *10* (1), 25−34.

(3) Khurgin, J. B. Fundamental Limits of Hot Carrier Injection from Metal in Nanoplasmonics. *Nanophotonics* **2020**, *9* (2), 453−471.

(4) Narang, P.; Sundararaman, R.; Atwater, H. A. Plasmonic Hot Carrier Dynamics in Solid-State and Chemical Systems for Energy Conversion. *Nanophotonics* **2016**, *5* (1), 96−111.

(5) Zhang, Y.; Guo, W.; Zhang, Y.; Wei, W. D. Plasmonic Photoelectrochemistry: In View of Hot Carriers. *Adv. Mater.* **2021**, *33* (46), 2006654.

(6) DuChene, J. S.; Tagliabue, G.; Welch, A. J.; Cheng, W.-H.; Atwater, H. A. Hot Hole Collection and Photoelectrochemical CO2 Reduction with Plasmonic Au/p-GaN Photocathodes. *Nano Lett.* **2018**, *18* (4), 2545−2550.

(7) Hirbodvash, Z.; Krupin, O.; Northfield, H.; Olivieri, A.; Baranova, E. A.; Berini, P. Infrared Surface Plasmons on a Au Waveguide Electrode Open New Redox Channels Associated with the Transfer of Energetic Carriers. *Sci. Adv.* **2022**, *8* (20), 9303.

(8) Mukherjee, S.; Libisch, F.; Large, N.; Neumann, O.; Brown, L. V.; Cheng, J.; Lassiter, J. B.; Carter, E. A.; Nordlander, P.; Halas, N. J. Hot Electrons Do the Impossible: Plasmon-Induced Dissociation of H2 on Au. *Nano Lett.* **2013**, *13* (1), 240−247.

(9) Clavero, C. Plasmon-Induced Hot-Electron Generation at Nanoparticle/Metal-Oxide Interfaces for Photovoltaic and Photocatalytic Devices. *Nat. Photonics* **2014**, *8* (2), 95−103.

(10) Tang, H.; Chen, C. J.; Huang, Z.; Bright, J.; Meng, G.; Liu, R. S.; Wu, N. Plasmonic Hot Electrons for Sensing, Photodetection, and Solar Energy Applications: A Perspective. *J. Chem. Phys.* **2020**, *152* (22), 220901.

(11) Berini, P. Surface Plasmon Photodetectors and Their Applications. *Laser Photon. Rev.* **2014**, *8* (2), 197−220.

(12) Alavirad, M.; Olivieri, A.; Roy, L.; Berini, P. High-Responsivity Sub-Bandgap Hot-Hole Plasmonic Schottky Detectors. *Opt. Express* **2016**, *24* (20), 22544−22554.

(13) Knight, M. W.; Sobhani, H.; Nordlander, P.; Halas, N. J. Photodetection with Active Optical Antennas. *Science* **2011**, *332* (6030), 702−704.

(14) Sobhani, A.; Knight, M. W.; Wang, Y.; Zheng, B.; King, N. S.; Brown, L. V.; Fang, Z.; Nordlander, P.; Halas, N. J. Narrowband Photodetection in the Near-Infrared with a Plasmon-Induced Hot Electron Device. *Nat. Commun.* **2013**, *4* (1), 1643.

(15) Pertsch, P.; Kullock, R.; Gabriel, V.; Zurak, L.; Emmerling, M.; Hecht, B. Tunable Nanoplasmonic Photodetectors. *Nano Lett.* **2022**, *22* (17), 6982−6987.

(16) Mennemanteuil, M. M.; Buret, M.; Colas-Des-Francs, G.; Bouhelier, A. Optical Rectification and Thermal Currents in Optical Tunneling Gap Antennas. *Nanophotonics* **2022**, *11* (18), 4197−4208.

(17) Li, W.; Valentine, J. G. Harvesting the Loss: Surface Plasmon-Based Hot Electron Photodetection. *Nanophotonics* **2017**, *6* (1), 177−191.

(18) Ward, D. R.; Hüser, F.; Pauly, F.; Cuevas, J. C.; Natelson, D. Optical Rectification and Field Enhancement in a Plasmonic Nanogap. *Nat. Nanotechnol.* **2010**, *5* (10), 732−736.

(19) Stolz, A.; Berthelot, J.; Mennemanteuil, M.-M.; Colas des Francs, G.; Markey, L.; Meunier, V.; Bouhelier, A. Nonlinear Photon-Assisted Tunneling Transport in Optical Gap Antennas. *Nano Lett.* **2014**, *14* (5), 2330−2338.

(20) Lambe, J.; Mccarthy, S. L. Light Emission from Inelastic Electron Tunneling. *Phys. Rev. Lett.* **1976**, *37* (14), 923−925.

(21) Kern, J.; Kullock, R.; Prangsma, J.; Emmerling, M.; Kamp, M.; Hecht, B. Electrically Driven Optical Antennas. *Nat. Photonics* **2015**, *9* (9), 582−586.
(22) Buret, M.; Uskov, A. V.; Dellinger, J.; Cazier, N.; Mennemanteuil, M.-M.; Berthelot, J.; Smetanin, I. V.; Protsenko, I. E.; Colas-des-Francs, G.; Bouhelier, A. Spontaneous Hot-Electron Light Emission from Electron-Fed Optical Antennas. *Nano Lett.* **2015**, *15* (9), 5811−5818.
(23) Zhang, C.; Hugonin, J. P.; Coutrot, A. L.; Sauvan, C.; Marquier, F.; Greffet, J.-J. Antenna Surface Plasmon Emission by Inelastic Tunneling. *Nat. Commun.* **2019**, *10* (1), 4949.
(24) Kullock, R.; Ochs, M.; Grimm, P.; Emmerling, M.; Hecht, B. Electrically-Driven Yagi-Uda Antennas for Light. *Nat. Commun.* **2020**, *11* (1), 115.
(25) Qian, H.; Hsu, S.-W.; Gurunatha, K.; Riley, C. T.; Zhao, J.; Lu, D.; Tao, A. R.; Liu, Z. Efficient Light Generation from Enhanced Inelastic Electron Tunnelling. *Nat. Photonics* **2018**, *12* (8), 485−488.
(26) Cazier, N.; Buret, M.; Uskov, A. V.; Markey, L.; Arocas, J.; Colas Des Francs, G.; Bouhelier, A. Electrical Excitation of Waveguided Surface Plasmons by a Light-Emitting Tunneling Optical Gap Antenna. *Opt. Express* **2016**, *24* (4), 3873−3884.
(27) Du, W.; Wang, T.; Chu, H.-S.; Nijhuis, C. A. Highly Efficient On-Chip Direct Electronic-Plasmonic Transducers. *Nat. Photonics* **2017**, *11* (10), 623−627.
(28) Davids, P. S.; Jarecki, R. L.; Starbuck, A.; Burckel, D. B.; Kadlec, E. A.; Ribaudo, T.; Shaner, E. A.; Peters, D. W. Infrared Rectification in a Nanoantenna-Coupled Metal-Oxide-Semiconductor Tunnel Diode. *Nat. Nanotechnol.* **2015**, *10* (12), 1033−1038.
(29) Wang, Z.; Wang, X.; Liu, J. An Efficient Nanophotonic Hot Electron Solar-Blind UV Detector. *ACS Photonics* **2018**, *5* (10), 3989−3995.
(30) Matsui, T.; Li, Y.; Hsu, M. H. M.; Merckling, C.; Oulton, R. F.; Cohen, L. F.; Maier, S. A. Highly Stable Plasmon Induced Hot Hole Transfer into Silicon via a SrTiO3 Passivation Interface. *Adv. Funct. Mater.* **2018**, *28* (17), 1705829.
(31) Güsken, N. A.; Lauri, A.; Li, Y.; Matsui, T.; Doiron, B.; Bower, R.; Regoutz, A.; Mihai, A.; Petrov, P. K.; Oulton, R. F.; Cohen, L. F.; Maier, S. A. TiO_{2-x}-Enhanced IR Hot Carrier Based Photodetection in Metal Thin Film−Si Junctions. *ACS Photonics* **2019**, *6* (4), 953−960.
(32) Olivieri, A.; Chen, C.; Hassan, S.; Lisicka-Skrzek, E.; Tait, R. N.; Berini, P. Plasmonic Nanostructured Metal-Oxide-Semiconductor Reflection Modulators. *Nano Lett.* **2015**, *15* (4), 2304−2311.
(33) Siadat Mousavi, S.; Olivieri, A.; Berini, P. Fabrication of a High-Speed Plasmonic Reflection/Transmission Modulator. *AIP Adv.* **2021**, *11* (2), 025023.
(34) Palik, E. D. *Handbook of Optical Constants of Solids*; Academic Press, 1998; Vol. *III*.
(35) Khoshman, J. M.; Kordesch, M. E. Optical Properties of A-HfO2 Thin Films. *Surf. Coat. Technol.* **2006**, *201* (6), 3530−3535.
(36) SU-8 2000 Permanent Epoxy Negative Photoresist. Microchem, 2019.
(37) Conley, J. F.; Ono, Y.; Solanki, R.; Stecker, G.; Zhuang, W. Electrical Properties of HfO2 Deposited via Atomic Layer Deposition Using Hf(NO3)4 and H2O. *Appl. Phys. Lett.* **2003**, *82* (20), 3508−3510.
(38) Scarel, G.; Spiga, S.; Wiemer, C.; Tallarida, G.; Ferrari, S.; Fanciulli, M. Trends of Structural and Electrical Properties in Atomic Layer Deposited HfO2 Films. *Mater. Sci. Eng., B* **2004**, *109* (1−3), 11−16.
(39) King, P. J. Hafnium Oxide-Based Dielectrics by Atomic Layer Deposition. Doctoral Dissertation, University of Liverpool: Liverpool, UK, 2013.
(40) Sze, S. M.; Li, Y.; Ng, K. K. *Physics of Semiconductor Devices*; John Wiley & Sons, 2021.
(41) Liang, S. Fowler-Nordheim Theory. *Quantum Tunneling and Field Electron Emission Theories*; World Scientific, 2013.
(42) Oh, S. J.; Yeow, Y. T. A Modification to the Fowler-Nordheim Tunneling Current Calculation for Thin MOS Structures. *Solid-State Electron.* **1988**, *31* (6), 1113−1118.
(43) Weinberg, Z. A. Tunneling of Electrons from Si into Thermally Grown SiO2. *Solid-State Electron.* **1977**, *20* (1), 11−18.
(44) Stern, F. Self-Consistent Results for n-Type Si Inversion Layers. *Phys. Rev. B* **1972**, *5* (12), 4891−4899.
(45) Zhu, W. J.; Ma, T.-P.; Tamagawa, T.; Kim, J.; Di, Y. Current Transport in Metal/Hafnium Oxide/Silicon Structure. *IEEE Electron Device Lett.* **2002**, *23* (2), 97−99.
(46) Stuart, R. N.; Wooten, F.; Spicer, W. E. Mean Free Path of Hot Electrons and Holes in Metals. *Phys. Rev. Lett.* **1963**, *10* (1), 7−9.
(47) Brown, A. M.; Sundararaman, R.; Narang, P.; Goddard, W. A.; Atwater, H. A. Nonradiative Plasmon Decay and Hot Carrier Dynamics: Effects of Phonons, Surfaces, and Geometry. *ACS Nano* **2016**, *10* (1), 957−966.
(48) Simmons, J. G. Generalized Formula for the Electric Tunnel Effect between Similar Electrodes Separated by a Thin Insulating Film. *J. Appl. Phys.* **1963**, *34* (6), 1793−1803.
(49) Baffou, G.; Bordacchini, I.; Baldi, A.; Quidant, R. Simple Experimental Procedures to Distinguish Photothermal from Hot-Carrier Processes in Plasmonics. *Light Sci. Appl.* **2020**, *9* (1), 108.

https://doi.org/10.1021/acsphotonics.3c00766
ACS Photonics 2023, 10, 3321−3330

Supplementary Information:

Infrared surface plasmons open a hole tunneling channel in metal-oxide-semiconductor structures

Maryam Sadat Amiri Naeini[a, b], Pierre Berini[a, b, c*]

[a]Department of Physics, University of Ottawa, 150 Louis-Pasteur Pvt., Ottawa, ON, K1N 6N5, Canada

[b]Nexus for Quantum Technologies Institute-NEXQT, University of Ottawa, 25 Templeton St., Ottawa, ON, K1N 6N5, Canada

[c]School of Electrical Engineering and Computer Science, University of Ottawa, 800 King Edward Ave., Ottawa, ON, K1N 6N5, Canada

*Email: .....

Contents

S1. CV characteristics 2

S2. Energy band diagram construction 3

S3. Theoretical modeling of dark tunneling current under inversion 4

S4. Alternate hypothesis: Enhanced tunneling of inversion electrons 5

Computational results 5

MFN fit of the photocurrent assuming tunneling inversion electrons 6

References 7

List of Figures

Figure S1: Calculated absorptance spectra due to absorption in different layers of the MOS device 6

Figure S2: Surface number density and barrier height for tunneling electrons/holes, extracted by considering two different hypotheses for the photocurrent 7

S1. CV characteristics

The oxide breakdown field was measured under a positive bias (inversion) as $E_{bd} = |V_{HfO_2}|/d \sim 6000$ kV/cm and under a negative bias (accumulation) as $E_{bd} = |V_{HfO_2}|/d \sim 6600$ kV/cm. These breakdown fields agree with the values reported in the literature for ALD HfO_2.[1] V_{HfO_2} is the potential difference across the hafnia layer, given by:[2]

$$V_{HfO_2} = V_b - \phi_s - \phi_{ms} \tag{S1}$$

with ϕ_s being the surface potential and $e\phi_{ms} =$ -0.0258 eV being the work function difference between the metal and the semiconductor (Au, p-Si), and e is the electron charge.

The flat band capacitance of the MOS structure was computed via:[2]

$$C_{FB} = \frac{\epsilon_0 \epsilon_{HfO_2} A_c}{d + \left(\frac{\epsilon_{HfO_2}}{\epsilon_{si}}\right)\sqrt{V_T \frac{\epsilon_0 \epsilon_{si}}{eN_a}}} \tag{S2}$$

where ϵ_{si} is the relative permittivity of the silicon substrate, and V_T is the thermal voltage at room temperature. The computed C_{FB} value was then used with the CV characteristics of Fig. 3a to deduce the flat band voltage as $V_{FB} =$ -0.8 V.

The surface density of charge trapped in the oxide was then calculated using:[2]

$$Q_{ss} = -\frac{C_{HfO_2}(V_{FB} - \phi_{ms})}{A_c} \tag{S3}$$

yielding $Q_{ss} = 1.43 \times 10^{-6}\ C/cm^2$.

S2. Energy band diagram construction

The condition for strong inversion of the introduced MOS device is as follows:[2]

$$e\phi_S = 2e\phi_{Fp} = 2(E_F - E_i) = -2kT\ln\left(\frac{N_a}{n_i}\right) \quad \text{(S4)}$$

where ϕ_{Fp} is the potential difference between the intrinsic and Fermi levels in the bulk silicon. The band bending under inversion was calculated using the above as $e\phi_S = 1.12\ \text{eV}$ for an acceptor doping concentration of $N_a = 2.13_{\times}10^{19}\ \text{cm}^{-3}$.

The surface potential relative to the silicon substrate under our accumulation bias voltage was determined to be $e\phi_S = -0.15\ \text{eV}$ using:[2]

$$\phi_S = 2\frac{kT}{e}\ln\left(\frac{eQ_S L_D}{\sqrt{2}\epsilon_0\epsilon_{Si}kT}\right) \quad \text{(S5)}$$

In the above, L_D is the diffusion length (extrinsic Debye length) for holes, and Q_S is the surface charge density of holes in the accumulation region, given by:

$$Q_S = Q_{SS} + \frac{C_{HfO_2}V_{HfO_2}}{A_C} \quad \text{(S6)}$$

S3. Theoretical modeling of dark tunneling current under inversion

The relationship between the tunneling current density and the electric field amplitude inside the oxide layer, E_{HfO_2}, in a Fowler-Nordheim tunneling process is given by:[2, 3]

$$J_{Dark} = a_D E_{HfO_2}^2 e^{-\frac{b_D}{E_{HfO_2}}} \quad \text{(S7)}$$

where

$$a_D = \frac{e^2}{16\pi^2 \hbar \phi_B}\left(\frac{m_0}{m^*_{HfO_2}}\right) = \frac{1.54\ [\mu A][eV][V]^{-2}}{\phi_B}\left(\frac{m_0}{m^*_{HfO_2}}\right) \quad \text{(S8)}$$

and

$$b_D = \frac{4\sqrt{2m^*_{HfO_2}}(e\phi_B)^{\frac{3}{2}}}{3e\hbar} \quad \text{(S9)}$$

In the above, ϕ_B [eV] and $m^*_{HfO_2}$ are the barrier height for the tunneling electrons and electron effective tunneling mass inside the oxide, respectively, and $\hbar$ is Planck's reduced constant.

The modified Fowler-Nordheim tunneling theory yields a relationship between tunneling current density and the electric field inside the oxide layer as:[4]

$$J_{Dark} = a'_D N_{inv} E_{HfO_2} e^{-\frac{b_D}{E_{HfO_2}}} \quad \text{(S10)}$$

where N_{inv} is the surface number density of electrons (cm^{-2}) available for tunneling residing in the inversion layer and the coefficient a'_D is related to the parameter a_D in Eq. S8 by:

$$a'_D = \frac{e a_D}{\epsilon_0 \epsilon_{HfO_2}} \quad \text{(S11)}$$

The threshold inversion voltage of the MOS device beyond which the dark current fitting has been performed, is given by:[2]

$$V_T = \frac{\sqrt{2\epsilon_0 \epsilon_{si} e N_a (2\phi_{Fp})}}{C_{HfO_2}} + 2\phi_{Fp} + V_{FB} \quad \text{(S12)}$$

S4. Alternate hypothesis: Enhanced tunneling of inversion electrons

Computational results

To investigate the absorption of the incident beam in different layers of the MOS device, we calculated the absorptance spectrum of an infinitely periodic 2D grating structure with grating pitch of Λ = 441 nm, ridge width $W_G =$ 220 nm, and ridge thickness $H =$ 79 nm which approximates well our finite device structure. Periodic boundary conditions were applied at the sidewalls of the computational domain, a plane wave excitation was sent towards a unit cell using an active port above the structure and the transmitted wave was read using a listener port at the bottom of structure layers. The absorptance was then calculated as $A = 1 - T - R$.

We chose a periodic structure rather than one of a finite width for the absorptance calculations in order to account for the laterally propagating SPPs that are leaving the computational domain. The periodic boundary conditions used at the sidewalls, replicate the unit cell to model an infinite periodic structure and the waves leaving the unit cell are still considered in the computational domain. So, the only way that these waves could end up increasing the absorptance is if they get absorbed in any of the structure layers.

The absorptance of the thin gold layer and the gold grating ridges thereon was then computed by simulating the structure while turning off the loss of all other layers (by setting the imaginary part of the relative permittivity of the material is zero). To calculate the absorptance in the inversion layer of the MOS device a similar approach was taken, assuming a 1 nm thick inversion layer under the oxide layer. The complex relative permittivity of the inversion layer was taken as that of n-doped silicon of the same doping level as our p-Si substrate.

Fig. S1 gives the absorptance response due to absorption in gold only and in the inversion layer only. Both absorptance spectra show a peak around the resonance wavelength of the plasmonic grating, λ_0 = 1540 nm, where coupling of the incident beam to SPPs is maximum, leading to maximum absorptance due to the decay of SPPs. The absorptance of the thin inversion layer is two orders of magnitude smaller than the absorptance of the gold layer. This leads to the conclusion that most of the SPPs (or incident photons) decay into hot electron-hole pairs inside the gold with a negligible fraction exciting inversion electrons to higher energies. This fact reduces the chance of inversion electrons having a major role in generating the photocurrent relative to hot holes in the metal.

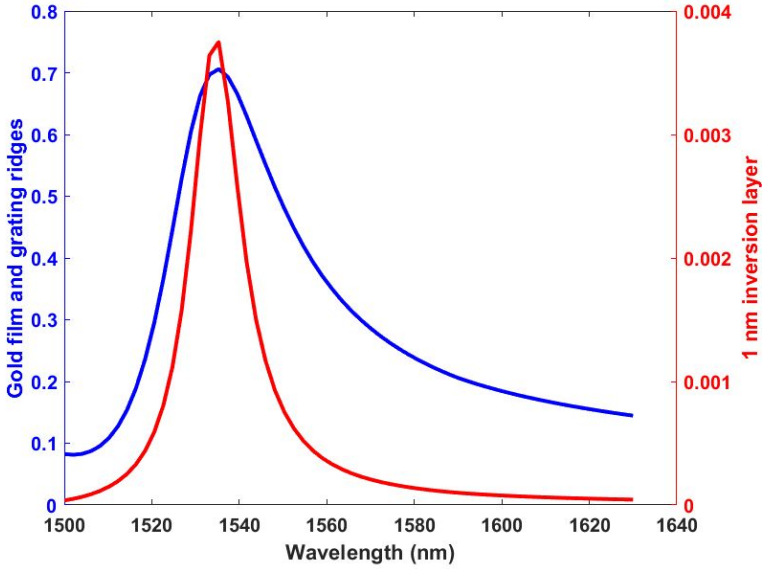

Figure S2. Calculated absorptance spectra due to absorption in different layers of the MOS device.

MFN fit of the photocurrent assuming tunneling inversion electrons

To further investigate the hypothesis that tunneling inversion electrons may be responsible for the photocurrent, we fit the measured photocurrent data in Fig. 3d (main text) to the MFN model. The same fitting parameter b_{Ph} extracted from the three photocurrent fits were used, but assuming a barrier height of $\phi_B = 2.05 - E_0 - \hbar\omega \simeq 0.91$ eV for excited inversion electrons at a working wavelength of λ_0 = 1540 nm. A tunneling effective mass of $m^*_{HfO_2,e,ph} = 0.48m_0$ was then extracted for electrons in hafnia, which is 3× greater than the value extracted from the dark current data. Since in both cases inversion electrons are tunneling through the same oxide, the tunneling effective mass should be similar. This inconsistency therefore precludes attribution of the measured photocurrent to SPP-excited tunneling inversion electrons.

Fig. S2a shows the surface number density of tunneling inversion electrons extracted from the photocurrent fits of Fig. 3d (main text), using the corresponding barrier height and tunneling effective mass of excited inversion electrons. Fig. S2a also plots, for comparison, the surface number density of hot holes available in gold for tunneling, extracted from same data but using the corresponding barrier height and tunneling effective mass of holes. In both cases the number of tunneling carriers available under illumination follows a linear trend with respect to the incident optical power, but the required number density of inversion electrons is 3× to 5× larger.

Fig. S2b shows that the tunneling barrier height for excited inversion electrons decreases with photon energy, but the slope of the best fitting linear model is -0.5, compared to a slope of -1 as was observed in Fig. 6d of the main text for tunneling hot holes. This observation further motivates assignment of the photocurrent to hot holes tunneling from the gold.

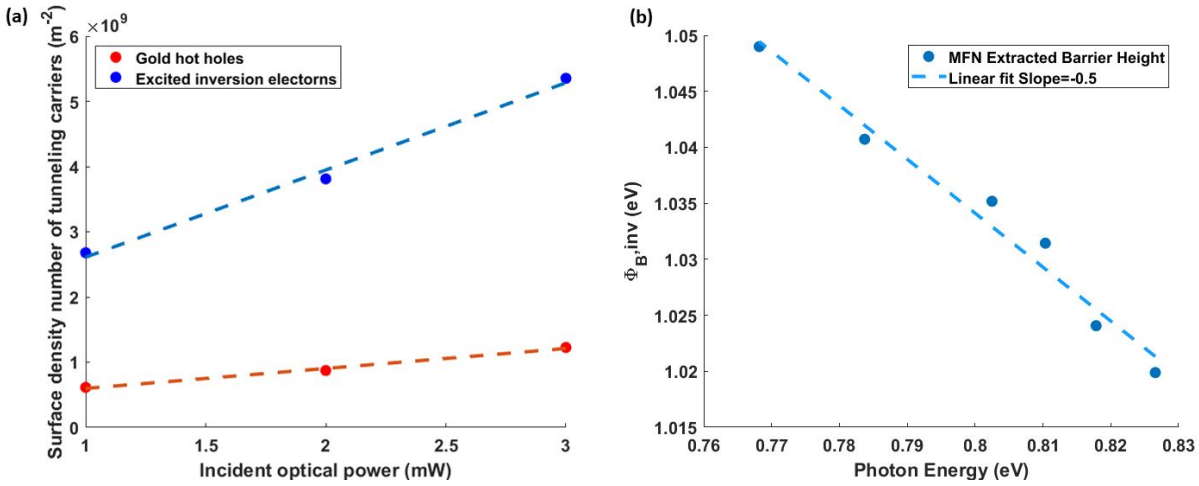

Figure S2. (a) Surface number density of available carriers for tunneling extracted from the photocurrent data of Fig. 3d (main text), considering tunneling of hot holes in gold and excited inversion electrons in silicon. (b) Tunneling barrier height seen by excited inversion electrons *vs*. incident photon energy for wavelength pairs in Fig. 6 yielding a slope of -0.5.

References

(1) Conley, J. F.; Ono, Y.; Solanki, R.; Stecker, G.; Zhuang, W. Electrical Properties of HfO2 Deposited via Atomic Layer Deposition Using Hf(NO3)4 and H2O. *Appl. Phys. Lett.* **2003**, *82* (20), 3508–3510. https://doi.org/10.1063/1.1575934.

(2) Sze, S. M.; Li, Y.; Ng, K. K. *Physics of Semiconductor Devices*; John Wiley & Sons, 2021.

(3) Liang, S. Fowler-Nordheim Theory. In *Quantum Tunneling and Field Electron Emission Theories*, World Scientific, 2013.

(4) Oh, S. J.; Yeow, Y. T. A Modification to the Fowler-Nordheim Tunneling Current Calculation for Thin MOS Structures. *Solid-State Electron.* **1988**, *31* (6), 1113–1118. https://doi.org/10.1016/0038-1101(88)90414-5.

5 Surface Plasmon Enhanced Photoluminescence of Carbon Dots Formed *in-situ* on Silver Gratings

5.1 Summary

Following the results shown in section 7.3 of this thesis, SPP mediated fluorescence emission enhancement and lifetime shortening was investigated theoretically and experimentally for the carbon based emitters. SPP modes on the plasmonic silver grating first create hot carriers required for creating the carbon quantum dots, and then modify the emitters decay rate via Purcell effect and by modifying the local density of states (LDOS) available at the emitters environment. The plasmonic gratings also provide the momentum mismatch compensation between fluorescence SPP modes on the structure and free-space emission channels via diffraction orders. As a result, a plasmonic grating not only creates and excites these fluorescent emitters but also provides an effective channel for radiative decay of emitters and outcoupling their emission. The lifetime of emitters close to plasmonic grating is theoretically and experimentally investigated showing a decay rate of around 200 and lifetime of below or close to 100 ps.

5.2 Contribution

Jaspreet Walia measured and prepared results in Fig. 3(a) and Fig. 2(c). Luis-Angel Mayoral-Astorga helped with the setup shown in Fig. 1(a). Hyung Woo Choi fabricated the grating structures.

I designed and built the lifetime measurement setup and built the Raman microscopy setup. I performed all the SERS and TCSPC histogram measurements and performed all the analysis on the measurements. I performed both FEM and FDTD numerical analysis for decay rate and emission patterns and calculated the fitting models for the measured fluorescence decay to extract lifetime of species and wrote the manuscript. Professors Berini and Weck supervised the project. Professor Berini also contributed to the data analysis and writing the manuscript.

The results in this chapter will be published in a peer-reviewed journal.

Surface plasmon enhanced photoluminescence of carbon dots formed *in-situ* on silver gratings

Maryam Sadat Amiri Naeini[1,2], Jaspreet Walia[2,3], Luis-Angel Mayoral-Astorga[2], Hyung Woo Choi[2], Arnaud Weck[1,2,4], Pierre Berini[1,2,3]

[1]Department of Physics, University of Ottawa, Ottawa, Ontario, Canada
[2]Nexus for Quantum Technologies Institute, University of Ottawa, Ottawa, Ontario, Canada
[3]School of Electrical Engineering and Computer Science, University of Ottawa, Ottawa, Ontario, Canada
[4]Department of Mechanical Engineering, University of Ottawa, Ontario, Canada

KEYWORDS: Surface plasmon, silver, grating, carbon dot, SERS, plasmon-enhanced fluorescence, fluorescence lifetime

Abstract

We present a comprehensive study of the photoluminescence of carbon dots formed *in situ* on silver gratings via plasmonic reduction of a carbonaceous seed layer located thereon. Our fabricated silver gratings bear carbon-based residue which transforms into photoluminescent carbon dots catalysed by surface plasmon polaritons (SPPs) excited thereon by a pump laser. The pump SPPs subsequently excite the carbon dots into photoluminescence emitted at longer wavelengths. The photoluminescence is strongly influenced by the local electromagnetic environment (local optical density of states), which is dominated by SPPs propagating on and diffracting from the silver grating. We experimentally observe SPP enhanced photoluminescence, SPP induced coherence, surface enhanced Raman scattering, and lifetime reduction (Purcell effect) of the emitters. A method for modeling an ensemble of random, incoherent emitters using finite-difference time-domain (FDTD) simulations is proposed, and the results are in agreement with observed far-field images and measured Purcell factors. Purcell factors of about 70 are deduced from lifetimes of 30 to 40 ps for carbon dots measured using time-correlated single photon counting. FDTD and experimental results confirm that mediation via SPPs accelerates radiative decay and introduces directional emission channels via grating diffraction conferring coherence to a random arrangement of luminescent carbon dots. Our results provide quantitative insight into carbon dot - SPP interactions, and have implications for designing plasmon-enhanced biosensors, quantum emitters, and carbon-based light sources.

1. Introduction

It was initially explained by Purcell that the lifetime of an excited fluorophore is greatly affected by the electromagnetic environment in which the emitter resides [1]. In fact, modifying the local density of optical states (LDOS) near the emitter results in modification of its total decay rate to lower energy states, and accordingly changes its spontaneous emission rate relative to that in free-space, by controlling the emission channels into which quanta decay [2] [3]. It is then expected that quantum emitters placed on a metallic surface which supports surface plasmon polariton (SPP) modes will

interact strongly with the SPPs through absorption and emission processes. The former leads to efficient pumping, and the latter increases the fluorophore decay rate and the quantum yield, and introduces emission directionality resulting in a modified radiation pattern compared to the fluorophore in free space [2] [4] [5] [6].

SPPs are surface waves comprising collective oscillations of electrons coupled to electromagnetic fields. SPPs are known to be highly confined and to have enhanced electromagnetic fields at specific locations on the surface of metallic structures – often termed hot spots. In addition to enhancing the emission rate of fluorophores via increased LDOS and field enhancement [7], these hot spots also provide opportunity to excite (pump) fluorophores at a higher rate compared to free space. This increase is proportional to the square of the electric field enhancement factor [8]. Furthermore, plasmonic structures can be designed to compensate wavevector mismatch between SPP modes on the surface and radiative emission channels into free space. As a result, once fluorescence emission couples to SPP modes, the structure can be engineered to outcouple the SPP modes into desirable free space radiation channels. Modifying the radiation pattern of fluorophores is thus the third important role that a plasmonic nanostructure placed in proximity to a quantum emitter may play [9], after enhancing the emission rate [7] and the pump efficiency [8].

Plasmonic enhanced fluorescence and light emitting nanostructures have been the subjects of extensive research, culminating in several review papers (e.g., [2] [6] [10] [11]). For example, it's been shown that plasmonic grating structures enhance spontaneous emission of fluorophores [12], and for emitters that have an inherently small radiative efficiency, this can be beneficial for applications such as sensing [13]. Fluorescence enhancement by nanoantennas and their prospective application to high-speed LEDs are discussed in [14]. Greffet *et al*. introduced a new formulation as the local form of Kirchhoff's law to design and analyze thermal emitters and complex photo- or electro-luminescent systems [15] [16], building on earlier work reporting a coherent thermal light source with a polarised, highly directive, and spectrally narrow emission beam [17]. A silver 2D metasurface hosting semiconductor nanocrystals and emitting at a narrow spectral range, with high directivity was also designed using this method [9]. Knoll *et al*. measured the enhanced fluorescence emission of dye molecules coupled via SPPs to diffraction orders of a gold plasmonic grating [18] [19]. In a different study they reported the spatial correlation between the excitation and emission of dye molecules close to a grating surface, due to localized plasmonic fields [20]. Barnes *et al*. explored dye molecule emission enhancement on plasmonic gratings and concluded that there are optimum grating ridge height and dye layer thickness for enhancing the emission intensity [21]. Also, they compared shallow (weakly perturbative) grating structures with a metallic mirror revealing that the lifetime of Eu^{3+} ions does not differ significantly on these two types of structure [22].

Thus, plasmonic gratings are great candidates to enhance the pumping of fluorophores, their emission rate, their quantum efficiency, and to control the emission channels for polarisation and directionality along a desired direction. A plasmonic grating has a broad resonance spectrum and the grating pitch can be engineered so that its resonance covers both the absorption and emission wavelengths of emitters that have a small Stokes shift [23]. Alternatively, grating structures can also be designed to have two resonances, one overlapping with the absorption wavelength and the other with the emission wavelength of a species [24]. The grating wavenumber provides momentum mismatch compensation between free space photons and SPPs, beneficial for plasmon assisted pumping and fluorescence emission outcoupling to desired free space radiative channels [25]. SPP

modes on a grating also create strongly confined electromagnetic fields over the illuminated portion of the metallic surface hosting the fluorescent species.

In previous work, we reported the plasmon-catalysed formation of photoluminescent carbon dots on gratings [26] [27]. In this paper we report the theoretical and experimental investigation of plasmon-mediated pumping, emission, and outcoupling into free-space radiation of photoluminescence produced by carbon dots formed *in situ* via plasmonic catalysis from a carbonaceous seed layer on shallow silver gratings. We also determine the lifetime of the carbon dots on silver gratings from which we deduce the Purcell factor of the system, and the corresponding free-space lifetime of the carbon dots. We investigate the far field radiation patterns of the emission and observe coherence in the form of directional and polarised emission. The role of plasmons in our study is threefold – firstly, pump plasmons catalyse the seed layer into photoluminescent carbon dots; secondly, pump plasmons excite the carbon dots; and thirdly, plasmons mediate photoluminescence by the carbon dots, significantly altering their spontaneous emission characteristics. The paper is organised following these distinct roles.

2. Carbon Dot Formation Catalysed by Surface Plasmons

The structures consist of silver gratings of pitch $\Lambda = 500\ \mathrm{nm}$ and ridge height $h = 25\ \mathrm{nm}$ with a 50% duty cycle, formed by helium-beam lithography, evaporation and lift-off (as detailed in [27]), on a $100\ \mathrm{nm}$ thick silver layer on a silicon substrate. The gratings were designed for efficient coupling to a normally-incident *p*-polarised loosely focussed beam at a free-space wavelength of $\lambda = 532\ \mathrm{nm}$. Each grating has an area of $10\ \mu\mathrm{m} \times 10\ \mu\mathrm{m}$. The inset in Fig. 1(a) shows a helium ion microscope (HIM) image of a grating structure.

The gratings fabricated in this manner bear carbonaceous residue left behind after lift-off, which act as a seed layer for the formation of carbon dots [27]. The gratings were then inserted in a gas chamber with gas flow of CO_2 or N_2 at ~1.95 atm pressure, and a grating was excited with a *p*-polarised continuous wave (CW) laser beam at $\lambda = 532\ \mathrm{nm}$ in the oxygen depleted environment to transform the carbonaceous residue into light-emitting carbon dots. The surface enhanced Raman scattering (SERS) spectra of a structure were then measured using an in-house built setup as presented in Fig. 1(a). In this set-up, the CW laser beam at $\lambda = 532\ \mathrm{nm}$ of power ~10 mW was delivered to the grating via a dichroic mirror and a 20× objective (Thorlabs RMS20X-PF) to transform and pump the residue on the grating. The emission was collected with the same objective, passing through the dichroic mirror and two 6 OD notch filters (for a total of 12 OD at the notch) to attenuate the reflected pump beam. The emission was then focused into a multimode fiber using another objective and redirected to an electron-multiplying intensified CCD (emICCD) camera connected to a spectrometer (Princeton Instruments). Spectra were compared against a commercial Raman microscope for consistency (*cf*. Fig. 2(c), below).

Fig. 1(b) shows the SERS spectra collected from a grating of pitch $\Lambda = 500\ \mathrm{nm}$ under ~1.95 atm $\mathrm{CO_2}$ and $\mathrm{N_2}$ gases for over 30 minutes illumination in the setup shown in Fig. 1(a). Individual spectra were collected with an integration time of 1 sec, then averaged over 30 spectra. Overall, 60 averaged SERS spectra are plotted, highlighting the evolution of the system over time as the grating is pumped. Graphene-like peaks at $\lambda = 572\ \mathrm{nm}$ (D-band) and $\lambda = 580\ \mathrm{nm}$ (G-band) emerge from the residue on the structure. The peaks do not move but their intensity grows over time, suggesting the continual

transformation of residue on the structure to organised carbon dots, via surface plasmon catalysed transformation in an oxygen depleted environment [27]. These peaks are found precisely at Raman shifts of 1350 cm^{-1} and 1580 cm^{-1}, respectively, from the pump wavelength corresponding to graphene-like material. The broad photoluminescence (PL) peaks at $\lambda = 620\ \mathrm{nm}$ in CO_2 and $\lambda = 690\ \mathrm{nm}$ in N_2 grow over 30 minutes, then remain stable afterwards, while the laser power and gas pressure are maintained. The initial SERS spectrum of the residue in air is also plotted showing residue with weak PL, D- and G-band peaks.

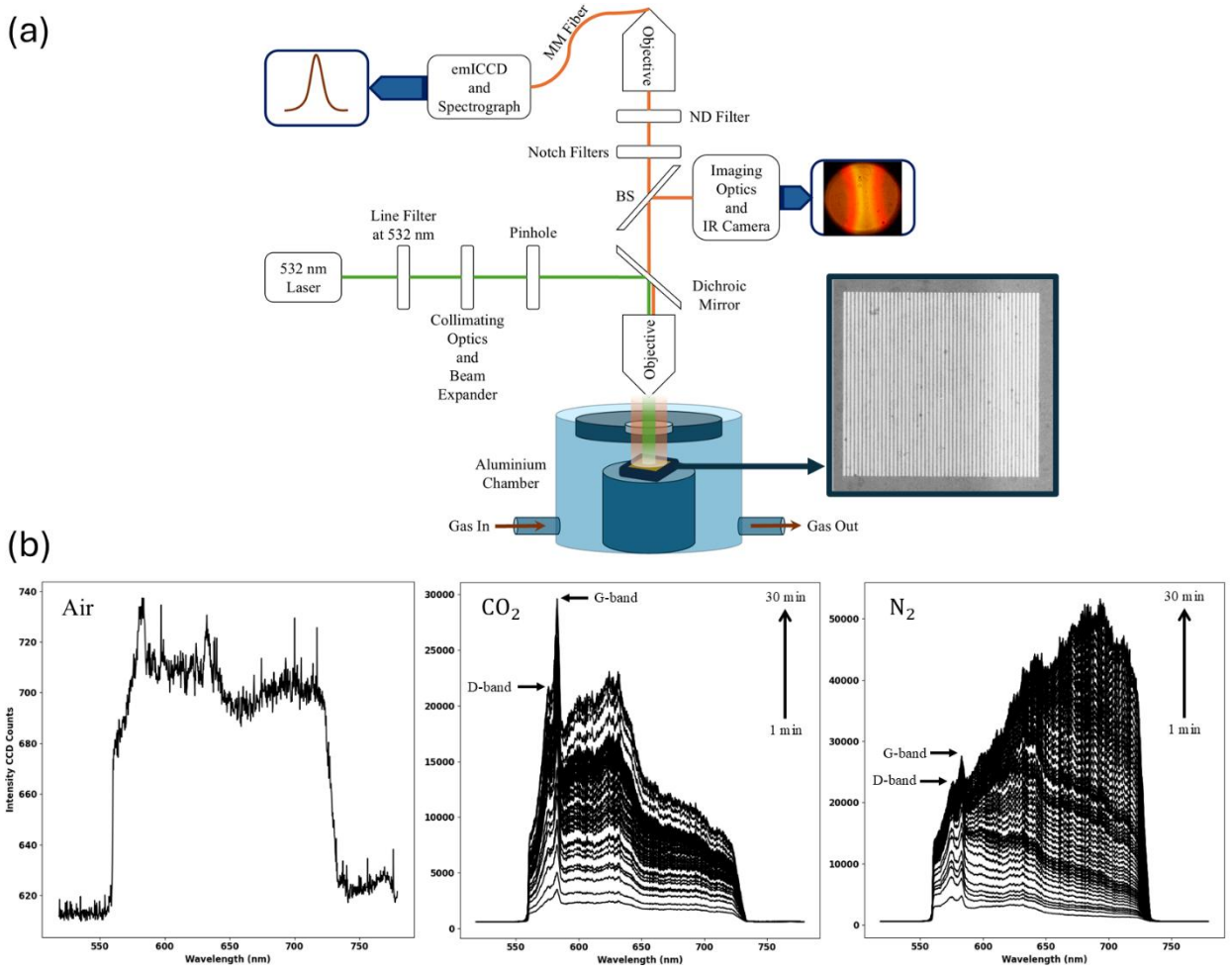

Figure 1. (a) In-house Raman microscopy measurement setup using a CW laser emitting at λ = 532 nm. The setup includes the gas chamber containing grating structures and gas flow at ~1.95 atm. A spectrometer coupled to an emICCD camera is used to measure the spectra of the gratings in air and in both gases. The two insets show a camera image of a grating fluorescing in N_2, and a HIM image of a grating structure post-fabrication. (b) Initial SERS spectrum of the carbonaceous residue on the grating collected in air and evolution of SERS spectra emanating from two gratings under 1.95 atm CO_2 and N_2 gases respectively. The structures are pumped at λ = 532 nm in all cases.

3. Carbon Dot Pumping by Surface Plasmons

Fig. 2(a) shows the electric field enhancement over a unit cell of an infinitely periodic silver grating, illuminated by a normally-incident plane wave at $\lambda = 532\ \mathrm{nm}$ (on resonance) for different polarisation angles, computed using a commercial FEM analysis tool. The grating ridge corners were rounded to a radius of 20 nm to avoid electric filed divergence. Fig. 2(b) shows the absorptance of the

structure at the corresponding polarisation angles, computed over the operating bandwidth of the grating. A (normally-incident) *p*-polarised ($\theta = 0$) plane wave at $\lambda = 532$ nm couples most efficiently to SPPs on the grating, which leads to stronger local fields and greater absorptance. Thus, rotating the polarisation provides means for controlling the strength of the plasmonic pump on the grating, and the degree to which carbon dots thereon are excited.

Once the photoluminescence emanating from a grating stabilised after the formation of carbon dots, SERS spectra were collected as a function of incident polarisation angle, as shown in Fig. 2(c). (These spectra were collected using a commercial Raman microscope - WiTec a300 - operating at $\lambda = 532$ nm , and are observed to be consistent with those of Fig. 1(b) using our custom set-up.) The spectrum obtained under *p*-polarisation ($\theta = 0$) is the strongest, from which D and G peaks are readily observed, as well as a strong broadband photoluminescent background. As the incident polarisation is rotated, the strength of the spectra drops to become barely measurable for *s*-polarisation ($\theta = 90^{o}$) but remains otherwise qualitatively similar. This behaviour is readily understood considering Fig. 2(a): under *s*-polarisation, coupling to SPPs is not possible so the grating behaves essentially as a flat mirror along which the total fields are weak. Conversely, under *p*-polarisation, SPPs are efficiently excited resulting in strong (enhanced) fields along the surface, thereby enabling far more efficient pumping of the carbon dots thereon. Thus, polarisation rotation conveniently enables control over the strength of the emission by modulating the pump interaction with the system.

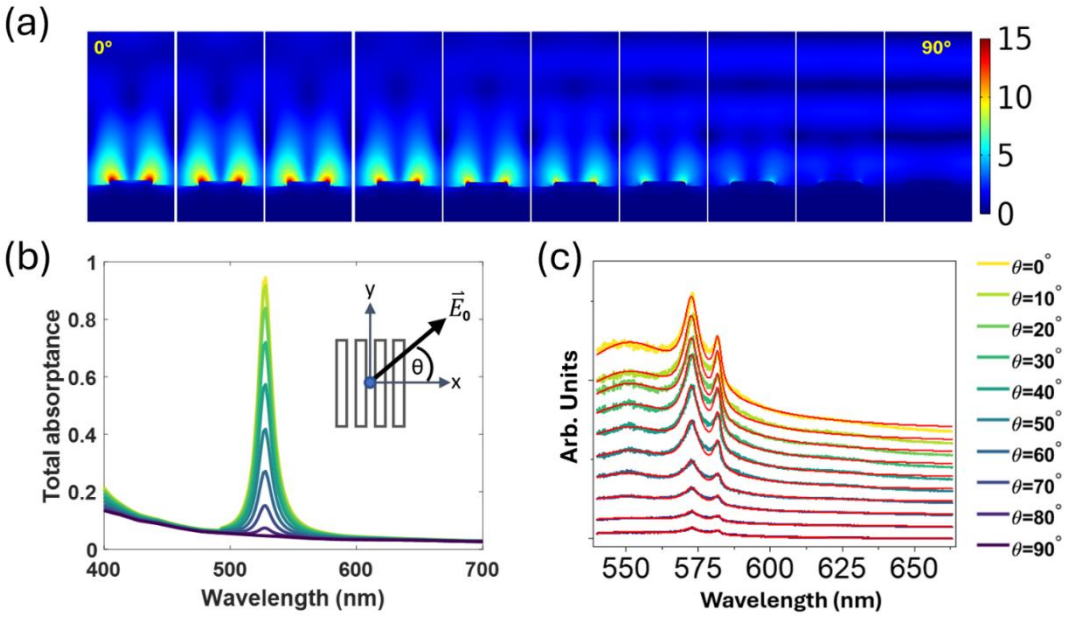

Figure 2. (a) Computed normalized total electric field distribution (E/E_0) over a unit cell of an infinitely periodic silver grating of pitch $\Lambda = 500$ nm and height 25 nm, illuminated by a plane wave at $\lambda = 532$ nm (on resonance) and different polarisation angles θ as noted on the panels and defined in inset to Part (b). (b) Computed absorptance of an infinitely periodic grating illuminated by a plane wave at different polarisation angles (yellow: $\theta = 0$; dark purple: $\theta = 90^{o}$). (c) Measured SERS spectra of the structure in a gas chamber containing CO_2, pumped at $\lambda = 532$ nm at different polarisation angles. The solid curves are fitted to the measured data by decomposition of the spectra into a sum of Lorentzian functions (*cf*. Fig. 3). The spectra are offset vertically for clarity. Parts (b) and (c) share the same colour bar.

Decomposition of the measured spectra of Fig. 2(c) into a sum of Lorentzian functions was performed, and the values of the Lorentzian peak position, linewidth, and integrated intensity were extracted for each excitation polarisation. Results are summarized in Fig. 3. Each spectrum fits very well to three Lorentzian functions, as shown for one case in Fig. 3(a), first panel.

From Fig. 3(b), first and second panels, we observe that the center wavelength and width of the peaks remain unchanged at different polarisation angles. The D-band peak is centered at $\lambda = 572\ \mathrm{nm}$ and the G-band peak is centered at $\lambda = 580\ \mathrm{nm}$, as observed on other gratings in this study and reported in Fig. 1(b). However, the PL peak is centered at $\lambda = 550\ \mathrm{nm}$, which differs from the wavelength of the PL peak observed in Fig. 1(b) for CO_2. Indeed, it was observed through investigation of several structures over many fabrication iterations that the wavelength of the PL peak varies.

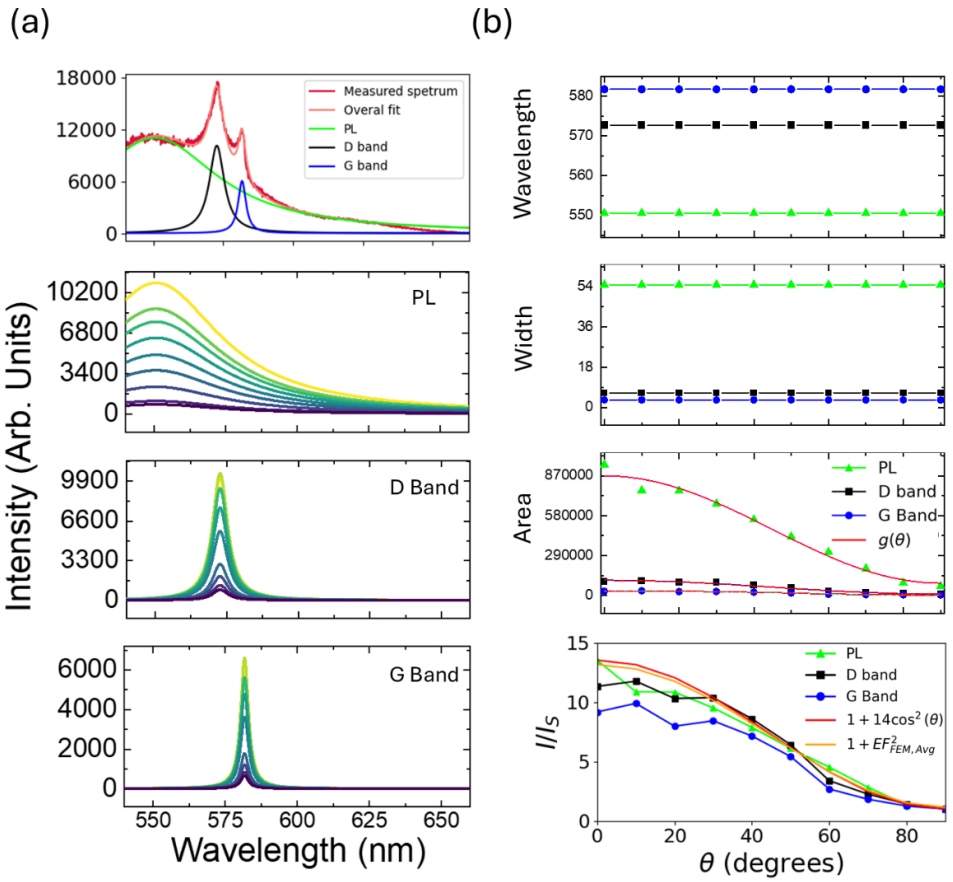

Figure 3. (a) Lorentzian decomposition extracted from the SERS spectra plotted in Fig. 2(c) for different polarisation angles. The top panel shows the decomposition and overall fit to experimental data for *p*-polarisation ($\theta = 0$). (b) Peak parameters of the extracted Lorentzian functions of Part (a). The bottom two panels show the integrated intensity and the integrated intensity relative to *s*-polarisation ($\theta = 90^{o}$) of the peaks in panel (a) against polarisation angle (θ). The integrated intensities follow Malus's law with an offset, $g(\theta) = A\cos^2\theta + B$. The bottom panel of Part (b) also includes FEM simulation results in the form of the normalised squared mean field enhancement factor, $EF^2_{FEM,Avg}$ (*cf.* Fig. 2(a)).

The third panel of Fig. 3(b) reveals that the integrated PL, D- and G-band intensities, taken as the area under each Lorentzian, increase as the incident polarisation becomes aligned with *p*-polarisation. The integrated intensities vary as a function of polarisation angle similarly to Malus's law for the intensity of linearly polarised light passing through a polariser [28]. Functions of the form $g(\theta) = A\cos^2\theta + B$ fit the integrated intensities with good agreement for the PL-band ($g(\theta) = 7.8 \times$

$10^5 \cos^2\theta + 9 \times 10^4$), D-band ($g(\theta) = 1 \times 10^5 \cos^2\theta + 1 \times 10^4$), and G-band ($g(\theta) = 2.9 \times 10^4 \cos^2\theta + 2.6 \times 10^3$). The offset (B) in these expressions captures the weak intensity in the *s*-polarised case.

Fig. 3(b) bottom panel shows the integrated intensity of the three peaks normalised to their respective values in the *s*-polarisation case against polarisation angle. Malus's law scaled to the maximum experimental value with an offset is also plotted for comparison (red curve). The computed distribution of the field enhancement factor shown in Fig. 2(a) was sampled 3 nm above the silver surface and averaged over 15 points spanning the unit cell for each polarisation angle, then normalized to the *s*-polarisation case, squared, and scaled to match the maximum experimental PL value, yielding the yellow curve which is nearly identical to the offset Malus law (red curve). All of the measurement curves are observed to collapse approximately to this trend, which further corroborates our interpretation that the excitation of SPPs increases the strength of the SERS spectra including the PL, due to the more efficient excitation of the carbon dots on the surface.

The localized enhanced electromagnetic fields of SPPs increase the absorption cross-section of emitters as follows [8]:

$$\sigma(x, y) = |EF(x, y)|^2 \sigma_0 \tag{1}$$

with $\sigma(x, y)$ and σ_0 being the emitter's absorption cross-section within the SPP electromagnetic fields, and in free space, respectively, and $EF(x, y)$ being the electric field enhancement factor of the SPP as a function of position (e.g., Fig. 2(a)). This relationship is corroborated by the results presented in Figs. 2(c) and 3. A *p*-polarised beam illuminating the structure on resonance excites SPPs most effectively, leading to stronger localized fields, greater field enhancement factor, more efficient pumping of the carbon dots, and consequently brighter emitted spectra.

4. Carbon Dot Photoluminescence Mediated by Surface Plasmons

4.1 Photoluminescence Lifetime - Theory and Modelling

Once excited, the carbon dots emit into an electromagnetic environment that includes SPPs on the grating, or more generally that is described by the LDOS on and near the grating. The SPPs on the grating increase the LDOS which opens a quick radiative channel that competes better against nonradiative ones [7]. Following Eq. 1 and the reciprocity theorem [29], it has been shown that the radiative decay rate of emitters coupled to SPPs (γ_r) increases proportionally with the square of the field enhancement factor (EF) with respect to the unperturbed (*e.g.*, free space) emitter decay rate (γ_r^0) [30]:

$$\gamma_r = |EF|^2 \gamma_r^0 \tag{2}$$

As a result, the quantum yield (η) of such emitters depends on both their intrinsic and engineered radiative and nonradiative decay rates [5]:

$$\eta = \frac{\gamma_r}{\gamma_r + \gamma_{nr}^0 + \gamma_{LSW} + \gamma_{abs}} \tag{3}$$

where γ_r is the total radiative decay rate of the emitter in its environment (near the grating in this case) and is related to the emitter's intrinsic radiative decay rate by the field enhancement factor following

Eq. 2. γ_{nr}^{0}, γ_{LSW}, and γ_{abs} are the intrinsic nonradiative decay rate of the emitter, the dissipation rate into lossy and nonradiative electromagnetic modes that may be present on the structure surface (*e.g.*, dark SPP resonant modes), and the absorption rate into the environment and the metal, respectively. The denominator in Eq. 3 is the total decay rate (γ) of the grating and emitter system:

$$\gamma = \gamma_{\mathrm{r}} + \gamma_{\mathrm{nr}}^{0} + \gamma_{\mathrm{LSW}} + \gamma_{\mathrm{abs}} \tag{4}$$

and

$$\tau = 1/\gamma \tag{5}$$

is the lifetime of the species in this system.

Figure 4 shows numerical FDTD results for the total decay rate (Eq. (4)) of a single point electric dipole with $\eta_0 = 1$, oscillating at different wavelengths, placed $3\ \mathrm{nm}$ above a 3D finite grating structure of 9 periods and $2\ \mu\mathrm{m}$ ridge length (along the y axis), normalized to the total decay rate of the dipole in free space (far from the grating). This normalized total decay rate is calculated by dividing the power dissipated by the dipole into the simulation environment, by the power radiated by the dipole in free space (far from the structure) [31] [32] [33]. The normalised decay rate is also termed the Purcell factor. The simulation volume is surrounded by perfectly matched layers to avoid unwanted field reflections from the walls terminating the calculation volume. In each numerical calculation, a single dipole oscillating along the x, y, or z axes is placed at one of the locations identified by the orange balls in Fig. 4(a) and the table inset into Fig. 4(a). The locations are chosen to sample the entire central unit cell of the grating while maintaining the required computational resources at a reasonable level. The average decay rate of emitters close to the grating structure is then found by averaging over the decay rates of all dipole orientations at positions sampling the entire central unit cell. Locations highlighted by red dashed contours around the orange balls are mirrored locations corresponding to positions 2 to 6, and produce the same decay rate as their mirrored counterparts. Thus, an independent calculation was not performed for these locations, but their response was included in the decay rate averaging. This approach purports to model an ensemble of dipoles oriented randomly and located randomly over the grating surface. Further details on these computations and validation of our approach using the FDTD can be found in Section S.1 of the Supplementary Materials.

The calculated average decay rate of dipoles near a plane silver surface is also included for comparison, taken as the average over 3 simulations of single dipoles oscillating along the x, y, or z axes, but not over position given the uniformity of the structure in the x-y plane. It can be seen from Fig. 4(b) that the average decay rate of emitters close to the plane silver surface is similar to the average decay rate close to the grating structure - this is expected because the grating is shallow so the SPPs thereon are similar to those on the plane silver surface. In both systems the decay rate increases as the wavelength decreases because SPPs become increasingly enhanced and localised to the interface. Thus dipoles couple as efficiently to SPPs on a shallow metal grating as they do on a plane metal surface. However, importantly, the grating has diffraction orders that provide efficient outcoupling of SPPs to free space emission, as will be discussed further below.

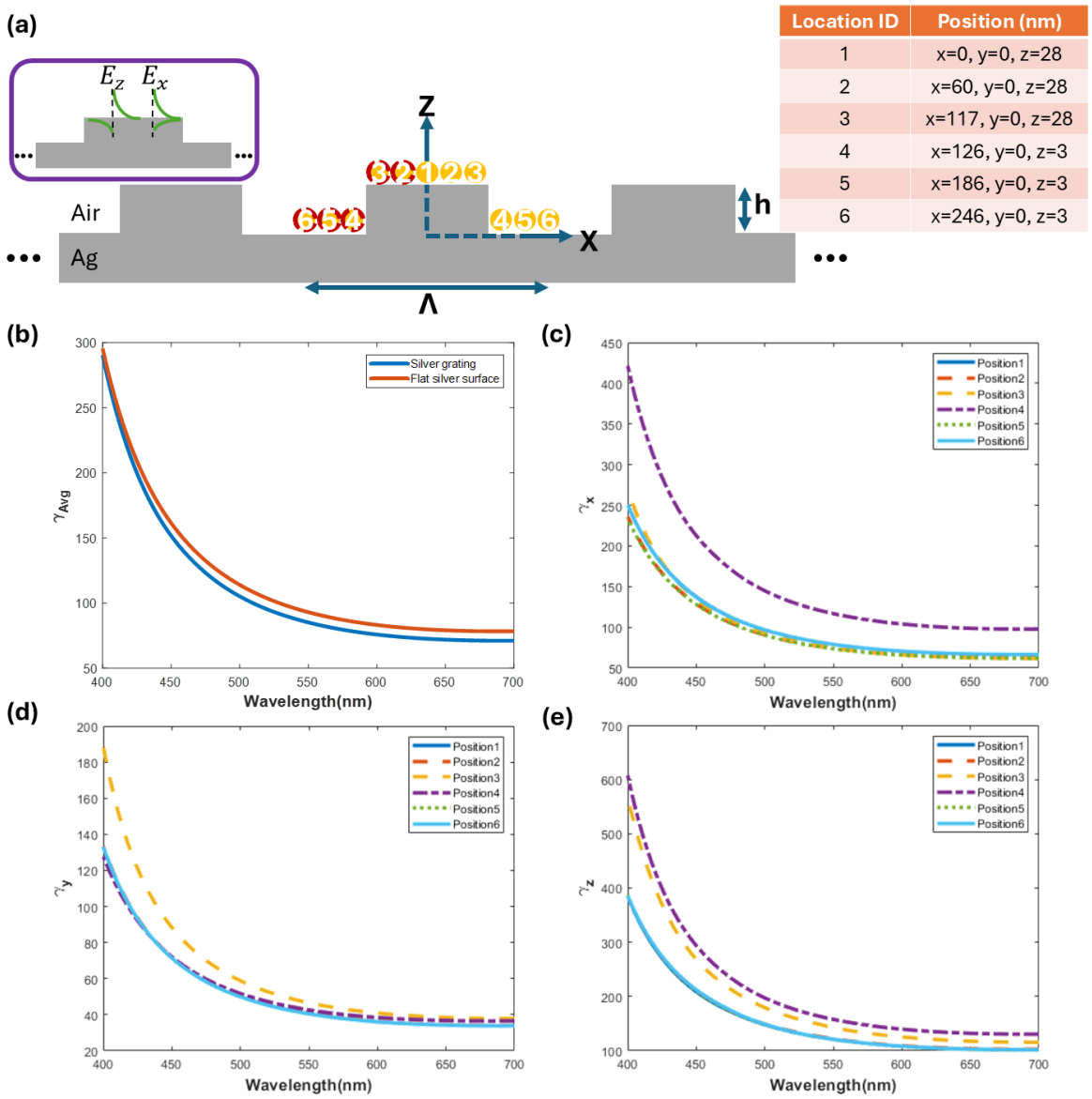

Location ID	Position (nm)
1	x=0, y=0, z=28
2	x=60, y=0, z=28
3	x=117, y=0, z=28
4	x=126, y=0, z=3
5	x=186, y=0, z=3
6	x=246, y=0, z=3

Figure 4. (a) Cross-sectional schematic of a silver grating of pitch Λ = 500 nm, ridge height h = 25 nm, and extension along y of 2 μm, bearing dipoles, as modelled using the 3D FDTD method. The numbered orange balls identify the locations of point electric dipoles which may be polarised along the x, y or z directions (the red dashed contours are locations mirrored relative to the z axis). All dipoles were placed 3 nm above the metal surface. The inset on the left sketches the SPP mode fields for propagation along the x axis. (b) Normalized decay rate averaged over all positions considered and over three dipole orientations (x, y, z), for the grating sketched in Part (a). Averaging for the case of the flat silver surface was taken only over dipole orientation given the uniformity of the structure in the x-y plane. (c)-(e) Decay rate for dipoles located near the grating at positions 1 through 6, and oriented along the x, y and z directions, respectively.

The dipole oscillating along the z axis has the highest decay rate, as observed by comparing Figs. 4(c)-4(e). The SPP mode is transverse magnetic (TM) (*p*-polarised), with its main component of electric field normal to the metal/dielectric interface (E_z). This causes the dipole oscillating along the z orientation (normal to the surface) to couple most efficiently to the SPP, resulting in a higher decay rate. SPPs excited by z-oriented dipoles are launched isotopically (in all directions) in the x-y plane of a shallow grating.

The SPP also possesses a longitudinal electric field (parallel to the propagation direction), which is generally in the x-y plane. For example, SPPs that propagate in the x direction (perpendicular to the grating ridges) have an E_x field component, as sketched in left inset to Fig. 4(a), and SPPs that propagate in the y-direction (parallel to the grating ridges) have an E_y field component. Thus dipoles that oscillate in the x or y directions also couple to SPPs, launching them in these specific directions. These dipole orientations exhibit a lower decay rate compared to z-oriented dipoles (γ_x, $\gamma_y < \gamma_z$), as observed by comparing Figs. 4(c) and 4(d) with Fig. 4(e), because the longitudinal field component of a SPP mode is weaker than the perpendicular one. The dipoles oscillating in other directions, *e.g.*, at a 45 degree angle with respect to the x axis, are not considered in our simulations because all other in-plane propagating modes can be decomposed into two orthogonally propagating modes along the x and y axes, and their effect is included by averaging.

Among all dipole positions considered, positions 3 and 4 correspond to locations where the dipole is near corners where SPP fields are more enhanced relative to other locations (*cf*. Fig. 2(a)). As a result, the decay rate at these two locations are usually higher than at other locations. To prevent the sharpness of grating structure edges affecting our results, the dipoles considered at these locations are placed at a lateral distance of three and six nanometers from the edges respectively. Also, since the perpendicular component of electric field to the metal/dielectric interface rotates in these two locations (to stay normal to the grating ridge walls), γ_x at location 4 and γ_y at location 3 become larger than other cases.

Equation 3 gives the quantum yield of an emitter into SPPs supported by the grating, but it does not include efficiency terms for diffraction into various orders, which could be calculated to assess the efficiency of a particular channel. Nonetheless, emission into free space due to outcoupling of SPPs by the grating can be detected, and measuring the lifetime of the emitted intensity can provide insight on the emission channels of the carbon dots formed on the grating.

4.1 Photoluminescence Lifetime - Measurements

If the sample incorporates a single type of carbon dot with uniform excitation and decay timing properties, the excited state population at each moment "t" after an excitation pulse, depends on the initial population of excited species, which results in a single exponential intensity decay against time [7]:

$$\mathrm{I}(\mathrm{t}) = \mathrm{I}_0 \exp\left(-\frac{\mathrm{t}}{\tau}\right) \tag{6}$$

where I_0 is the intensity at time 0 and τ is the lifetime of the emitters following Eq. (5). When using the time correlated single photon counting (TCSPC) method, the measured decay curve of the emission, R(t), is a convolution of the sample and measurement system time responses:

$$\mathrm{R}(\mathrm{t}) = \mathrm{P}(\mathrm{t}) \otimes \mathrm{I}(\mathrm{t}) \tag{7}$$

where $\mathrm{I}(\mathrm{t})$ is the sample response time and $\mathrm{P}(\mathrm{t})$ is the impulse or instrument response function (IRF) of the TCSPC measurement system. The latter is a convolution of the temporal response of all components involved in the measurement method such as the laser pulse, detector diffusion and transit time spread (TTS), electronic jitter, and dispersion in the optical components [67]. Convolution is required in Eq. (7) because the excitation pulse and the detector's response are not

immediate, and both have some temporal duration or reaction time. As a result, to extract the decay curve of emitters, I(t), one needs to deconvolve the impulse respone function of the system from the measured histogram or decay curve. Such calculations are most critical for lifetime values comparable to or shorter than the IRF temporal width, and result in a more accurate decay curve including only the response of emitters. The slope of the decay curve plotted on a semilog scale, can be used to extract the lifetime of sample with minimal errors.

The optical setup used to measure the emitter lifetime is shown in Fig. 5(a). It uses a supercontinuum source (NKT SuperK Extreme) as the pump, with a tunable acousto-optic filter and a bandpass (line) filter of central wavlength $\lambda = 532\ \mathrm{nm}$, to deliver a ~75 ps pulsed beam of repetition rate of ~78 MHz to the sample placed inside the gas chamber containing N_2 or CO_2 at a pressure of ~1.95 atm. The beam is expanded to fill the aperture of the focusing objective for the best focusing resolution. The emission collected from the sample using the same objective is redirected to the collection arm by a dichroic mirror (Thorlabs DMLP550R). The pump signal reflected by the sample is attenuated by the dichroic mirror and two narrow bandstop (notch) filters each of OD 6 at $\lambda = 532\ \mathrm{nm}$ (for a total OD of 12) placed in the collection path. The collected emission is either coupled to a multimode fiber which is redirected to a spectrograph and an emICCD camera to measure the emission spectrum (as in Fig. 1(a)), or is focused into a single photon avalanche diode (SPAD) (MPD PDM series) connected to a TCSPC board (PicoQuant TimeHarp 260) to measure the emission lifetime. To measure the emission lifetime at $\lambda = 633\ \mathrm{nm}$ a bandpass line filter is added in the collection arm right before the notch filters to only pass the emission component at $\lambda = 633\ \mathrm{nm}$.

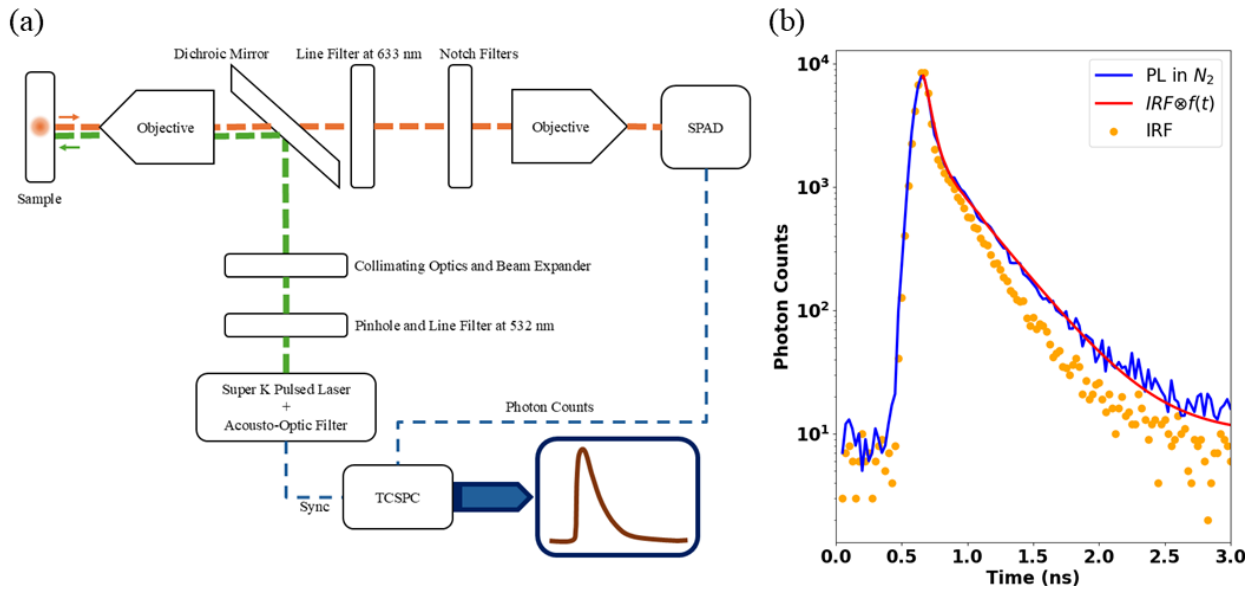

Figure 5. (a) Optical setup for the emission lifetime measurement of carbon dots on a silver grating. (b) IRF measured for setup of Part (a) (orange dots) on a silver surface, and lifetime measurement of the emission intensity emanating from a grating in N_2 (blue curve). A theoretical fit extracting an exponential function of the form $f(t) = Ae^{-t/\tau} + Be^{-t/\tau_{SPAD}} + C$ is also plotted (red curve), where τ and τ_{SPAD} are the lifetime of the emitters and the decay time of carrier diffusion in the SPAD, respectively.

To measure the IRF, a sample of zero lifetime consisting of a bare silver surface near a grating of interest (Fg. 5(b)), or a bare silicon surface (Fig. 6(a)), was placed in the set-up and the lifetime measured. The only difference in the set-up between the IRF measurement and the lifetime measurement of a sample is exchanging the samples in the chamber and replacing neutral density (ND) filters with the notch filters to block the pump. The decay curves measured as the setup IRF are shown in Figs. 5(b) and 6(a), and posses a Gaussian peak of temporal width ~100 ps followed by an exponential tail with time delay of ~330 ps due to carrier diffusion in the SPAD [34] [35]. The measurements in Fig. 5(b) were obtained using a multimode fiber to redirect the emission into the SPAD, while in Fig. 6 all of the curves were collected by free space coupling the eimission into the SPAD to avoid pulse dispersion in the multimode fiber. These IRF functions are taken as the time-discretised form of P(t) in Eq. (7).

Figure 5(b) shows the measured emission decay curve (blue) collected from a silver grating in ~1.95 atm N_2, prepared as discussed in Sub-section 2. This measured decay curve is taken as the time-discretised form of R(t) in Eq. (7). We cannot use the single exponential I(t) (Eq. (6)) to model the decay of the species because the latter combines with the decay of diffused carriers in the SPAD. Instead we adopt a sum of exponentials of the form $f(t) = Ae^{-t/\tau} + Be^{-t/\tau_{SPAD}} + C$ where τ and τ_{SPAD} represent the lifetime of the carbon dots (Eq. (5)) and the SPAD diffusion tail respectively. $f(t)$ is then time discretised and used in the discretised form of Eq. (7), treating A, B, C, τ and τ_{SPAD} as fitting parameters. The resulting curve is plotted in Fig. 5(b) (red). The corresponding fitting parameters are reported in Table 1 along with the reduced Poisson weighted χ^2 representing the goodness of fit.

Figure 6(a) shows the measured IRF, and Figs. 6(b)-6(d) the PL decay of the two gratings reported in Fig. 1(b) in ~1.95 atm CO_2 and N_2, collected during the same experimental run but after 30 minutes of CW beam exposure to grow and stabilise the PL spectra (*cf*. Fig. 1). The PL in these cases were directly focused onto the SPAD in a free-space arrangement to achieve the fastest IRF possible, resulting in our highest fidelity lifetime measurements. The curves $f(t)$ fitted to measurements follow the same form as in Fig. 5(b), and the fitting parameters with χ^2 are reported in table 1 for each case.

The fitting results compiled in Table 1 show lifetimes of $\tau = 30 - 40$ ps for carbon dots on silver gratings in different gases (holding the decay time for carrier diffusion in the SPAD constant at $\tau_{SPAD} = 330$ ps in all cases). These lifetimes are shorter than the temporal width of the IRF (~ 100 ps) and confirm the need for deconvolution of the IRF from experimental decay curves to achieve accurate results (*cf*. Eq. (7)). Our lifetimes for carbon dots on a silver grating are much smaller than the reported lifetimes for carbon dots in a dielectric volume which are in the range of 3 to 20 ns [36] [37], supporting the large Purcell factors predicted in Fig. 4, particularly the averaged value in Fig. 4(b) of $\gamma_{Avg} \sim 80$ at $\lambda \sim 600$ nm. Taking $\tau = 30 - 40$ ps as the lifetime of our carbon dots on the silver grating, with $\gamma_{Avg} = 80$ yields $\tau_0 \sim 2 - 3$ ns for the lifetime of the dots in free space.

These results were corroborated via reference measurements using R6G dye as described in Section S.2 of the Supplementary Materials. Briefly, the lifetimes of R6G in solution and as a dried layer on a silver surface were measured, yielding a Purcell factor of about 70, in good agreement with the predicted value in Fig. 4(b) of $\gamma_{Avg} \sim 80$ at $\lambda \sim 600$ nm for a flat silver surface.

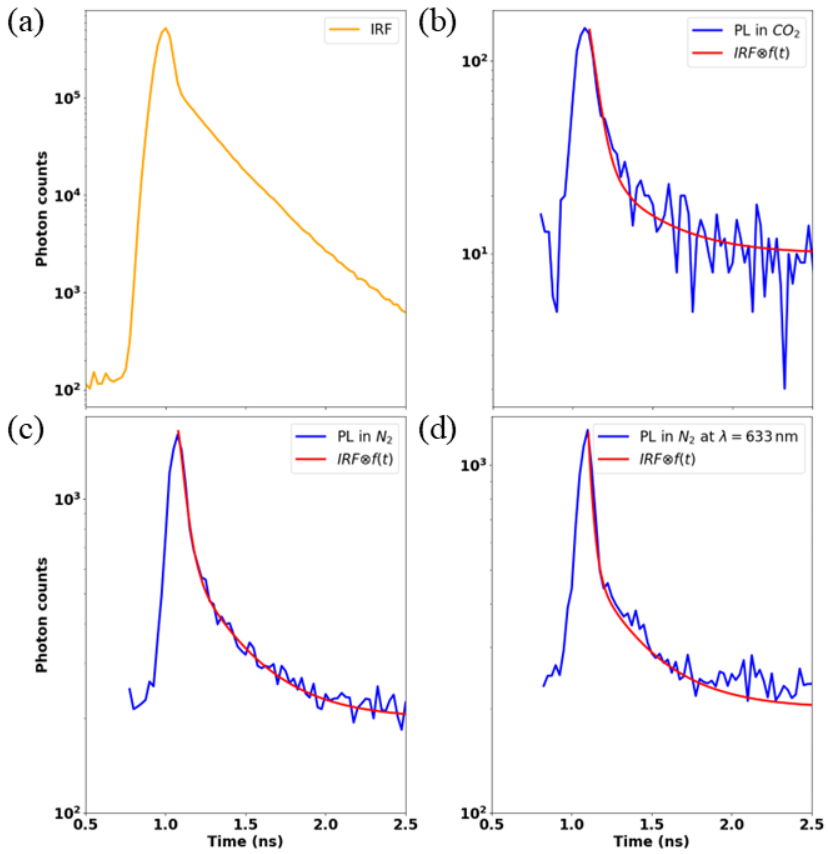

Figure 6. (a) IRF measured on a Si surface. Emission decay curves (blue) of the gratings characterised in Fig. 1(b) in: (b) CO_2, (c) N_2, and (d) N_2 through a line filter centered at $\lambda = 633$ nm. Theoretical fits extracting an exponential function of the form $f(t) = Ae^{-t/\tau} + Be^{-t/\tau_{SPAD}} + C$ are also plotted (red curves), where τ and τ_{SPAD} are the lifetime of the emitters and the decay time of carrier diffusion in the SPAD, respectively.

Table 1. Fitting parameters of the function $f(t) = Ae^{-t/\tau} + Be^{-t/\tau_{SPAD}} + C$ extracted from the lifetime measurements of Figs. 5(b) and 6. The lifetime of the carbon dots on silver gratings in different gas environments is τ. The reduced Poisson weighted χ^2 values are also listed as goodness of fits.

Experiment	A	B	C	τ_{SPAD} (ps)	τ (ps)	χ^2
Grating 1 in N_2 (Fig. 5(b))	4×10^{13}	1.4×10^4	10	330	30	1.635
Grating 2 in CO_2 (Fig. 6(b))	9×10^{13}	5×10^2	10	330	40	1.933
Grating 3 in N_2 (Fig. 6(c))	2.5×10^{16}	1.2×10^4	200	330	35	1.890
Grating 3 in N_2, emission at λ=633 nm, (Fig. 6(d))	2.5×10^{18}	8×10^4	200	330	30	1.389
Dried dye coated on a silver surface (Supplementary Materials, Fig. S3)	6.9×10^{19}	3.8×10^5	500	330	30	1.969
1 ppm R6G solution in Ethanol (Supplementary Materials, Fig. S3)	9.9×10^3	-	10	-	3960	-

4.3 Photoluminescence Radiation Patterns

The main difference between the behavior of emitters close to a plane surface *vs*. a grating is that the latter produces far field radiated fields, whereas the former in the ideal case does not (roughness could weakly outcouple SPPs into normally isotropic radiation). The SPPs excited on the grating by

the emitters are efficiently outcoupled into various free-space diffraction orders following energy and momentum conservation with the grating compensating for any momentum mismatch between the SPPs and the radiated orders.

The momentum conservation equation relating the SPPs propagating on the grating in the x-direction to the diffraction orders is written:

$$\frac{\omega}{c_0}\sin\theta \pm N\frac{2\pi}{\Lambda} = \pm k_{SPP} = \pm\frac{\omega}{c_0}\sqrt{\frac{\varepsilon_d\varepsilon_m}{\varepsilon_d+\varepsilon_m}} \tag{8}$$

where Λ is the grating pitch, N is the grating order, and θ and ω are the emission beam angle and frequency respectively. k_{SPP} is the surface plasmon wavenumber in the x-direction on the grating, and ε_d and ε_m are the relative permittivity of air and silver, respectively.

Figure 7(a) shows near-field plots of the magnitude of the total electric field ($|E_t|$) excited by a single dipole oscillating at $\lambda = 560$ nm and above the center of the grating structure (position 1), for the 3 dipole orientations. The colour bars in these cases are saturated in order to better render the near and radiated fields. Fig. 7(b) shows the corresponding radiated far field squared magnitude ($|E_t|^2$). The far fields were computed by projecting middle fields on the x-y plane at a distance of 10 μm from the grating to a far field sphere of radius of one meter centered at the grating surface [38]. The far field plots are normalized to the maximum magnitude of the electric field produced at the same distance by a dipole oscillating in free space, and thus represent intensity enhancement or directivity.

As discussed earlier, it can be observed from these plots that the dipole oscillating normal to the surface (z-orientation), excites the SPP modes more strongly and as a result can couple into free space emission channels more strongly as observed from the bottom panels of Fig. 7. On the other hand, the dipole oscillating parallel to the grating ridges (y-orientation) produces weaker coupling to SPP modes (*cf*. Fig. 4(d)) and the weakest radiation, because the SPPs propagate along the y-direction and are not outcoupled efficiently by the grating, as observed from the middle panels of Fig. 7.

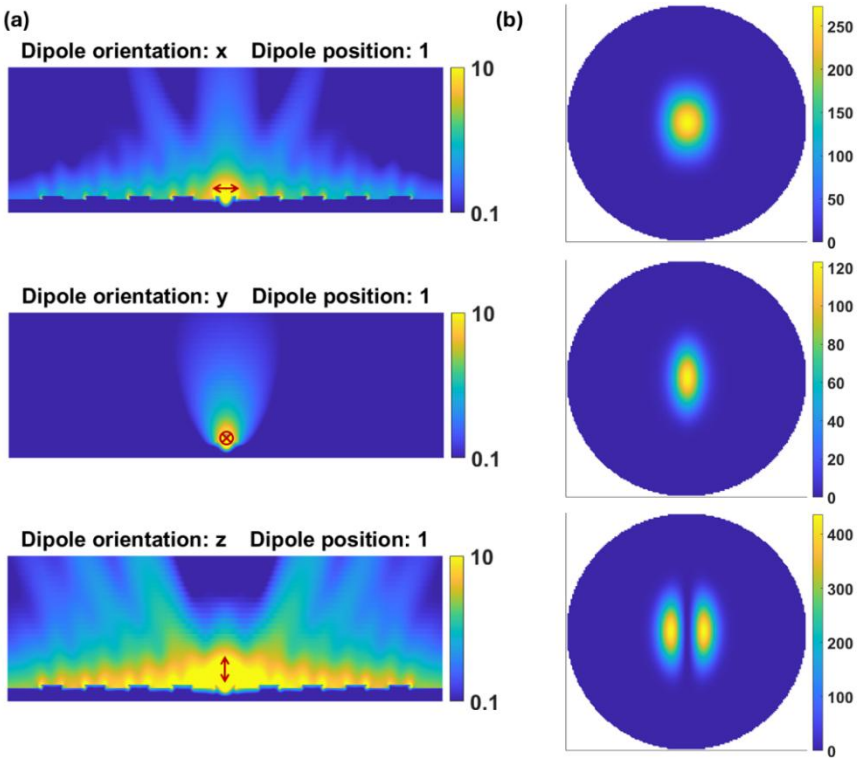

Figure 7. FDTD Simulations of a single electric dipole exciting a finite silver grating. (a) Near field plots of the magnitude of the total electric field $|E_t|$ for different dipole orientations placed at position 1 (*cf*. Fig. 3 (a)). The color bar is in arbitrary units and saturated to better render the field distribution. (b) corresponding far field plots of $|E_t|^2$ normalized to the maximum squared magnitude of the far field radiated at the same location by an identical dipole oscillating in free space. The far field plots are produced from the fields at an x-y plane 10 μm above the grating and projected on a 1-meter radius sphere centered at the grating surface.

The far field plot for the dipole oscillating normal to the surface (z-orientation), shows a central null with two lobes, as observed in Fig. 7(b), bottom panel. Recall that this dipole orientation launches SPPs propagating in phase and isotopically in the x-y plane from the point of origin. The two emission lobes appear at specific angles in the z-x plane relative to normal, determined by the first diffraction orders of the grating at the dipole wavelength. Substituting N = ±1 in Eq. (8) yields emission angles of $\theta \cong \pm 6°$, which agree very well with the angles observed in the FDTD simulations of Fig. 7, bottom panels. There is no emission in the normal direction because SPPs are in phase at the location of the dipole.

The field plots for the dipole oscillating in the x-orientation reveal emission also along the first diffraction orders at the same angles, but additionally along the grating normal, as observed in Fig. 7 top panels. These emission directions satisfy Eq. (8) with N = ±1. In this case normal emission is possible because an x-oriented dipole launches SPPs in the ±x directions that are of opposite phase (as for grating in-coupling at normal incidence, *cf*. Figs. 2(a) and 2(b)).

Fig. 8(a) shows a microscope image captured by a visible camera of a grating in N_2 luminescing after 30 minutes of CW laser pumping (image captured by a commercial Raman microscope). Figs. 8(b) and 8(c) show images of two different gratings, luminescing after 30 minutes of CW pump exposure in N_2 captured using a CMOS visible color microscope camera (UCMOS03100KPA) in the set-up of

Fig. 1(a). These images corroborate the modelling of Fig. 7 in that the aggregate emission is primarily directed normal to the grating and into the first order diffraction lobes.

Fig. 8(d) gives the polarisation dependence of the PL emission captured in Fig. 8(c), measured using the set-up of Fig. 1(a), but with a film polariser added before the PL emission is coupled to the multimode fiber and the spectrometer. Counts are summed over the entire emission spectrum for each angle of the polariser, then normalized to the case where the polariser transmission axis is aligned to pass *s*-polarised light relative to the grating. Fig. 8(d) also plots the simulated intensity as a function of its polarisation. This result was obtained from the electric far field generated by dipoles placed at the locations illustrated in Fig. 4(a), and oscillating along the 3 axes (x, y, z). The vectorial far field produced by each dipole source was passed numerically through a polariser aligned at a specific angle relative to the grating, and summed vectorially for each dipole to obtain the total vectorial electric far field and the associated intensity. This calculation was repeated for each angle of the polariser, and the results normalised to the *s*-polarised case. A good agreement between measured and simulated results with theoretical Malus's law is obtained, as observed from Fig. 8(d). The polarisation extinction ratio of the emitted PL is directly observed to be approximately 3:1 (5 dB).

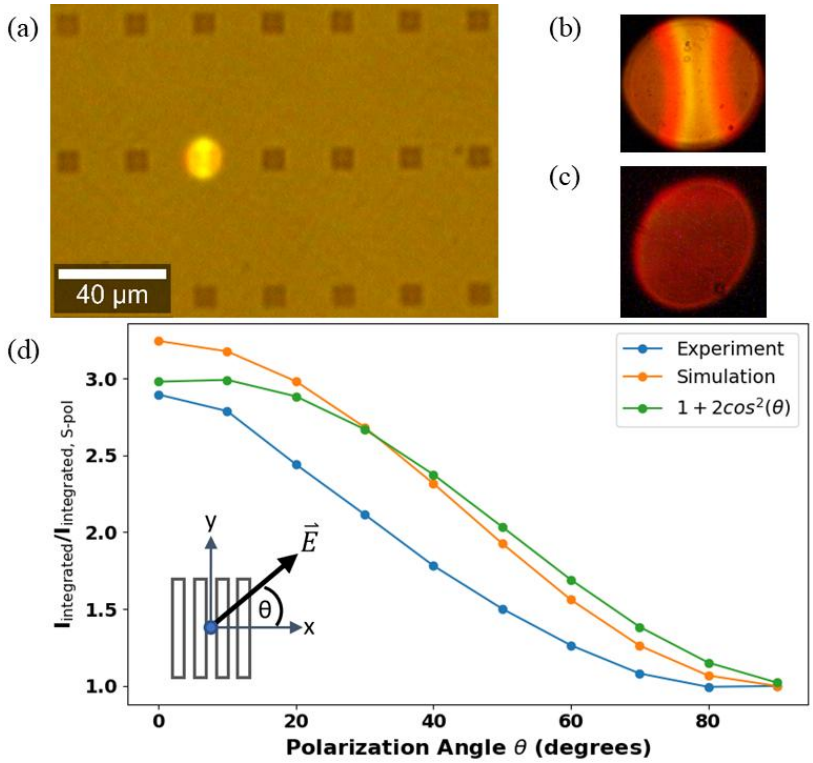

Figure 8. (a)-(c) Visible camera image of a luminescing grating in N_2 collected with (a) commercial Raman microscope (Witec a300), and (b), (c) via the inspection arm of setup of Fig. 1(a). (d) Polarisation of the PL emission from experimental measurements and simulation compared with Malus's law. The polarisation angle of the PL is relative to the grating ridges, as defined in inset, *i.e.*, $\theta = 0°$ implies *p*-polarised PL, whereas $\theta = 90°$ implies *s*-polarised PL).

The results in Figs. 7 and 8 show that a set of randomly aligned and positioned incoherent emitters (carbon dots in this case) on a plasmonic metal grating produces light in the far field that exhibits

characteristics of coherence such as directional emission in prescribed directions at specific wavelengths and with a specific polarisation, as was previously shown for thermal emission [17].

5. Conclusions

In this work, we have demonstrated both experimentally and theoretically how plasmonic gratings significantly influence the formation and emission characteristics of nearby emitters. Incoherent, randomly positioned and randomly aligned carbon dots, created *in situ* on a silver grating, are shown to produce polarised photoluminescence in prescribed directions and at specific wavelengths, which are properties normally associated with coherent light sources. Specifically, photoluminescence emerges preferentially along the grating normal and in the ± 1 diffraction directions, at wavelengths in the range of 560 to 700 nm (depending on the sample) when pumped at 532 nm, and with a *p*-polarisation exhibiting a 3:1 polarisation extinction ratio. These coherence properties emerge because the emitters preferentially decay onto SPPs supported by the grating, which then diffract from the grating with coherent characteristics. The photoluminescence lifetime of the carbon dots on gratings was measured to be in the range of 30 to 40 ps, which is about 80$\times$ shorter than the lifetime of carbon dots in free space. This is attributed to enhanced spontaneous emission into SPPs, for which a Purcell factor of about 80 is deduced. Our modeling shows strong agreement with experimental results, confirming the critical role of SPPs on a grating in shaping emission dynamics. These findings provide a deeper understanding of interactions between incoherent emitters and SPP modes, particularly carbon dots on silver gratings. The ability to localise and form carbon dots *in situ* on nanostructured surfaces, and then control their emission characteristics, opens new possibilities for biosensing, inexpensive light sources, and quantum optics.

Acknowledgements

Financial support provided by the Natural Sciences and Engineering Research Council of Canada, and the Canada Research Chairs program is gratefully acknowledged.

References

[1] E. Purcell, "Spontaneous emission probabilities at radio frequencies," *Physical Review,* vol. 69, no. 11-1, pp. 681-681, 1946.

[2] W. Barnes, "Fluorescence near interfaces: the role of photonic mode density," *Journal of Modern Optics,* vol. 45, no. 4, pp. 661-699, 1998.

[3] E. Fermi, "Quantum theory of radiation. , 4(1), p.87.," *Reviews of Modern Physics,* vol. 4, no. 1, p. 87, 1932.

[4] K. Drexhage, "IV interaction of light with monomolecular dye layers," in *Progress in Optics*, vol. 12, Elsevier, 1974, pp. 163-232.

[5] G. Ford and W. Weber, "Electromagnetic interactions of molecules with metal surfaces," *Physics Reports,* vol. 113, no. 4, pp. 195-287, 1984.

[6] M. Bauch, K. Toma, M. Toma, Q. Zhang and J. Dostalek, "Plasmon-enhanced fluorescence biosensors: a review," *Plasmonics,* vol. 9, pp. 781-799, 2014.

[7] J. Lakowicz, Principles of fluorescence spectroscopy, 3rd ed., New York: Springer, 2006.

[8] J. Farahani, D. Pohl, H. Eisler and B. Hecht, "Single quantum dot coupled to a scanning optical antenna: a tunable superemitter," *Physical review letters,* vol. 95, no. 1, p. 017402, 2005.

[9] E. Bailly, J. Hugonin, J. Coudevylle, C. Dabard, S. Ithurria, B. Vest and J.-J. Greffet, "2D Silver-Nanoplatelets Metasurface for Bright Directional Photoluminescence, Designed with the Local Kirchhoff's Law," *ACS Nano,* vol. 18, no. 6, pp. 4903-4910, 2024.

[10] J. Dong, Z. Zhang, H. Zheng and M. Sun, "Recent progress on plasmon-enhanced fluorescence," *Nanophotonics,* vol. 4, no. 4, pp. 472-490, 2015.

[11] A. Vaskin, R. Kolkowski, A. Koenderink and I. Staude, "Light-emitting metasurfaces," *Nanophotonics,* vol. 8, no. 7, pp. 1151-1198, 2019.

[12] C. Galloway, P. Etchegoin and E. Le Ru, "Ultrafast nonradiative decay rates on metallic surfaces by comparing surface-enhanced Raman and fluorescence signals of single molecules," *Physical review letters,* vol. 103, no. 6, p. 063003., 2009.

[13] J. Khurgin, G. Sun and R. Soref, "Enhancement of luminescence efficiency using surface plasmon polaritons: figures of merit," *JOSA B,* vol. 24, no. 8, pp. 1968-1980, 2007.

[14] K. Tsakmakidis, R. Boyd, E. Yablonovitch and X. Zhang, "Large spontaneous-emission enhancements in metallic nanostructures: towards LEDs faster than lasers," *Optics Express,* vol. 24, no. 16, pp. 17916-17927, 2016.

[15] J.-J. Greffet, P. Bouchon, G. Brucoli and F. Marquier, "Light emission by nonequilibrium bodies: local Kirchhoff law," *Physical Review X,* vol. 8, no. 2, p. 021008, 2018.

[16] H. Monin, A. Loirette-Pelous, E. De Leo, A. Rossinelli, F. Prins, D. Norris, E. Bailly, J. Hugonin, B. Vest and J.-J. Greffet, "Controlling light emission by a thermalized ensemble of colloidal quantum dots with a metasurface," *Optics Express,* vol. 31, no. 3, pp. 4851-4861, 2023.

[17] J.-J. Greffet, R. Carminati, K. Joulain, J. Mulet, S. Mainguy and Y. Chen, "Coherent emission of light by thermal sources," *Nature,* vol. 416, no. 6876, pp. 61-64, 2002.

[18] A. Nicol and W. Knoll, "Characteristics of fluorescence emission excited by grating-coupled surface plasmons," *Plasmonics,* vol. 13, no. 6, pp. 2337-2343, 2018.

[19] W. Knoll, M. Philpott, J. Swalen and A. Girlando, "Emission of light from Ag metal gratings coated with dye monolayer assemblies," *The Journal of Chemical Physics,* vol. 75, no. 10, pp. 4795-4799, 1981.

[20] M. Kreiter, T. Neumann, S. Mittler, W. Knoll and J. Sambles, "Fluorescent dyes as a probe for the localized field of coupled surface plasmon-related resonances," *Physical Review B,* vol. 64, no. 7, p. 075406, 2001.

[21] S. Kitson, W. Barnes, J. Sambles and N. Cotter, "Excitation of molecular fluorescence via surface plasmon polaritons," *Journal of modern optics,* vol. 43, no. 3, pp. 573-582, 1996.

[22] P. Andrew and W. Barnes, "Molecular fluorescence above metallic gratings," *Physical Review B,* vol. 64, no. 12, p. 125405, 2001.

[23] F. Miomandre, J. Audibert, Q. Zhou, P. Audebert, P. Martin and J. Lacroix, "Electrochemically monitored fluorescence on plasmonic gratings: A first step toward smart displays with multiple inputs," *Electrochimica Acta,* vol. 110, pp. 56-62, 2013.

[24] Y. Chai, T. Li, M. Zhang, M. Liu, G. Yang, P. Karvinen, M. Kuittinen and G. Kang, "Brilliant quantum dots' photoluminescence from a dual-resonance plasmonic grating," *Optics Express,* vol. 32, no. 11, pp. 19950-19962, 2024.

[25] M. Angelini, E. Manobianco, P. Pellacani, F. Floris and F. Marabelli, "Fluorescence emission angular dependence on a nanostructured plasmonic grating," *Applied Research,* vol. 3, no. 5, p. e202300090, 2024.

[26] J. Walia, S. Rashid, G. Killaire, F. Variola, A. Weck and P. Berini, "Reconfigurable carbon quantum emitters from CO2 gas reduced via surface plasmons," *Optica,* vol. 8, no. 5, pp. 708-709, 2021.

[27] J. Walia, S. Rashid, M. Amiri Naeini, G. Killaire, F. Variola, A. Weck and P. Berini, "Surface plasmons on silver gratings transform pyrolytic carbon into luminescent graphitized carbon dots," *The Journal of Chemical Physics,* vol. 161, no. 14, 2024.

[28] E. Collett, "Field guide to polarization," Spie, Bellingham, WA, 2005.

[29] R. Carminati, M. Nieto-Vesperinas and J.-J. Greffet, "Reciprocity of evanescent electromagnetic waves," *JOSA A,* vol. 15, no. 3, pp. 706-712, 1998.

[30] Y. Wang, T. Yang, M. Tuominen and M. Achermann, "Radiative rate enhancements in ensembles of hybrid metal-semiconductor nanostructures," *Physical Review Letters,* vol. 102, no. 16, p. 163001, 2009.

[31] P. Bharadwaj, B. Deutsch and L. Novotny, "Optical antennas," *Advances in Optics and Photonics,* vol. 1, no. 3, pp. 438-483, 2009.

[32] F. Kaminski, V. Sandoghdar and M. Agio, "Finite-difference time-domain modeling of decay rates in the near field of metal nanostructures," *Journal of Computational and Theoretical nanoscience,* vol. 4, no. 3, pp. 635-643, 2007.

[33] L. Novotny and B. Hecht, Principles of Nano-Optics, Cambridge Univ., 2006.

[34] A. Tosi, A. Mora, F. Zappa, A. Gulinatti, D. Contini, A. Pifferi, L. Spinelli, A. Torricelli and R. Cubeddu, "Fast-gated single-photon counting technique widens dynamic range and speeds up acquisition time in time-resolved measurements.," *Optics express,* vol. 19, no. 11, pp. 10735-10746, 2011.

[35] X. Qian, W. Jiang, A. Elsharabasy and M. Deen, "Modeling for single-photon avalanche diodes: State-of-the-art and research challenges," *Sensors,* vol. 23, no. 7, p. 3412, 2023.

[36] K. Mintz, Y. Zhou and R. Leblanc, "Recent development of carbon quantum dots regarding their optical properties, photoluminescence mechanism, and core structure," *Nanoscale,* vol. 11, no. 11, pp. 4634-4652, 2019.

[37] A. Siddique, S. Hossain, A. Pramanick and M. Ray, "Excitation dependence and independence of photoluminescence in carbon dots and graphene quantum dots: insights into the mechanism of emission," *Nanoscale,* vol. 13, no. 39, pp. 16662-16671, 2021.

[38] A. Taflove and S. Hagness, Computational electromagnetics: the finite-difference time-domain method., Artech House, 2005.

Surface plasmon enhanced photoluminescence of carbon dots formed *in-situ* on silver gratings

Maryam Sadat Amiri Naeini[1,2], Jaspreet Walia[2,3], Luis-Angel Mayoral-Astorga[2], Hyung Woo Choi[2], Arnaud Weck[1,2,4], Pierre Berini[1,2,3]

[1]Department of Physics, University of Ottawa, Ottawa, Ontario, Canada
[2]Nexus for Quantum Technologies Institute, University of Ottawa, Ottawa, Ontario, Canada
[3]School of Electrical Engineering and Computer Science, University of Ottawa, Ottawa, Ontario, Canada
[4]Department of Mechanical Engineering, University of Ottawa, Ontario, Canada

S.1 Theory of luminescent emitters near metal surfaces

In the main text the lifetime of emitters close to a silver grating was studied. For such an investigation, it is educational to study emission near a metal surface. In a classical approach, emitters are considered as dipole oscillators, the spontaneous emission of which is back-reflected towards the emitters by the surface, driving them more strongly or weakly depending on the phase difference between the original emission and the reflected wave at the emitter's location [1] [2]. As a result, the influence of a metal layer on the emission properties depends on the distance (h) between the emitter and the surface.

At distances of the order of $\lambda_{\mathrm{emission}}$ or slightly larger, the emitter couples to photons that can also be reflected from the surface. As a result, the lifetime as a function of perpendicular distance from the surface ($\tau(h)$), possesses an oscillatory behavior due to constructive or destructive interference between emission and its reflection [2], as shown experimentally and theoretically [3] [4].

At distances larger than atomic dimensions (h > 5 nm) but smaller than $\lambda_{\mathrm{emission}}$, the emission is strongly coupled to the SPP modes supported by the metal, which then can be converted to free space photons by a grating coupler [2]. At very small distances, nonradiative decay channels into the metal, such as interband absorption (electron-hole pair generation), dipole-dipole interaction, and electron scattering, will dominate the process [2].

A theoretical model suggested in [4], considers the emitter as a point dipole and expands its field into a sum of plane waves of different wavevectors in the interface plane. By calculating the reflection coefficients for vertical and horizontal dipole orientations, and integrating over the reflected and original dipole fields, the spontaneous emission rate and dipole lifetime can be determined. Since the model uses the complex dielectric permittivity of the metal, it naturally includes the excitation of SPP modes at intermediate distances.

The normalized decay rate of a dipole located at a distance h from a metallic mirror is written [1] [5]:

$$\hat{\gamma}(\mathrm{h}) = \hat{\gamma}_{\mathrm{nr}}^{0} + \eta_0 \int_0^{\infty} \widehat{\mathrm{P}}(\mathrm{u},\mathrm{h})\mathrm{du} \qquad (\mathrm{S1})$$

where $\hat{\gamma}_{nr}^{0} = 1 - \eta_0$ and η_0 are the normalized nonradiative decay rate and quantum efficiency of the dipole respectively. $u = k_{\parallel}/k$ is the wavenumber in the plane of the metal, normalized to the far field wavenumber. $\hat{P}(u,h)$ is the power dissipation density of the dipole as a function of u and h, normalized to the far field dissipated power. $\hat{P}(u,h)$ is averaged over the power dissipation of all possible dipole orientations, resulting in an isotropic power dissipation:

$$\hat{P}(u,h) = \frac{2}{3}\hat{P}_{\parallel}(u,h) + \frac{1}{3}\hat{P}_{\perp}(u,h) \tag{S2}$$

The normalized power dissipation components for the perpendicular ($\hat{P}_{\perp}$) and parallel ($\hat{P}_{\parallel}$) dipole orientations can be calculated as:

$$\hat{P}_{\perp}(u,h) = \text{Real}\left\{\frac{3}{2}\frac{u^3}{\sqrt{1-u^2}}\left[1 + r_p e^{i2k_{\perp}h}\right]\right\}$$
$$\hat{P}_{\parallel}(u,h) = \text{Real}\left\{\frac{3}{4}\frac{u}{\sqrt{1-u^2}}\left[\left(1 + r_s e^{i2k_{\perp}h}\right) + (1-u^2)\left(1 - r_p e^{i2k_{\perp}h}\right)\right]\right\} \tag{S3}$$

where r_p and r_s are Fresnel reflection coefficients of the multilayer structure (which includes a layer of thickness h composed of dipole emitters) for waves polarized parallel (p) and perpendicular (s) to the interface, respectively. This model can be extended for a three-layer environment (two semi-infinite media with a layer of dipole emitters at their interface) with r_p and r_s modified to represent the Fresnel coefficient considering all layers.

So, the lifetime of an isotropically oriented dipole above a metal surface can be written as a function of distance from the surface:

$$\tau(h) = \hat{\gamma}(h)^{-1}\tau_0 \tag{S4}$$

with τ_0 being the intrinsic lifetime of the molecule.

Figure S1 shows results of calculations for a reference case consisting of R6G dye on a silver substrate in air. In solution, the dye has an emission peak at $\lambda_{emission} = 560\ \text{nm}$, a quantum efficiency of $\eta_0 = 0.9$ and an intrinsic lifetime of $\tau_0 = 3.9\ \text{ns}$ at a concentration of 5 mM [5]. The dye was modelled as a thin layer of permittivity $\varepsilon_r(\lambda_{emission}) = 1.8039$ in a three-layer model as discussed in relation to Eq. S3.

Three different regimes on Fig. S1(a) can be identified. For small values of wavenumber (u), the emitters couple increasingly to far-field radiation with separation. The sharp peak around u = 1.46 shows coupling to the SPP mode, which has a wavevector larger than that of free-space, and as a result, is bound to the surface. This coupling increases as the emitter approaches the surface. At smaller distances, a broad feature at very large wavenumbers appears in the dissipated power trend which grows as the separation decreases. This represents coupling to non-radiative decay channels caused by any loss mechanism available in the metal (referred to as lossy surface waves in [1]).

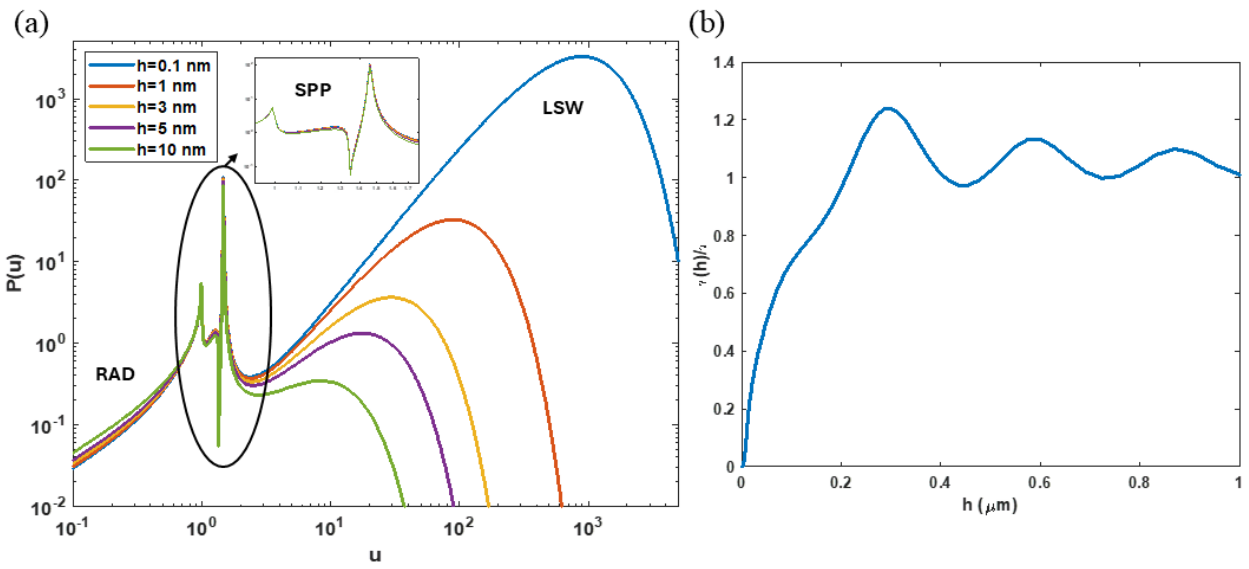

Figure 1 (a) Normalized power dissipation density *vs*. normalised wavenumber u for an isotropically oriented dipole near a silver surface at different distances. (b) Normalized lifetime of the same dipole as a function of distance from the surface.

Figure S1(b) shows the normalized lifetime of an isotropically oriented dipole in air and close to a silver surface. The lifetime of dipole reaches to small values and eventually zero, with nonradiative decay channels dominating, as the dipole gets close to metal surface. At intermediate distances below $\lambda_{\text{emission}} = 560$ nm, emission couples to SPP modes and enhancement in lifetime is observed compared to the dipole intrinsic lifetime. SPPs provide means for the emission to couple into free space channels through surface roughness. At distances of order of $\lambda_{\text{emission}} = 560$ nm and above, the lifetime shows an oscillatory behaviour with respect to the dipole distance from the surface as discussed and due to constructive or destructive interference between dipole emitted fields with the reflected fields from the surface.

To confirm the lifetime results calculated by the FDTD method in the main text, a comparison is made with the theoretical formulation. The quantum efficiency of the dipole source applied in the FDTD method is limited to a value of $\eta_0 = 1$. Figure S2 compares the FDTD simulations of the normalised lifetime of a dipole near a silver surface as a function of its distance, to the theoretical results computed for $\eta_0 = 0.9$ (Fig S2(a)) and for $\eta_0 = 1$ (Fig. S2(b)). In this case the silver surface was covered with a medium of refractive index n = 1.343. Good agreement is observed in both cases, confirming the accuracy of the FDTD method for quantum efficiencies of $\eta_0 = 0.9$ to $\eta_0 = 1$.

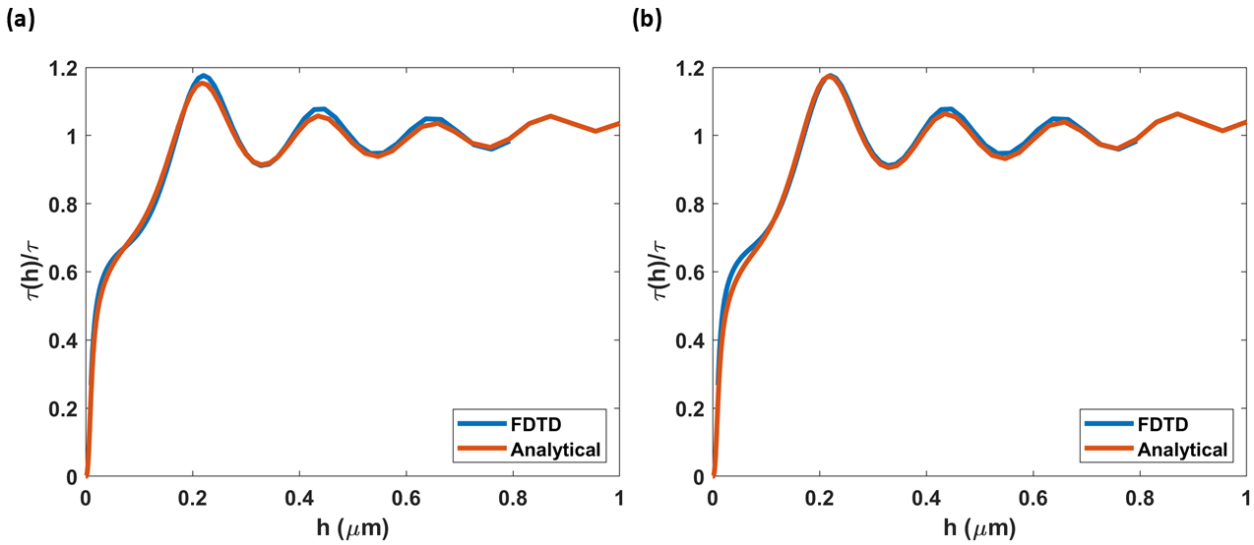

Figure S2. Normalized analytical lifetime (red curves) of isotropically oriented dipoles of quantum efficiency (a) η_0 = 0.9 and (b) η_0 = 1, in a medium of refractive index n = 1.343, as a function of height above a silver surface. The normalised lifetime computed under the same conditions using the FDTD method with η_0 = 1 is plotted on both graphs for comparison (blue curves).

S.2 Lifetime measurements of R6G dye

Figure S3(a) gives the measured emission spectra of R6G dye solved in ethanol at a 10^{-6} M concentration, and as a coating of dried solution on a silver surface. The spectrum of the dye in solution is as expected based on the manufacturer's data (Exciton, Rhodamine 590). The spectrum of the dried dye solution on the silver surface, captured under the same measurement conditions, is weaker and red-shifted. Weaker emission is not surprising because the dye is not efficiently pumped as a layer on a mirror (*cf*. Section 2 of the main text), and emission on the surface is preferentially into bound SPPs propagating thereon. The red-shifting of the spectrum is attributable to the dried layer of dye, which as an organic molecule, has a higher index of refraction than the ethanol used to form the solution. Emission therefore occurs in a higher index medium, leading to a change in the Stokes shift and thus the spectrum of emission based on the Lippert-Mataga equation [6].

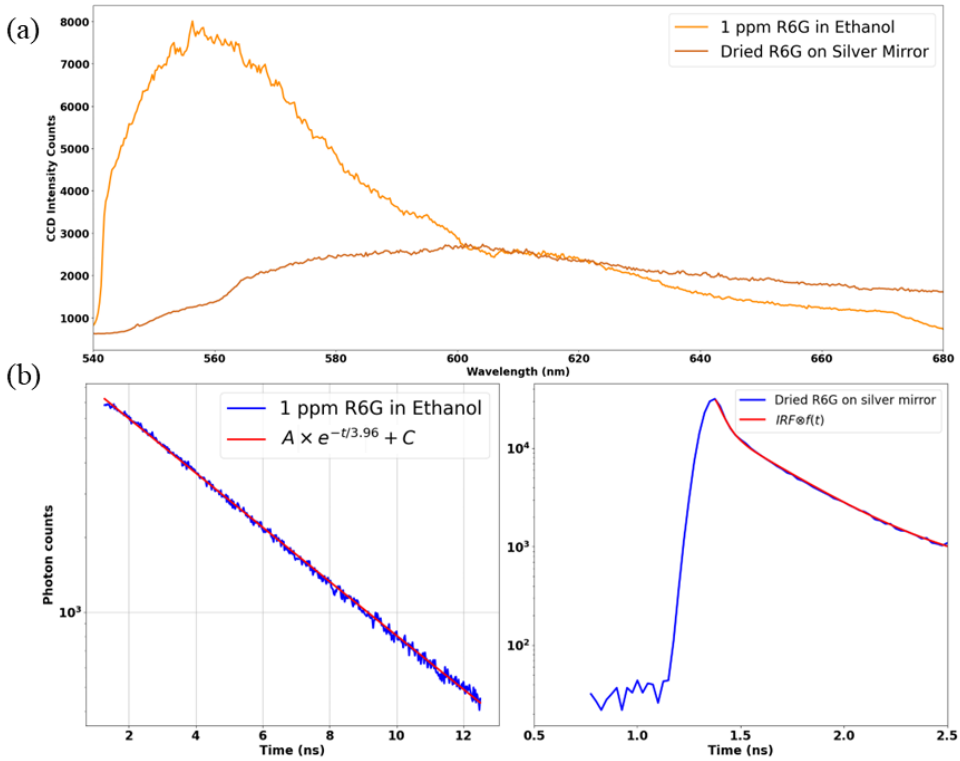

Figure 23. (a) Measured fluorescence emission spectra of the dye solution and of the dried layer on a silver surface. (b) Measured PL decay and extracted lifetime for R6G dye in a 10^{-6} M solution in ethanol, and as a dried layer of solution on a silver surface.

Fig. S3(a) gives PL decay of these spectra, measured using the optical setup shown in Fig. 5(a) of the main text. The best fit to the measured data for the dye solution consists of a single exponential decay function with an extracted lifetime of $\tau_s \simeq 3.96$ ns (Fig. S3(a), left panel), which agrees well with data available from the manufacturer (Exciton, Rhodamine 590). The decay of the dried solution on the silver mirror (Fig. S3(a), right panel) was modelled using the same double exponential function $f(t)$ as defined in the caption of Fig. 5(b) of the main text, from which a lifetime of $\tau_m \simeq 30$ ps was extracted for the dried dye.

The lifetime τ_s was measured in solution and is different than the intrinsic lifetime of the dye molecules in free space τ_0. To determine the Purcell factor of the dye on the silver mirror, τ_0 for the dye molecules must be calculated. The local density of optical states (LDOS) of a homogeneous dielectric volume is proportional to the square of the refractive index of the dielectric [7], and the decay rate is proportional to the LDOS following Fermi's golden rule [1] [8]. As a result, the lifetime of dye molecules in free space decreases by a factor of n_e^2 with respect to the lifetime in ethanol. Using $n_e \simeq 1.36$ for ethanol over $\lambda \simeq 500 - 600$ nm, yields a Purcell factor of $\gamma = (\tau_s/n_e^2)/\tau_m \simeq 70$, which is very close to the computed values for γ_{Avg} in Fig. 4(b) of the main text over the same wavelength range.

References

[1] W. Barnes, "Fluorescence near interfaces: the role of photonic mode density," *Journal of Modern Optics,* vol. 45, no. 4, pp. 661-699, 1998.

[2] G. Ford and W. Weber, "Electromagnetic interactions of molecules with metal surfaces," *Physics Reports,* vol. 113, no. 4, pp. 195-287, 1984.

[3] K. Drexhage, "IV interaction of light with monomolecular dye layers," in *Progress in Optics*, vol. 12, Elsevier, 1974, pp. 163-232.

[4] I. Prigogine and S. Rice, "Molecular Fluorescence and Energy Transfer Near Interfaces," in *Advances in chemical physics*, John Wiley & Sons, 2009, p. Vol. 37.

[5] I. De Leon and P. Berini, "Modeling surface plasmon-polariton gain in planar metallic structures," *Optics Express,* vol. 17, no. 22, pp. 20191-20202, 2009.

[6] B. Czaplińska, K. Malarz, A. Mrozek-Wilczkiewicz, A. Slodek, M. Korzec and R. Musiol, "Theoretical and experimental investigations of large stokes shift fluorophores based on a quinoline scaffold," *Molecules,* vol. 25, no. 11, p. 2488, 2020.

[7] W. Barnes, S. Horsley and W. Vos, "Classical antennas, quantum emitters, and densities of optical states," *Journal of Optics,* vol. 22, no. 7, p. 073501, 2020.

[8] E. Fermi, "Quantum theory of radiation. , 4(1), p.87.," *Reviews of Modern Physics,* vol. 4, no. 1, p. 87, 1932.

5.3 Additional Measurements (Amplified Spontaneous Emission)

After creating carbon emitters on grating structures and when the fluorescence emission is stabilized after 30 minutes of CW laser exposure, the structures were investigated for possibility of amplified spontaneous emission, the results of which is shown in Fig. 20. To ensure that the population and characteristics of emitters created on the silver grating won't change during the experiment, the grating was exposed to the highest optical power (~490 mW) initially and for ten minutes to stabilize the fluorescence emission. Incident optical power was then decreased and the emission spectrum was recorded for 14 different incident optical power ranging from 490 mW down to 64 mW. Figure 20 (a) shows no significant change in the spectrum features as the power is decreased. Figure 20 (b) shows the integrated intensities of 14 recorded spectrums for each incident power. It's observed that the integrated intensity increases linearly with incident optical power, showing no sign of amplified spontaneous emission.

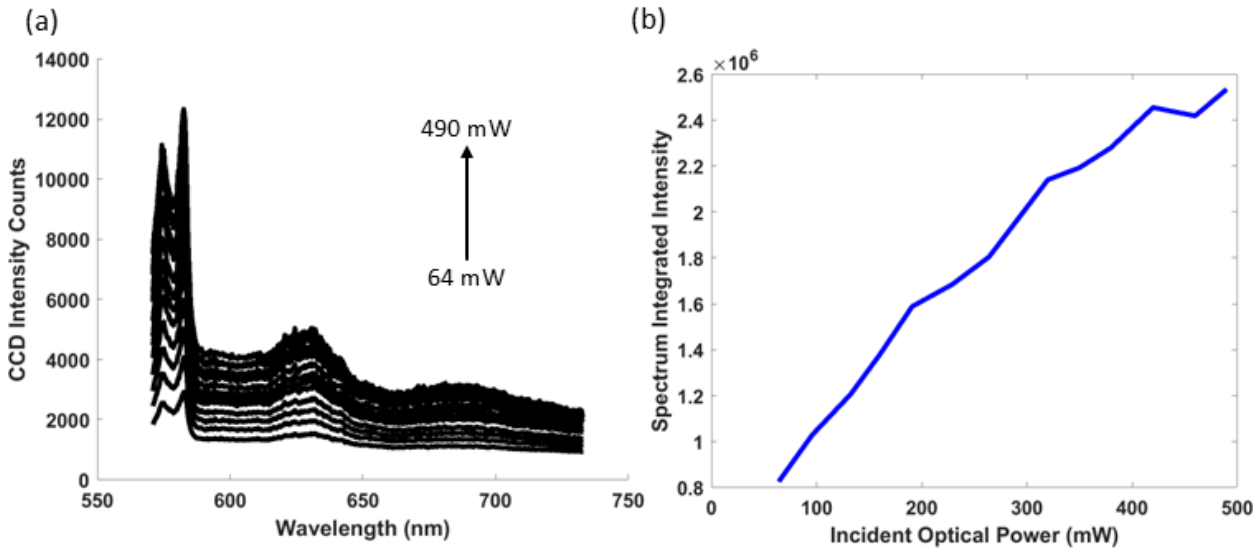

Figure 20 ASE investigation of carbon dots on silver gratings. (a) Recorded emission spectrum for 14 different incident pump powers. (b) Spectrums integrated intensity vs incident pump power.

6 Conclusion and Future Work

6.1 Concluding Remarks

The articles included in this thesis, explored the potentials of plasmonic gratings in advancing device physics, chip manufacturing processes, and fluorescence emission engineering. Nano structuring of metallic surfaces with periodic nano bars, creates plasmonic gratings, which are well-known for the efficient SPP mode excitation upon illumination with an optical beam. Presence of SPPs on the grating structures provided various opportunities from enhanced light-matter interaction used in designing active telecommunication devices and enabling new device physics, to engineering the emission intensity and direction of fluorophores.

The modeling, measurement, and analysis of a plasmonic-grating-assisted MOS electro-optic modulator was provided, marking a significant contribution to high-speed optical device engineering. The device leverages carrier refraction effects in silicon to modulate the coupling of light to SPPs, offering a compact and efficient platform for non-contact wafer-level testing—a critical bottleneck in modern semiconductor manufacturing. Operating at 22 GHz with low insertion loss and broad optical bandwidth, the modulator presents a promising path toward integrated optical testing solutions compatible with shrinking technology nodes.

In parallel, theoretical and experimental studies of tunneling currents in similar MOS structures revealed a modified Fowler-Nordheim tunneling regime under inversion conditions. The identification of a plasmon-induced energetic hole tunneling channel provides new insights into optically enhanced charge transport in nanostructured MOS systems, with implications for future photodetectors and hot-carrier-based devices.

Investigation of the fluorescence enhancement on plasmonic gratings further highlighted the versatile role of SPPs. By enhancing spontaneous emission via the Purcell effect, and coupling surface plasmons to radiation channels through grating diffraction, these structures offer powerful means for controlling emission intensity and directionality. Experimental lifetime measurements validated theoretical models and provided information about the emitters characteristics and their behaviour close to plasmonic modes.while proposed strategies for nanoantenna design and lifetime-based sensing pave the way for localized and tunable fluorescence applications.

6.2 Future work

The research presented in this thesis opens several promising directions for future exploration.

One key avenue is the further optimization and miniaturization of the plasmonic based MOS modulators for high-speed applications. Enhancing the modulation depth and reducing power consumption, could bring CMOS compatible plasmonic modulators to practical deployment in on-chip optical communication systems.

In the context of tunneling phenomena, additional studies may focus on engineering the metal–oxide interface and exploring alternative high-κ dielectrics to tailor the tunneling barrier properties. Investigating the role of different plasmonic materials, structures, and excitation wavelengths could deepen understanding of the mechanisms behind plasmon-induced energetic carrier generation and open new applications in photodetection and energy harvesting.

For fluorescence enhancement, expanding the plasmonic grating designs to include tunable or reconfigurable structures may enable dynamic control of emission properties. Combining these structures

with site-selective nanoantenna arrays could allow spatial and spectral tailoring of fluorescence at the nanoscale, benefiting applications in biosensing, imaging, and quantum photonics.

Additionally, the proposed frequency domain lifetime measurement method presents a valuable tool for accurately characterizing fluorescence emitters with complex mixtures in various environments.

7 Appendix

7.1 Silver Dipole Nano Antenna for Fluorescence Enhancement

Following the results represented in chapter 5 of this thesis, silver dipole nanoantenna periodic structures were designed to resonate at the absorption wavelength of our carbon dots. Plasmonic nanoatennas have been a matter of interest in surface enhanced Raman spectroscopy (SERS) and surface enhanced fluorescence (SEF) due to their advantageous features [124]. It was discussed in chapter 5 that plasmonic grating structures have broad but weak resonance spectrums compared to nanoantenna resonance. On the other hand, grating structures excite fluorophores on the entire surface of the structure whereas nanoantenna periodic structures provide localized excitation and fluorescence enhancement resulting from the fact that the electromagnetic fields are localized very strongly and tightly around the nanoantenna structures rather than other parts of the metasurface. As a result, it is expected that dipole nanoantennas which have extensive field enhancement in the gap area, are efficient nanostructures in both exciting the fluorophores upon illumination and providing a bright and highly directive radiation. Dipole nanoantennas are flexible structures and can be designed and tuned to work with fluorophores emitting in visible to near infrared frequencies. They can have two plasmonic resonance modes each coinciding with excitation or emission wavelengths [125] [126].

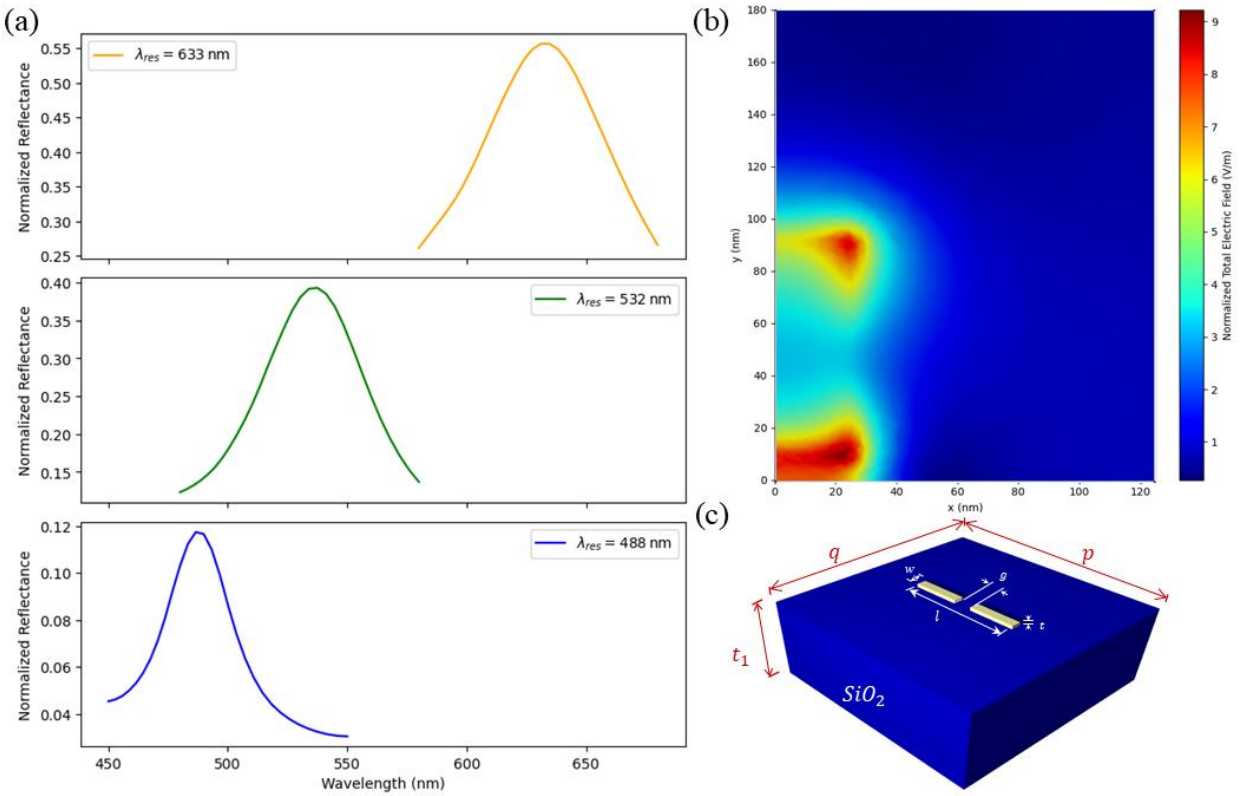

Figure 21 (a) Normalized reflectance spectrum of plasmonic dipole nanoantenna periodic structures designed to resonate at different visible wavelengths. (b) Magnitude of normalized total electric field at a plane 5 nm above the nanoantenna in numerical calculation environment including a quarter of unit cell plotted at the resonance wavelength of the structure designed at λ=633 nm. (c) schematic of a unit cell of the periodic structure.

Figure 20 shows the numerical simulation results for three silver dipole nanoantenna periodic structures, designed to resonate at $\lambda_{res} = 488\,nm$, $\lambda_{res} = 532\,nm$, and $\lambda_{res} = 633\,nm$. Antennas are laid on an

infinitely thick SiO_2 substrate. Simulations were performed using commercial finite element method (FEM) tool for a quarter of a unit cell. On the simulation environment walls, perfect electric conductor (PEC) and perfect magnetic conductor (PMC) boundary conditions were used to complete the unit cell, together with the periodic boundary conditions to replicate the unit cell and create an infinitely large periodic structure. The structure is in air and illuminated with plane wave polarized along the dipole nanoantenna. Relative permittivities of silver and silicon dioxide were adopted from literature [127]. The designed dimensions of the structure are represented in Table 1 for each resonance wavelength.

Table 1 Silver dipole nanoantenna designs dimensions for periodic structures resonating at visible wavelengths.

	$\boldsymbol{\lambda_{res} = 488\ nm}$	$\boldsymbol{\lambda_{res} = 532\ nm}$	$\boldsymbol{\lambda_{res} = 633\ nm}$
p (nm)	280	290	360
q (nm)	200	220	250
t (nm)	50	30	30
w (nm)	40	50	50
l (nm)	100	135	185
g (nm)	20	20	20

7.2 Surface Plasmons on Silver Gratings Transform Pyrolytic Carbon into Luminescent Graphitized Carbon Dots

Summary

The creation of carbon-based emitters and their fluorescence emission enhancement mediated by SPP modes, is experimentally investigated. SPP modes excited on a silver grating, provide energetic carriers which drive plasmonic based catalysis reactions transforming pyrolyzed residue on the grating into carbon based fluorescence emitters. Reactions happen under high pressure, O_2 depleted gas (Ar, N_2, CO_2) flow inside a closed chamber, and yellow luminescence along with Raman signals from carbon bonds appears in the spectrum and grows over time upon continuous excitation. If SPPs are not excited or in the presence of Oxygen, no emission is observed.

Contribution

The research work provided in this chapter was published in and is reproduced with permission from The Journal of Chemical Physics (AIP Publishing group) [103]. I performed the data fit and analysis to extract the parameters of the peaks present in the measured spectrums under four different gases flowing in the chamber. Figure 8 in the main text and all graphs and discussions in the supplementary file are my work.

The Journal of Chemical Physics

RESEARCH ARTICLE | OCTOBER 08 2024

Surface plasmons on silver gratings transform pyrolytic carbon into luminescent graphitized carbon dots

Special Collection: Plasmon-mediated Nonlinear Optics and Dynamics

Jaspreet Walia ; Sabaa Rashid; Maryam Sadat Amiri Naeini ; Graham Killaire ; Fabio Variola ; Arnaud Weck ; Pierre Berini

Check for updates

J. Chem. Phys. 161, 144702 (2024)
https://doi.org/10.1063/5.0222268

View Online
Export Citation

Articles You May Be Interested In

Structural Dependence of the Tracer-Level Diffusion of Thorium in Pyrolytic Carbons

J. Appl. Phys. (August 1967)

Reflection polarized light microscopy and its application to pyrolytic carbon deposits

J. Appl. Phys. (May 2004)

An investigation of the electrical properties of pyrolytic carbon in reduced dimensions: Vias and wires

J. Appl. Phys. (June 2010)

19 June 2025 19:33:55

AIP Publishing

The Journal of Chemical Physics

Special Topics Open for Submissions

Learn More

AIP Publishing

The Journal of Chemical Physics ARTICLE pubs.aip.org/aip/jcp

Surface plasmons on silver gratings transform pyrolytic carbon into luminescent graphitized carbon dots

Cite as: J. Chem. Phys. 161, 144702 (2024); doi: 10.1063/5.0222268
Submitted: 6 June 2024 • Accepted: 21 September 2024 •
Published Online: 8 October 2024

View Online Export Citation CrossMark

Jaspreet Walia,[1,2] Sabaa Rashid,[1,a)] Maryam Sadat Amiri Naeini,[1,3] Graham Killaire,[1,3] Fabio Variola,[4] Arnaud Weck,[1,3,4] and Pierre Berini[1,2,3,b)]

AFFILIATIONS

[1] Nexus for Quantum Technologies Institute, University of Ottawa, Ottawa, Ontario K1N 6N5, Canada
[2] School of Electrical Engineering and Computer Science, University of Ottawa, Ottawa, Ontario K1N 6N5, Canada
[3] Department of Physics, University of Ottawa, Ottawa, Ontario K1N 6N5, Canada
[4] Department of Mechanical Engineering, University of Ottawa, Ottawa, Ontario K1N 6N5, Canada

Note: This paper is part of the JCP Special Topic on Plasmon-Mediated Nonlinear Optics and Dynamics.
a) **Now at:** Canadian Centre for Electron Microscopy, McMaster University, Hamilton, Ontario L8S 4M1, Canada
b) **Author to whom correspondence should be addressed:** .....

ABSTRACT

Plasmonic catalysis holds the promise of opening new reaction pathways that are inaccessible thermally or via direct UV–vis electronic transitions. Here, energetic carriers produced via the decay of surface plasmons excited by visible light at 532 nm (2.33 eV, green) on a Ag-grating-bearing pyrolytic carbon residue drive its transformation into light-emitting graphitized carbon dots. The pyrolytic carbon residue is detectable via high-magnification surface-enhanced Raman scattering but cannot be directly observed using optical, electron, atomic force, or helium ion microscopy. When a Ag-grating-bearing pyrolyzed residue is introduced into a high-purity O_2-depleted gas environment (Ar, N_2, and CO_2) and excited with 532 nm light, bright yellow luminescence emerges and is readily observed. Light emission is not observed without the pyrolytic carbon, without the excitation of plasmons, or in air or an Ar/O_2 gas mixture. This process, driven by visible light and a nanostructured Ag surface bearing pyrolytic carbon, will be of interest to researchers involved in plasmonic catalysis, catalytic processes involving carbon, and luminescent plasmonic surfaces.

Published under an exclusive license by AIP Publishing. https://doi.org/10.1063/5.0222268

19 June 2025 19:33:55

INTRODUCTION

Metallic nanostructures and arrangements of nanoparticles that harvest light to excite energetic (hot) carriers via the decay of surface plasmons are opening new chemical transformation pathways.[1–5] The chemical transformation of a molecule adsorbed onto a metal surface can occur, e.g., via hot-electron transfer from occupied states above the Fermi energy in the metal to unoccupied states in the adsorbate[6] or via local heating.[7,8] Silver has no interband transitions over the visible range and is remarkably effective at supporting surface plasmons which can decay by creating high concentrations of excited surface charge carriers. For instance, chemical transformations were recently investigated on Ag nanoparticles excited by 532 nm light in a CO_2 gas environment,[9,10] where a variety of products were detected, including CO, formaldehyde, formic acid, methanol, carbonates, and amorphous carbon. Also, graphene was observed to form from the condensation of C_2H_4 via a photo-driven process at 514.5 nm on Ag nanoparticles.[11]

Metal nanoparticles, with their subtle differences in size, shape, interparticle spacing, and different degrees of surface oxidation, can create an intractable mix of optical and thermal responses under the illumination spot. In turn, difficulty arises in assigning specific physical mechanisms to the creation of products. Alternatively, surface plasmons propagating on waveguides[12,13] or shallow gratings[14] present deterministic systems on which optical and structural details are well understood. Furthermore, deterministic systems facilitate the isolation of effects due to energetic carriers from thermal effects, which is essential to interpreting results. This was emphasized

Published under an exclusive license by AIP Publishing

in recent work on plasmon-enhanced electrochemistry,[12,13] where novel redox channels enabled by energetic electrons and holes were identified, and on plasmon-induced luminescence from Ag gratings[14] where emission was surmised to originate from carbon dots (CDs).

Carbon dots (CDs)—a new class of nanoscale quantum emitters—are known to exhibit strong luminescence.[15–22] The term CD encompasses a family of carbon-based quantum-sized materials, including carbon nanodots (CNDs),[15] carbon quantum dots (CQDs),[16] graphene quantum dots (GQDs),[17,18,20–22] and carbon nano-onions (CNOs).[19] There are different degrees of crystallinity associated with each type of carbon nanostructure. High-resolution transmission electron microscopy (HRTEM) has revealed that GQDs are generally single-layer carbon structures with lattice parameters that correspond to single-layer graphene, and CQDs are generally more graphite-like.[18,21,22] GQDs have a Raman spectral signature consisting predominantly of a D-band and G-band.[18] Conversely, CNDs are amorphous carbon structures without an obvious crystal lattice,[15] and CNOs consist of concentric sheets of graphite-like carbon.[19] The wavelength emitted from CDs depends on the size of the dots and on the pump wavelength and is generally in the visible (400–600 nm) and broadband (50–100 nm).[15] Emission mechanisms occurring throughout this diverse set of materials remain a matter of investigation.[20]

Building on initial observations briefly reported in Ref. 14, we report here consistent, repeatable, bright, and visible luminescence from CDs on Ag gratings formed and excited by surface plasmons at 532 nm (2.33 eV). A well-designed Ag grating supports a well-defined periodic distribution of excited charge carriers over the entire illuminated area through the efficient excitation and decay of surface plasmons while providing an effective heat sink that minimizes thermal effects. The CDs are formed by plasmonic transformation in an O_2-depleted environment of a carbonaceous seed layer consisting of partially pyrolyzed residue originating from polymethylmethacrylate (PMMA) used in the lithography process applied to fabricate the gratings. The residue, and the CDs, cannot be seen using a visible microscope, a helium ion microscope (HIM), a scanning electron microscope (SEM), or by atomic force microscopy (AFM) but is detectable using Raman spectroscopy since the Ag gratings are also excellent surface-enhanced Raman scattering (SERS) substrates when excited with 532 nm light. The transformation of the residue into CDs and the growth of luminescence were monitored in real-time and *in situ* using SERS in several O_2-depleted gaseous environments. Raman spectra confirm the presence of sp^2 carbon and strong luminescence, suggesting that graphitized CDs have formed, possibly in the form of GQDs. The role of surface plasmons is twofold—initially, they transform the pyrolytic carbon residue into luminescent CDs, and then, the plasmons pump the CDs leading to luminescence. The role of energetic carriers in the formation of CDs is discussed.

RESULTS

Grating fabrication and pyrolytic carbon residue

A schematic of the fabrication process used to create the Ag gratings bearing pyrolytic carbon residue, and the experimental set-up incorporating a gas flow cell, are shown in Fig. 1. As sketched in Fig. 1(a), the grating structures were defined by exposing a PMMA layer spun and cured on a 100 nm thick Ag layer (on a Si substrate) with a He^+ beam,[23] then developing the exposed regions of PMMA (used as a positive tone resist), followed by deposition and lift-off of a Ag layer to form the grating ridges. Details in connection with the fabrication materials and chemicals used are given in the section on Methods.

19 June 2025 19:33:55

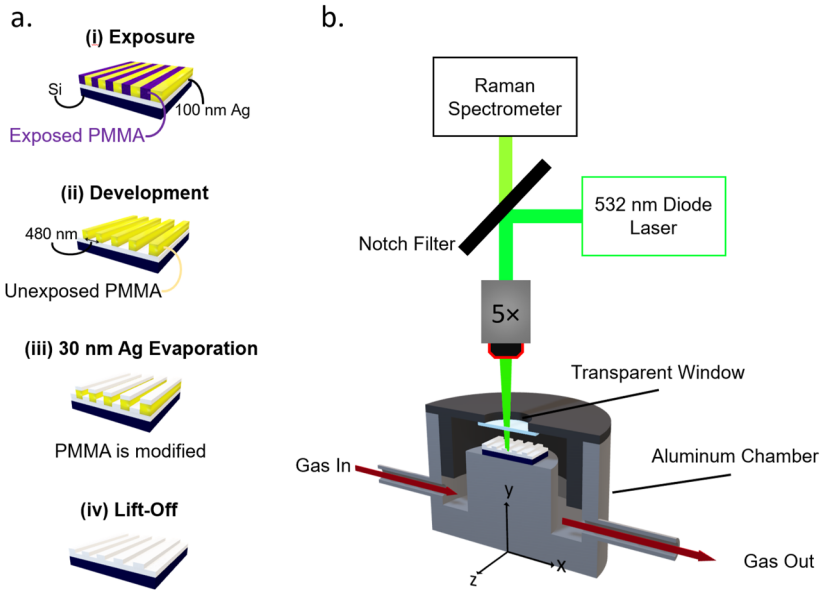

FIG. 1. (a) Schematic of the Ag grating fabrication process and the formation of pyrolytic carbon residue. (b) Raman spectroscopy set-up driven by a 532 nm continuous-wave (CW) laser incorporating a gas flow cell.

Published under an exclusive license by AIP Publishing

The grating surface was illuminated over a large area by a low magnification objective to reduce divergence and maximize coupling into surface plasmons. The gas chamber used was, therefore, designed to work with a 5× objective [Fig. 1(b)], and the grating design was optimized to couple x-polarized 532 nm continuous wave (CW) light into surface plasmons at normal incidence. The same optical input also induces Raman scattering from the surface that is detected and used as an *in situ* spectral probe. This scattered intensity is significantly enhanced by the electric fields of the plasmons (SERS effect). Details on the optimization of the grating design to couple normally incident 532 nm laser light to plasmons are given in the section on Methods.

A representative helium ion microscope (HIM) image of a fabricated Ag grating is presented in Fig. 2(a). A HIM provides high-resolution images of surface features at the nanoscale and generates images with exceptionally good material contrast.[24,25] From analysis of the HIM image, the pitch was measured to be 477 nm, the ridge width to be 253 nm, and the groove width to be 224 nm. The ridge height, rms roughness (R_q), average roughness (R_a), and maximum roughness height (R_t) of a grating were measured using AFM [Fig. 2(b)] and found to be 30.6, 2.1, 2.6, and 11.0 nm, respectively.

The HIM image and AFM scans in Figs. 2(a) and 2(b) do not reveal any evidence of residue after fabrication. However, following the lift-off step of Fig. 1(a)(iv), Raman spectral analysis of the grating surface reveals that organic residue remains on the Ag surface, as shown by the black trace in Fig. 2(c). The residue spectrum was recorded after fabrication using a 100× objective lens, in air, without the use of the gas chamber shown in Fig. 1(b) (the spectrum of the residue was poorly resolved with a 5× objective lens). For reference, the Raman spectrum measured from the original PMMA layer is shown as the red trace in Fig. 2(c) and is consistent with the literature.[23,26] The residue spectrum shares several peaks with the PMMA spectrum, but the spectra differ sufficiently that the residue cannot be identified as leftover PMMA. The residue remains after lift-off [Fig. 1(a)(iv)], suggesting that it may be chemisorbed to the Ag surface.

A closer look at the residue spectrum [black trace, Fig. 2(c)] reveals that a D and G band structure is present. The G-band arises from sp^2 bonding in carbon rings and chains, and the D-band arises from disorder in graphite. It has been demonstrated that the presence of a D-band and G-band is strictly indicative of sixfold rings in amorphous carbon matrices and of graphite-like carbon.[27–30] This, taken with the presence of peaks corresponding to C–O, C=O, and CH_2/CH_3 groups, allows for an assignment of the residue to a mixture of alkenes and aromatic rings containing different amounts of sp^2 bonded carbon atoms (graphitized) with a variety of R groups (e.g., esters, epoxides, lactones, ketones, phenol, and carboxyl groups) originating from PMMA.

We surmise that PMMA was modified to form the residue during exposure by He^+ [Fig. 1(a)(i)],[31] or evaporation of Ag to form the grating ridges [Fig. 1(a)(iii)] (thermal or e-beam evaporation of Ag produced a similar residue), or both. It is known that energetically charged particles, high energy photons (UV and x ray), and high temperatures can modify resists in physical vapor deposition chambers, such as evaporators.[32] The Raman scattering spectrum of the residue post-fabrication resembles pyrolytic carbon, although signals corresponding to C–O, C=O, and CH_2/CH_3 vibrations indicate incomplete pyrolysis of PMMA.

19 June 2025 19:33:55

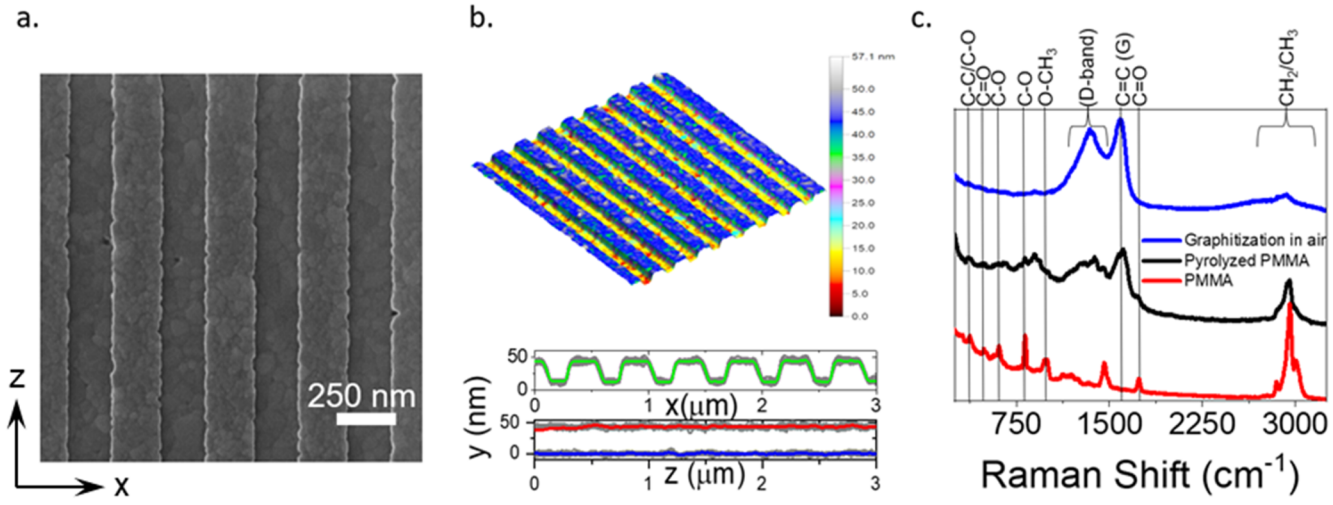

FIG. 2. (a) Top view HIM image of a fabricated Ag grating with a pitch of 477 nm. (b) Representative AFM topographical scan (top) and extracted line profiles (gray traces) for the Ag grating, and the corresponding averages along the x-direction (green trace) and along the z-direction on the ridges (red trace) and between the ridges (blue trace) (bottom). The height of the grating is 30.6 nm. (c) Raman spectrum recorded from the Ag grating surface post fabrication (black trace). The Raman spectrum from the PMMA starting layer is also shown for reference (red). D and G bands are present in the residue indicating the onset of graphitization in the PMMA (black trace). Residual signals corresponding to C–O, C=O, and CH_2/CH_3 vibrations indicate that incomplete pyrolysis has occurred. Further graphitization is achieved with prolonged or higher power laser irradiation of the pyrolyzed PMMA in air (blue trace). All signal intensities are comparable and remain essentially constant over time.

Published under an exclusive license by AIP Publishing

Grating performance

Figure 3 summarizes our Ag grating design along with measurements taken on 36 fabricated gratings of varying pitch. Figure 3(b) shows the computed reflectance (red curve) and absorptance (blue curve) vs pitch for 50/50 duty cycle rectangular gratings of height 25 nm, excited by an x-polarized perpendicularly incident plane wave at a free-space wavelength of 532 nm. Theoretically, the reflectance reaches almost zero and the absorptance is almost unity for a pitch of Λ = 492.5 nm, indicating close to 100% coupling of the incident light into surface plasmons. Figure 3(a) shows the computed spatial distribution of the electric field enhancement over the grating of pitch Λ = 492.5 nm, revealing a field enhancement up to 15× around the ridges.

The reflectance was measured by illuminating a grating with a normally incident x-polarized 532 nm laser beam, focused through a 5× objective, yielding a low-divergence 10–15 μm diameter spot on grating, and then normalizing relative to the nearby flat Ag surface. Comparing the experimental (black) and theoretical (red) curves in Fig. 3(b) reveals good agreement, although as shown in Fig. 2(b), the fabricated grating ridges are thicker (30.6 nm) and have a slight roughness compared to the modeled ones. Experimentally, the grating of pitch Λ = 480 nm was found to couple up to 80% of the beam into surface plasmons [black curve, Fig. 3(b)], and so was selected for the remainder of this study.

Graphitization in ambient air

A grating excited by an x-polarized 532 nm laser beam carrying 10 mW of power in ambient air (1 atm) produced no change in the Raman spectrum discernible with the 5× objective. However, the Raman spectrum measured subsequently at high magnification (100× objective), plotted as the blue trace in Fig. 2(c), shows sharper well-defined D and G band line shapes relative to the spectrum taken after fabrication [black trace, Fig. 2(c)]. Furthermore, the peaks related to the C–O and C=O groups have essentially disappeared and those related to the CH_2/CH_3 groups have dropped significantly. These observations indicate that the initial residue consisting of partially pyrolyzed PMMA (black trace, Fig. 2(c) is carbonized into graphite-like material by plasmonic excitation in air [blue trace, Fig. 2(c)]. Subsequent investigation of the sample surface via HIM did not reveal any discernible change.

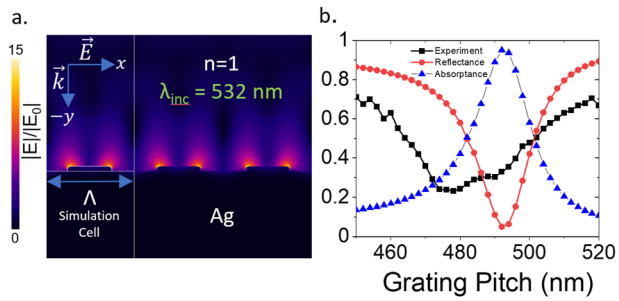

FIG. 3. Ag grating design and characterization. (a) Computed spatial distribution of the electric field enhancement over an ideal Ag grating of pitch Λ = 492.5 nm. The simulation cell used in the calculations is outlined in white. (b) Experimental (black) and computed (red) specular reflectance for several 50/50 duty cycle Ag gratings of pitch ranging from Λ = 450–520 nm and height 25 nm, for normally incident light at a free-space wavelength of 532 nm. The simulated absorptance (blue trace) is also plotted.

Graphitization and luminescence in CO_2

Ag gratings bearing pyrolytic carbon residue [cf., black trace, Fig. 2(c)] were then placed in a continuous flow CO_2 environment at a gauge pressure of 14 psig (1.95 atm) in the set-up shown in Fig. 1(b) and excited with an x-polarized 532 nm laser beam carrying 10 mW of power. Significant spectral changes take place immediately and then evolve over 30 min as revealed by time-evolution Raman spectroscopy of the surface, as shown in Figs. 4(a) and 4(b). In this case, the signals were easily detected and resolved with a 5× objective. In addition, a short 5 ms integration time was used to avoid detector saturation from the extreme emission produced. In contrast, to spectrally resolve the spectra of Fig. 2(c) in air, a minimum integration time of 1 s and use of a 100× objective were essential.

From the noise level at t = 0 [red trace in Fig. 4(a)], a very rapid spectral evolution shows the growth of three peaks: an extremely intense broad spectral contribution that red-shifts with time assigned to a photoluminescence (PL) peak, and two peaks characteristic of scattering from D and G bands (commonly observed from graphite-like carbon,[27–30] as mentioned previously). Interestingly, the position of the PL peak would vary from one experimental trial to the other but not the D and G bands. The D and G bands are Raman scattering peaks and, therefore, remain at specific shift values. The two datasets shown in Fig. 4 represent two

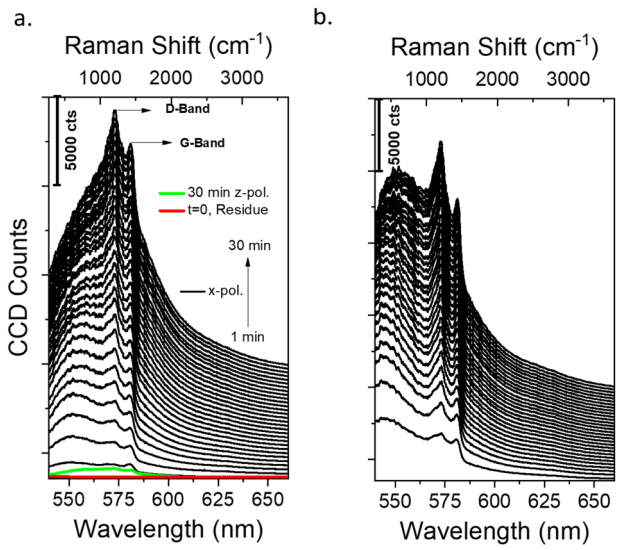

FIG. 4. *In situ* measurements of Raman spectral evolution in CO_2 gas. (a) and (b) Time evolution (30 min) SERS spectra recorded from nominally identical Ag gratings bearing pyrolytic carbon residue, each excited by x-polarized 532 nm laser light (10 mW incident power), exposed to 1.95 atm of high-purity (99.99%) CO_2 gas under continuous flow (black stack plots—no offset, revealing change in response over 30 min). For comparison, the spectrum recorded after exciting a grating for over 30 min with z-polarized light (grating rotated by 90°) and the initial spectrum of the Ag grating bearing pyrolytic carbon residue [cf., Fig. 2(c)] are plotted on the same scale as the green and red traces, respectively, in (a).

19 June 2025 19:33:55

Published under an exclusive license by AIP Publishing

extremes that were observed for the PL peak position. This massive signal increase over time was always observed over many repeated experiments involving many gratings. It was also observed that the amount of PL and Raman scattering detected from the surface would plateau after ~30 min of exposure when the laser power was set to 10 mW.

Close inspection of the spectra [Figs. 4(a) and 4(b)] reveals that changes in scattering from modes associated with C–O and C=O vibrations are not resolved due to the extreme PL in this spectral region; thus, one cannot track conclusively changes in oxygen-containing groups if they are occurring. For example, lactones have characteristic vibrations in the 1680–1780 cm^{-1} range, so if they are forming or dissociating, their signals would be convolved into the PL and G band signals. Conversely, the PL signal is weak in the 3000 cm^{-1} range, which is where the CH_2 and CH_3 peaks would be revealed, and since they are absent, one can conclude that these hydrogen groups are no longer present.

Spectral deconvolution was performed to accurately extract the positions, linewidths, and intensities of the three peaks as a function of time, for both datasets in Figs. 4(a) and 4(b). All spectra fit very well to three Lorentzian peaks, as shown in the examples plotted in Figs. S1(a) and S1(b) (supplementary materials) at time intervals of 5, 15, and 30 min.

The corresponding time evolution of the Lorentzian parameters extracted from each of these peaks is plotted in Figs. 5(a) and 5(b), revealing that the PL contribution eventually becomes responsible for over 90% of the emission recorded (recall that the PL is initially inexistent at t = 0). In connection with the dataset in Fig. 4(a), the PL peak red-shifts from 552 to 565 nm (green/yellow) and broadens by 11 nm from 43 to 54 nm over the course of the experiment, as can be observed in Fig. 5(a). The PL emission peak extracted from the other dataset [Fig. 4(b)] behaves qualitatively similarly, red shifting from 544 to 552 nm, accompanied by a linewidth increase from 48 to 56 nm, as can be observed in Fig. 5(b).

The two peaks centered near 572 nm (D band) and 580 nm (G-band) do not shift with any statistical certainty and were always found in the 1335 to 1350 cm^{-1} and 1576 to 1588 cm^{-1} Raman spectral shift ranges, respectively, as can be observed in Fig. 5. Likewise, the G band linewidth remains essentially constant throughout the experiments. However, the D band linewidth narrows significantly from about 11 nm (330 cm^{-1}) to about 6 nm (180 cm^{-1}) for both datasets, as observed in Fig. 5. Also, the strength of both peaks increases with time. The spectral centers, linewidths, and overall line shape of the D and G bands remain consistent with Raman scattering from graphitized carbon throughout the experiment; however, the narrowing D band and the increase in the D and G peaks suggest increased graphitization and long-range order. All three peaks (PL, D, and G) related to both data sets tend toward an exponential plateau, indicating that equilibrium conditions are eventually established.

It was observed that replacing the CO_2 environment by air at any time during the experiment reverses the process, resulting in the eventual disappearance of visible PL over a similar timescale (30 min). The process then re-initiates and proceeds if CO_2 is reintroduced into the chamber. The reversible nature of the process was tested over many iterations.

Since the emergence and growth of PL occur on a timescale of several minutes, it was possible to examine how the spectral evolution proceeds vs laser power. Time evolution measurements of the total integrated emitted intensity (PL + Raman), I, for laser powers of 2, 4, 6, 8, and 10 mW are shown in Fig. 6(a) (laser powers measured before the objective). It is immediately apparent that I increases more rapidly with increasing laser power. We assume that the total area under each recorded spectrum is proportional to the amount of residue transforming, as the measured data fit well an

19 June 2025 19:33:55

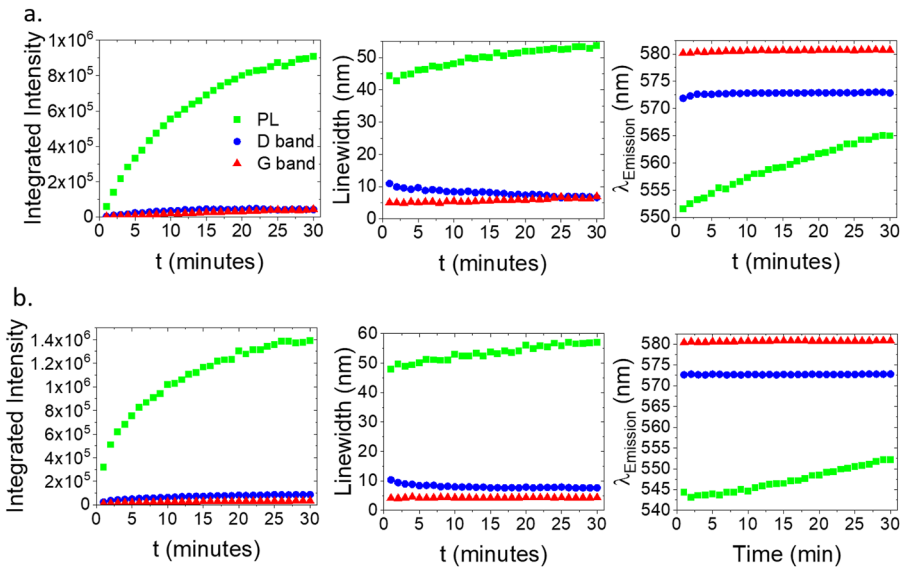

FIG. 5. Extracted peak parameters. Row (a) Integrated peak intensities, linewidths, and emission wavelengths extracted from deconvolving the dataset in Fig. 4(a). Row (b) Similarly for the dataset in Fig. 4(b).

Published under an exclusive license by AIP Publishing

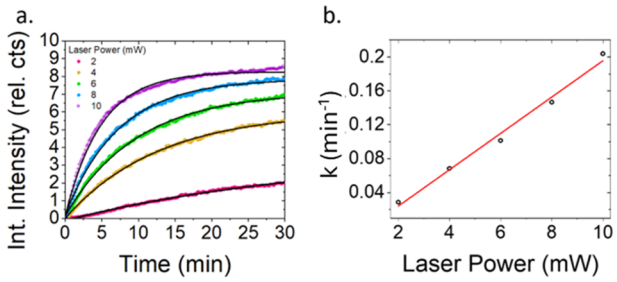

FIG. 6. Effect of laser power. (a) Total integrated intensity (Raman + PL) over 30 min of exposure to CO_2 gas for laser powers of 2, 4, 6, 8, and 10 mW. The data fits well an exponential model of the form: $I = I_\infty (1 - e^{-kt})$, where k is the rate constant and I_∞ is the total integrated emission intensity at $t = \infty$. (b) Plotting k vs laser power results in a linear trend, without any obvious onset of parabolic behavior.

exponential model of the form $I = I_\infty (1 - e^{-kt})$, where k is the rate constant and I_∞ is the total integrated emission intensity at $t = \infty$. A plot of the extracted rate constant vs incident optical power forms a linear trend, as shown in Fig. 6(b), from which we note that the emission saturates in a characteristic time $\tau = 1/k$ ranging from 5 to 25 min depending on the incident laser power.

Significant thermal effects are not expected in our experiments given the heat sinking ability of the Ag structure on a p-doped Si substrate in thermal contact with the Al gas chamber [cf., Fig. 1(b)]. In general, a reaction rate k increases exponentially with temperature following the Arrhenius law, which we write to account for laser heating as:[33] $k = A \cdot \exp[-E_a/(R(T_0 + cI))]$, where E_a is the molar activation energy, R is the gas constant, T_0 is the nominal temperature, c is a photothermal conversion coefficient, and A is a constant depending on the reaction. As long as the optical response remains linear, the temperature of a plasmonic structure increases linearly with incident laser intensity ($T \propto cI$).[8] It then follows that the reaction rate would produce an exponential trend with I for a thermally driven process, which is not the case as observed from Fig. 6(b) where a linear trend is evident over a 5× increase in laser intensity. Thus, thermal effects are ruled out in the transformation of the residue (i.e., the photothermal conversion coefficient, c, is small in our system). Alternatively, the reaction rate should be linear with laser intensity if energetic carriers play a role because their number is proportional to the number of surface plasmon quanta absorbed, which depends on the number of incident photons (intensity).

Graphitization and luminescence in other gases

Contrary to illumination in a CO_2 environment, an illuminated grating in ambient air produces no discernible PL, even if the residue may undergo graphitization [blue trace, Fig. 2(c)]. Motivated by these observations, the behavior of illuminated Ag gratings bearing pyrolytic carbon residue [cf., black trace, Fig. 2(c)] was explored with other gases injected into the chamber. Figure 7 shows the time evolution of SERS spectra measured while illuminating gratings exposed sequentially to high-purity CO_2, N_2, Ar, and Ar/O_2 mixture (20% O_2). The gratings are nominally identical and located on the same Ag substrate, so the spectra can be directly compared. An experimental run consisted of purging the chamber with the gas of interest at a gauge pressure of 14 psig (1.95 atm) using the set-up shown in Fig. 1(b), then under continuous gas flow exciting a grating with an x-polarized 532 nm laser beam carrying 10 mW of power. Spectra were recorded periodically over a duration of about 30 min to produce the stack plots shown in Fig. 7. The insets to each part of Fig. 7 are low-magnification visible camera images captured *in situ* via the Raman microscope after illuminating each grating in gas for about 30 min.

The spectra generated in CO_2, N_2, and Ar are qualitatively similar to each other, and to the spectra reported in Fig. 4, all revealing increased graphitization of the residue and strong PL over about 30 min of illumination. However, there are significant differences in the intensity of the PL, as can be appreciated by comparing the counts (vertical scales) and the camera images in the inset. The grating exposed to N_2 [Fig. 7(b)] yields about 4× greater PL intensity than that exposed to CO_2 [Fig. 7(a)], and about 2× more PL intensity than that exposed to Ar [Fig. 7(c)]. The sample exposed to the Ar/O_2 mixture produced no discernible PL [Fig. 7(d)]. Thus, the emission intensity follows the trend $N_2 > Ar > CO_2 > Ar/O_2$ (no emission).

Spectral deconvolutions were performed on the datasets of Figs. 7(a)–7(c), and the time evolution of the fitted Lorentzian parameters is plotted in Fig. 8. The spectra measured in the Ar/O_2 mixture [Fig. 7(d)] do not evolve enough with time to warrant deconvolution. All spectra measured in CO_2 were very well deconvolved using three Lorentzian functions [Figs. 4 and 7(a)], but a fourth Lorentzian function was required to improve the fit of the spectra measured in N_2 [Fig. 7(b)]. The fit to the spectra measured in Ar [Fig. 7(c)] benefited only marginally by adding a fourth Lorentzian, so only three Lorentzian functions were retained in this case. Very good fits were generally obtained, as seen in the examples plotted in Figs. S2(a)–S2(c) (supplementary materials) at time intervals of 5, 15, and 30 min.

Similar to Fig. 5, we observe from Fig. 8 for the three gases that the PL emission eventually dominates the spectra and that it broadens and red shifts with time. The fourth Lorentzian required to improve the fit in the case of N_2 [Fig. 8(b)] is centered near 630 nm, and given its linewidth (~40 nm), is attributed to a second PL emission process (PL2), which is weaker and red-shifted relative to the much stronger PL emerging near 560 nm (PL1). Qualitatively, a second PL emission may be inferred by comparing the camera image acquired in N_2 [Fig. 7(b), inset], which appears orange, with the images obtained in CO_2 [Fig. 7(a), inset] and in Ar [Fig. 7(c), inset], which appear yellow—the former is consistent with color mixing, i.e., green/yellow ($PL_1 \sim 560$ nm) mixed with red ($PL_2 \sim 630$ nm) can be perceived as orange.

Figure 8(d) shows the comparison on expanded scales of the D and G peak parameters extracted from the time responses in the three gases (CO_2, N_2, and Ar). The D and G peaks both strengthen with time, significantly more in N_2 than in the other gases. The D peak linewidth drops considerably with time, from about 14 to 9 nm in all gases, whereas the G peak linewidth remains approximately constant near 4 nm. The D and G peaks eventually stabilize near 573 and 581 nm, corresponding to Raman shifts relative to the pump (532 nm) of 1335–1350 cm^{-1} and 1576–1588 cm^{-1}, respectively. These observations suggest increasing graphitization with time, consistent with Fig. 5, but over a broader set of gases including Ar and N_2.

19 June 2025 19:33:55

Published under an exclusive license by AIP Publishing

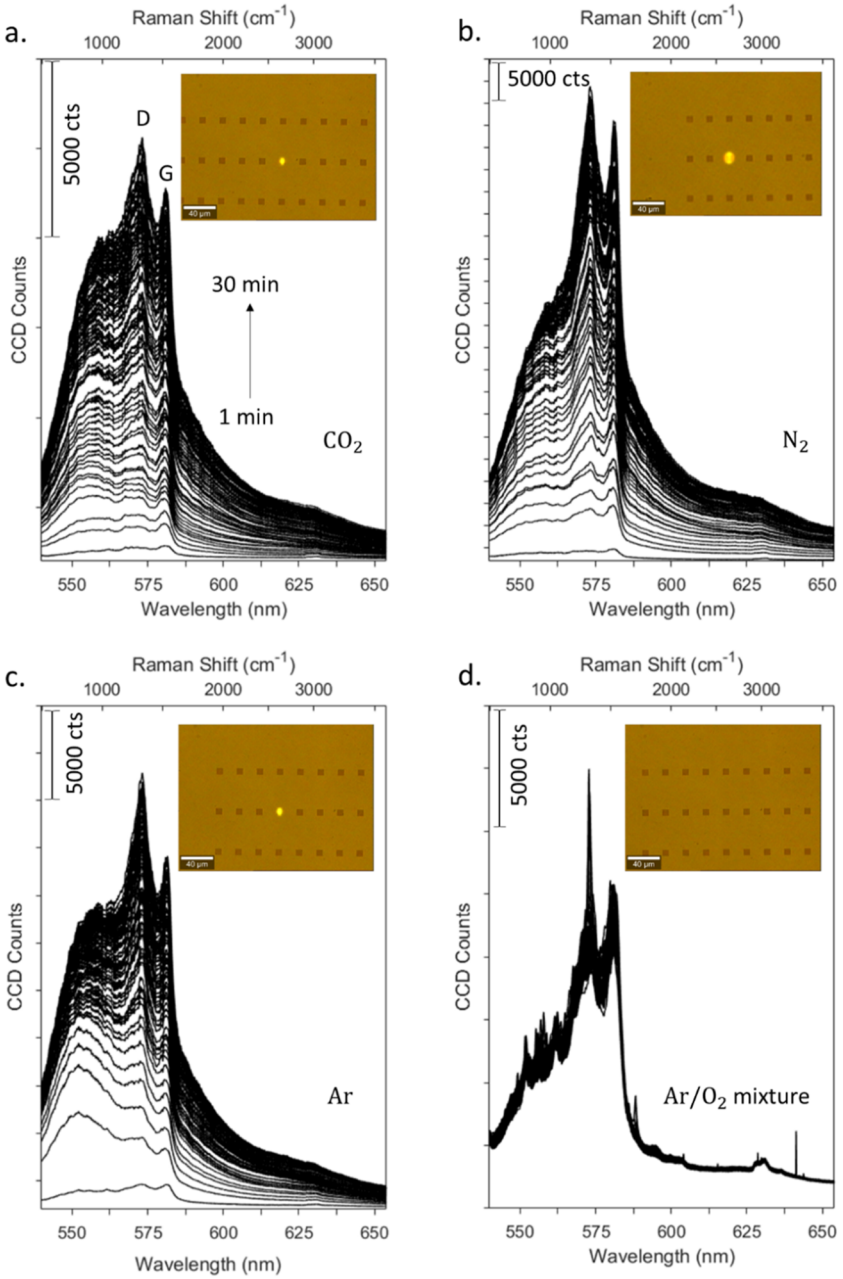

FIG. 7. *In situ* measurement of time evolution (30 min) SERS spectra of Ag gratings exposed to various gases at 1.95 atm under continuous flow: (a) CO_2, (b) N_2, (c) Ar, and (d) Ar/O_2 mixture (black stack plots—no offset, revealing change in response over 30 min). The gratings are nominally identical and located on the same sample, and they were excited by x-polarized 532 nm laser light (10 mW incident power). The insets show images of the gratings, captured *in situ* using a camera operating in the visible after about 30 min, revealing significant PL emerging in the cases of CO_2, N_2, and Ar.

Control experiments

If surface plasmons are not effectively excited, for example, when the grating is illuminated with z-polarized light, only a weak spectrum characteristic of the pyrolytic carbon residue is observed, shown as the green trace in Fig. 4(a). Several control experiments were performed under z-polarized excitation in a 14 psig (~1.95 atm) CO_2 environment for 30 min, each followed by a single Raman spectral acquisition using x-polarized light to exploit the same SERS effect for readout, yielding no discernible PL. Similarly,

19 June 2025 19:33:55

Published under an exclusive license by AIP Publishing

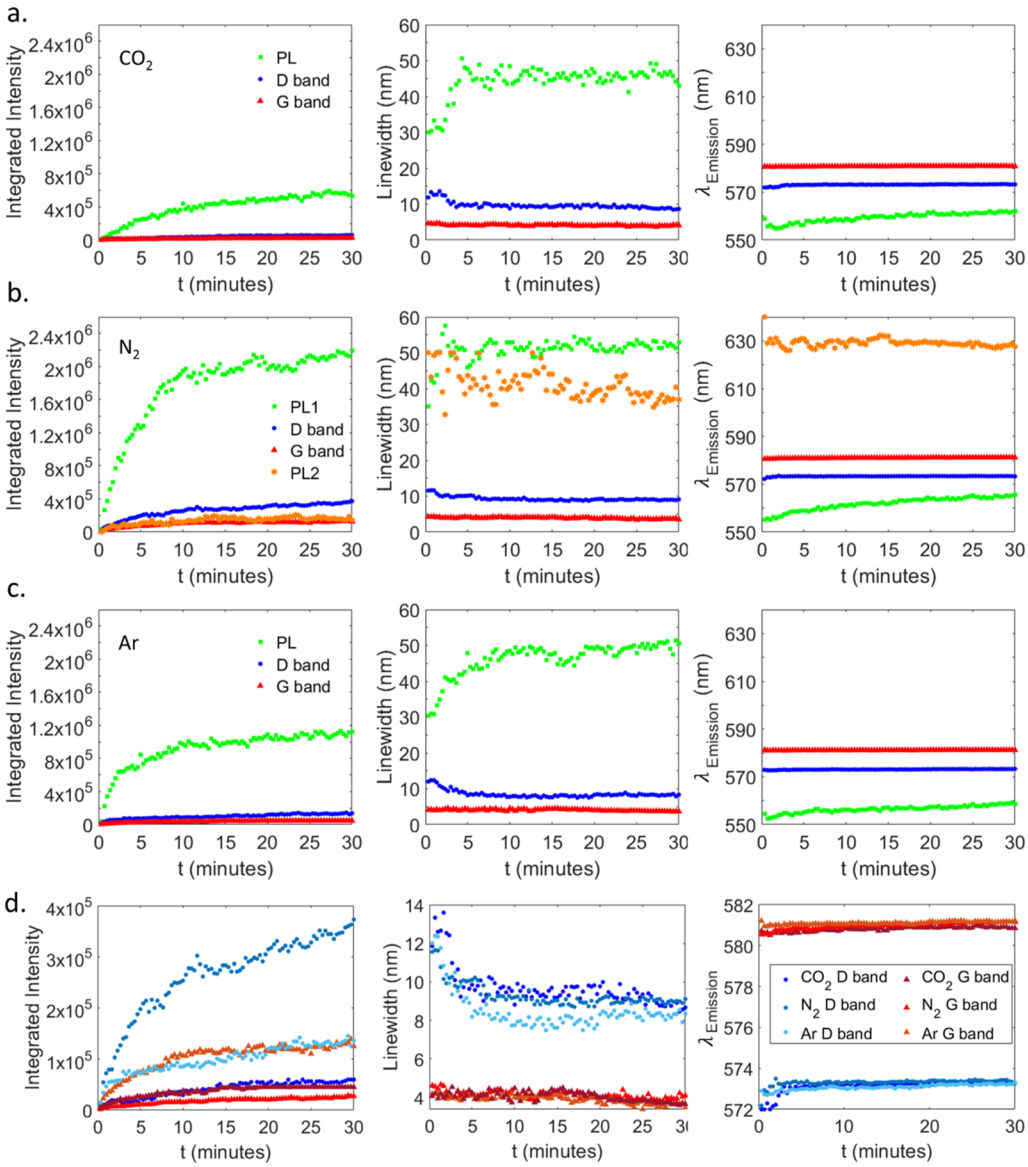

FIG. 8. Extracted peak parameters. Row (a) Integrated peak intensities, linewidths, and emission wavelengths extracted from deconvolving the CO_2 gas dataset in Fig. 7(a). Rows (b) and (c) similarly, for the N_2 and Ar gas datasets of Figs. 7(b) and 7(c), respectively. Scaling is consistent throughout (a)–(c) such that the graphs may be compared directly. Row (d) Summary of extracted D and G peak parameters in CO_2, N_2, and Ar, plotted on expanded scales.

flat Ag regions close to gratings on the same sample were tested in the same CO_2 environment, yielding no PL. Thus, excitation of surface plasmons is essential to the observation of visible PL.

The pyrolytic carbon residue that remains on the surface post-fabrication [cf., black trace, Fig. 2(c)] is also critical to the observation of PL. A control experiment conducted with Ag gratings that were milled using a Ga ion beam produced reasonable optical coupling into surface plasmons yet yielded no PL. In another control, 200 nm of silver was deposited onto a grating fabricated following the process of Fig. 1(a) to cover the residue without compromising the optical performance of the grating, and the structure did not yield any PL.

DISCUSSION

Formation of luminescent carbon dots

PL emerged only when the gratings were excited in gases devoid of O_2, such as high-purity CO_2, N_2, and Ar [Figs. 7(a)–7(c)]. Molecular O_2 is a known quencher of fluorescence by direct

19 June 2025 19:33:55

Published under an exclusive license by AIP Publishing

energy transfer via collisions where de-excitation of a fluorescent molecule results in the promotion of a π electron in an O_2 molecule ($\pi \rightarrow \pi^*$).[34] An example process is captured by the following quenching relation: $^1A^* + {}^3O_2 \rightarrow {}^1A + {}^1O_2$, where $^1A^*$ and ^1A represent the fluorescent species in its excited and ground singlet states, respectively, $^3O_2$ represents an O_2 molecule in its ground triplet state $^3\Sigma$, and $^1O_2$ represents an O_2 molecule in either of its lowest energy excited singlet states $^1\Delta$ or $^1\Sigma$, the former ($^1\Delta$) lying 0.98 eV above the ground state and the latter ($^1\Sigma$) lying 1.63 eV above the ground state.[34] O_2 state transitions from $^3\Sigma$ to $^1\Delta$ or $^1\Sigma$ are optically forbidden (triplet-singlet transition) but may occur in molecular collisions, and given the low energies involved in these transitions, are likely (in general) if O_2 is abundant. Although we cannot rule out that some quenching by molecular O_2 may occur in our experiments in air and in Ar/O_2, the emergence of PL requires more than the removal of O_2 from the environment. For instance, PL did not emerge in CO_2 when the polarization was rotated by 90° [green trace, Fig. 4(a)] or when a flat region of the same sample was illuminated. PL also did not emerge when the sample was left in an O_2-depleted environment for some time and then illuminated. Furthermore, the times required for PL to emerge and saturate are about 5 and 25 min (Figs. 5, 6, and 8), in a chamber where O_2 was evacuated and replaced with CO_2 before the illumination was applied—these timescales are inconsistent with the evacuation of a quenching gas.

In order for PL to emerge from the Ag gratings, pyrolytic carbon residue and surface plasmons are required in addition to an O_2-depleted environment. The pyrolytic carbon residue provides a source of carbonaceous material on the surface. Plasmonic excitation then induces graphitization of the residue, as evidenced by the sharpening and strengthening of D and G band Raman signals [Figs. 5 and 8(d)]. Although it was not possible to track changes in scattering from modes associated with C–O and C=O vibrations due to the extreme PL in the same spectral region, it was possible to observe the weakening or disappearance of the CH_2 and CH_3 peaks, indicating the removal of these hydrogen species. Thus, in an O_2-depleted environment, plasmonic excitation induces dehydrogenation (and possibly deoxygenation) of the residue and its graphitization. With experimental evidence supporting graphitization together with the strong luminescence observed spectrally and visually (Fig. 7), it is apparent that the residue is at least partially transformed into graphitized CDs,[15] possibly taking the form of graphene quantum dots (GQDs) as the latter are luminescent[15,17] and have a Raman spectral signature consisting predominantly of a D-band and G-band.[18] The varying emission peak of the PL observed on nominally identical gratings [cf., Fig. 4 and 7(a)–7(c)] suggests the formation of CDs of different sizes. This could also speak to sensitivity to the He^+ doses applied because PL differences were observed in the same gas but for different samples (cf., Fig. 4).

The roles of the surface plasmons in our experiments are multiple—initially, the surface plasmons transform the pyrolytic carbon residue into CDs, and then, the plasmons excite the CDs leading to relaxation via luminescence. These roles should be highly efficient given the strong overlap of surface plasmons, initially with

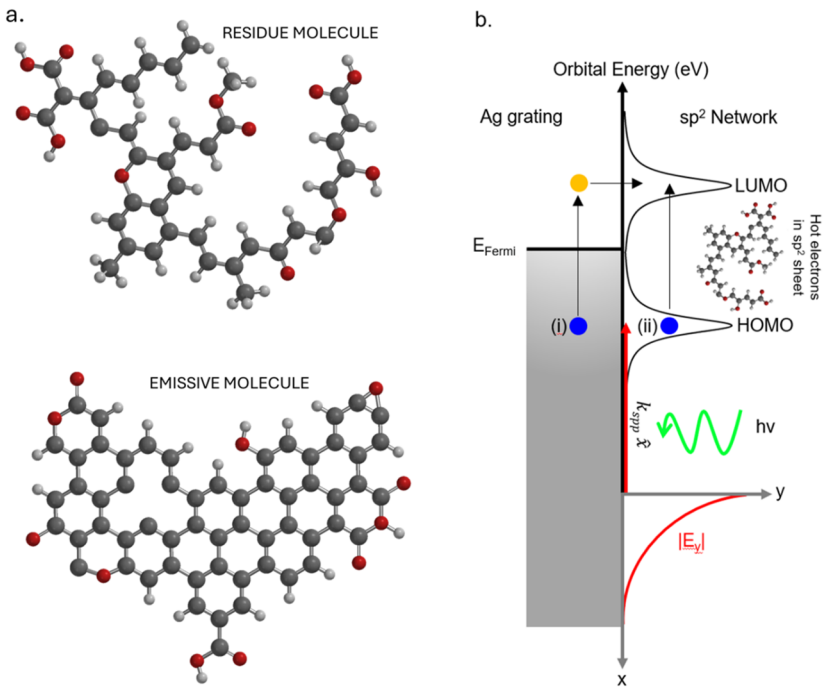

FIG. 9. (a) Models for the pyrolytic carbon residue on the Ag gratings post fabrication. The residue is represented as a defective sp^2 carbon network with terminal groups in addition to edge and basal plane defects (red: O, light gray: H, and dark gray: C). (b) Schematic illustrating the excitation of surface plasmons on the Ag surface. The formation of hot electrons and their transfer from excited Ag states above the Fermi energy to the delocalized LUMO π-states (i), as well as excitation of an electron from HOMO to LUMO states via plasmon decay (ii) are two possible mechanisms to induce the transformation of the residue into CDs.

19 June 2025 19:33:55

Published under an exclusive license by AIP Publishing

the residue, and then with the CDs formed thereon. The roles of the Ag grating are also multiple—the first consists of coupling the incident laser light into surface plasmons, and the second of modifying the emission of the CDs by altering the local optical density of states.[35] Specifically, the grating couples the incident beam at 532 nm to surface plasmons, and then tailors the Stokes-shifted emission from the CDs to peak at green/yellow wavelengths (550–565 nm, Figs. 5 and 8), which remain within the resonance bandwidth of the grating. Surface plasmons are likely playing a role in mediating the emission process, as the CDs relax spontaneously into surface plasmons that are outcoupled by the grating.

Surface inspections

The surface of some of our Ag gratings was imaged via high-resolution AFM and HIM after exposure to CO_2 gas under plasmonic excitation (cf., Fig. 4). CDs could not be observed on the surface with these techniques even after the emergence of strong luminescence, likely because their size and contrast are below the resolution of these techniques on Ag surfaces exhibiting low but non-zero roughness.

Mechanistic picture

A mechanistic picture is proposed for the transformation of pyrolytic carbon residue into CDs in our experiments. The pyrolytic carbon residue is thought to consist of 2D aromatic complexes with various terminal groups, open edge sites, and defects within the basal plane, as sketched in Fig. 9(a). The residue would also be highly disordered: in general, the sp^2-bonded domains would have random orientations and include terraces, steps, and sp^3 bonds that create a highly defective structure. Large sheets of graphene have bandgaps that approach zero, but smaller aromatic fragments (molecular) have non-zero HOMO–LUMO gaps, as sketched in Fig. 9(b).

We propose two schemes where surface plasmons assist in the transformation of the residue. The first scheme illustrated in Fig. 9(b)(i) invokes the decay of surface plasmons in Ag by creating energetic (non-equilibrium) electrons therein, with excess energies up to $h\nu$ (=2.33 eV) above the Fermi energy.[6] These energetic electrons in the Ag grating are localized to the surface and are continuously generated by the CW laser excitation. These energetic electrons can escape Ag and transfer to the aromatic complexes adsorbed on the surface, for instance, into sp^2 framework LUMO states, effectively creating a charge separation layer[36–39] (without an sp^2 network electron–hole recombination in Ag would take place at very short timescales). In an alternative scheme, sketched in Fig. 9(b)(ii), surface plasmons may decay via direct absorption by aromatic complexes adsorbed on the Ag surface, such that the plasmon energy $h\nu$ (=2.33 eV) raises electrons from HOMO to LUMO states. In either scheme [Figs. 9(b)(i) or 9(b)(ii)], excited electrons populate LUMO states of aromatic complexes, and in an O_2-depleted environment (N_2, Ar, and CO_2) induce dehydrogenation (and possibly deoxygenation) of the residue, leading to graphitized CDs.

CONCLUSIONS

In situ Raman scattering measurements reveal the consistent and repeatable formation of CDs on Ag gratings excited by surface plasmons at 532 nm (2.33 eV). The CDs are formed by plasmonic transformation of a carbonaceous seed layer consisting of partially pyrolyzed residue originating from PMMA used in the lithography process applied to fabricate the Ag gratings. The CDs produce bright visible yellow luminescence (~560 nm) under surface plasmon excitation when they are formed in an O_2-depleted environment, specifically, N_2, Ar, and CO_2. The luminescence was ~4× brighter in N_2 relative to CO_2, and ~2× brighter in Ar relative to CO_2. A weak secondary luminescence peak was observed near 630 nm in the case of N_2. Once luminescence was achieved, replacing the environment with air resulted in the eventual disappearance of the luminescence. Luminescent CDs did not form in air or in an Ar/O_2 mixture.

The residue post-fabrication produces weak D and G Raman peaks and peaks corresponding to C–O, C=O, and CH_2/CH_3 vibrations, indicating incomplete pyrolysis of PMMA. Plasmonic excitation of Ag gratings bearing residue graphitizes the latter, as evidenced by the growth of sharp well-defined D and G peaks and the reduction of CH_2/CH_3 peaks relative to the spectrum taken after fabrication. The changes in Raman spectra of the residue and the emergence of luminescence point to plasmon-induced dehydrogenation (and possibly deoxygenation) of the residue leading to graphitized CDs, potentially in the form of GQDs.

O_2 molecular quenching was ruled out by the timescales required for luminescence to emerge and the need for surface plasmon excitation. Thermal effects were ruled out given the linear dependence of the measured rate constant on incident optical power. Mechanistic models were proposed where the decay of surface plasmons into energetic electrons along the Ag surface drives the transformation of the residue into CDs.

Surface plasmons play multiple roles in our experiments: Initially, the plasmons transform the pyrolytic carbon residue into CDs, and then they excite (optically pump) the CDs leading to luminescence. These roles are very efficient given the field enhancement and the strong localization of surface plasmons to the Ag surface. The Ag grating also plays multiple roles: The first consists of coupling the incident laser light into surface plasmons, and the second of modifying the emission of the CDs by altering the local optical density of states. Surface plasmons are also likely to play a role in mediating the emission process.

This light-driven process on a Ag-grating-bearing pyrolytic carbon is of interest in plasmonic catalysis, catalytic processes involving carbon, and luminescent plasmonic devices.

METHODS

FEM simulations

Simulated reflectance and absorptance spectra and electromagnetic field distributions were calculated using commercially available software (COMSOL Mutliphysics) implementing the FEM method. Periodic boundary conditions were used such that only one unit cell of the structure needed to be modeled. A tetrahedral mesh was used with elements ranging from 0.1 to 10 nm in size. The grating design was optimized by calculating the pitch and height (using the parametric sweep feature) to couple normally incident x-polarized 532 nm light to surface plasmons. A 50/50 duty cycle was assumed. The optical parameters of Ag were taken from the literature, interpolated using a cubic-spline function, and used throughout the simulations.[40] As shown in Figs. 3(a) and 3(b), the optimized

19 June 2025 19:33:55

Published under an exclusive license by AIP Publishing

geometry to couple normally incident light at a free-space wavelength of 532 nm is a 50/50 duty cycle rectangular grating of pitch 492.5 nm and ridge height 25 nm. On resonance, the electric field is enhanced over the illuminated area of the grating surface such that this entire area continuously supplies hot electrons under continuous wave irradiation. The magnitude of the electric field near the surface of the Ag grating increases by a factor of 15 upon absorption of 532 nm light, and the strongest electric fields occur near the corners of the Ag ridges. These locations will have the highest density of excited charge carriers; thus, the chemical transformation of an adsorbate, driven by hot electrons, has the highest probability of occurring there.

Ag grating fabrication and AFM characterization

A Si substrate was first cleaned in ultrasonic baths of acetone and IPA, followed by drying with nitrogen gas. Ag pellets (99.99% purity) were electron-beam evaporated (Angstrom Engineering NEXDEP physical vapor deposition system) to grow a 100 nm thick film, at a rate of 5 Å/s, onto a 10 nm thick Ti adhesion layer, on the Si substrate. A 70 nm thick layer of polymethylmethacrylate (PMMA) resist (950 k mol. wt., Kayaku Advanced Materials) was spin-coated onto the Ag layer (Laurell WS-650-23NPP spin coater), and then baked at 180 °C for an hour.

During fabrication, imperfections, such as surface roughness, as well as small deviations in duty cycle and ridge amplitude, alter the optical response of realized Ag gratings, causing the resonant pitch to intractably shift from the theoretical value. To compensate, 36 grating arrays were fabricated with pitches ranging from 450 to 520 nm (but otherwise identical), and their specular reflectance responses were measured at 532 nm for x-polarized light (see below).

Patterning of the photoresist was carried out using a helium ion beam lithography process described elsewhere.[23] Briefly, the grating structures were patterned into the PMMA resist using a Zeiss Orion NanoFab HIM. The layout and exposure were controlled using the Fibics Nanopatterning and Visualization Engine (NPVE). A beam current of 0.5 pA at a landing energy of 25 kV was used to deliver a dot-dose exposure with an x = y step size of 2 nm, and a dwell time of 0.5 μs (for a dose of 7 μC/cm^2), to pattern 50/50 duty-cycle gratings over an area of 30 × 30 μm^2. PMMA was developed in a 1:3 mixture of methyl isobutyl ketone (MIBK) and isopropanol (IPA) for 2 min at 20 °C, followed by a 30 second IPA bath.

A 25 nm (target thickness) thick Ag layer was then evaporated at a rate of 0.5 Å/s by an electron beam evaporator, operating at 10^{-8} Torr, to form the grating ridges. The sample was then submerged in acetone for 24 h at room temperature to carry out PMMA lift-off, leaving behind silver grating ridges. AFM topographical scans of the Ag gratings were obtained in tapping mode using a Park Systems NX10 AFM equipped with a Tap300Al-G tip from NanoAndMore to determine the final step height and roughness. The actual height of the fabricated gratings presented in this study is 30.6 nm.

HIM imaging

High-resolution HIM imaging was carried out on a Zeiss Orion NanoFab HIM. The top-down image appearing in Fig. 2(a) was acquired using a gas-field ion source field of view (GFIS-FOV) of 2 μm, a beam current of 1.33 pA, and a dwell time of 1 μs (1024 × 1024 pixels).

Specular reflectance, Raman, and PL spectroscopy

All optical and Raman measurements were carried out on a WiTec a300 Raman microscope. A CCD camera (Princeton Acton SP300) cooled to −70 °C, and a 600 groove/mm grating blazed at 500 nm, provided spectral readout at a resolution of ~4 cm^{-1}. Generally, a Raman microscope will also naturally detect any laser-induced PL in a sample. With the filter removed, the Raman microscope was used to perform specular reflectance measurements on freshly fabricated gratings. Since the experiment relies on coupling 532 nm light to Ag gratings, and the simulations employed plane-wave approximations, a loosely focused beam formed by a 5 × 0.25 N.A. objective was used for all measurements involving gasses and/or the excitation of surface plasmons [cf., Fig. 1(b)]. Specular reflectance measurements were performed at normal incidence using less than 50 μW of laser power to avoid damage to the camera (Raman notch filter removed). The laser was aligned to a grating and fine x–y–z adjustments were made to minimize counts on the spectrograph. Each value was normalized to the measured specular reflectance of a nearby unstructured region of the same Ag film.

Raman and PL emission measurements were performed *in situ*, in the backscattering configuration, using a custom gas flow cell. The cell was machined from aluminum and has ports to introduce and evacuate gas from the chamber. A 100 μm thick microscope cover slip positioned 1.2 cm away from the sample surface provided a transparent window for laser excitation and detection of backscattered light. The large distance between the window and the sample surface also ensured that Raman signals from the coverslip were not detected. Time evolution measurements were performed with the sample exposed to ~1.95 atm (14 psig) of CO_2, N_2, Ar, and 20% O_2/Ar mixture (Messer Canada) under continuous flow while being illuminated by 10 mW of 532 nm CW laser light. The intense emission recorded after 30 min of gas exposure required the use of an extremely short 5 ms integration time. Each spectrum plotted was averaged from 200 spectral acquisitions (total time 1 s) recorded at a set time interval. All spectra with gratings exposed to gases were acquired using the same measurement parameters. The residue remaining post-fabrication was examined using a high-magnification 100× objective. Residue signals were notoriously difficult to resolve using a 5× objective lens.

SUPPLEMENTARY MATERIALS

The supplementary materials file describes the method used to deconvolve the measured spectra reported in Figs. 4 and 7(a)–7(c) into Lorentzian contributions, and Figs. S1 and S2 plot representative deconvolutions.

ACKNOWLEDGMENTS

The authors acknowledged the Natural Sciences and Engineering Research Council of Canada (NSERC), the Canada Foundation for Innovation (CFI), the Ontario Ministry of Research and Innovation (MRI), and the Department of National Defense through

19 June 2025 19:33:55

Published under an exclusive license by AIP Publishing

its IDEaS program. They also acknowledged CMC Microsystems for providing access to the COMSOL Multiphysics software environment.

AUTHOR DECLARATIONS

Conflict of Interest

The authors have no conflicts to disclose.

Author Contributions

J.W. conceived the project, performed FEM calculations and Raman scattering measurements, analyzed all data/developed models, and wrote and revised the manuscript. S.R. developed the HIM FIB exposure process, fabricated the grating structures, and performed the HIM imaging and AFM measurements, and contributed writing to the manuscript. G.K. and M.S.A.N. contributed to the analysis. F.V. contributed to the Raman and PL characterization measurements. P.B. conceived and supervised the project with A.W. All authors contributed to data interpretation and helped revise the manuscript.

Jaspreet Walia: Conceptualization (equal); Formal analysis (lead); Investigation (lead); Methodology (equal); Visualization (lead); Writing – original draft (lead); Writing – review & editing (supporting). **Sabaa Rashid**: Conceptualization (equal); Formal analysis (equal); Investigation (equal); Methodology (equal); Visualization (lead); Writing – original draft (supporting). **Maryam Sadat Amiri Naeini**: Formal analysis (supporting); Visualization (supporting); Writing – review & editing (supporting). **Graham Killaire**: Formal analysis (supporting); Investigation (supporting); Methodology (supporting); Visualization (supporting); Writing – original draft (supporting); Writing – review & editing (supporting). **Fabio Variola**: Investigation (supporting); Resources (supporting); Supervision (supporting); Visualization (supporting); Writing – review & editing (supporting). **Arnaud Weck**: Formal analysis (equal); Investigation (supporting); Methodology (supporting); Resources (supporting); Supervision (supporting); Writing – review & editing (supporting). **Pierre Berini**: Conceptualization (equal); Formal analysis (equal); Funding acquisition (lead); Investigation (supporting); Methodology (equal); Project administration (lead); Resources (lead); Supervision (lead); Writing – review & editing (supporting).

DATA AVAILABILITY

The data that support the findings of this study are available within the article and its supplementary materials.

REFERENCES

[1]S. Linic, P. Christopher, and D. B. Ingram, "Plasmonic-metal nanostructures for efficient conversion of solar to chemical energy," Nat. Mater. **10**(12), 911–921 (2011).
[2]P. Christopher, H. Xin, and S. Linic, "Visible-light-enhanced catalytic oxidation reactions on plasmonic silver nanostructures," Nat. Chem. **3**(6), 467–472 (2011).
[3]Y. Zhang, S. He, W. Guo, Y. Hu, J. Huang, J. R. Mulcahy, and W. D. Wei, "Surface-plasmon-driven hot electron photochemistry," Chem. Rev. **118**(6), 2927–2954 (2017).
[4]E. Cortés, W. Xie, J. Cambiasso, A. S. Jermyn, R. Sundararaman, P. Narang, S. Schlücker, and S. A. Maier, "Plasmonic hot electron transport drives nano-localized chemistry," Nat. Commun. **8**(1), 14880 (2017).
[5]L. Zhou, D. F. Swearer, C. Zhang, H. Robatjazi, H. Zhao, L. Henderson, L. Dong, P. Christopher, E. A. Carter, P. Nordlander, and N. J. Halas, "Quantifying hot carrier and thermal contributions in plasmonic photocatalysis," Science **362**(6410), 69–72 (2018).
[6]P. Narang, R. Sundararaman, and H. A. Atwater, "Plasmonic hot carrier dynamics in solid-state and chemical systems for energy conversion," Nanophotonics **5**(1), 96–111 (2016).
[7]W. Ni, H. Ba, A. A. Lutich, F. Jäckel, and J. Feldmann, "Enhancing single-nanoparticle surface-chemistry by plasmonic overheating in an optical trap," Nano Lett. **12**(9), 4647–4650 (2012).
[8]G. Baffou, R. Quidant, and F. J. García de Abajo, "Nanoscale control of optical heating in complex plasmonic systems," ACS Nano **4**(2), 709–716 (2010).
[9]G. Kumari, R. Kamarudheen, E. Zoethout, and A. Baldi, "Photocatalytic surface restructuring in individual silver nanoparticles," ACS Catal. **11**, 3478–3486 (2021).
[10]G. Kumari, X. Zhang, D. Devasia, J. Heo, and P. K. Jain, "Watching visible light-driven CO_2 reduction on a plasmonic nanoparticle catalyst," ACS Nano **12**(8), 8330–8340 (2018).
[11]X. Zhang, G. Kumari, J. Heo, and P. K. Jain, "In situ formation of catalytically active graphene in ethylene photo-epoxidation," Nat. Commun. **9**, 3056 (2018).
[12]Z. Hirbodvash, O. Krupin, H. Northfield, A. Olivieri, E. A. Baranova, and P. Berini, "Infrared surface plasmons on a Au waveguide electrode open new redox channels associated with the transfer of energetic carriers," Sci. Adv. **8**, eabm9303 (2022).
[13]Z. Hirbodvash, E. A. Baranova, and P. Berini, "Real-time convolutional voltammetry enhanced by energetic (hot) electrons and holes on a surface plasmon waveguide electrode," Anal. Chem. **94**, 13145–13152 (2022).
[14]J. Walia, S. Rashid, G. Killaire, F. Variola, A. Weck, and P. Berini, "Reconfigurable carbon quantum emitters from CO_2 gas reduced via surface plasmons," Optica **8**(5), 708 (2021).
[15]S. N. Baker and G. A. Baker, "Luminescent carbon nanodots: Emergent nanolights," Angew. Chem., Int. Ed. **49**, 6726–6744 (2010).
[16]Y. P. Sun, B. Zhou, Y. Lin, W. Wang, K. A. S. Fernando, P. Pathak, M. J. Meziani, B. A. Harruff, X. Wang, H. Wang, and P. G. Luo, "Quantum-sized carbon dots for bright and colorful photoluminescence," J. Am. Chem. Soc. **128**(24), 7756–7757 (2006).
[17]X. T. Zheng, A. Ananthanarayanan, K. Q. Luo, and P. Chen, "Glowing graphene quantum dots and carbon dots: Properties, syntheses, and biological applications," Small **11**(14), 1620–1636 (2015).
[18]E. Dervishi, Z. Ji, H. Htoon, M. Sykora, and S. K. Doorn, "Raman spectroscopy of bottom-up synthesized graphene quantum dots: Size and structure dependence," Nanoscale **11**(35), 16571–16581 (2019).
[19]K. M. Tripathi, T. S. Tran, Y. J. Kim, and T. Kim, "Green fluorescent onion-like carbon nanoparticles from flaxseed oil for visible light induced photocatalytic applications and label-free detection of Al(III) ions," ACS Sustainable Chem. Eng. **5**(5), 3982–3992 (2017).
[20]S. Zhu, Y. Song, X. Zhao, J. Shao, J. Zhang, and B. Yang, "The photoluminescence mechanism in carbon dots (graphene quantum dots, carbon nanodots, and polymer dots): Current state and future perspective," Nano Res. **8**(2), 355–381 (2015).
[21]L. Li, G. Wu, G. Yang, J. Peng, J. Zhao, and J. J. Zhu, "Focusing on luminescent graphene quantum dots: Current status and future perspectives," Nanoscale **5**(10), 4015–4039 (2013).
[22]K. Lingam, R. Podila, H. Qian, S. Serkiz, and A. M. Rao, "Evidence for edge-state photoluminescence in graphene quantum dots," Adv. Funct. Mater. **23**(40), 5062–5065 (2013).
[23]S. Rashid, J. Walia, H. Northfield, C. Hahn, A. Olivieri, A. C. Lesina, F. Variola, A. Weck, L. Ramunno, and P. Berini, "Helium ion beam lithography and liftoff," Nano Futures **5**(2), 025003 (2021).

19 June 2025 19:33:55

Published under an exclusive license by AIP Publishing

[24]D. C. Bell, "Contrast mechanisms and image formation in helium ion microscopy," Microsc. Microanal. **15**(2), 147–153 (2009).
[25]B. W. Ward, J. A. Notte, and N. P. Economou, "Helium ion microscope: A new tool for nanoscale microscopy and metrology," J. Vac. Sci. Technol., B: Microelectron. Nanometer Struct.-Process., Meas., Phenom. **24**(6), 2871–2874 (2006).
[26]F. Pallikari, G. Chondrokoukis, M. Rebelakis, and Y. Kotsalas, "Raman spectroscopy: A technique for estimating extent of polymerization in PMMA," Mater. Res. Innovations **4**(2-3), 89–92 (2001).
[27]J. Robertson and E. P. O'Reilly, "Electronic and atomic structure of amorphous carbon," Phys. Rev. B **35**(6), 2946–2957 (1987).
[28]A. Cuesta, P. Dhamelincourt, J. Laureyns, A. Martinez-Alonso, and J. D. Tascón, "Raman microprobe studies on carbon materials," Carbon **32**(8), 1523–1532 (1994).
[29]A. C. Ferrari and J. Robertson, "Interpretation of Raman spectra of disordered and amorphous carbon," Phys. Rev. B **61**(20), 14095 (2000).
[30]A. C. Ferrari and J. Robertson, "Raman spectroscopy of amorphous, nanostructured, diamond–like carbon, and nanodiamond," Philos. Trans. R. Soc., A **362**(1824), 2477–2512 (2004).
[31]J. Walia, S. Rashid, F. Variola, and P. Berini, "Focussed helium ion beam exposure of polymethylmethacrylate: Positive or negative tone images, polyenes, and fluorescent carbon layers," Adv. Eng. Mater. **25**, 2201707 (2023).
[32]F. Volmer, I. Seidler, T. Bisswanger, J. S. Tu, L. R. Schreiber, C. Stampfer, and B. Beschoten, "How to solve problems in micro- and nanofabrication caused by the emission of electrons and charged metal atoms during e-beam evaporation," J. Phys. D: Appl. Phys. **54**(22), 225304 (2021).
[33]M. J. Kale, T. Avanesian, and P. Christopher, "Direct photocatalysis by plasmonic nanostructures," ACS Catal. **4**(1), 116–128 (2014).
[34]B. Valeur and M. N. Berberan-Santos, *Molecular Fluorescence Principles and Applications*, 2nd ed. (Wiley VCH, 2012).
[35]W. L. Barnes, "Fluorescence near interfaces: The role of photonic mode density," J. Mod. Opt. **45**(4), 661–699 (1998).
[36]S. Nabil, A. S. Hammad, H. M. El-Bery, E. A. Shalaby, and A. H. El-Shazly, "The CO_2 photoconversion over reduced graphene oxide based on Ag/TiO_2 photocatalyst in an advanced meso-scale continuous-flow photochemical reactor," Environ. Sci. Pollut. Res. **28**(27), 36157–36173 (2021).
[37]N. Shehzad, M. Tahir, K. Johari, T. Murugesan, and M. Hussain, "Improved interfacial bonding of graphene-TiO_2 with enhanced photocatalytic reduction of CO_2 into solar fuel," J. Environ. Chem. Eng. **6**(6), 6947–6957 (2018).
[38]J. Hou, H. Cheng, O. Takeda, and H. Zhu, "Three-dimensional bimetal-graphene-semiconductor coaxial nanowire arrays to harness charge flow for the photochemical reduction of carbon dioxide," Angew. Chem., Int. Ed. **54**(29), 8480–8484 (2015).
[39]H. Zhang, T. Wang, J. Wang, H. Liu, T. D. Dao, M. Li, G. Liu, X. Meng, K. Chang, L. Shi, T. Nagao, and J. Ye, "Surface-plasmon-enhanced photodriven CO_2 reduction catalyzed by metal–organic-framework-derived iron nanoparticles encapsulated by ultrathin carbon layers," Adv. Mater. **28**(19), 3703–3710 (2016).
[40]A. D. Rakić, A. B. Djurišić, J. M. Elazar, and M. L. Majewski, "Optical properties of metallic films for vertical-cavity optoelectronic devices," Appl. Opt. **37**(22), 5271–5283 (1998).

19 June 2025 19:33:55

Published under an exclusive license by AIP Publishing

Surface plasmons on silver gratings transform pyrolytic carbon into luminescent graphitized carbon dots

Jaspreet Walia,[a,b,*] Sabaa Rashid,[c] Maryam Sadat Amiri Naeini,[a,d] Graham Killaire,[a,d] Fabio Variola,[e] Arnaud Weck,[a,d,e] and Pierre Berini[a,b,d,*]

[a]Nexus for Quantum Technologies Institute, University of Ottawa, Ontario, Canada
[b]School of Electrical Engineering and Computer Science, University of Ottawa, Ottawa, Ontario, Canada
[c]Formerly with: Nexus for Quantum Technologies Institute, University of Ottawa, Ontario, Canada; now with: Canadian Centre for Electron Microscopy, McMaster University, Hamilton, Ontario, Canada
[d]Department of Physics, University of Ottawa, Ottawa, Ontario, Canada
[e]Department of Mechanical Engineering, University of Ottawa, Ontario, Canada

[*]Corresponding Author:
Pierre Berini, ...

Spectral deconvolution

To fit the measured Raman spectra to a sum of Lorentzian functions, a step-by-step fitting procedure was applied to the measurements in each gas. In this procedure, the Raman spectrum measured at the middle time point (15 minutes) for a gas was selected, and the overall spectrum was fit to a first Lorentzian function accounting for the main peak attributed to the PL contribution. Then, fixing this Lorentzian function, a second was introduced to fit the D band contribution. Then fixing the first two Lorentzian functions, a third was added to fit the G band contribution. The area, centres, and linewidths were manually adjusted to achieve a good fit by eye. Finally, the three Lorentzian functions were simultaneously optimized numerically using the Levenburg-Marquadt algorithm to improve the overall fit to the measured spectrum.

Once a good fit was achieved to the measured spectrum at the middle time point (15 minutes), the fit results were then used as the initial guess to fit the preceding (succeeding) time points. Fitting continued in this manner to the first (last) time points, using the fit results of the succeeding (preceding) time point as the initial guess.

All spectra in CO_2 were very well deconvolved using only 3 Lorentzian functions (Figs. 4, 7a), but a fourth Lorentzian function (extracted in the same manner) was required to improve the fit in N_2 (Fig. 7b). The fit to the spectra measured in Ar benefitted only marginally by adding a fourth Lorentzian and so 3 were retained.

a.

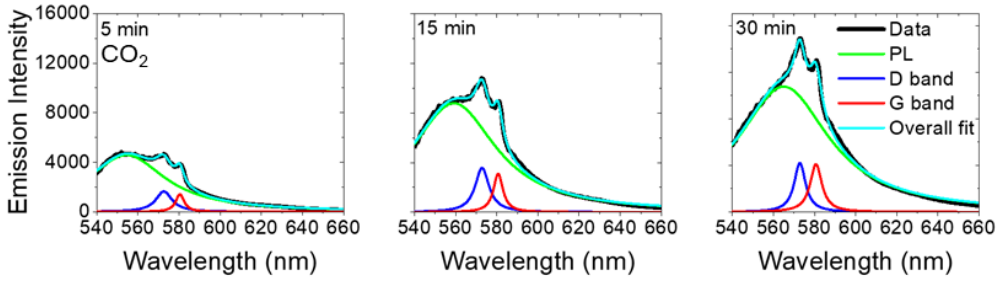

b.

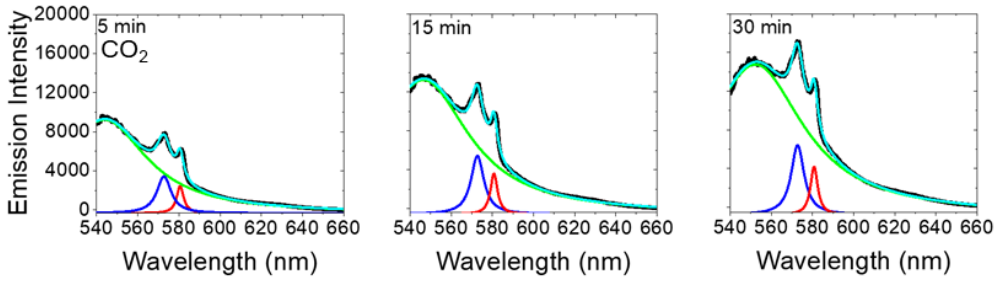

Fig. S1: a, Representative deconvolutions of the measured data appearing in Fig. 4a (main text) after 5, 15 and 30 min in CO_2 into three Lorentzian contributions: PL emission band (green curve), and two Raman scattering bands assigned to D and G peaks (blue and red curves) from graphite-like carbon. b, Representative deconvolutions of the measured data appearing in Fig. 4b (main text), also in CO_2.

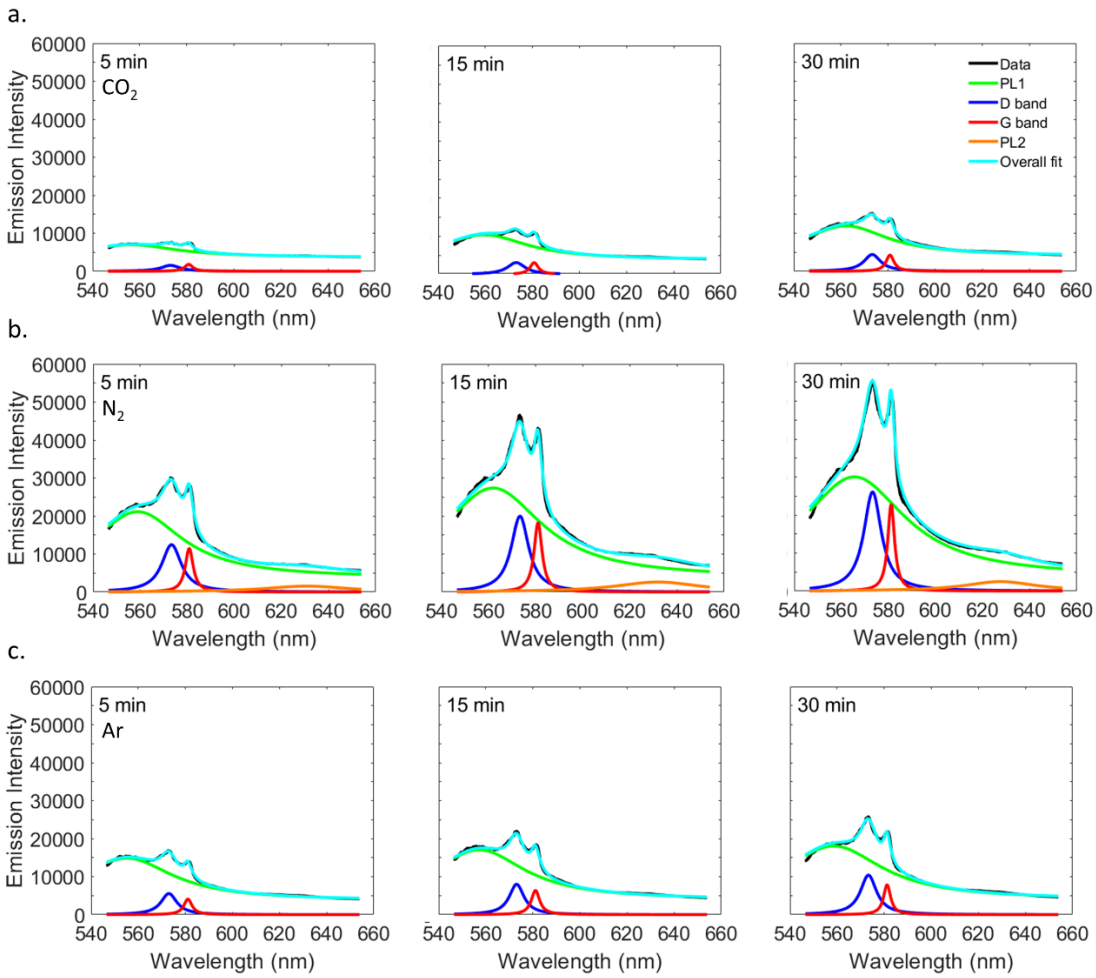

Fig. S2: a, Representative deconvolutions of the measured data appearing in Fig. 7a after 5, 15 and 30 min in CO_2 into three Lorentzian contributions: PL emission band (green curve), and two Raman scattering bands assigned to D and G peaks (blue and red curves) from graphite-like carbon. b and c, Representative deconvolutions of the measured data appearing in Figs. 7b and 7c for N_2 and Ar, respectively. The N_2 data fits to four Lorentzian contributions including a weak second PL emission band at longer wavelengths (orange curve).

References

[1] N. Alfaraj and A. Helmy, "Silicon-Integrated Next-Generation Plasmonic Devices for Energy-Efficient Semiconductor Applications," *arXiv preprint arXiv:2503.19235,* 2025.

[2] A. Shrivastav, U. Cvelbar and I. Abdulhalim, "A comprehensive review on plasmonic-based biosensors used in viral diagnostics," *Communications biology,* vol. 4, no. 1, p. 70, 2021.

[3] Z. Hirbodvash and P. Berini, "Surface plasmon electrochemistry: Tutorial and Review," *Chemosensors,* vol. 11, no. 3, p. 196, 2023.

[4] Y. Guo, Z. Xu, A. Curto, Y. Zeng and D. Van Thourhout, "Plasmonic semiconductors: materials, tunability and applications," *Progress in Materials Science,* vol. 138, p. 101158, 2023.

[5] D. Semeniak, D. Cruz, A. Chilkoti and M. Mikkelsen, "Plasmonic fluorescence enhancement in diagnostics for clinical tests at point-of-care: A review of recent technologies," *Advanced Materials,* vol. 35, no. 34, p. 2107986, 2023.

[6] Q. Yang, Y. Wu, J. Chen, M. Lu, X. Wang, Z. Zhang, H. Xiong, J. Choo and L. Chen, "Plasmonic nanomaterial-enhanced fluorescence and Raman sensors: Multifunctional platforms and applications," *Coordination Chemistry Reviews,* vol. 507, p. 215768, 2024.

[7] M. Bauch, K. Toma, M. Toma, Q. Zhang and J. Dostalek, "Plasmon-enhanced fluorescence biosensors: a review," *Plasmonics,* vol. 9, pp. 781-799, 2014.

[8] A. Traverso, J. Huang, T. Peyronel, G. Yang, T. Tiecke and M. Mikkelsen, "Low-loss, centimeter-scale plasmonic metasurface for ultrafast optoelectronics," *Optica,* vol. 8, no. 2, pp. 202-207, 2021.

[9] B. Liang, Y. Xu, N. Yu, Z. Yang, M. Wilson, D. Xu, R. Shams, L. Wang, C. Lui, R. Yan and M. Liu, "Enhanced Plasmonic Trapping and Fluorescent Emission of Nitrogen-Vacancy Nanodiamonds Using a High-Efficiency Nanofocusing Device," *Nano Letters,* vol. 24, no. 37, pp. 11661-11668, 2024.

[10] S. A. Maier, Plasmonics: Fundamentals and Applications, Springer, 2007.

[11] S. V. Gaponenko, Introduction to Nanophotonics, Cambridge University Press, 2010.

[12] G. K. P. Ramanandan, G. Ramakrishnan, N. Kumar, A. J. L. Adam and P. C. M. Planken, "Emission of terahertz pulses from nanostructured metal surfaces," *Journal of Physics D: Applied Physics,* vol. 47, pp. 374003-374018, 2014.

[13] H. Raether, Surface Plasmons on Smooth and Rough Surfaces and on Gratings, Springer Tracts in Modern Physics (STMP, volume 111), 1988.

[14] C. Huang and J. Huang, "Integrated plasmonics nanocircuits," in *Plasmonic Materials and Metastructures*, Elsevier, 2024, pp. 245-283.

[15] H. Reddy and V. Shalaev, "Plasmonic hot-carriers and their applications: opinion," *Optical Materials Express,* vol. 11, no. 11, pp. 3827-3832, 2021.

[16] D. Lei, D. Su and S. Maier, "New insights into plasmonic hot-electron dynamics," *Light: Science & Applications,* vol. 13, no. 1, p. 243, 2024.

[17] Y. Yu, J. Zhang, L. Wang, Z. Ni, J. Lu and L. Gao, "Hot-carrier engineering for two-dimensional integrated infrared optoelectronics," *InfoMat,* vol. 6, no. 9, p. e12556, 2024.

[18] A. Chen and E. Murphy, Broadband Optical Modulators: Science, Technology, and Applications, CRC press, 2011.

[19] M. Xu and X. Cai, "Advances in integrated ultra-wideband electro-optic modulators," *Optics express,* vol. 30, no. 5, pp. 7253-7274, 2022.

[20] G. T. Reed, G. Mashanovich, F. Y. Gardes and D. J. Thomson, "Silicon Optical Modulators," *Nature Photonics,* vol. 4, no. 8, pp. 518-526, 2010.

[21] K. Luke, P. Kharel, C. Reimer, L. He, M. Loncar and M. Zhang, "Wafer-scale low-loss lithium niobate photonic integrated circuits," *Optics Express,* vol. 28, no. 17, pp. 24452-24458, 2020.

[22] N. Chen, Y. Yu, K. Lou, Q. Mi and T. Chu, "High-efficiency thin-film lithium niobate modulator with highly confined optical modes," *Optics Letters,* vol. 48, no. 7, pp. 1602-1605, 2023.

[23] X. Y. D. Zhou, D. Chan and H. Tsang, "Silicon photonics for high-speed communications and photonic signal processing," *npj Nanophotonics,* vol. 1, no. 1, p. 27, 2024.

[24] E. Li and A. Wang, "Theoretical analysis of energy efficiency and bandwidth limit of silicon photonic modulators," *Journal of Lightwave Technology,* vol. 37, no. 23, pp. 5801-5813, 2019.

[25] C. Han, Z. Zheng, H. Shu, M. Jin, J. Qin, R. Chen, Y. Tao, B. Shen, B. Bai, F. Yang and Y. Wang, "Slow-light silicon modulator with 110-GHz bandwidth," *Science Advances,* vol. 9, no. 42, p. eadi5339, 2023.

[26] J. Liu, M. Beals, A. Pomerene, S. Bernardis, R. Sun, J. Cheng, L. Kimerling and J. Michel, "Waveguide-integrated, ultralow-energy GeSi electro-absorption modulators," *Nature photonics,* vol. 2, no. 7, pp. 433-437, 2008.

[27] J. Fujikata, M. Noguchi, K. Kawashita, R. Katamawari, S. Takahashi, M. Nishimura, H. Ono, D. Shimura, H. Takahashi, H. Yaegashi and T. Nakamura, "High-speed Ge/Si electro-absorption optical modulator in C-band operation wavelengths," *Optics express,* vol. 28, no. 22, pp. 33123-33134, 2020.

[28] Y. Kuo, Y. Lee, Y. Ge, S. Ren, J. Roth, T. Kamins, D. Miller and J. Harris, "Strong quantum-confined Stark effect in germanium quantum-well structures on silicon," *Nature,* vol. 437, no. 7063, pp. 1334-1336, 2005.

[29] J. Roth, O. Fidaner, E. Edwards, R. Schaevitz, Y. Kuo, N. Helman, T. Kamins, J. Harris and D. Miller, "C-band side-entry Ge quantum-well electroabsorption modulator on SOI operating at 1 V swing," *Electronics Letters,* vol. 44, no. 1, pp. 49-50, 2008.

[30] J. Roth, O. Fidaner, R. Schaevitz, Y. Kuo, T. Kamins, J. Harris and D. Miller, "Optical modulator on silicon employing germanium quantum wells," *Optics Express,* vol. 15, no. 9, pp. 5851-5859, 2007.

[31] Y. Kuo, Y. Lee, Y. Ge, S. Ren, J. Roth, T. Kamins, D. Miller and J. Harris, "Quantum-confined Stark effect in Ge/SiGe quantum wells on Si for optical modulators," *IEEE Journal of selected topics in quantum electronics,* vol. 12, no. 6, pp. 1503-1513, 2006.

[32] D. Steckler, S. Lischke and L. Zimmermann, "Integrating high-speed germanium modulators with silicon photonics and fast electronics," PIC Magazine.net, 2024.

[33] Y. Chang and M. Lipson, "Nanophotonic devices for power-efficient communications," *In Optical fiber telecommunications VII Academic Press,* pp. 103-141, 2020.

[34] V. Petrov, P. Agruzov, V. Lebedev, I. Il'ichev and A. Shamray, "Broadband integrated optical modulators: Achievements and prospects," *Physics-Uspekhi,* vol. 64, no. 7, p. 722, 2021.

[35] C. Shih and C. Sanders, "Low-loss plasmonic metals epitaxially grown on semiconductors," in *Plasmonic Materials and Metastructures*, Elsevier, 2024, pp. 73-101.

[36] M. a. S. V. Brongersma, "The case for plasmonics," *science,* vol. 328, no. 5977, pp. 440-441, 2010.

[37] U. Koch, C. Uhl, H. Hettrich, Y. Fedoryshyn, D. Moor, M. Baumann, C. Hoessbacher, W. Heni, B. Baeuerle, B. Bitachon and A. Josten, "Plasmonics—High-speed photonics for co-integration with electronics," *Japanese Journal of Applied Physics,* vol. 60, no. SB, p. SB0806, 2021.

[38] Y. Fang and M. Sun, "Nanoplasmonic waveguides: towards applications in integrated nanophotonic circuits," *Light: Science & Applications,* vol. 4, no. 6, pp. e294-e294, 2015.

[39] M. Fukuda, S. Okahisa, Y. Tonooka, M. Ota, T. Aihara and Y. Ishikawa, "Feasibility of plasmonic circuits in nanophotonics," *IEEE Access,* vol. 8, pp. 142495-142506, 2020.

[40] D. Chauhan, Z. Sbeah, R. Dwivedi, J. Nunzi and M. Thakur, "An investigation and analysis of plasmonic modulators: a review," *Journal of Optical Communications,* vol. 45, no. 3, pp. 483-511, 2024.

[41] J. Smajic and J. Leuthold, "Plasmonic Electro-Optic Modulators–A Review," *IEEE Journal of Selected Topics in Quantum Electronics,* vol. 30, no. 4: Adv. Mod. and Int. beyond Si and InP-based Plt, pp. 1-13, 2024.

[42] J. Brosi, C. Koos, L. Andreani, M. Waldow, J. Leuthold and W. Freude, "High-speed low-voltage electro-optic modulator with a polymer-infiltrated silicon photonic crystal waveguide," *Optics Express,* vol. 16, no. 6, pp. 4177-4191, 2008.

[43] C. Hössbacher, A. Josten, B. Baeuerle, Y. Fedoryshyn, H. Hettrich, Y. Salamin, W. Heni, C. Haffner, C. Kaiser, R. Schmid and D. e. a. Elder, "Plasmonic modulator with> 170 GHz bandwidth demonstrated at 100 GBd NRZ," *Optics Express,* vol. 25, no. 3, pp. 1762-1768, 2017.

[44] M. Burla, C. Hoessbacher, W. Heni, C. Haffner, Y. Fedoryshyn, D. Werner, T. Watanabe, H. Massler, D. Elder, L. Dalton and J. Leuthold, "500 GHz plasmonic Mach-Zehnder modulator enabling sub-THz microwave photonics," *Apl Photonics,* vol. 4, no. 5, 2019.

[45] M. Ayata, Y. Fedoryshyn, W. Heni, B. Baeuerle, A. Josten, M. Zahner, U. Koch, Y. Salamin, C. Hoessbacher, C. Haffner, D. Elder, L. Dalton and J. Leuthold, "High-speed plasmonic modulator in a single metal layer," *Science,* vol. 358, no. 6363, pp. 630-632, 2017.

[46] U. Koch, C. Uhl, H. Hettrich, Y. Fedoryshyn, C. Hoessbacher, W. Heni, B. Baeuerle, B. Bitachon, A. Josten, M. Ayata and H. e. a. Xu, "A monolithic bipolar CMOS electronic–plasmonic high-speed transmitter," *Nature electronics,* vol. 3, no. 6, p. 338–345, 2020.

[47] C. Haffner, D. Chelladurai, Y. Fedoryshyn, A. Josten, B. Baeuerle, W. Heni, T. Watanabe, T. Cui, B. Cheng, S. Saha and D. e. a. Elder, "Low-loss plasmon-assisted electro-optic modulator," *Nature,* vol. 556, no. 7702, pp. 483-486, 2018.

[48] M. Eppenberger, A. Messner, B. Bitachon, W. Heni, T. Blatter, P. Habegger, M. Destraz, E. De Leo, N. Meier, N. Del Medico and C. e. a. Hoessbacher, "Resonant plasmonic micro-racetrack modulators with high bandwidth and high temperature tolerance," *Nature Photonics,* vol. 17, no. 4, pp. 360-367, 2023.

[49] J. Dionne, K. Diest, L. Sweatlock and H. Atwater, "PlasMOStor: a metal− oxide− Si field effect plasmonic modulator," *Nano letters,* vol. 9, no. 2, pp. 897-902, 2009.

[50] S. Tan, L. Wu, J. Yang, P. Bai, M. Bosman and C. Nijhuis, "Quantum Plasmon Resonances Controlled by Molecular Tunnel Junctions," *Science,* vol. 343, no. 6178, pp. 1496-1499., 2014.

[51] P. Nordlander, "Molecular tuning of quantum plasmon resonances," *Science,* vol. 343, no. 6178, pp. 1444-1445, 2014.

[52] M. Tame, K. McEnery, Ş. Özdemir, J. Lee, S. Maier and M. Kim, "Quantum plasmonics," *Nature Physics,* vol. 9, no. 6, pp. 329-340, 2013.

[53] J. Lee, D. Jeon and J. Yeo, "Quantum plasmonics: energy transport through plasmonic gap," *Advanced Materials,* vol. 33, no. 47, p. 2006606, 2021.

[54] J. Zuloaga, E. Prodan and P. Nordlander, "Quantum description of the plasmon resonances of a nanoparticle dimer," *Nano letters,* vol. 9, no. 2, pp. 887-891, 2009.

[55] R. Esteban, A. Zugarramurdi, P. Zhang, P. Nordlander, F. García-Vidal, A. Borisov and J. Aizpurua, "A classical treatment of optical tunneling in plasmonic gaps: extending the quantum corrected model to practical situations," *Faraday discussions,* vol. 178, pp. 151-183, 2015.

[56] J. Scholl, A. García-Etxarri, A. Koh and J. Dionne, "Observation of quantum tunneling between two plasmonic nanoparticles," *Nano letters,* vol. 13, no. 2, pp. 564-569, 2013.

[57] K. Savage, M. Hawkeye, R. Esteban, A. Borisov, J. Aizpurua and J. Baumberg, "Revealing the quantum regime in tunnelling plasmonics," *Nature,* vol. 491, no. 7425, pp. 574-577, 2012.

[58] R. Esteban, A. Borisov, P. Nordlander and J. Aizpurua, "Bridging quantum and classical plasmonics with a quantum-corrected model," *Nature communications,* vol. 3, no. 1, p. 825, 2012.

[59] H. Duan, A. Fernández-Domínguez, M. Bosman, S. Maier and J. Yang, "Nanoplasmonics: classical down to the nanometer scale," *Nano letters,* vol. 12, no. 3, pp. 1683-1689, 2012.

[60] S. Tan, "Quantum Plasmon Resonances Controlled by Molecular Tunnel Junction," in *Molecular Electronic Control Over Tunneling Charge Transfer Plasmons Modes*, Singapore, Springer, 2018, pp. 51-67.

[61] Y. Li, S. Lin, C. Zhang, Y. Chen, S. Zhou, L. Wang, S. Chen and T. Ding, "Charge Transfer Plasmons Enabled by Supramolecular Plug: From Optoelectronic Switching to Enhanced Chiral Sensing," *Journal of the American Chemical Society,* vol. 146, no. 42, pp. 28739-28747, 2024.

[62] P. Zhang, "Scaling for quantum tunneling current in nano-and subnano-scale plasmonic junctions," *Scientific reports,* vol. 5, no. 1, p. 9826, 2015.

[63] S. Sze, Y. Li and K. Ng, Physics of semiconductor devices, John wiley & sons, 2021.

[64] L. Wu, H. Duan, P. Bai, M. Bosman, J. Yang and E. Li, "Fowler–Nordheim tunneling induced charge transfer plasmons between nearly touching nanoparticles," *ACS nano,* vol. 7, no. 1, pp. 707-716, 2013.

[65] A. Stolz, J. Berthelot, M. Mennemanteuil, G. Colas des Francs, L. Markey, V. Meunier and A. Bouhelier, "Nonlinear photon-assisted tunneling transport in optical gap antennas," *Nano letters,* vol. 14, no. 5, pp. 2330-2338, 2014.

[66] G. Aguirregabiria, D. Marinica, R. Esteban, A. Kazansky, J. Aizpurua and A. Borisov, "Role of electron tunneling in the nonlinear response of plasmonic nanogaps," *Physical Review B,* vol. 97, no. 11, p. 115430, 2018.

[67] J. Tang, Q. Guo, Y. Wu, J. Ge, S. Zhang and H. Xu, "Light-emitting plasmonic tunneling junctions: current status and perspectives," *ACS nano,* vol. 18, no. 4, pp. 2541-2551, 2024.

[68] P. Février and J. Gabelli, "Tunneling time probed by quantum shot noise," *Nature communications,* vol. 9, no. 1, p. 4940, 2018.

[69] S. Zhou, K. Chen, M. Cole, Z. Li, M. Li, J. Chen, C. Lienau, C. Li and Q. Dai, "Ultrafast Electron Tunneling Devices—From Electric-Field Driven to Optical-Field Driven," *Advanced Materials,* vol. 33, no. 35, p. 2101449, 2021.

[70] J. Park, H. Kim, I. Lee, S. Kim, J. Jung and B. Lee, "Resonant tunneling of surface plasmon polariton in the plasmonic nano-cavity," *Optics express,* vol. 16, no. 21, pp. 16903-16915, 2008.

[71] M. Parzefall, P. Bharadwaj, A. Jain, T. Taniguchi, K. Watanabe and L. Novotny, "Antenna-coupled photon emission from hexagonal boron nitride tunnel junctions," *Nature nanotechnology,* vol. 10, no. 12, pp. 1058-1063, 2015.

[72] M. Parzefall, Á. Szabó, T. Taniguchi, K. Watanabe, M. Luisier and L. Novotny, "Light from van der Waals quantum tunneling devices," *Nature communications,* vol. 10, no. 1, p. 292, 2019.

[73] P. Wang, A. Krasavin, M. Nasir, W. Dickson and A. Zayats, "Reactive tunnel junctions in electrically driven plasmonic nanorod metamaterials," *Nature nanotechnology,* vol. 13, no. 2, pp. 159-164, 2018.

[74] H. Chalabi, D. Schoen and M. Brongersma, "Hot-electron photodetection with a plasmonic nanostripe antenna," *Nano letters,* vol. 14, no. 3, pp. 1374-1380, 2014.

[75] L. Meng, N. Xin, C. Hu, H. Sabea, M. Zhang, H. Jiang, Y. Ji, C. Jia, Z. Yan, Q. Zhang and L. Gu, "Dual-gated single-molecule field-effect transistors beyond Moore's law," *Nature communications,* vol. 13, no. 1, p. 1410, 2022.

[76] H. Zhang, J. Li, C. Yang and X. Guo, "Single-Molecule Functional Chips: Unveiling the Full Potential of Molecular Electronics and Optoelectronics," *Accounts of Materials Research,* vol. 5, no. 8, pp. 971-986, 2024.

[77] T. Wang and C. Nijhuis, "Molecular electronic plasmonics," *Applied Materials Today,* vol. 3, pp. 73-86, 2016.

[78] D. Ward, F. Hüser, F. Pauly, J. Cuevas and D. Natelson, "Optical rectification and field enhancement in a plasmonic nanogap," *Nature nanotechnology,* vol. 5, no. 10, pp. 732-736, 2010.

[79] P. Février, J. Basset, J. Estève, M. Aprili and J. Gabelli, "Role of optical rectification in photon-assisted tunneling current," *Communications Physics,* vol. 6, no. 1, p. 29, 2023.

[80] P. Davids, R. Jarecki, A. Starbuck, D. Burckel, E. Kadlec, T. Ribaudo, E. Shaner and D. Peters, "Infrared rectification in a nanoantenna-coupled metal-oxide-semiconductor tunnel diode," *Nature nanotechnology,* vol. 10, no. 12, pp. 1033-1038, 2015.

[81] J. Kim, B. Kang, J. Park, Y. Bahk, W. Kim, J. Rhie, H. Jeon, F. Rotermund and D. Kim, "Terahertz quantum plasmonics of nanoslot antennas in nonlinear regime," *Nano Letters,* vol. 15, no. 10, pp. 6683-6688, 2015.

[82] D. Kos, D. Assumpcao, C. Guo and J. Baumberg, "Quantum tunneling induced optical rectification and plasmon-enhanced photocurrent in nanocavity molecular junctions," *ACS nano,* vol. 15, no. 9, pp. 14535-14543, 2021.

[83] S. Namgung, D. Mohr, D. Yoo, P. Bharadwaj, S. Koester and S. Oh, "Ultrasmall plasmonic single nanoparticle light source driven by a graphene tunnel junction," *ACS nano,* vol. 12, no. 3, pp. 2780-2788, 2018.

[84] H. Qian, S. Hsu, K. Gurunatha, C. Riley, J. Zhao, D. Lu, A. Tao and Z. Liu, "Efficient light generation from enhanced inelastic electron tunnelling," *Nature Photonics,* vol. 12, no. 8, pp. 485-488, 2018.

[85] J. Kern, R. Kullock, J. Prangsma, M. Emmerling, M. Kamp and B. Hecht, "Electrically driven optical antennas," *Nature Photonics,* vol. 9, no. 9, pp. 582-586, 2015.

[86] W. Du, T. Wang, H. Chu and C. Nijhuis, "Highly efficient on-chip direct electronic–plasmonic transducers," *Nature Photonics,* vol. 11, no. 10, pp. 623-627, 2017.

[87] C. Zhang, J. Hugonin, A. Coutrot, C. Sauvan, F. Marquier and J. Greffet, "Antenna surface plasmon emission by inelastic tunneling," *Nature communications,* vol. 10, no. 1, p. 4949, 2019.

[88] A. Paoletta, N. Hoffmann, D. Cheng, E. York, D. Xu, B. Zhang, M. Delor, T. Berkelbach and L. Venkataraman, "Plasmon-Exciton Strong Coupling in Single-Molecule Junction Electroluminescence," *Journal of the American Chemical Society,* vol. 146, no. 50, pp. 34394-34400, 2024.

[89] E. Purcell, "Spontaneous emission probabilities at radio frequencies," *Physical Review,* vol. 69, no. 11-1, pp. 681-681, 1946.

[90] W. Barnes, "Fluorescence near interfaces: the role of photonic mode density," *Journal of Modern Optics,* vol. 45, no. 4, pp. 661-699, 1998.

[91] E. Fermi, "Quantum theory of radiation. , 4(1), p.87.," *Reviews of Modern Physics,* vol. 4, no. 1, p. 87, 1932.

[92] K. Drexhage, "IV interaction of light with monomolecular dye layers," in *Progress in Optics*, vol. 12, Elsevier, 1974, pp. 163-232.

[93] G. Ford and W. Weber, "Electromagnetic interactions of molecules with metal surfaces," *Physics Reports,* vol. 113, no. 4, pp. 195-287, 1984.

[94] M. Bauch, K. Toma, M. Toma, Q. Zhang and J. Dostalek, "Plasmon-enhanced fluorescence biosensors: a review," *Plasmonics,* vol. 9, pp. 781-799, 2014.

[95] J. Farahani, D. Pohl, H. Eisler and B. Hecht, "Single quantum dot coupled to a scanning optical antenna: a tunable superemitter," *Physical review letters,* vol. 95, no. 1, p. 017402, 2005.

[96] J. Lakowicz, Principles of fluorescence spectroscopy, 3rd ed., New York: Springer, 2006.

[97] E. Bailly, J. Hugonin, J. Coudevylle, C. Dabard, S. Ithurria, B. Vest and J. Greffet, "2D Silver-Nanoplatelets Metasurface for Bright Directional Photoluminescence, Designed with the Local Kirchhoff's Law," *ACS Nano,* vol. 18, no. 6, pp. 4903-4910, 2024.

[98] K. Shimizu, W. Woo, B. Fisher, H. Eisler and M. Bawendi, "Surface-enhanced emission from single semiconductor nanocrystals," *Physical review letters,* vol. 89, no. 11, p. 117401, 2002.

[99] J. Azoulay, A. Débarre, A. Richard and P. Tchénio, "Quenching and enhancement of single-molecule fluorescence under metallic and dielectric tips," *Europhysics Letters,* vol. 51, no. 4, p. 374, 2000.

[100] R. Carminati, M. Nieto-Vesperinas and J. Greffet, "Reciprocity of evanescent electromagnetic waves," *JOSA A,* vol. 15, no. 3, pp. 706-712, 1998.

[101] Y. Wang, T. Yang, M. Tuominen and M. Achermann, "Radiative rate enhancements in ensembles of hybrid metal-semiconductor nanostructures," *Physical Review Letters,* vol. 102, no. 16, p. 163001, 2009.

[102] J. Dong, Z. Zhang, H. Zheng and M. Sun, "Recent progress on plasmon-enhanced fluorescence," *Nanophotonics,* vol. 4, no. 4, pp. 472-490, 2015.

[103] J. Walia, S. Rashid, M. Amiri Naeini, G. Killaire, F. Variola, A. Weck and P. Berini, "Surface plasmons on silver gratings transform pyrolytic carbon into luminescent graphitized carbon dots," *The Journal of Chemical Physics,* vol. 161, no. 14, 2024.

[104] A. Vaskin, R. Kolkowski, A. Koenderink and I. Staude, "Light-emitting metasurfaces," *Nanophotonics,* vol. 8, no. 7, pp. 1151-1198, 2019.

[105] J. Khurgin, G. Sun and R. Soref, "Enhancement of luminescence efficiency using surface plasmon polaritons: figures of merit," *JOSA B,* vol. 24, no. 8, pp. 1968-1980, 2007.

[106] J. Greffet, R. Carminati, K. Joulain, J. Mulet, S. Mainguy and Y. Chen, "Coherent emission of light by thermal sources," *Nature,* vol. 416, no. 6876, pp. 61-64, 2002.

[107] J. Greffet, P. Bouchon, G. Brucoli and F. Marquier, "Light emission by nonequilibrium bodies: local Kirchhoff law," *Physical Review X,* vol. 8, no. 2, p. 021008, 2018.

[108] H. Monin, A. Loirette-Pelous, E. De Leo, A. Rossinelli, F. Prins, D. Norris, E. Bailly, J. Hugonin, B. Vest and J. Greffet, "Controlling light emission by a thermalized ensemble of colloidal quantum dots with a metasurface," *Optics Express,* vol. 31, no. 3, pp. 4851-4861, 2023.

[109] E. Bailly, K. Chevrier, C. Perez de la Vega, J. Hugonin, Y. De Wilde, V. Krachmalnicoff, B. Vest and J. Greffet, "Method to measure the refractive index for photoluminescence modelling," *Optical Materials Express,* vol. 12, no. 7, pp. 2772-2781, 2022.

[110] A. Nicol and W. Knoll, "Characteristics of fluorescence emission excited by grating-coupled surface plasmons," *Plasmonics,* vol. 13, no. 6, pp. 2337-2343, 2018.

[111] W. Knoll, M. Philpott, J. Swalen and A. Girlando, "Emission of light from Ag metal gratings coated with dye monolayer assemblies," *The Journal of Chemical Physics,* vol. 75, no. 10, pp. 4795-4799, 1981.

[112] S. Kitson, W. Barnes, J. Sambles and N. Cotter, "Excitation of molecular fluorescence via surface plasmon polaritons," *Journal of modern optics,* vol. 43, no. 3, pp. 573-582, 1996.

[113] M. Kreiter, T. Neumann, S. Mittler, W. Knoll and J. Sambles, "Fluorescent dyes as a probe for the localized field of coupled surface plasmon-related resonances," *Physical Review B,* vol. 64, no. 7, p. 075406, 2001.

[114] P. Andrew and W. Barnes, "Molecular fluorescence above metallic gratings," *Physical Review B,* vol. 64, no. 12, p. 125405, 2001.

[115] I. Pockrand, "Reflection of light from periodically corrugated silver films near the plasma frequency," *Physics Letters A,* vol. 49, no. 3, pp. 259-260, 1974.

[116] B. Paget, K. Ram, S. Zhang, J. Perumal, S. Vedraine, G. Humbert, M. Olivo and U. Dinish, "A review on photonic crystal fiber based fluorescence sensing for chemical and biomedical applications," *Sensors and Actuators B: Chemical,* vol. 400, p. 134828, 2024.

[117] M. Wahl, "Time-Correlated Single Photon Counting," PicoQuant GmbH, Berlin, Germany, 2014.

[118] W. Becker, A. Castleman, J. Toennies and W. Zinth, Advanced Time-Correlated Single Photon Counting Techniques, Berlin, Germany: Springer, 2005.

[119] W. Becker, Advanced time-correlated single photon counting applications, Switzerland: Springer, 2015.

[120] D. V. O'Connor and D. Phillips, Time-correlated single-photon counting, London, UK: Academic Press, 1984.

[121] "A practical guide to time-resolved luminescence lifetime determination using dedicated Time-Correlated Single-Photon Counting systems," Horiba Jobin Yvon IBH Ltd, Glasgow, Scotland, UK.

[122] M. Naeini and P. Berini, "High-speed electro-optic plasmonic modulator for CMOS non-contact wafer-level testing," *IEEE Journal of Selected Topics in Quantum Electronics,* vol. 30, no. 4, pp. Adv. Mod. and Int. beyond Si and InP-based Plt., pp. 1-9, 2024.

[123] M. Amiri Naeini and P. Berini, "Infrared surface plasmons open a hole tunneling channel in metal–Oxide–Semiconductor structures," *ACS Photonics,* vol. 10, no. 9, pp. 3321-3330, 2023.

[124] N. Li, Y. Lai, S. Lam, H. Bai, L. Shao and J. Wang, "Directional control of light with nanoantennas," *Advanced optical materials,* vol. 9, no. 1, p. 2001081, 2021.

[125] S. Liu, L. Huang, J. Li, C. Wang, Q. Li, H. Xu, H. Guo, Z. Meng, Z. Shi and Z. Li, "Simultaneous excitation and emission enhancement of fluorescence assisted by double plasmon modes of gold nanorods," *The Journal of Physical Chemistry C,* vol. 117, no. 20, pp. 10636-10642, 2013.

[126] W. Zhao, X. Tian, Z. Fang, S. Xiao, M. Qiu, Q. He, W. Feng, F. Li, Y. Zhang, L. Zhou and Y. Tan, "Engineering single-molecule fluorescence with asymmetric nano-antennas," *Light: Science & Applications,* vol. 10, no. 1, p. 79, 2021.

[127] E. Palik, Handbook of optical constants of solids, Academic press, 1998.

[128] I. Prigogine and S. Rice, "Molecular Fluorescence and Energy Transfer Near Interfaces," in *Advances in chemical physics*, John Wiley & Sons, 2009, p. Vol. 37.

[129] I. De Leon and P. Berini, "Modeling surface plasmon-polariton gain in planar metallic structures," *Optics Express,* vol. 17, no. 22, pp. 20191-20202, 2009.